# Numerical Analysis of a Large-Scale Levee on Soft Soil Deposits Using Two-Phase Finite Deformation Theory

2010

Mojtaba MIRJALILI

# Abstract

A multilayered ground composed of alluvial sand layers and soft clay layers is a common stratigraphic profile of most urban areas in Japan. Urban development with respect to natural disaster countermeasures often necessitates the construction of rather massive structures on soft soil deposits, e.g., the construction of a large-scale river embankment along the riverbank. The large-scale river embankment or super levee is an embankment with a broad width which can withstand even overflow, so that destruction by a dike break and its resultant flooding can be prevented.

In the present research, the numerical analysis of a large-scale levee construction in Torishima, Osaka City, Japan is presented in terms of the long-term consolidation analysis and the dynamic analysis. The ground consists of alluvial sandy layers and soft clay deposits, which have been locally improved by several methods, including deep mixing beneath the main levee, and combination of sand drains and sand compaction piles under the extended back slope part. Almost 10 years after the completion of the Torishima super levee, subsidence and superficial cracks were observed around the road pavement on the top of the super levee. Subsequently, a comprehensive investigation was conducted to find the causes of the deformations in this case, as well as the evaluation of the super levee behavior under dynamic loadings.

Firstly, modeling of Osaka soft clay obtained from Torishima site was conducted using an elasto-viscoplastic constitutive model. The effect of destructuration, demonstrated by the shrinkage of the yield and the overconsolidation boundary surfaces, and the strain dependency of elastic shear modulus, were studied through a comparison of the simulations with the experimental results for the undrained triaxial compression tests. The strain dependency of shear modulus is newly introduced in this study to reproduce the soil behavior more precisely, particularly at the earlier stage of loading.

Secondly, the long-term consolidation analysis of this super levee has been carried out through the finite element simulations. The finite element formulations, within the finite deformation theory for a Biot's type two-phase mixture, were applied in the numerical analysis. The construction sequence for the super levee was included in the numerical simulation by implementing the simulation in several stages based on the real loading profile of the embankment construction. The simulations were conducted in two phases, namely, the first phase for the natural (unimproved) ground case, and the second for the improved ground case. The effects of the destructuration aspects in clay layers were studied in terms of the consolidation behavior of the unimproved ground case. For the improved case, the analysis was performed by including the ground-improved zones in the finite element simulation. The field observation data obtained during the preloading process, prior to the construction of the super levee, were employed to verify the assumptions and to calibrate the material

properties of the improved layers. The effects of destructuration in the natural ground cases were observed as the excess pore pressure buildup after the construction and the strain localization. The effects of the ground improvement techniques were studied by comparison of the deformation results and the excess pore water pressure responses with the natural ground case. The numerical results show that it is important to carefully estimate the unequal long-term settlement for the construction of large-scale embankment on soft soil deposits.

Thirdly, a cyclic elasto-viscoplastic constitutive model was presented by which the characteristics parameters of the Torishima soft clay were determined through the integration of the constitutive equations. The simulation results were compared with the cyclic triaxial test data for the stress-strain relations and stress paths. Attempts were made to obtain the parameters so as the best agreement can be achieved between the simulated results and experimental data. The dynamic finite element formulation for a two-phase mixture theory was then derived within the finite deformation theory with updated Lagrangian scheme. The finite deformation theory based formulations were applied to appropriately simulate the large deformation phenomena. Using the derived formulations, a sophisticated three-dimensional computer program entitled COMVI3D-DY10 was developed for large deformation analysis of the multilayered systems subjected to dynamic loading conditions. The cyclic elasto-viscoplastic and the cyclic elasto-plastic constitutive models have been included in the code. As an example of large deformation problems, the strain localization analysis of soft clay samples subjected to a compelled acceleration were conducted under plane strain conditions. The shear banding process was examined through the strain distributions and the mean effective stress distributions in the specimen.

Finally, the dynamic analysis of the Torishima super levee was conducted through two cases; as the natural (unimproved) ground case and the improved ground case. The cyclic triaxial test simulations were carried out on the sand specimens from the upper sand layer of Torishima site, to obtain the material parameters using the cyclic elasto-plastic constitutive model. The dynamic behavior of the super levee on multilayered ground was thoroughly evaluated by the acceleration responses, the displacements, the excess pore pressure, and the strain distributions for the unimproved and improved ground cases. Moreover, the effects of the ground improvement techniques on the liquefaction-induced large deformation in the super levee were studied.

Based on the outcomes of this study, some recommendations were given for the construction and design guideline of super levees, by which the occurrence of such local settlement and superficial cracks during the consolidation, like that happened in Torishima case, and/or during the earthquake loading can be prevented in the future projects.

# Acknowledgments

This doctoral dissertation arose in part out of three years of research in the Geomechanics Laboratory, Kyoto University. It is a pleasure to express my gratitude to all the people; I have worked with during that time, in my profound acknowledgment.

In the first place, I would like to express my profound gratitude and appreciation to Professor Fusao Oka for his supervision, advice, and guidance in all aspects throughout of this research work. His patience and availability with most dynamic and encouraging personality, for any assistance whenever needed during my doctoral course study, are highly appreciated. His scientist intuition and vast knowledge in the field of geomechanics have greatly contributed to the success of this research. Furthermore, I am truly indebted to him for giving me such an opportunity to follow the International Doctoral Program in Engineering organized by the Graduate School of Engineering, Kyoto University.

I wish to express my gratitude to the dissertation committee member, Professor Takeshi Katsumi, for his valuable comments in reviewing this thesis. I would like to extent my thanks to Associate Professor Sayuri Kimoto for her valuable suggestions, constructive discussion, and comments during my doctoral research. I have also benefited by constructive advice and help from Assistant Professor Yosuke Higo on various occasions, which I would like to appreciate it. I gratefully thank Ms. Chikako Itou, secretary of Oka Laboratory, who has been so kind in assisting me with all Japanese daily life matters during these three years of my stay in Japan.

It has been a great experience for me to be a part of the research group in the Oka Laboratory. I would like to express my thanks, in general, to all the former and current members of Oka Laboratory, who have accompanied me during my period of study. Many thanks go in particular to my friend Edwin Garcia for all the help and the knowledge exchange during his contemporary research with me, to my friend Babak Shahbodagh Khan for his kindly assistance and helps in developing the computer program and checking the formulations, and also to formerly graduated, Dr. Huaiping Feng, Dr. Quoc Huy Nguyen, and Ms. Ana Heitor for their friendship and companionship during the daily life in Japan.

I would like to acknowledge the financial support provided by the Monbukagakusho Scholarship Program of the Ministry of Education, Culture, Sports, Science, and Technology (MEXT), Japan. This study has been partially supported by the new technological development study group of the Kinki Regional Development Bureau, Ministry of Land, Infrastructure, Transport, and Tourism (MLIT), whose support is acknowledged with thanks and appreciation. In addition, the support of the Yodogawa River Office is gratefully acknowledged.

Finally, with sincere love, I would like to thank my parents, my sisters, and my brothers, for all their endless support, concerns, and encouragement in my entire life and in particular during my study abroad at Kyoto University.

# TABLE OF CONTENTS

# LIST OF FIGURES

# LIST OF TABLES

# Chapter 1

# INTRODUCTION

## 1.1. Background and Objectives

Flooding and sediment-related disasters have been a main cause of damage all around the world. In Japan, due to the high precipitation and the specific characteristics of rivers, flooding has been one of the main natural disasters resulting in severe damage and destruction over the past several years. Most rivers in Japan flow directly from the mountains to the sea with a short stream length and a steep gradient, which results in a rapid flow and a high flood risk. One half of the entire country's population and 70 percent of the national assets are concentrated in the low-lying flood plains and in the basins of major rivers, which are designated as potential flood hazard areas. In such areas, levees or flood walls are conventionally constructed along the rivers to control inundation and consequent damages. These levees have been considered as important structures for the prevention of floods. In order to confine floods within rivers, continuous levee lines have been constructed along the rivers in Japan as part of a comprehensive flood control management plan (Takeuchi 2002)

The investigation of past flood disasters, such as Hurricane Katrina in 2005 which resulted in extensive devastation and more than 1000 fatalities due to the breaching of levees, has raised serious concerns regarding the vulnerability of levees and flood control structures, not only for disasters resulting from recent events, but also for worst-case scenarios like the combination of an earthquake and heavy rainfall, which may induce more severe damage to levees than flooding alone. Considering the low reliability and the weakness of conventional river embankments against disasters, a high-standard river embankment, so-called 'super levee', was firstly proposed in Japan as protection along

major rivers where absolutely no embankment collapse can be allowed (Kundzewicz and Takeuchi 1999). A super levee is constructed by widening the back slope of a normal river embankment to a broad width (200-500 m) with a gentle slope, on which urban buildings and traffic facilities are developed. The construction costs are justified since this process redevelops urban areas and increases the value of the developed lands. The super levees can withstand even overflow, so that destruction by an embankment break and its resultant flooding can be prevented. In addition, a super levee is expected to have more resistibility against earthquakes and the consequent damage they cause. Figure 1.1 shows an example plan of a super levee. As depicted in the figure, ordinary land use is permitted in the high-standard embankment areas.

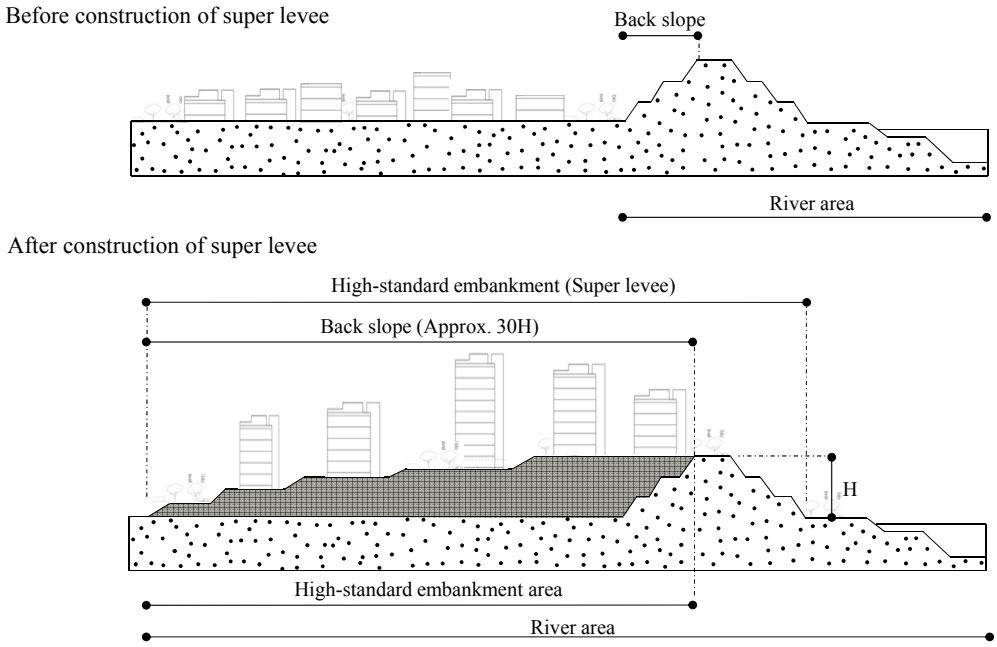


*Figure 1.1. Example plan of a super levee: normal levee vs. super levee.*

In the past few years, many parts of the continuous levee line in the downstream of the Yodo River in Osaka City, Japan have been widened to super levees. The Yodo River is the largest river in the Osaka metropolitan region and has a high risk of flooding. Any levee breakage alongside this river would result in severe damage and human fatalities. Despite the advantages of super levees, in comparison with normal levees, several unknown issues prevail concerning the construction of such massive embankments, particularly on soft ground deposits beside rivers. On the other hand, the necessity of super levee construction in that area, as part of the flood control management system, demands a comprehensive study on the failure and/or deformation mechanism and the overall behavior of the levee over soft soil strata.

In the present study as the main objective, consolidation and dynamic analyses of a super levee along the Yodo River at Torishima is carried out. The Torishima super levee is located at the left bank of the Yodo River, which flows into Osaka Bay, in the western part of Osaka City. The super levee extends about 450 m in length along the riverbank from kilopost 1k500 to 1k900. Figure 1.2 shows a general map of the area with a bird's-eye view of Torishima super levee site. Due to the 1995 Kobe (Great Hanshin) Earthquake, about 2000 m of the continuous levee line along the Yodo River, including the Torishima dike, were severely damaged by the liquefaction of the foundation soil (Matsuo 1996). Thereafter, the rebuilding of the levee on that site was initiated by the construction of a super levee. The main levee, with a height of 8.1 m, was built on a foundation improved by deep mixing. The back slope extension has been constructed on a foundation improved by sand drains and sand compaction piles, with a gentle slope of approximately 1V:29H. Prior to the construction of the super levee, the preloading process had been accomplished to improve the characteristics of the clay layers by pre-loading.

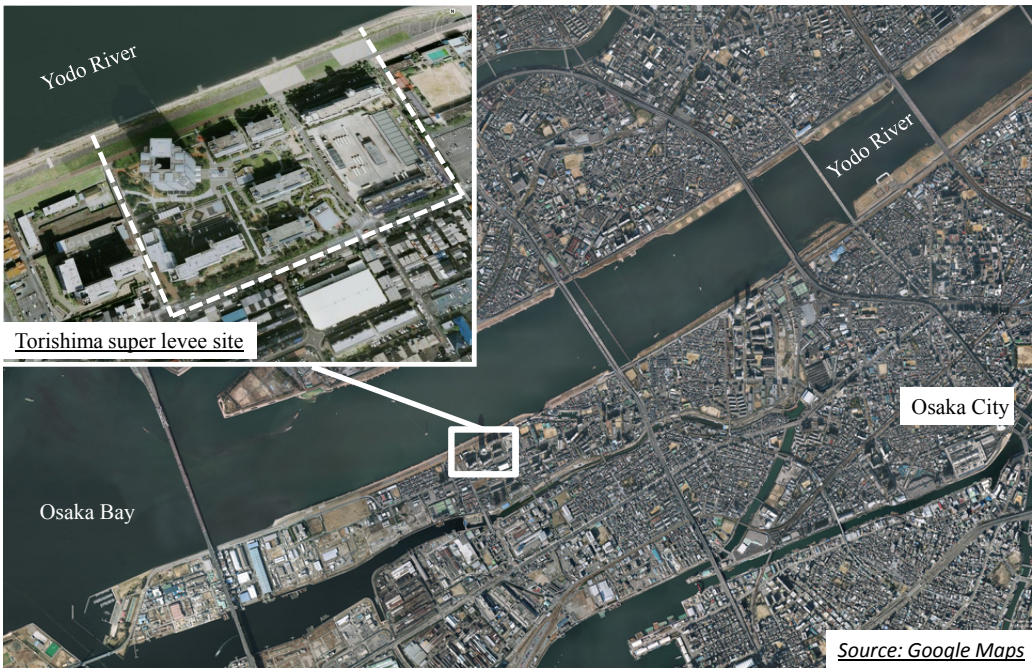


*Figure 1.2. Aerial view of Torishima super levee site.*

Almost 10 years after the completion of the Torishima super levee, ground settlement with superficial cracks were observed on the top of the super levee around the road pavement, as shown in Figure 1.3 (Oka 2009). Subsequently, a comprehensive investigation was conducted to find the causes of the deformations in this case and to evaluate the behavior of the super levee under static and dynamic loadings. The outcomes of the investigation could then be employed to revise the current

construction guidelines for super levees. According to the current Japanese construction manual for high-standard river embankments, the only criterion for settlement control is that the allowed settlement must be limited to 10 cm for design purposes.

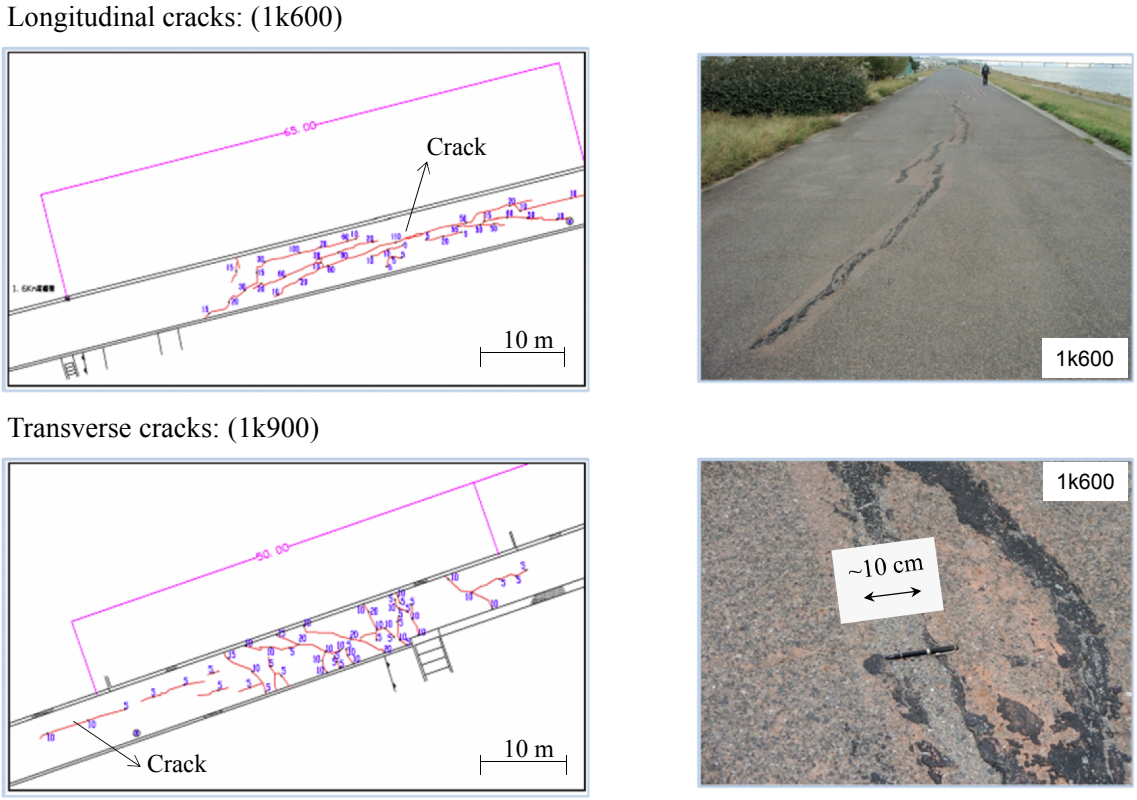


*Figure 1.3. Superficial cracks on the top of the Torishima super levee.*

Concerning the consolidation analysis of such a massive levee on soft soil deposits containing soft clay layers, the characteristics behavior of sensitive soft clay during shearing should be particularly taken into account. Soft clay specimens have shown complex behavior during shearing, which can be associated with the collapse of the soil structure and microstructural changes. The structure of natural soil consists of two components, namely, the fabric and the bonding between particles (Burland 1990). The term 'destructuration' is often used to describe the progressive damage to the bonding between soil particles during plastic straining. In many natural soft clays, the presence of interparticle bonding is demonstrated by sensitivity. The sensitivity of clay is defined as the ratio of its undisturbed strength to its remolded strength (Terzaghi 1944). The sensitivity may range from about 4, for sensitive clays, to values of over 100, for so-called extra-sensitive or quick clays. In fact, most clays, except for those which have been heavily overconsolidated, lose a portion of their original strength after remolding. For Osaka soft clay, sensitivity levels of 4 to 10 are quite common, which

indicates the high sensitivity for this type of clay. In some areas, however, larger values have been reported (e.g., Adachi et al. 1995, KG-NET 2007). Certain types of unstable behavior, such as the anomalous pore pressure response after the completion of loading and secondary creep caused by the destructuration in sensitive clays, have been reported by many researchers, e.g., Mesri and Choi (1979), Mitchell (1986), Lavallee et al. (1992), Hunter 2003, etc.

The destructuration of Osaka soft clay specimens from Torishima site is studied via the elasto-viscoplastic modeling under undrained triaxial conditions. The effect of the destructuration is then evaluated in a boundary value problem as the consolidation analysis of an embankment on one-layer foundation characterized by the material parameters of Osaka soft clay. For the numerical simulation of the boundary value problem, the finite element formulations within the framework of finite deformation theory are employed to appropriately simulate the large deformation phenomenon induced in soft clay layer under the embankment loading.

The behavior of the soils under embankment loading, like any other nonlinear materials, is dependent on the orientation of the applied principal stresses. In the analysis of embankment construction, the placing of the fill materials results in the rotation of the principal stresses in the ground foundation. This effect is considered by including the Lode angle in the constitutive equations. The inclusion of Lode angle is accomplished through the Mohr-Coulomb failure criterion as the variation of the stress ratio. The Lode angle describes the magnitude of the intermediate principal stress with respect to the maximum and minimum principal stress values. Figure 1.4 displays the projection of the principal stress axes in the $\pi$-plane with a definition of the Lode angle $\theta$, in which vector $\overrightarrow{B'A'}$ is the projection of the stress vector in the $\pi$-plane, $n_i^{(1)}$ is the unit vector along $\sigma_1$ axis, and vector $\overrightarrow{B'C'}$ is the projection of vector $\overrightarrow{B'A'}$ along the unit vector (Chen and Mizuno 1990).

The construction process of the embankment in the finite element models can be considered through the simplified approach, in which the embankment loading is applied as the incremental nodal forces on the embankment-ground interface elements, following the construction history of the embankment. This is the simplest possible approximation for the construction load. However, in order for the analysis to consider the stiffness and deformation of the embankment in an appropriate manner, the embankment layers must be included in the finite element model as it is. Construction of the material must be performed incrementally following the layered construction procedure. This procedure is presented in detail in Section 2.4.3.

In addition to the long-term consolidation behavior, the behavior of the super levee under the dynamic loading conditions needs to be evaluated. According to the subsurface layers profile, the existence of loose saturated sand layers justifies the high potential of liquefaction and the subsequent

large deformations at the ground levels and atop the super levee, which becomes more extensive since the large deformations induced by the sensitive soft clays are also likely to happen. In order to properly predict the behavior of soft clay under dynamic loading conditions, a cyclic elasto-viscoplastic constitutive model is introduced. The performance of the model is verified though the modeling of soft clay samples under cyclic triaxial loading conditions.

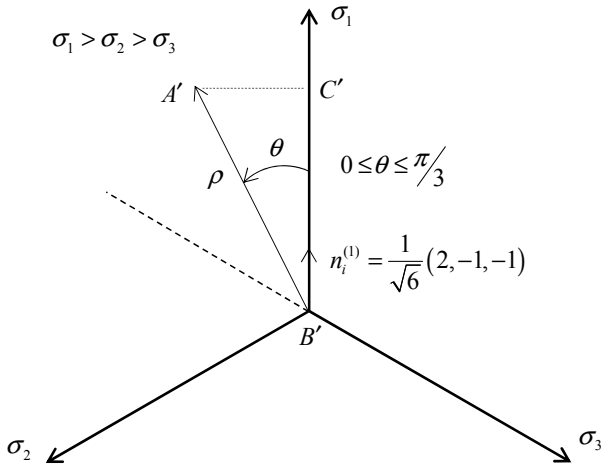


*Figure 1.4. Stress state on π-plane with the definition of Lode angle θ.*

To further the simulation of the super levee under dynamic loading, a sophisticated three-dimensional computer program is developed based on the finite element formulations in the framework of two-phase finite deformation theory. In order to suitably analyze the large deformation phenomenon, the finite deformation theory with updated Lagrangian scheme must be adopted. The cyclic elasto-viscoplastic model for the clay and the cyclic elasto-plastic constitutive model for the granular materials are incorporated in the code. The performance of the program is evaluated in the strain localization analysis of the Osaka soft clay specimen under dynamic loading conditions. Strain localization or shear banding is a phenomenon in materials under shearing, by which plastic deformations localize into finite narrow bands of intense straining. Finally, the dynamic analysis of Torishima super levee is carried out as the natural (unimproved) ground case and the improved ground case. The dynamic response of the super levee as well as the effect of ground improvement techniques are examined through the improved ground case and by comparison of the results with those for the natural ground case.

## 1.2. Organization of the Dissertation

This doctoral dissertation is organized in six chapters including the present one, which are outlined as follows:

Chapter 1 gives a brief introduction about the background and objectives of the current research.

Chapter 2 provides the elasto-viscoplastic modeling of Osaka soft clay specimen taking into account the destructuration aspects, namely, the microstructural degradation and the strain dependency of elastic shear modulus. The degradation of the elastic shear modulus as the strain dependency is introduced herein to improve the stress-strain relation results at the earlier stage of loading. The consolidation analysis of an embankment construction on a soft clay layer foundation is also presented in this chapter evaluating the effects of each destructuration aspects in a boundary value problem.

Chapter 3 presents the consolidation analysis of the Torishima super levee construction on soft soil deposits, in which the effects of destructuration of soft clay layers are studied through three cases on the natural ground, followed by the analysis of the improved ground case according to the project specifications. The embankments of the super levee are properly modeled in the finite element mesh so that the stiffness and the consolidation of the embankments can be considered in addition to the embankment loading.

Chapter 4 presents a cyclic elasto-viscoplastic model and its application to simulate the behavior of soft clay specimens under cyclic triaxial loading conditions. The characteristic parameters of the soft clay layers at Torishima super levee site are also determined by integration of the constitutive equations under the cyclic triaxial conditions and the comparison of the simulated results with the laboratory tests data.

Chapter 5 demonstrates the dynamic analysis of soft soil deposits using the finite deformation theory which contains the details of the dynamic finite element formulation for a two-phase mixture theory, in addition to the results of the dynamic strain localization analysis for a soft clay specimen under plane strain conditions. The dynamic analysis results of the Torishima super levee are also presented in this chapter considering the effect of the ground improvement techniques and the multilayered ground response on the super levee.

The last chapter, Chapter 6, highlights some remarkable conclusions of the study which is followed by a number of recommendations. Based on the results of present case study on the Torishima super levee, some practical recommendations are given regarding the construction

guideline of super levees. In addition, some recommendations are proposed for the further works in the context of this study.

# Chapter 2

# ELASTO-VISCOPLASTIC MODELING OF OSAKA SOFT CLAY CONSIDERING DESTRUCTURATION

## 2.1. Introduction

Certain types of unstable behavior, such as the anomalous pore pressure response after the completion of loading and secondary creep caused by the destructuration in sensitive clays, have been reported by many researchers. Prediction of these phenomena by numerical modeling has been investigated over the last few decades. Oka et al. (1991) have introduced the variation of the viscoplastic parameter into the original elasto-viscoplastic constitutive model, proposed by Adachi and Oka (1982), to represent the structural breakdown of clay. However, it was not able to successfully reproduce the field anomalous soil behavior during long-term consolidation. Later on, Kimoto and Oka (2005) improved the elasto-viscoplastic constitutive model for use in predicting the unstable behavior during consolidation. In their proposed model, structural changes are expressed as strain softening, with respect to the accumulation of viscoplastic strain, so that the model can describe the instability not only around the failure stress, but also during compressive deformation. A validation of the proposed model has been performed by applying it to simulate various laboratory and field tests in addition to practical problems (e.g., Kimoto and Oka 2005, Oka et al. 2008, Karim and Oka 2010). Although giving consideration to the effect of structural degradation on strain softening and post-peak responses has helped to improve reproductions of the stress-strain behavior of soft clays, the reproduced results,

particularly in the small strain range, have often differed from the laboratory test data. Hence, the strain dependency of the elastic shear modulus is employed to overcome this inadequacy in the modeling of soft clays.

It is well known that the deformation characteristics of soils, particularly the elastic shear modulus, are non-linear due to the microstructural changes that occur during loading. The shear modulus at small strain levels is often expressed as the function of the void ratio and the effective confining stress through the several empirical equations from the laboratory tests (Ishihara 1996). Consideration of the effective confining pressure has been made by normalizing the shear modulus through a power function of the mean effective stress. For large stains, however, the strain dependency of the shear modulus should also be taken into account. An evaluation of the variation in the shear modulus in the experiments reveals the significant reduction in the shear modulus when strain increases. Several empirical equations have been proposed for the strain-dependent shear modulus of geomaterials (e.g., Kovacs et al. 1971, Hardin and Drnevich 1972, Seed et al. 1986, etc.). For soft clays, Ogisako et al. (2007) have shown the normalized elastic shear modulus reduction function based on the viscoplastic shear strain and have proposed a hyperbolic equation for that expression in the elasto-viscoplastic constitutive model.

In this chapter, the effect of destructuration on soft clay behavior is studied. In order to predict the soil behavior, using the elasto-viscoplastic model proposed by Kimoto and Oka (2005), the model parameters are firstly determined based on the laboratory test data. Then, triaxial test simulations are performed considering the destructuration parameters, i.e., structural degradation and the strain-dependent shear modulus. Comparisons are made through the stress-strain relations and the stress paths under undrained triaxial compression conditions. The influences of the structural degradation and the strain-dependent shear modulus are particularly studied in a two-dimensional consolidation analysis of an embankment construction on a layer of Osaka soft clay. Several cases have been considered in order to properly study the effect of each aspect of destructuration in the two-dimensional problem.

## 2.2. Elasto-Viscoplastic Constitutive Model for Water-Saturated Soils

As mentioned earlier, the elasto-viscoplastic constitutive model proposed by Kimoto and Oka (2005) is adopted. The model is an extension of the rate-dependent model for water-saturated clay, firstly proposed by Adachi and Oka (1982), which combines the Cam-clay model (Roscoe, Schofield and Thurairajah 1963) and Perzyna's (1963) overstress type of viscoplasticity for the elasto-viscoplastic formulation. Kimoto and Oka (2005) improved the original model by Adachi and Oka (1982) in order

to overcome the structural degradation of the soil skeleton, considering the shrinkage of both the overconsolidation boundary surface and the static yield surface with respect to the accumulation of viscoplastic strain. In this section, the features of the model are described as can be found in Kimoto and Oka (2005). However, the model is modified here in several ways, namely, the variation in the stress ratio at failure by Lode's angle, the introduction of a new definition for the dilatancy coefficient, and the introduction of the strain dependency of the elastic shear modulus.

In the adopted constitutive model, Terzaghi's effective stress for water-saturated soil is used by considering that extension is positive even for the pore pressure, as

$$\sigma_{ij} = \sigma'_{ij} + U_w \delta_{ij} \tag{2.1}$$

where $\sigma_{ij}$ is the total stress tensor, $\sigma'_{ij}$ is the effective stress tensor, $U_w$ is the pore water pressure, and $\delta_{ij}$ is Kronecker's delta. In addition, total strain rate tensor $\dot{\varepsilon}_{ij}$ is assumed to be divided into two parts, namely,

$$\dot{\varepsilon}_{ij} = \dot{\varepsilon}^e_{ij} + \dot{\varepsilon}^{vp}_{ij} \tag{2.2}$$

where $\dot{\varepsilon}^e_{ij}$ denotes the elastic strain rate tensor and $\dot{\varepsilon}^{vp}_{ij}$ is the viscoplastic strain rate tensor. The elastic strain rate tensor is expressed as

$$\dot{\varepsilon}^e_{ij} = \frac{1}{2G}\dot{S}_{ij} + \frac{\kappa}{3(1+e)}\frac{\dot{\sigma}'_m}{\sigma'_m}\delta_{ij} \tag{2.3}$$

in which $G$ is the elastic shear modulus, $S_{ij}$ is the deviatoric stress tensor ($S_{ij} = \sigma'_{ij} - \sigma'_m \delta_{ij}$), $\sigma'_m$ is the mean effective stress, and the superimposed dot denotes the time differentiation. $\kappa$ is the swelling index and $e$ is the void ratio. The degradation of elastic shear modulus $G$ as a function of strain will be presented in the next section. In the present study, the initial void ratio $e_0$ is used in Equation (2.3) for simplicity.

### 2.2.1. Overconsolidation Boundary Surface

An overconsolidation boundary surface is assumed to delineate the normally consolidated (NC) region and the overconsolidated (OC) region as

$$f_b = \overline{\eta}^*_{(0)} + M^*_m \ln\left(\sigma'_m / \sigma'_{mb}\right) = 0 \tag{2.4}$$

where $f_b < 0$ indicates the overconsolidated region and $f_b \geq 0$ shows the normally consolidated region. $\bar{\eta}^*_{(0)}$ is the relative stress ratio defined by

$$\bar{\eta}^*_{(0)} = \sqrt{\left(\eta^*_{ij} - \eta^*_{ij(0)}\right)\left(\eta^*_{ij} - \eta^*_{ij(0)}\right)} \tag{2.5}$$

in which subscript (0) denotes the initial state before deformation and $\eta^*_{ij}$ is the stress ratio tensor. $\sigma'_{mb}$ controls the size of the OC boundary surface. $M^*_m$ is the value of $\eta^* = \sqrt{\eta^*_{ij}\eta^*_{ij}}$ when the volumetric strain increment changes from compression to swelling. In order to include Mohr-Coulomb's failure criterion with zero cohesion, stress ratio $M^*_m$ is considered to be a function of Lode's angle $\theta$ given by

$$\theta = \frac{1}{3} cos^{-1}\left[\frac{3\sqrt{3}}{2}\frac{J_3}{J_2^{3/2}}\right] \tag{2.6}$$

$$M^*_m(\theta) = \frac{6\sqrt{2}\sin\phi}{(3+3\sin\phi)\sin\theta + \sqrt{3}(3-\sin\phi)\cos\theta} \tag{2.7}$$

where $J_2$ and $J_3$ are the second and the third invariants of the deviatoric stress tensor, respectively, and $\phi$ is the internal frictional angle. Lode's angle varies in the range of $0 \leq \theta \leq \pi/3$, where $\theta = 0$ represents the triaxial compression mode and the maximum value shows the extension mode of loading under triaxial conditions. In Equation (2.7), by taking $\theta = 0$, the stress ratio at triaxial compression $M^*_{mc}$ can be obtained as

$$M^*_{mc} = \sqrt{\frac{2}{3}}\frac{6\sin\phi}{3-\sin\phi} \tag{2.8}$$

To describe the structural degradation of clay, strain softening with the accumulated viscoplastic strain is introduced in addition to strain hardening with the viscoplastic volumetric strain as

$$\sigma'_{mb} = \sigma'_{ma}\ \exp\left(\frac{1+e_0}{\lambda-\kappa}\varepsilon^{vp}_v\right) \tag{2.9}$$

where $\sigma'_{ma}$ is assumed to decrease with an increase in viscoplastic strain with

$$\sigma'_{ma} = \sigma'_{maf} + \left(\sigma'_{mai} - \sigma'_{maf}\right)\exp(-\beta z^h) \tag{2.10}$$

in which $z$ is the accumulation of the second invariant of the viscoplastic strain rate given by

$$z = \int_0^t \dot{z} dt \quad ; \quad \dot{z} = \sqrt{\dot{\varepsilon}_{ij}^{vp} \dot{\varepsilon}_{ij}^{vp}} \tag{2.11}$$

In Equation (2.10), $\sigma'_{mai}$ and $\sigma'_{maf}$ are the initial and the final values for $\sigma'_{ma}$, respectively. $\beta$ is a parameter that stands for the changing rate of $\sigma'_{ma}$, while the proportion of $n = \sigma'_{maf} / \sigma'_{mai}$ provides the degree of possible collapse of the soil structure at the initial state. $h$ is an additional degradation parameter with a non-negative value that controls the rate of degradation of the soil skeleton. In this study, the value of this parameter is assumed as $h = 1$.

### 2.2.2. Static Yield Function

In the following, static yield function $f_y$ has been proposed to explain the mechanical behavior of clay at its static equilibrium state as

$$f_y = \overline{\eta}_{(0)}^{*} + \tilde{M}^{*} \ln\left(\sigma'_m / \sigma'^{(s)}_{my}\right) = 0 \tag{2.12}$$

where $\sigma'^{(s)}_{my}$ denotes the static hardening parameter.

Static equilibrium state $f_y = 0$ refers to the case when no viscoplastic deformation occurs, which can only be reached after an infinite time. Incorporating the strain softening for the structural degradation, the hardening rule of $\sigma'^{(s)}_{my}$ can be expressed as

$$\sigma'^{(s)}_{my} = \frac{\left\{\sigma'_{maf} + \left(\sigma'_{mai} - \sigma'_{maf}\right)\exp(-\beta z)\right\}}{\sigma'_{mai}} \sigma'^{(s)}_{myi} \exp\left(\frac{1+e_0}{\lambda-\kappa}\varepsilon_v^{vp}\right) \tag{2.13}$$

### 2.2.3. Viscoplastic Potential Function

In the same manner as for the static yield function, viscoplastic potential function $f_p$ is given by

$$f_p = \overline{\eta}_{(0)}^{*} + \tilde{M}^{*} \ln\left(\sigma'_m / \sigma'_{mp}\right) = 0 \tag{2.14}$$

where dilatancy coefficient $\tilde{M}^*$ is defined separately for the overconsolidated region (OC) and the normally consolidated region (NC). In the original definition by Kimoto and Oka (2005), $\tilde{M}^*$ is given by

$$\tilde{M}^* = \begin{cases} M_m^*(\theta) & \text{:NC region} \\ -\dfrac{\sqrt{\eta_{ij}^* \eta_{ij}^*}}{\ln(\sigma_m^{'} / \sigma_{mc}^{'})} & \text{:OC region} \end{cases} \tag{2.15}$$

in which $\sigma'_{mc} = \sigma'_{mb}$ for isotropic consolidation. In general, it can be expressed as

$$\sigma'_{mc} = \sigma'_{mb} \exp\left(\frac{\sqrt{\eta^*_{ij(0)} \eta^*_{ij(0)}}}{M_m^*(\theta)}\right) \tag{2.16}$$

According to the above definition, the value of dilatancy coefficient $\tilde{M}^*$ becomes zero when the stress path coincides with the mean effective stress axis during cyclic loading. Therefore, a new definition for $\tilde{M}^*$ (Kimoto et al. 2007) is introduced here as

$$\tilde{M}^* = \begin{cases} M_m^*(\theta) & \text{:NC region} \\ \left(\sigma_m^* / \sigma'_{mb}\right) M_m^*(\theta) & \text{:OC region} \end{cases} \tag{2.17}$$

where $\sigma_m^*$ denotes the mean effective stress at the intersection of the surface, which has the same shape as $f_b$, and is given by

$$\sigma_m^* = \sigma'_m \exp\left(\frac{\overline{\eta}^*_{(0)}}{M_m^*(\theta)}\right) \tag{2.18}$$

The overconsolidation boundary surface, the static yield function, and the viscoplastic potential function are illustrated for isotropically consolidated soil in Figure 2.1.

### 2.2.4. Viscoplastic Flow Rule

Based on the overstress type of viscoplastic theory, first adopted by Perzyna (1963), viscoplastic strain rate tensor $\dot{\varepsilon}_{ij}^{vp}$ is defined as

$$\dot{\varepsilon}_{ij}^{vp} = C_{ijkl} \left\langle \Phi\left(f_y\right) \right\rangle \frac{\partial f_p}{\partial \sigma'_{kl}} \tag{2.19}$$

$$\left\langle \Phi\left(f_y\right) \right\rangle = \begin{cases} \Phi\left(f_y\right) & : f_y > 0 \\ 0 & : f_y \le 0 \end{cases} \tag{2.20}$$

$$C_{ijkl} = a\delta_{ij}\delta_{kl} + b\left(\delta_{ik}\delta_{jl} + \delta_{il}\delta_{jk}\right) \tag{2.21}$$

where $\langle\ \rangle$ are Macaulay's brackets, $\Phi\left(f_y\right)$ is the rate-sensitive material function, and $C_{ijkl}$ is a fourth order isotropic tensor. $a$ and $b$ in Equation (2.21) are material constants. $\Phi\left(f_y\right)$ is determined from the experimental correlation proposed by Adachi and Oka (1982) and Kimoto and Oka (2005) as

$$\Phi\left(f_y\right) = \sigma'_m \exp\left\{ m'\left( \overline{\eta}^*_{(0)} + \tilde{M}^* \ln \frac{\sigma'_m}{\sigma'_{mb}} \right) \right\} \tag{2.22}$$

in which $m'$ is the viscoplastic parameter.

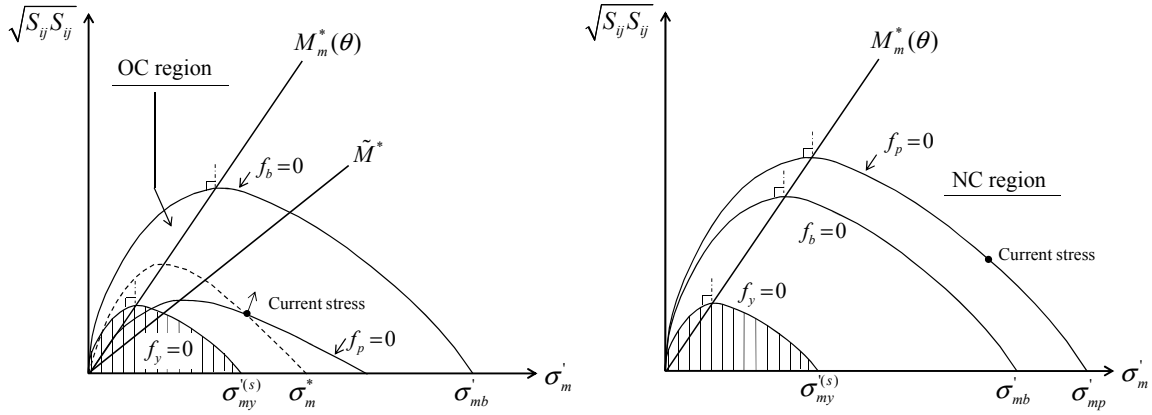


*(a) OC region* *(b) NC region*

*Figure 2.1. Overconsolidation boundary surface, static yield function and viscoplastic potential function.*

Deviatoric viscoplastic strain rate $\dot{e}_{ij}^{vp}$ and volumetric viscoplastic strain rate $\dot{\varepsilon}_{ij}^{vp}$ can be expressed as

$$\dot{e}_{ij}^{vp} = C_1 \exp\left\{ m'\left( \overline{\eta}^*_{(0)} + \tilde{M}^* \ln \frac{\sigma'_m}{\sigma'_{mb}} \right) \right\} \frac{\eta^*_{ij} - \eta^*_{ij(0)}}{\overline{\eta}^*} \tag{2.23}$$

$$\dot{\varepsilon}_{kk}^{vp} = C_2 \exp\left\{ m'\left( \bar{\eta}_{(0)}^{*} + \tilde{M}^{*} \ln \frac{\sigma_m'}{\sigma_{mb}'} \right) \right\} \left\{ \tilde{M}^{*} - \frac{\eta_{mn}^{*}(\eta_{mn}^{*} - \eta_{mn(0)}^{*})}{\bar{\eta}^{*}} \right\} \tag{2.24}$$

where $C_1 = 2b$ and $C_2 = 3a + 2b$ are the viscoplastic parameters for the deviatoric and the volumetric strain components, respectively.

### 2.2.5. Strain Dependency of the Elastic Shear Modulus

The non-linearity of soil stiffness has been studied extensively on materials such as sands, clays, and gravel, and has been well summarized by Ishihara (1996). For cohesive soils, several empirical equations have been proposed by considering the dependency of the shear modulus on the effective confining stress (Kokusho et al. 1982). In the original configuration by Kimoto and Oka (2005), the change in the elastic shear modulus of the elasto-viscoplastic model is given by the square root function of the normalized mean effective stress as

$$G = G_0 \sqrt{\frac{\sigma_m'}{\sigma_{m0}'}} \tag{2.25}$$

in which $G_0$ is the value for $G$ when $\sigma_m' = \sigma_{m0}'$.

Equation (2.25) considers only the effect of the confining pressure, which can accurately approximate the variation in shear modulus at very small levels of strain. In regions with large levels of strain, however, as demonstrated by the experimental results, the strain dependency of the shear modulus should be considered as well. Various empirical formulations have been provided from the laboratory test results to express the strain dependency of the shear modulus (e.g., Hardin and Drnevich 1972, Wang and Kuwano 1999). Ogisako et al. (2007) have introduced a normalized shear modulus reduction function based on the viscoplastic shear strain in soft clay specimens and have proposed a hyperbolic equation for that expression, namely,

$$G = G_0 \frac{1}{\left(1 + \alpha \left(\gamma^{vp}\right)^{r}\right)} \tag{2.26}$$

where $\alpha$ is the strain-dependent parameter, $r$ is the experimental constant, and $\gamma^{vp}$ is the accumulated viscoplastic shear strain given by an accumulation of the viscoplastic deviatoric strain rate as $\gamma^{vp} = \int \sqrt{de_{ij}^{vp}\, de_{ij}^{vp}}$ .

In this study, based on the experimental results, $r = 0.4$ is chosen. Therefore, the final formulation for the variation in shear modulus can be incorporated as

$$G = G_0 \frac{1}{\left(1+\alpha\left(\gamma^{vp}\right)^{0.4}\right)}\sqrt{\frac{\sigma'_m}{\sigma'_{m0}}} \tag{2.27}$$

## 2.3. Numerical Modeling of Osaka Soft Clay

The numerical modeling of Osaka soft clay specimens has been conducted using the described elasto-viscoplastic model. Material parameters have been determined by laboratory tests using natural samples. The sampling procedures were performed as part of a geotechnical investigation of a super-levee construction project along the Yodo River in Torishima, Osaka City, Japan. Geotechnical investigations have been performed through the drilling of two boreholes, which reach down to about 40 m below ground level. Standard penetration tests (SPT) and undisturbed tube samplings (Φ= 75 mm) in various layers have been performed. According to the boring results, the subsurface strata were composed of alluvial sand and soft clay layers overlying a diluvium dense gravel layer and a rather stiff clay layer at a depth of about 35 m. The cross section of the subsurface layers is schematically illustrated in Figure 2.2. B1 represents the topsoil material with a thickness of about 2.25 m, As2 is the upper alluvial sand layer with a thickness of approximately 8.5 m, Ac2 is the alluvial soft clay layer with a thickness of 12 m, As1 is the lower alluvial sand layer with a thickness of 5.5 m, and Ac1 is the alluvial clay deposit. Dg and Dc indicate the diluvium sandy gravel and rather stiff clay deposits, respectively.

Laboratory tests were conducted on the clay specimens obtained from the Ac2 layer, including undrained triaxial compression tests with different strain rates, and consolidation tests with different loading methods, namely, the constant rate of loading (CRL) and the standard incremental loading (STD) methods. The triaxial tests on the soft clay samples were conducted at two different strain rates, namely, 0.05 %/min and 0.005 %/min, and at three levels of confining pressure equal to 100, 200, and 400 kPa.

For the Ac2 layer in Torishima, the value of sensitivity has been reported as 6-8 (KG-NET 2007), which indicates the high sensitivity of the Osaka soft clay in this district. In order to predict the triaxial behavior of soft clay, elasto-viscoplastic model parameters have been determined from the laboratory test results following the proposed method by Kimoto and Oka (2005), as well as other characteristic parameters. Viscoplastic parameter $m'$ is determined from undrained triaxial

compression tests conducted at different strain rates. By having $m'$, the other viscoplastic parameters, $C_1$ and $C_2$, are obtained from Equations (2.23) and (2.24) in the triaxial stress state. The representative material parameters of the Ac2 layer are listed in Table 2.1. It is seen that the soft clay layer was divided into three individual sub-layers based on the soil properties. The stress-strain relations and the stress paths were used to evaluate the aspects of the destructuration in the constitutive modeling.

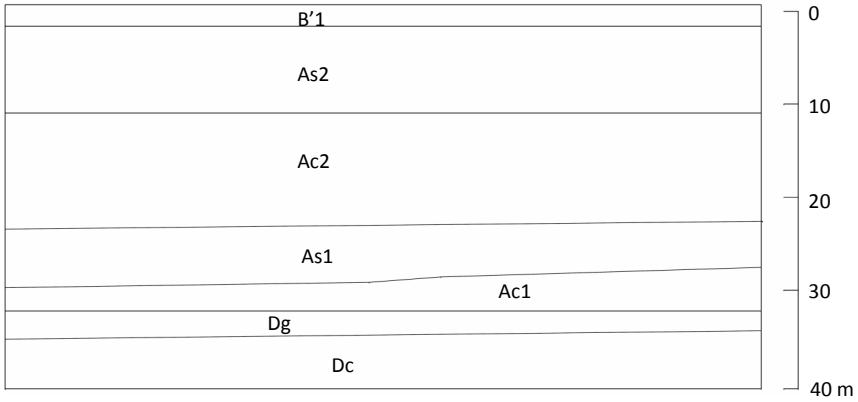


*Figure 2.2. Soil profile in Torishima, Osaka.*

### 2.3.1. Modeling of Soft Clay Considering Structural Degradation

As the first stage, the behavior of the soft clay specimens obtained from the Ac2 layer were simulated using the representative material parameters listed in Table 2.1, which were determined based on the triaxial test results. Comparisons were made with the experimental results through the stress-strain relations and the stress paths. The effect of structural parameters $n$ and $\beta$ on the stress-strain relations and the stress paths have been shown by Kimoto and Oka (2005) as softening behavior after the peak stress point, in which the larger structural parameter, $\beta$, promotes the rapid degradation of the shear strength. Nonetheless, the behavior before the peak stress point does not change with the structural parameters and it remains similar to that of the case in which no structural degradation is considered $(\beta = 0)$. Figure 2.3 shows the effect of the structural parameter $\beta$ on the stress-strain relations and stress paths of a clay specimen in the NC region presented by Kimoto (2002). By taking the larger value of $\beta$, the stress state reaches the residual state more quickly.

*Table 2.1. Material parameters of soft clay layer Ac2.*

| | | Ac2-U | Ac2-M | Ac2-L |
|---|---|---|---|---|
| Depth (m) | | 11.0 - 15.0 | 15.0 - 19.0 | 19.0 - 23.0 |
| Test no. | | Tw 2-1-2<br>Tw 2-1-2b | Tw 2-2-1<br>Tw 2-2-2 | Tw 2-3-1<br>Tw 2-3-2 |
| Initial void ratio | $e_0$ | 1.25 | 1.65 | 1.42 |
| Poisson's ratio | $\upsilon$ | 0.3 | 0.3 | 0.3 |
| Initial elastic shear modulus (1) | $G_0$ (kPa) | 3759 | 3927 | 5993 |
| Compression index | $\lambda$ | 0.341 | 0.593 | 0.652 |
| Swelling index | $\kappa$ | 0.019 | 0.027 | 0.014 |
| Stress ratio at failure | $M^*_m$ | 1.24 | 1.18 | 1.12 |
| Viscoplastic parameter | $m'$ | 24.68 | 28.2 | 21.15 |
| Viscoplastic parameter | $C_1$ (1/s) | $3.83\times10^{-11}$ | $1.85\times10^{-11}$ | $8.99\times10^{-11}$ |
| Viscoplastic parameter | $C_2$ (1/s) | $3.83\times10^{-11}$ | $1.85\times10^{-11}$ | $8.99\times10^{-11}$ |
| Structural parameter | $n=\sigma'_{maf}/\sigma'_{mai}$ | 0.83 | 0.67 | 0.60 |
| Structural parameter | $\beta$ | 5 | 10 | 15 |

*(1) Based on the mean effective stress at the depth of the specimen*

Figures 2.4 and 2.5 present the experimental results and the corresponding simulated results by the elasto-viscoplastic model, where the symbols show the experimental values and the solid lines represent the relevant simulated results. The stress-strain relations of the testing samples and the predicted results are presented in Figure 2.4. The results demonstrate quite a good tendency, in terms of strain softening and post-peak responses. However, considering the behavior around the peak stress point, the simulated results show smaller strain at the same shear stress level. This implies a larger shear modulus in the predicted results, which leads to a smaller accumulated deformation.

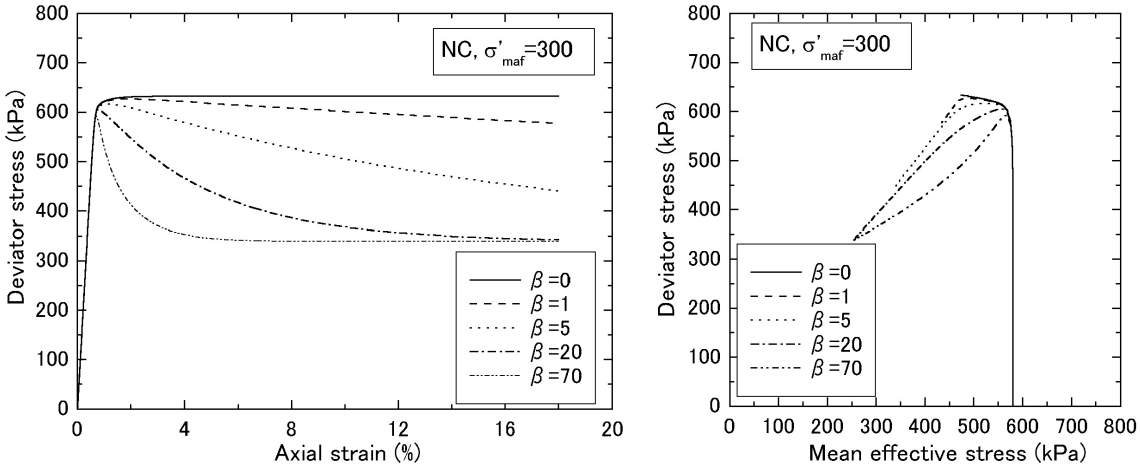


*Figure 2.3. Effects of parameter β on stress-strain relations and stress paths, (after Kimoto 2002).*

The simulated stress paths for the clay specimens under different levels of confining pressure, illustrated in Figure 2.5, follow the corresponding experimental results, although the initial part of the stress path curve in some cases does not agree with the experimental values. The simulations indicate the elastic behavior at the initial part of the stress paths in contrast to the experimental data.

In order to improve the predicted results, the inequality of the viscoplastic parameter for deviatoric strain component $C_1$ and the viscoplastic parameter for volumetric strain component $C_2$ was considered by taking different values for $C_2$, as $C_2 \geq C_1$. Nonetheless, the effect of this consideration was insignificant. The dissimilarity of the stress paths between the simulation and the experiments can be attributed to the influence of the sampling process and the consequent disturbance to the structured soil behavior, which results in less elasticity in the earlier stages of shearing in the laboratory tests. Furthermore, the pore water pressure in the tests, which is measured by means of a pressure sensor connected to the top and the bottom of the specimen, represents an average value of the pore water pressure within the entire sample. However, the simulation results, obtained by the integration of the constitutive equations, represent the one-point response in which the size or the boundary effect has been disregarded.

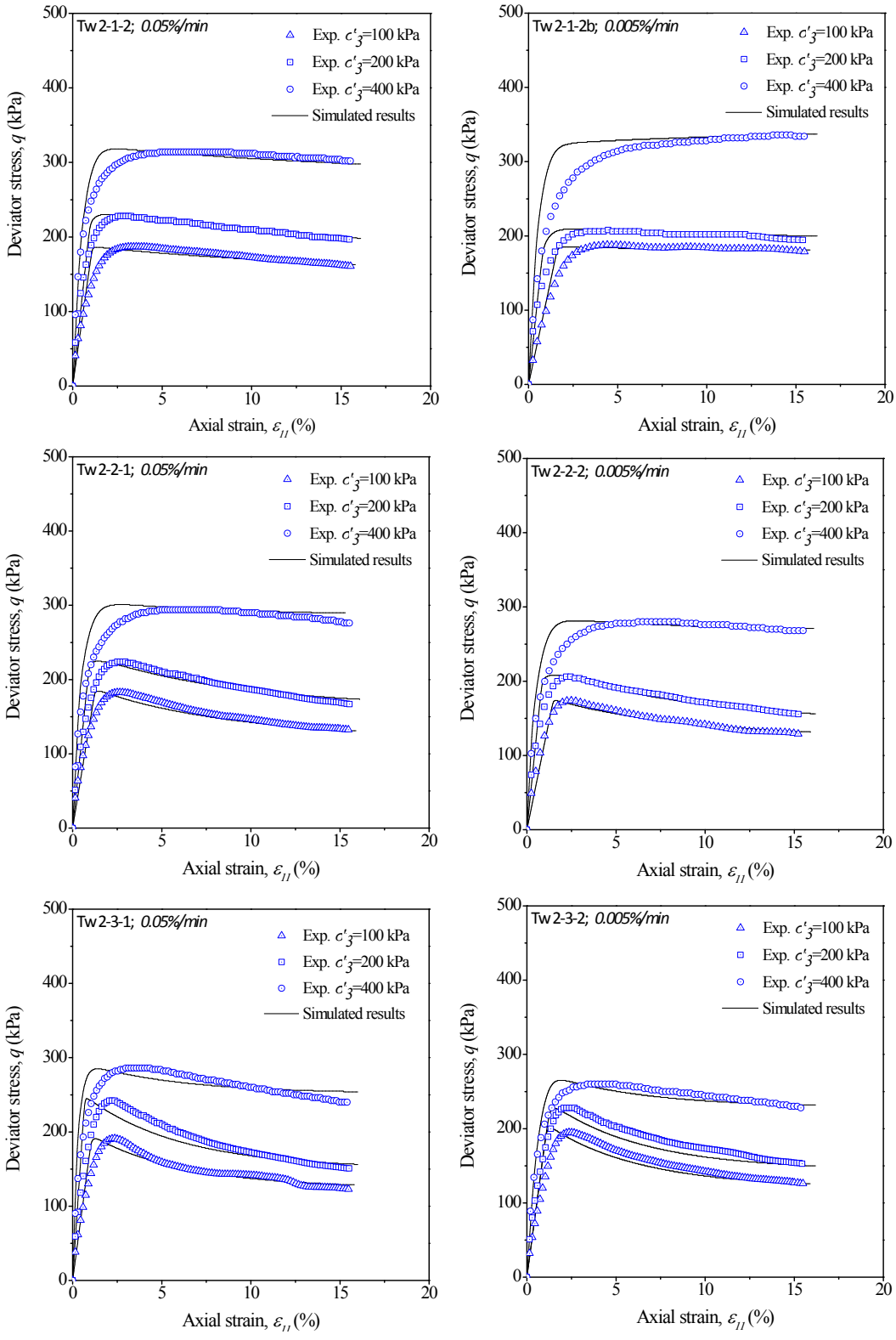


*Figure 2.4. Stress-strain relations during triaxial tests and simulated results considering only the structural degradation.*

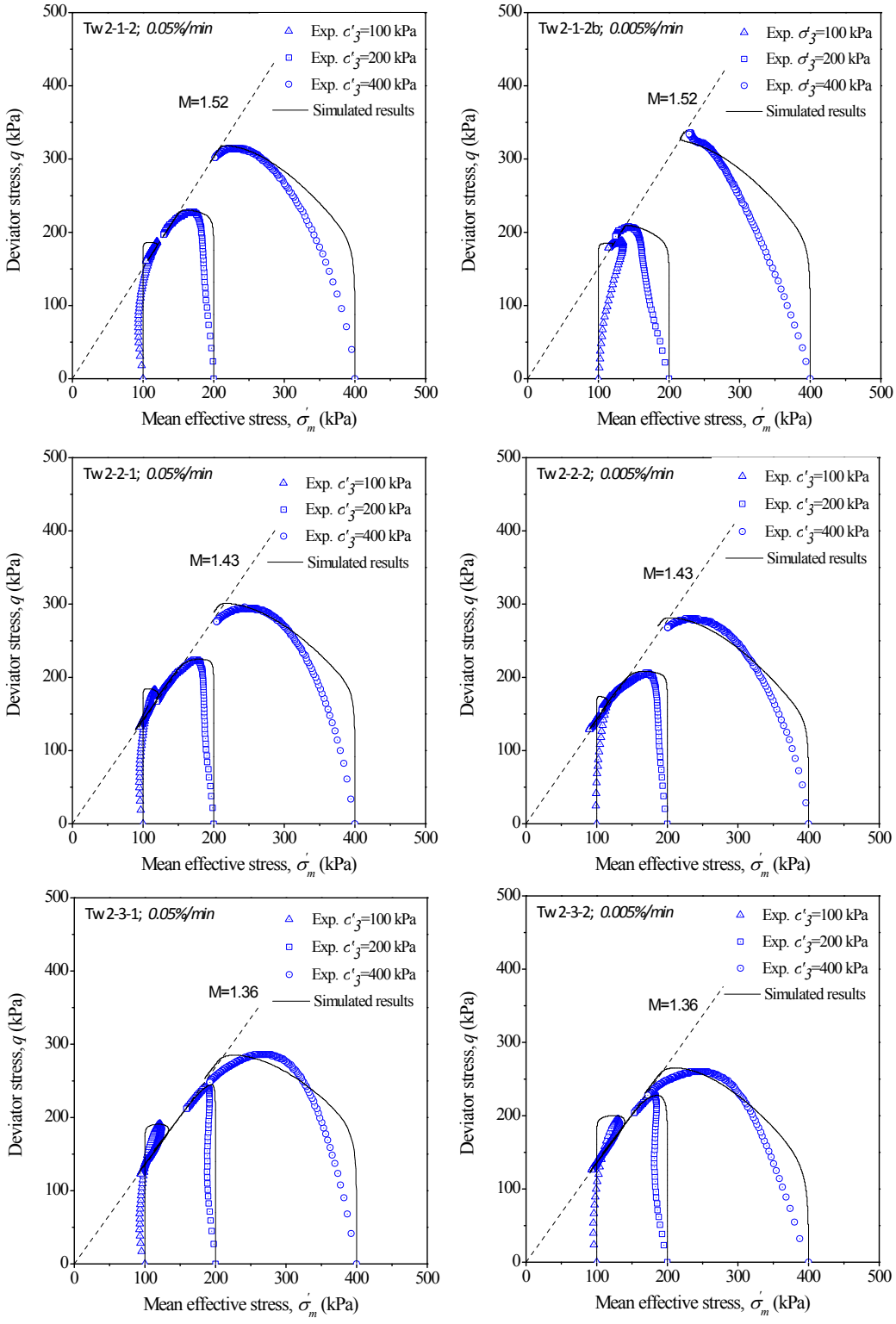


*Figure 2.5. Stress paths during triaxial tests and simulated results considering only the structural degradation,* $M = (q/\sigma'_m)_{failure}$.

### 2.3.2. Modeling of Soft Clay Considering Structural Degradation and Strain-Dependent Shear Modulus

In order to improve the predicted results, the strain-dependent elastic shear modulus was taken into consideration in addition to structural degradation. Giving consideration to the effect of the strain dependency of the shear modulus in the modeling changes the values of the structural parameter. The strain-dependent parameter $\alpha$, and the modified values for structural parameter $\beta$ are presented in Table 2.2.

*Table2.2. Strain-dependent parameter and modified values for the structural parameter.*

| | | Ac2-U | Ac2-M | Ac2-L |
|---|---|---|---|---|
| Test no. | | Tw 2-1-2<br>Tw 2-1-2b | Tw 2-2-1<br>Tw 2-2-2 | Tw 2-3-1<br>Tw 2-3-2 |
| Strain-dependent parameter | $\alpha$ | 20 | 10 | 10 |
| Structural parameter | $\beta$ | 10 | 15 | 20 |

Figure 2.6 indicates the stress-strain relations of the predicted results beside the experimental data, while the stress paths for both cases are presented in Figure 2.7. As mentioned above, the symbols in these figures represent the experimental data from laboratory tests and the solid lines show the corresponding predicted values when using the elasto-viscoplastic constitutive model. Applying the modified values for $\beta$ and the strain-dependent shear modulus leads to more accurately predicted results. Although giving consideration to strain-dependent shear modulus $G$ leads to an enormous improvement in the predictions of the stress-strain relations, particularly around the peak stress points, its effect on the stress paths under triaxial test conditions is insignificant. The predicted results emphasize the capability of the elasto-viscoplastic model to reproduce the sensitive soil behavior through the structural degradation parameters, of which a more accurate response is achieved by considering the strain dependency of the shear modulus.

The effect of different strain rates is studied through the results on the specimens from Ac2-U layer, namely, Tw2-1-2 and Tw2-1-2b, which have been compressed in the strain rates of 0.05%/min and 0.005%/min, respectively. Figure 2.8 illustrates the experimental and the simulated results on the samples at the confining pressure of 400 kPa. Using the lower rate of strain in the experiment leads to the slightly higher level of strength in the specimen. This fact is correspondingly observed in the simulated results, although the difference in the stress paths is insignificant.

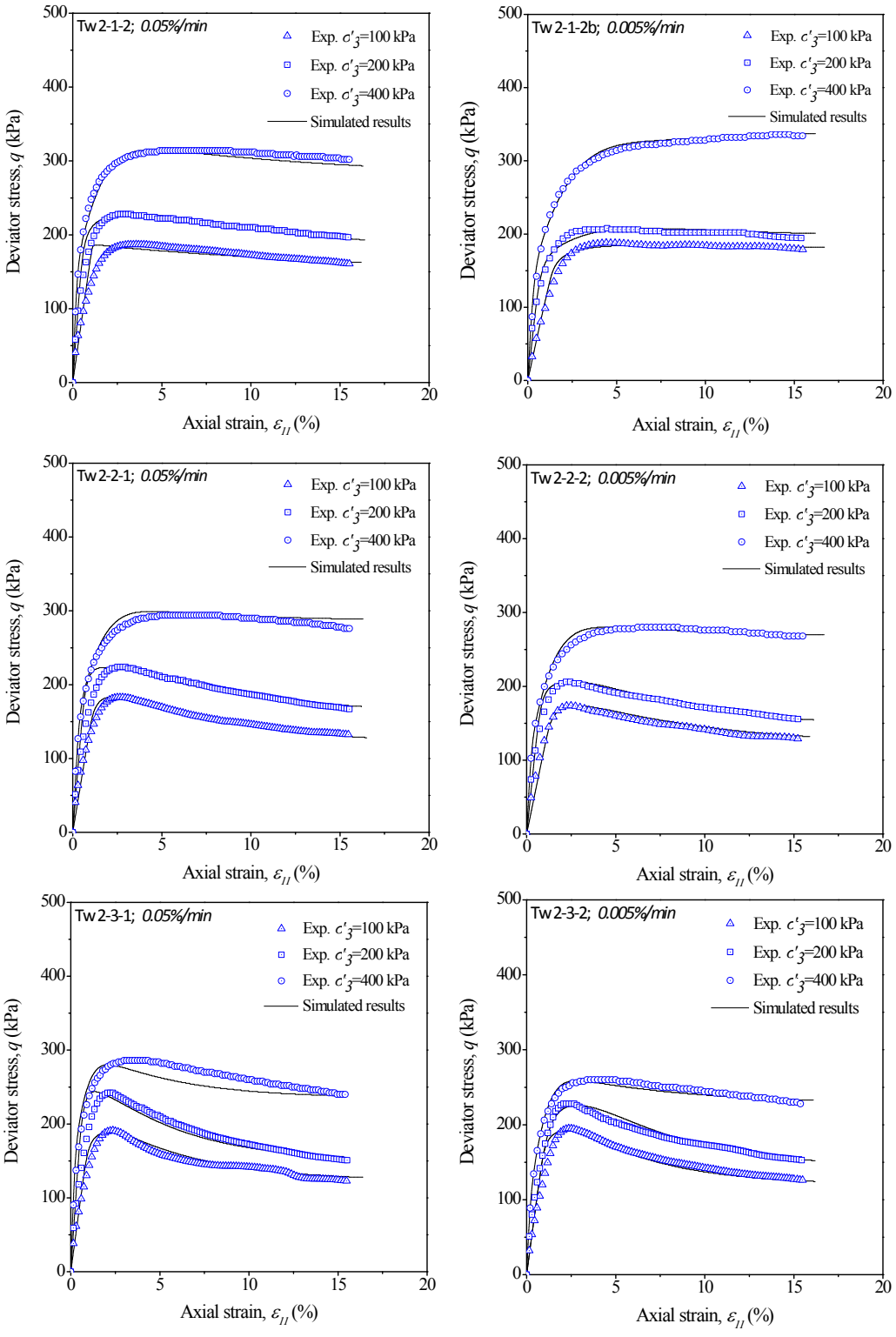


*Figure 2.6. Stress-strain relations during triaxial tests and simulated results considering the structural degradation and strain-dependent shear modulus.*

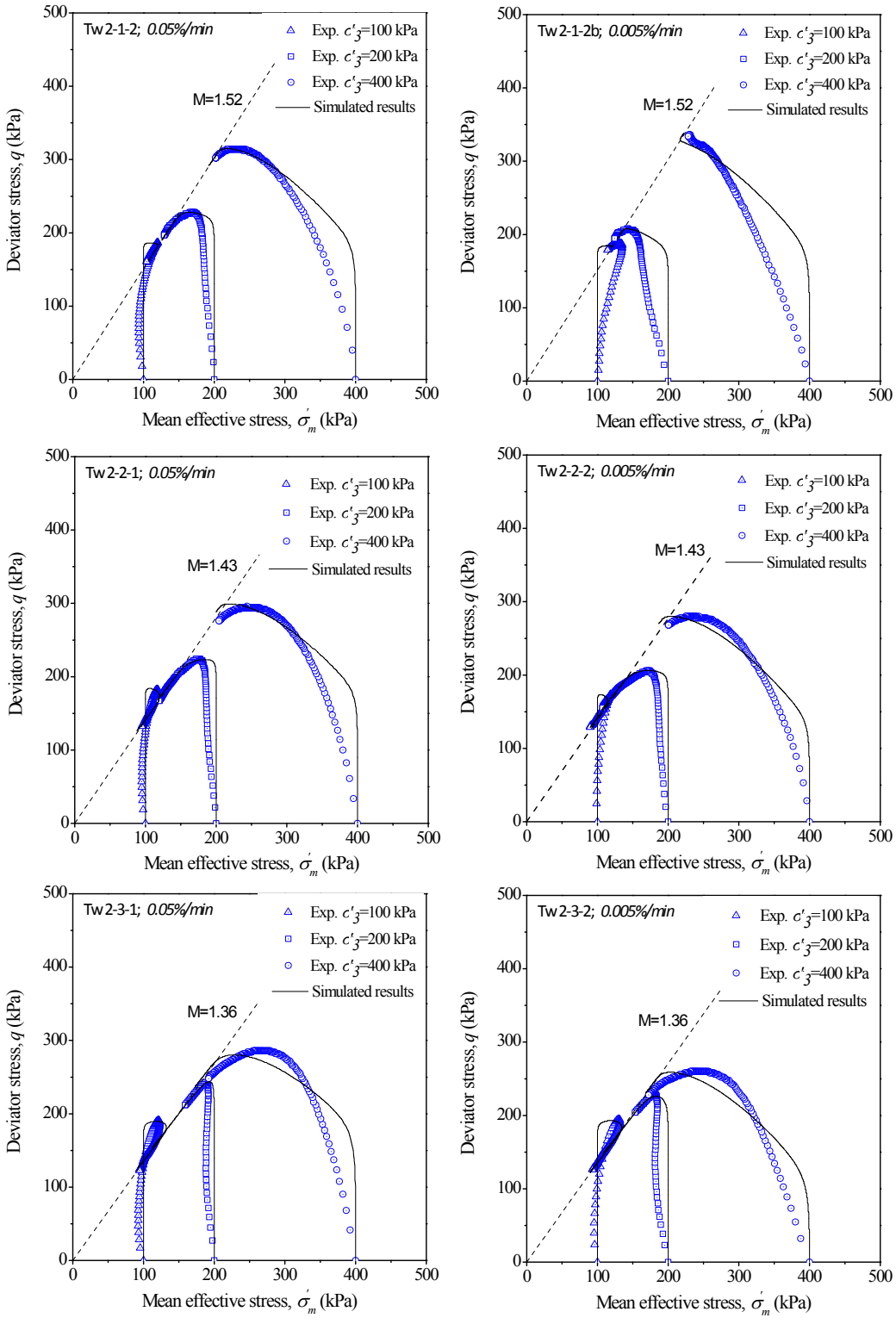


*Figure 2.7. Stress paths during triaxial tests and simulated results considering the structural degradation and strain-dependent shear modulus,* $M = (q/\sigma'_m)_{failure}$.

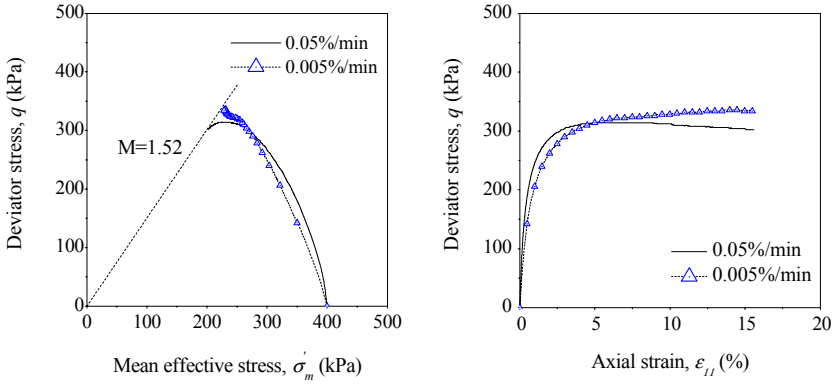


*(a) Experiments*

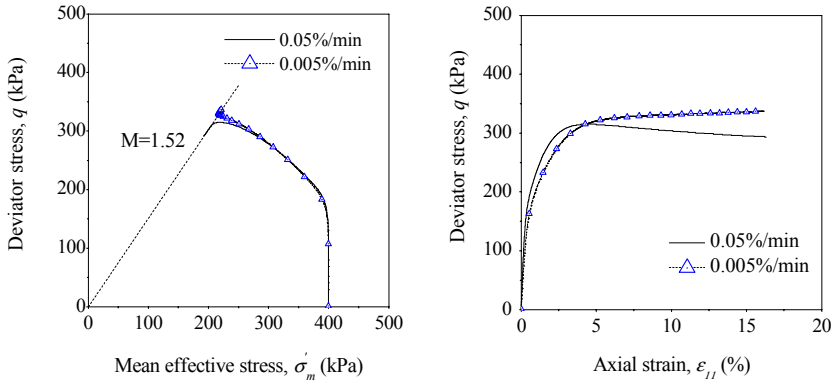


*(b) Simulation*

*Figure 2.8. Effect of different strain rates on the experimental and the simulated results.*

## 2.4. Consolidation Analysis of an Embankment Construction on Soft Clay

The effects of these two factors, structural degradation and the strain-dependent shear modulus, have been studied in the context of a typical geotechnical problem, namely, a two-dimensional embankment construction. The finite element consolidation analysis of an embankment on a soft clay foundation was performed for three cases. All cases assume the same initial conditions. In Case 1, both destructuration aspects were ignored by making $\beta$ and $\alpha$ equal to zero (no structural degradation). In Case 2, the effect of structural degradation was considered, while the original shear modulus formulation, Equation (2.25), was used. In Case 3, the effect of the strain-dependent shear modulus was considered in the simulation by applying Equation (2.27) and the modified values for structural parameter $\beta$. The overall features in each case of the finite element analysis are summarized in Table 2.3. Comparisons have been made among the results of these cases to evaluate the influence under plane strain conditions.

*Table 2.3. Specifications for each case in the 2D numerical analysis.*

| | Structural degradation | Strain dependency of shear modulus |
|---|---|---|
| Case 1 (No structural degradation: $\beta=0, \alpha=0$ ) | × | × |
| Case 2 (Structural degradation: $\beta=10, \alpha=0$) | ✓ | × |
| Case 3 (Structural degradation + Strain dependency of $G$: $\beta=15, \alpha=10$) | ✓ | ✓ |

✓*: Considered,* ×*: Not considered.*

### 2.4.1. Problem Description

The consolidation analysis of the Osaka soft clay foundation subjected to embankment construction was performed using the finite element method. The geometry and the finite element mesh of the problem are presented in Figure 2.9, where a typical embankment with a height of 3.2 m and a slope of 1:2, was constructed on a soft clay foundation with a thickness of 10 m and characterized by the parameters of Osaka soft clay.

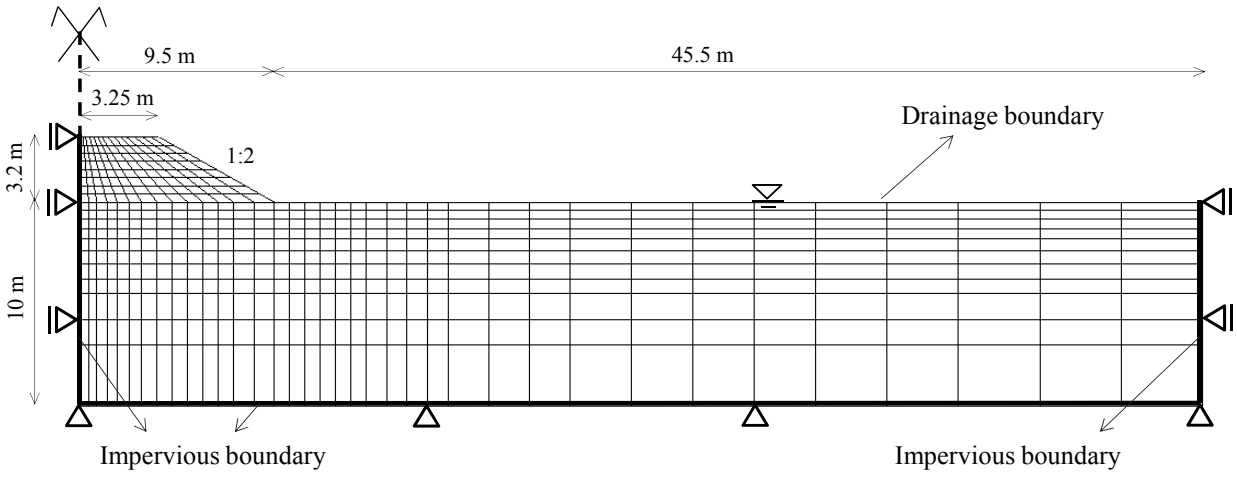


*Figure 2.9. Finite element mesh and boundary conditions for the embankment construction.*

As shown in Figure 2.9, the embankment layers were properly modeled in the finite element mesh so the stiffness and the consolidation of the embankment layers could be considered in the simulation in addition to the embankment loading. Due to symmetry, only half of the embankment was represented in the finite element mesh. The size of the modeled domain was determined so that the boundary effects would be negligible. A fully saturated condition was assumed, in which only the boundary located at the top was permeable. The displacement boundary at the bottom of the domain,

which is regarded as the base ground, was fixed in both vertical and horizontal directions, while the right- and the left-hand side boundaries were fixed only in the horizontal direction. Mesh sensitivity studies were done to confirm that the mesh was dense enough to produce converging results. The elasto-viscoplastic material parameters of the Ac2-M layer were applied for the soft ground layer, while the elastic behavior was adopted for the embankment layers assumed to be made of granular fill. Table 2.4 gives the material parameters, which were used in the finite element analysis.

*Table 2.4. Material parameters for the embankment and the ground layer.*

| Parameters | $k$ *(m/s)* | $\gamma_t$ *(kN/m$^3$)* | $e_0$ | $G_0$ *(kPa)* | *OCR* | $\lambda$ | $\kappa$ | $M^*_{mc}$ | $m'$ | $C_1, C_2$ *(1/s)* | $n$ | $\beta$ | $\alpha$ |
|---|---|---|---|---|---|---|---|---|---|---|---|---|---|
| Embankment | $1.00\times10^{-5}$ | 19.8 | 0.8 | 4300 | | | | | | | | | |
| Ground (Ac2-M) | $3.85\times10^{-10}$ | 16.0 | 1.65 | 3930 | 1.10 | 0.593 | 0.027 | 1.18 | 28.2 | $1.85\times10^{-11}$ | 0.67 | 10,15(1) | 0,10 |

*(1) Modified value after strain-dependent shear modulus consideration*

### 2.4.2. Finite Element Formulations Based on Finite Deformation Theory

In the numerical simulation, the finite element method for two-phase mixtures, based on the finite deformation theory and the updated Lagrangian approach, is adopted with the objective Jaumann rate of Cauchy stress for the weak form of the equilibrium equation (Oka et al. 2002a; Kimoto et al. 2004). A Biot's type of two-phase mixture theory is used with a velocity-pore pressure formulation. The grain size particles and the fluid are assumed to be incompressible. An eight-node quadrilateral isoparametric element with reduced Gaussian (2×2) integration is employed for the displacement. The pore water pressure is defined by a four-node quadrilateral isoparametric element. Figure 2.10 shows the quadrilateral elements and Gauss points for the soil skeleton and the pore water pressure.

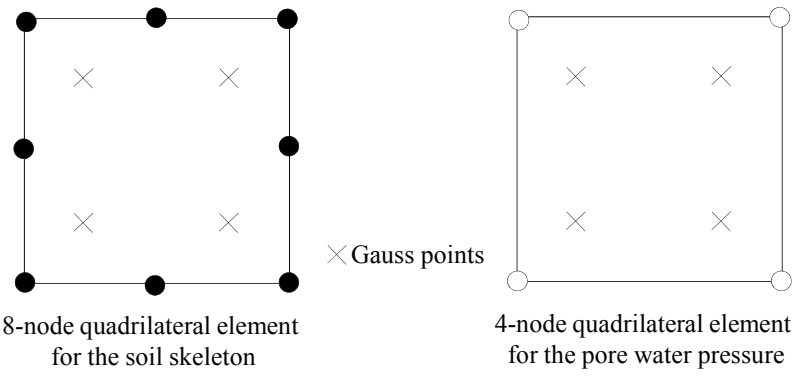


*Figure 2.10. Isoparametric elements for the soil skeleton and the pore water pressure.*

Concerning the finite deformation framework, strain rate tensor $\dot{\varepsilon}_{ij}$ in the previous section, i.e., the section that described the constitutive model, is replaced by stretching (or rate of deformation) tensor $D_{ij}$. The finite element formulation, based on the updated Lagrangian method, is explained here, including the discretization of the equilibrium equation followed by the continuity equation.

### 2.4.2.1. Updated Lagrangian Approach

In Lagrangian methods, the nodes, the elements, and the quadrature points move with the material, so that constitutive equations are always evaluated at the same material points, which is an advantage for history-dependent materials such as soils. On the other hand, in Eulerian descriptions, the elements do not deform with the material and they retain their original shape regardless of the magnitude of the deformation.

Finite element discretization with Lagrangian descriptions are commonly classified as the total Lagrangian approach and the updated Lagrangian approach. For the total Lagrangian approach, the discrete equations are formulated with respect to the reference configuration. For the updated Lagrangian approach, the discrete equations are formulated in the current configuration, which is assumed to be the new reference configuration. Figure 2.11 shows the motion of a continuum body in a stationary Cartesian coordinates, in which $X = X_i$, $x = x_i$, and $x' = x'_i$, are coordinates of the point P at time $t = 0$, $t = t$, and $t = t + \Delta t$, respectively. The configuration at time $t = 0$ is the initial configuration, where the body is not deformed yet, the configuration at time $t = t$ is the current configuration, i.e., the latest known configuration, and the configuration at time $t = t + \Delta t$ is unknown.

In the present study, the incremental boundary value problem is applied by the rate type of the equilibrium equations with incremental constitutive equations and appropriate boundary conditions. Thus, the configuration at time $t = t + \Delta t$ is provided by solving the rate type of equilibrium equation at the current configuration $(t = t)$ with a linear approximation in terms of time. By integrating this procedure from time $t = 0$ to $\Delta t, 2\Delta t, \ldots$, approximate solutions of nonlinear equations can be obtained. The finite element formulation based on the updated Lagrangian approach is effective for strongly nonlinear problem inducing large deformation and rotation, since the reference configuration is consecutively updated at each step of calculation to the latest deformed configuration.

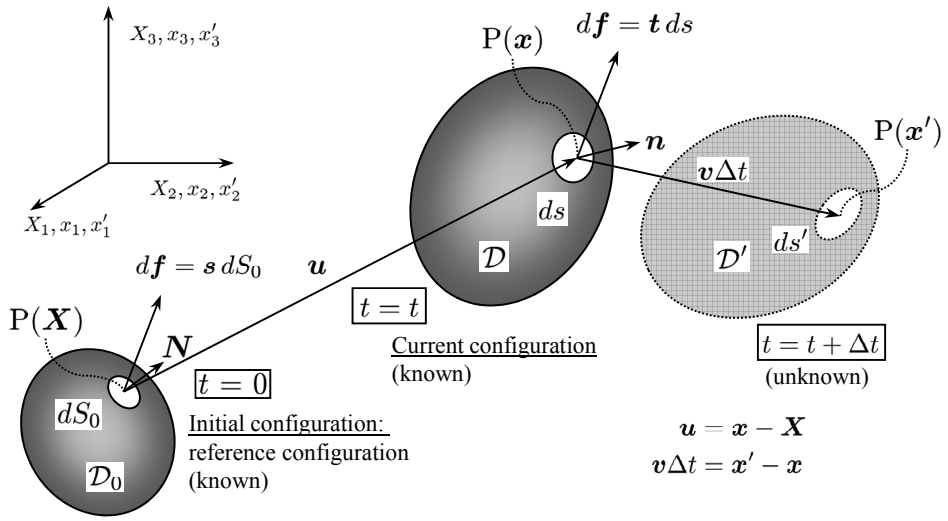


(a) Total Lagrangian formulation

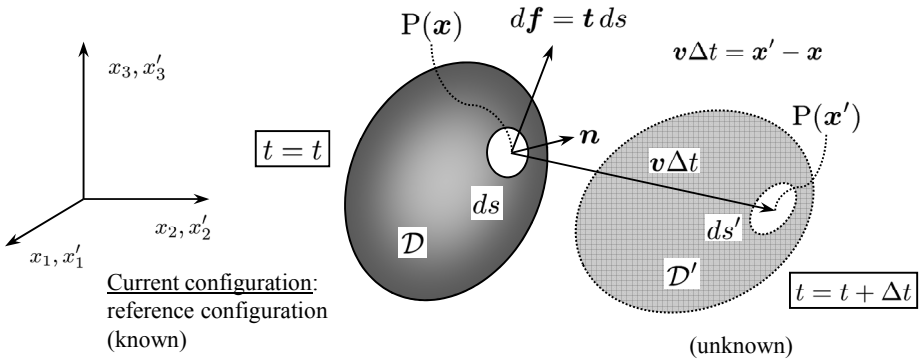


(b) Updated Lagrangian formulation

*Figure 2.11. Motion of a continuum body in stationary Cartesian coordinate system, (a) total Lagrangian formulation, (b) updated Lagrangian formulation.*

### 2.4.2.2. Equilibrium Equation

Terzaghi's effective stress is adopted for the two-phase soil medium as

$$T_{ij} = T'_{ij} + U_w \delta_{ij} \tag{2.28}$$

where $T_{ij}$ is the Cauchy stress tensor, $T'_{ij}$ is the effective Cauchy stress tensor, $U_w$ is the pore water pressure, and $\delta_{ij}$ is Kronecker's delta.

Taking the time derivative of Equation (2.28) yields

$$\dot{T}_{ij} = \dot{T}'_{ij} + \dot{U}_w \delta_{ij} \tag{2.29}$$

For the finite element method, we used a rate type of equilibrium equation for the updated Lagrangian formulation. Assuming fully saturated conditions, the weak form of the equilibrium equation for the entire fluid-solid mixture in domain $V$ can be expressed as

$$\int_V \dot{\hat{S}}_{ji,j} \delta v_i \, dV = 0 \tag{2.30}$$

in which $\dot{\hat{S}}_{ij}$ is the total nominal stress rate tensor with respect to the current configuration and $\delta v_i$ is the virtual velocity vector component.

The relationship between the nominal stress rate tensor and the Cauchy stress rate tensor is given by

$$\dot{\hat{S}}_{ij} = \dot{T}_{ij} + L_{kk} T_{ij} - T_{ik} L_{jk} \tag{2.31}$$

$$\dot{\hat{S}}'_{ij} = \dot{T}'_{ij} + L_{kk} T'_{ij} - T'_{ik} L_{jk} \tag{2.32}$$

where $\dot{\hat{S}}'_{ij}$ is the effective nominal stress rate tensor and $L_{ij}$ is the velocity gradient tensor.

Combining Equations (2.28) to (2.32), the total nominal stress rate tensor can be related to the effective nominal stress rate tensor as

$$\dot{\hat{S}}_{ij} = \dot{\hat{S}}'_{ij} + \dot{U}_w \delta_{ij} + L_{kk} U_w \delta_{ij} - U_w \delta_{ik} L_{jk} \tag{2.33}$$

Using Green's theorem and Gauss's divergence theorem, Equation (2.30) can be written as

$$\int_\Gamma (\dot{\hat{S}}_{ji} \delta v_i) n_j \, d\Gamma - \int_V \dot{\hat{S}}_{ji} \delta L_{ij} dV = 0 \tag{2.34}$$

where $\Gamma$ denotes a boundary surface of the closed domain, $V$, and $n$ is the unit normal vector to boundary surface $\Gamma$. Incorporating Equation (2.33) into Equation (2.34) leads to

$$\int_V \dot{\hat{S}}'_{ij} \delta L_{ij} dV + \int_V \dot{U}_w \delta L_{ij} \delta_{ij} dV + \int_V \left( L_{kk} U_w \delta_{ij} - U_w \delta_{ik} L_{jk} \right) \delta L_{ij} dV = \int_\Gamma (\dot{\hat{S}}_{ji} \delta v_i) n_j \, d\Gamma \tag{2.35}$$

Using the Cauchy stress theorem, Equation (2.35) becomes as follows:

$$\int_V \hat{\dot{S}}'_{ij}\delta L_{ij}dV + \int_V \dot{U}_w \delta D_{kk}dV + \int_V \left(L_{kk}U_w\delta_{ij} - U_w\delta_{ik}L_{jk}\right)\delta L_{ij}dV = \int_\Gamma \overline{S}_{ti}\,\delta v_i d\Gamma \tag{2.36}$$

where $D_{ij}$ is the stretching tensor defined by $D_{ij} = \frac{1}{2}\left(L_{ij} + L_{ji}\right)$ and $\overline{S}_{ti}$ is the nominal traction vector given by $\overline{S}_{ti} = \hat{\dot{S}}_{ji} n_j$.

Substituting Equation (2.32) into Equation (2.36) results in

$$\begin{aligned}&\int_V \dot{T}'_{ij}\ \delta D_{ij}dV - \int_V T'_{ik}\ L_{jk}\delta L_{ij}dV + \int_V L_{kk}T'_{ij}\ \delta L_{ij}dV + \int_V \dot{U}_w \delta D_{kk}dV \\ &+ \int_V \left(L_{kk}U_w\delta_{ij} - U_w\delta_{ik}L_{jk}\right)\delta L_{ij}dV = \int_\Gamma \overline{S}_{ti}\delta v_i d\Gamma\end{aligned} \tag{2.37}$$

The objective Jaumann rate of Cauchy stress tensor $\hat{T}'_{ij}$ is defined by means of Cauchy stress rate tensor $\dot{T}'_{ij}$ and spin tensor $W_{ij}$ as

$$\hat{T}'_{ij} = \dot{T}'_{ij} - W_{ik}T'_{kj} + T'_{ik}W_{kj} \tag{2.38}$$

The constitutive equation is described using the Jaumann rate of Cauchy stress tensor $\hat{T}'_{ij}$ and stretching tensor $D_{ij}$ as

$$\hat{T}'_{ij} = C^e_{ijkl}(D_{kl} - D^{vp}_{kl}) \tag{2.39}$$

where $C^e_{ijkl}$ is the elastic tangential stiffness matrix and $D^{vp}_{ij}$ is the viscoplastic stretching tensor, which is related to the total stretching tensor as

$$D_{ij} = D^e_{ij} + D^{vp}_{ij} \tag{2.40}$$

where $D^e_{ij}$ is the elastic stretching tensor defined as

$$D^e_{ij} = \frac{1}{2G}\dot{S}_{ij} + \frac{\kappa}{3(1+e)}\frac{\dot{T}'_m}{T'_m}\delta_{ij} \tag{2.41}$$

in which $\dot{S}_{ij}$ is the deviatoric stress tensor rate ($\dot{S}_{ij} = \dot{T}'_{ij} - \dot{T}'_m\,\delta_{ij}$). Viscoplastic stretching tensor $D^{vp}_{ij}$ is given by

$$D_{ij}^{vp} = C_{ijkl} \left\langle \Phi\left(f_y\right) \right\rangle \frac{\partial f_p}{\partial T'_{kl}} \tag{2.42}$$

where $\langle\ \rangle$ are Macaulay's brackets; $\left\langle \Phi\left(f_y\right) \right\rangle = \Phi\left(f_y\right)$, if $f_y > 0$ and $\left\langle \Phi\left(f_y\right) \right\rangle = 0$, if $f_y \le 0$.

The tangent modulus method (Pierce, Shih and Needleman 1984) is implemented here to determine the viscoplastic stretching tensor. Hence, Equation (2.39) can be rewritten in matrix form as

$$\left\{\hat{T}'\right\} = [C]\{D\} - \{Q\} \tag{2.43}$$

where $[C]$ is the tangential stiffness matrix and $\{Q\}$ is the relaxation stress vector.

The substitution of Equation (2.38) into Equation (2.43) gives

$$\left\{\dot{T}'\right\} = [C]\{D\} - \{Q\} + \{W'\} \tag{2.44}$$

in which $\{W'\}$ is the vector defined as $\{W'\} = \{WT - TW\}$.

For the discretization of the weak form of the equilibrium equation, we adopt FEM with an isoperimetric element. The velocity and the pore water pressure are approximated as

$$\{v\} = [N]\left\{v^*\right\} \tag{2.45}$$

$$\{U_w\} = [N_h]\left\{U_w^*\right\} \tag{2.46}$$

where $[N]$ and $[N_h]$ are the shape functions of the eight-node quadrilateral element for the nodal velocity vector and the four-node quadrilateral element for the pore water pressure, respectively.

Combining Equation (2.37) and Equation (2.44) and using the finite element approximations, the final weak form of the equilibrium equation becomes

$$[K]\left\{v^*\right\} - \int_V [B]^T \{Q\}\, dV + \int_V [B]^T \{W'\}\, dV + [K_L]\left\{v^*\right\} + [K_v]\left\{\dot{U}_w^*\right\} = \left\{\dot{F}\right\} \tag{2.47}$$

in which,

$$[K] = \int_V [B]^T [C][B]\, dV \tag{2.48}$$

$$[K_L] = \int_V [B_M]^T [D_s][B_M]\, dV + \int_V [B_M]^T [U][B_M]\, dV + \int_V [B_M]^T \{T'\}\{B_v\}^T\, dV \tag{2.49}$$

$$[K_v] = \int_V \{B_v\}\{N_h\}^T\, dV \tag{2.50}$$

$$\{\dot{F}\} = \int_\Gamma [N]^T \{\bar{S}_t\}\, d\Gamma \tag{2.51}$$

$[B_M]$ is the matrix which transforms the nodal velocity vector $\{v^*\}$ into the velocity gradient vector $\{L\}$, i.e., $\{L\} = [B_M]\{v^*\}$. Also, $[D_S]\{L\} = -T'_{ik}\, L_{jk}$, and $[U]\{L\} = L_{kk}U_w\delta_{ij} - U_w\delta_{ik}L_{jk}$.

Using Euler's scheme, the nodal velocity vector and pore water pressure can be obtained as

$$\{v^*\} = \frac{\{\Delta u^*\}}{\Delta t} \tag{2.52}$$

$$\{\dot{U}_w^*\} = \frac{\{U_w^*\}_{t+\Delta t} - \{U_w^*\}_t}{\Delta t} \tag{2.53}$$

where $\{\Delta u^*\}$ is the vector of the incremental nodal displacement. Incorporating Equations (2.52) and (2.53) into Equation (2.47) becomes

$$[[K] + [K_L]]\{\Delta u^*\}_{t+\Delta t} + [K_v]\{U_w^*\}_{t+\Delta t} = \Delta t\{\dot{F}\} + [K_v]\{U_w^*\}_t + \Delta t\{\dot{F}^*\} - \Delta t\{\dot{F}^w\} \tag{2.54}$$

where

$$\{\dot{F}^*\} = \int_V [B]^T \{Q\}\, dV \tag{2.55}$$

$$\{\dot{F}^w\} = \int_V [B]^T \{W'\}\, dV \tag{2.56}$$

### 2.4.2.3. Continuity Equation

Assuming the incompressibility of the soil particles and the pore water, the continuity equation is obtained from the mass conservation equation of the soil-water mixture as

$$\frac{k}{\gamma_w} U_{w,ii} + D_{ii} = 0 \tag{2.57}$$

where $k$ is the coefficient of permeability, $D_{ii}$ is the stretching tensor, and $\gamma_w$ is the density of the pore water.

The weak form of the continuity equation is given by

$$\int_V \left( \frac{k}{\gamma_w} U_{w,ii} + D_{ii} \right) \overline{W}\, dV = \frac{k}{\gamma_w} \int_V U_{w,ii} \overline{W}\, dV + \int_V D_{ii} \overline{W}\, dV = 0 \tag{2.58}$$

in which $\overline{W}$ is a Galerkin weighted function for the continuity equation as $\overline{W} = \{N_h\}$. Proceeding with the similar procedure as described for the equilibrium equation, Equation (2.58) becomes

$$\frac{k}{\gamma_w} \int_\Gamma \overline{W} U_{w,i} n_i d\Gamma - \frac{k}{\gamma_w} \int_V \overline{W}_{,i} U_{w,i} dV + \int_V \overline{W} D_{ii} dV = 0 \tag{2.59}$$

where $n$ is the unit normal vector to boundary surface $\Gamma$.

Using finite element approximations for the pore water pressure, as described by Equation (2.46), the discrete form of the continuity equation is given by

$$[K_v]^T \{\Delta u^*\} - \Delta t \left( [K_h] + [V] \right) \{U_w^*\}_{t+\Delta t} = 0 \tag{2.60}$$

where

$$[K_v]^T = \int_V \{N_h\} \{B_v\}^T dV \tag{2.61}$$

$$[K_h] = \frac{k}{\gamma_w} \int_V [B_h]^T [B_h] dV \tag{2.62}$$

$$\{V\} = -\frac{k}{\gamma_w} \int_\Gamma \{N_h\} \{n\}^T [B_h] d\Gamma \tag{2.63}$$

#### 2.4.2.4. Discrete Equation

Combining the equilibrium equation and the continuity equation, the final system of equations for the FEM analysis, based on the finite deformation theory, can be obtained as

$$\begin{bmatrix} [K]+[K_L] & [K_v] \\ [K_v]^T & -\Delta t([K_h]+[V]) \end{bmatrix} \begin{Bmatrix} \{\Delta u^*_{t+\Delta t}\} \\ \{U^*_{w,t+\Delta t}\} \end{Bmatrix} = \begin{Bmatrix} \Delta t\{\dot{F}^t\}+[K_v]\{U^*_{w,t}\} \\ 0 \end{Bmatrix} \tag{2.64}$$

where

$$\{\dot{F}^t\} = \{\dot{F}\} + \{\dot{F}^*\} - \{\dot{F}^w\} \tag{2.65}$$

### 2.4.3. Construction Procedure of the Embankment

The simplest approximation for simulation of the new material placing in a finite element analysis is by applying the increment of the weight of the fill as the external load on the nodes of the embankment foundation interface. However for a more accurate analysis, the embankment construction procedure should be implemented by which the stiffness and the consolidation of the embankment can be considered in addition to the embankment loading.

When constructing material, the following procedure is recommended (Potts and Zdravkovic 1999):

*a.* Divide the analysis into a set of increments. For a particular increment the element to be constructed are inserted and given a constitutive model appropriate to the material behavior during placing. This often means that the material has a low stiffness. In the current study, the elastic behavior with a low stiffness equal to 75% of the original stiffness of the material is assumed for the material during placing.

*b.* Nodal forces due to the self body forces of the constructed materials are calculated and applied on the corresponding nodes.

*c.* The global stiffness matrix and all other the boundary conditions are assembled for the increment. The analysis is performed to obtain the incremental changes in displacements, strains, and stresses.

*d.* Before application of the next increment, the constitutive model for the elements just constructed is changed to represent the behavior of the fill material once placed. Incremental

displacements of any nodes which are only connected to the constructed elements (i.e., not connected to elements that were active at the previous increment) are zeroed.

*e.* Apply the next increment of analysis.

The incremental procedure is schematically depicted in Figure 2.12.

The linearized construction sequence of the embankment is schematically shown in Figure 2.13. As shown, it was assumed that the embankment would be constructed in four layers within 40 consecutive days. A consolidation analysis was performed until 1000 days after the end of the construction.

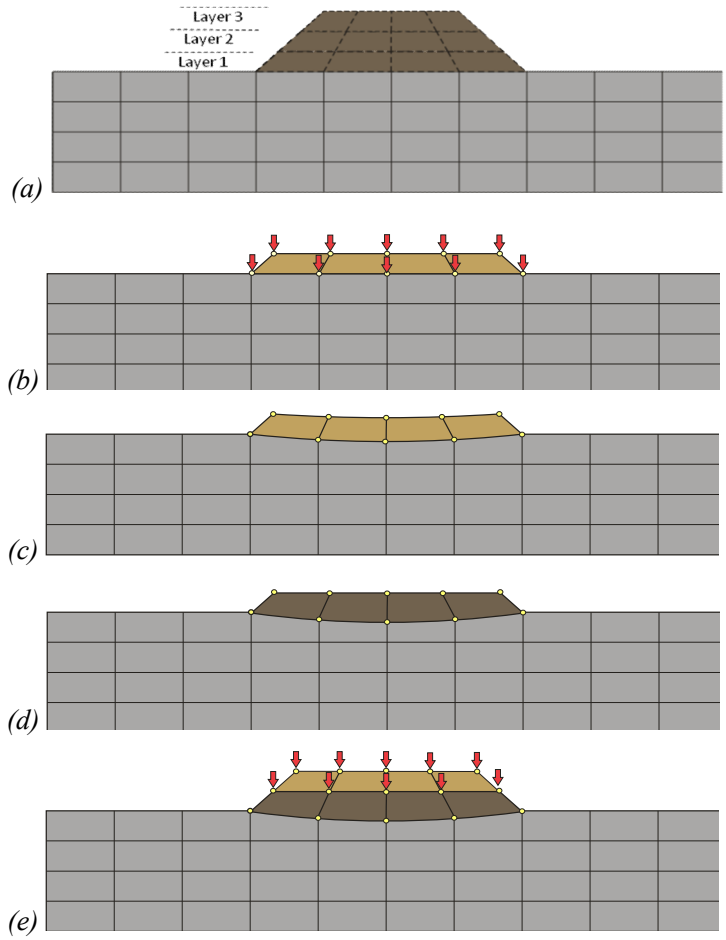


*Figure 2.12. The procedure for implementing the embankment construction in the finite element analysis.*

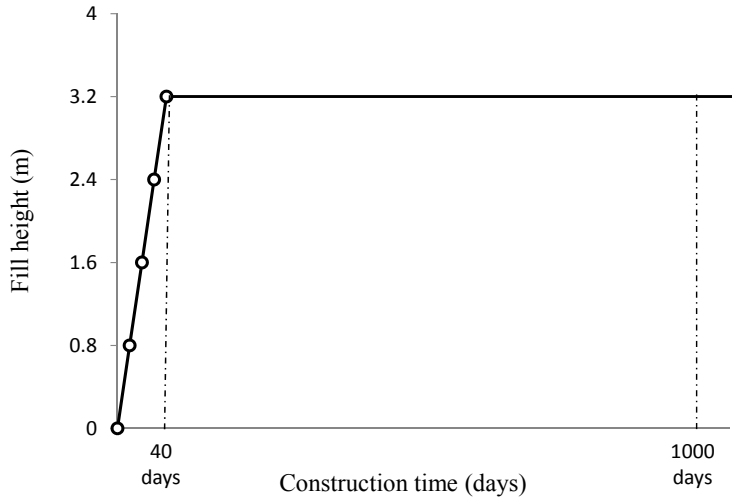


*Figure 2.13. Loading profile based on the construction stages.*

## 2.4.4. Numerical Analysis Results and Discussion

### 2.4.4.1. Vertical Displacements

The predicted results for the vertical displacements at the ground level due to the construction of the embankment are presented in Figure 2.14 for all three cases on various days. The settlements at the ground level are shown corresponding to each construction stage and consolidation after the end of construction. All cases show a trough-shaped ground settlement beneath the embankment with a surface heave around the toe of the embankment. Despite the increases in ground settlement beneath the embankment, during and after construction, the surface heave around the toe decreases during consolidation. The maximum settlement at each construction stage occurs at the node which is located just beneath the centerline of the embankment.

All the cases, i.e., Case 1 with no structural degradation, Case 2 with structural degradation, and Case 3 with structural degradation and strain-dependent shear modulus, demonstrate the same general features in terms of ground settlement, although the settlement values are different for each case. Regarding the settlement at the embankment centerline after 40 days, Cases 1 and 2 have almost similar settlements with a value of 2.17 cm. Thereafter, however, during consolidation, the strain rate in Case 2 increases (due to the softening in the soft clay layer) and leads to a larger displacement, i.e., 7.67 cm, at the embankment centerline after 1000 days versus a displacement of 4.65 cm in Case 1 at the same time. In Case 3, where the effect of the strain-dependent shear modulus has been incorporated, the settlement becomes significantly large not only during consolidation, but also during the construction of the embankment.

The surface settlement that develops at the embankment centerline after the final construction step, after 40 days, is 2.4 cm in Case 3 which increases up to 8.9 cm after 1000 days during consolidation. Figure 2.15 shows the vertical ground displacements at the embankment centerline versus time for all three cases. An evaluation of the development of settlement over time for all three cases clearly indicates the effect of both the structural degradation and the strain dependency of the shear modulus considerations.

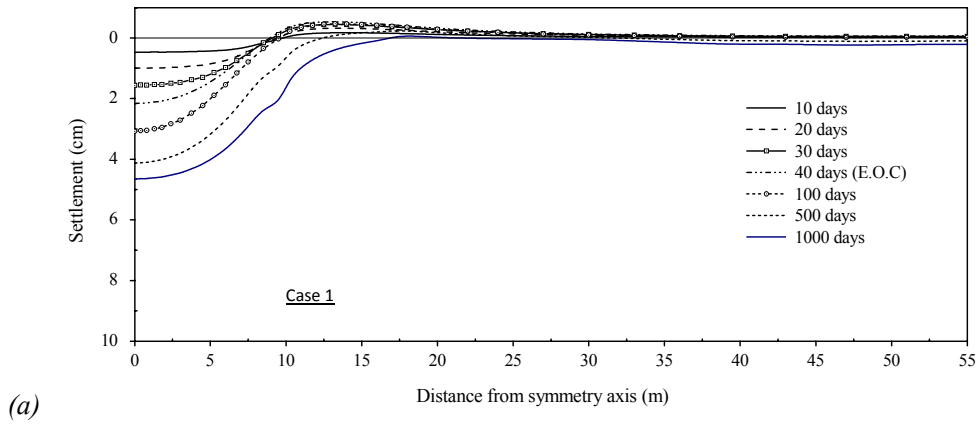


*(a)*

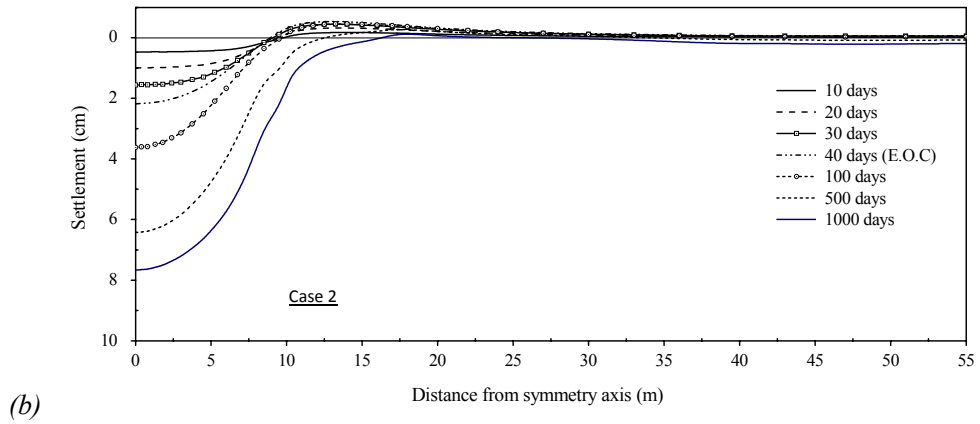


*(b)*

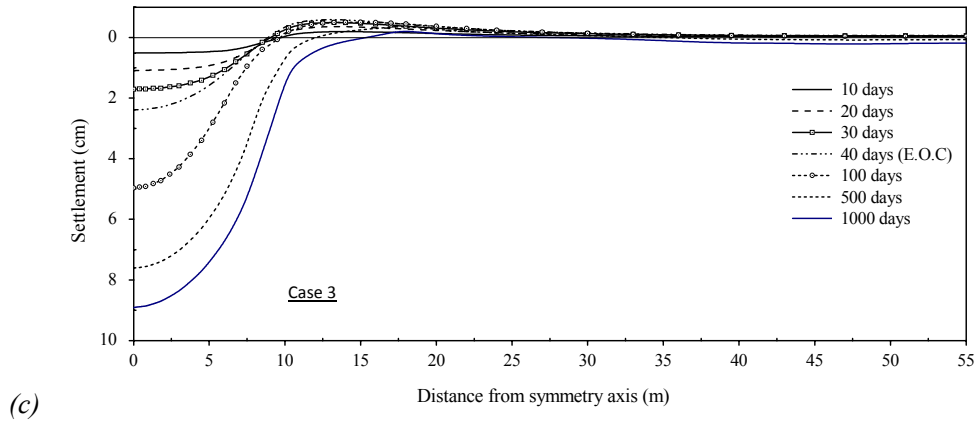


*(c)*

*Figure 2.14. Ground settlement profiles during and after construction for the different cases.*

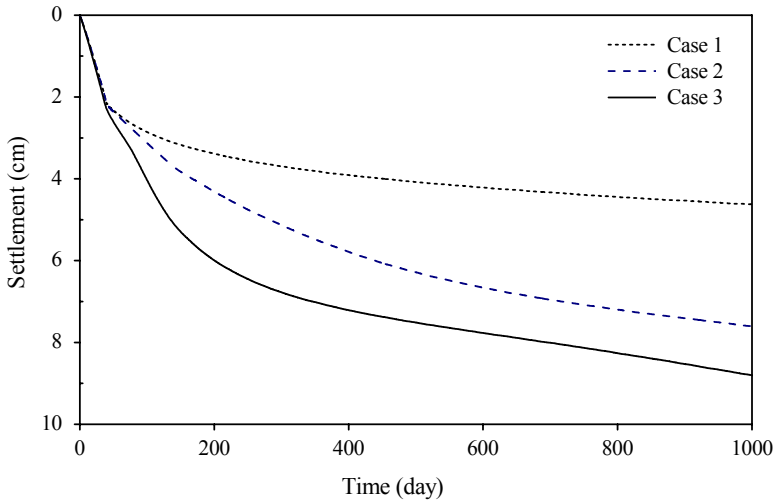


*Figure 2.15. Ground settlements versus time at the embankment centerline.*

### 2.4.4.2. Lateral Displacements

The variations in lateral displacement along the depth beneath the toe of the embankment are shown in Figure 2.16. As the displacements of the nodes located at the bottom of the model were fixed in both directions, the lateral displacement at a depth of 10 m is zero. The lateral displacement at the toe of the embankment develops during the construction and reaches the maximum positive value at a depth of 3.0 m upon completion of loading. Thereafter, it decreases with time as consolidation occurs and achieves negative values after 1000 days of consolidation at the same depth. When comparing the horizontal displacement at the toe of the embankment after the end of construction, after 40 days, Cases 1 and 2 present nearly identical lateral displacements with a value of 1.22 cm at a depth of 3.0 m, as shown in Figures 2.16(a) and (b). On the other hand, Case 3, which considers the strain-dependent shear modulus, shows a slightly larger lateral displacement with a value of 1.35 cm at the same depth, as shown in Figure 2.16(c). The values of the lateral displacement after 1000 days at a depth of 3.0 m are -1.62 cm for Case 1, -1.35 cm for Case 2, and -1.14 cm for Case 3. This indicates a backward movement during consolidation. An evaluation of the ground settlements and the lateral displacements at the toe of the embankment in the three cases indicates that in the case of a larger ground settlement, a smaller lateral displacement will develop due to consolidation.

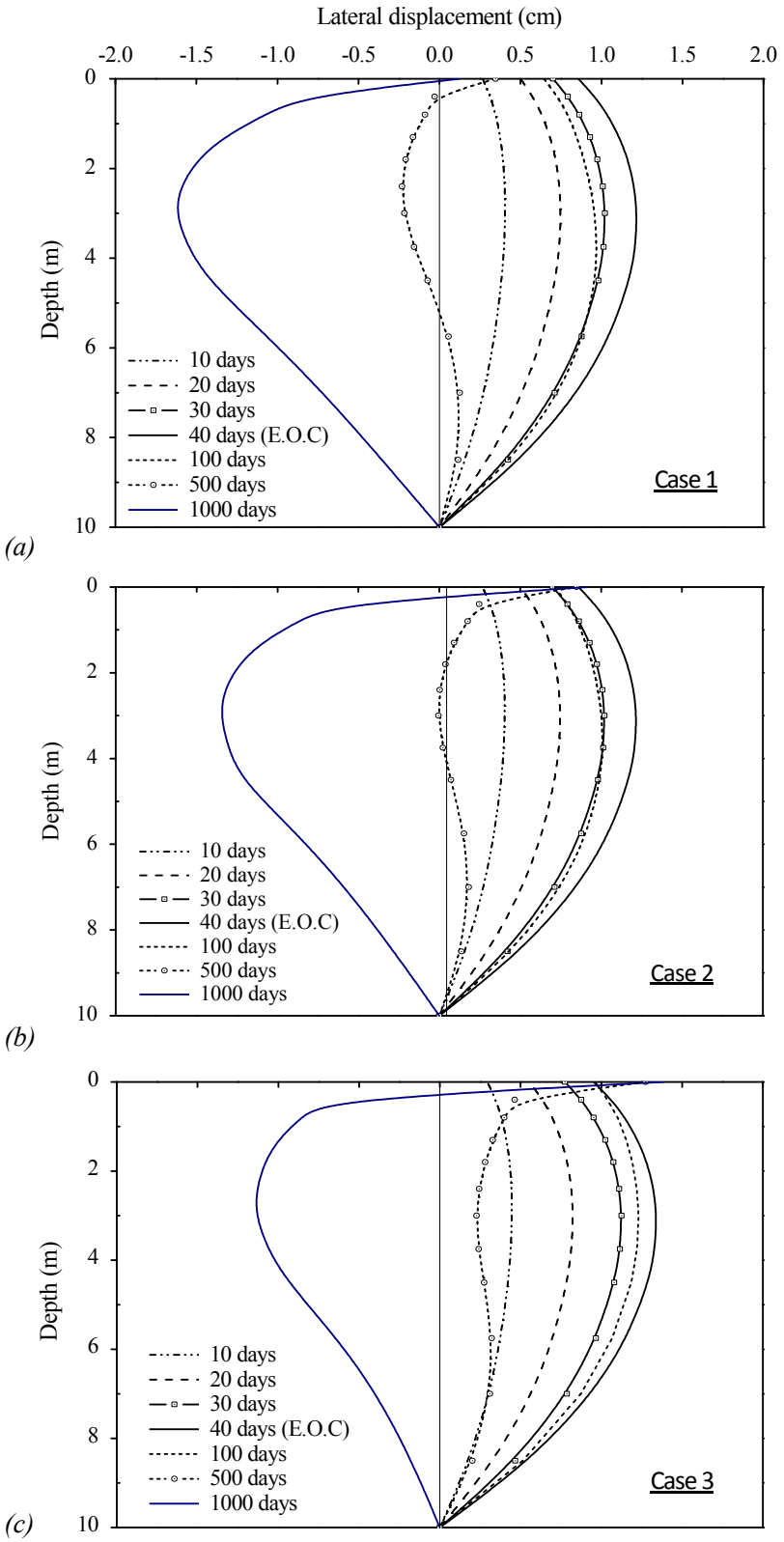


*Figure 2.16. Lateral displacements under the toe of the embankment during and after construction.*

### 2.4.4.3. Overall Deformation

The deformed meshes of the model after 1000 days of consolidation in the three cases are presented in Figure 2.17, in which the deformations have been enlarged to 10 times the actual values. Since the deformations during and just after the construction were rather small, the final deformations after 1000 days are presented here for comparison. In all cases, the deformations are particularly localized in the upper part of the subsurface layer beneath the embankment. The deformation of the embankment is insignificant compared with that of the ground layer. For Case 1, a small deformation occurs below the embankment, as shown in Figure 2.17(a), while for Case 2, a large deformation is observed in Figure 2.17(b). The deformation becomes even larger when considering the strain dependency of the shear modulus and the structural degradation in Case 3, as the distorted mesh beneath the embankment can be seen in Figure 2.17(c).

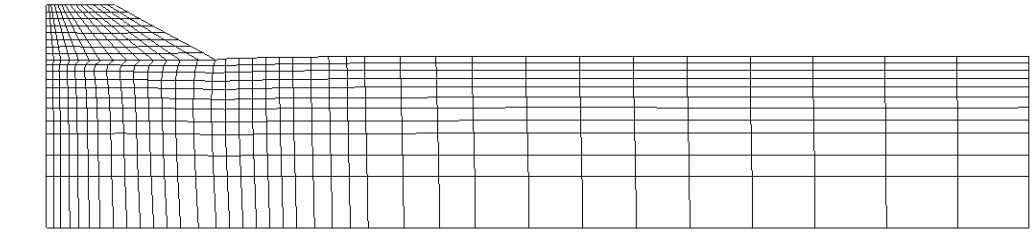

*(a)*

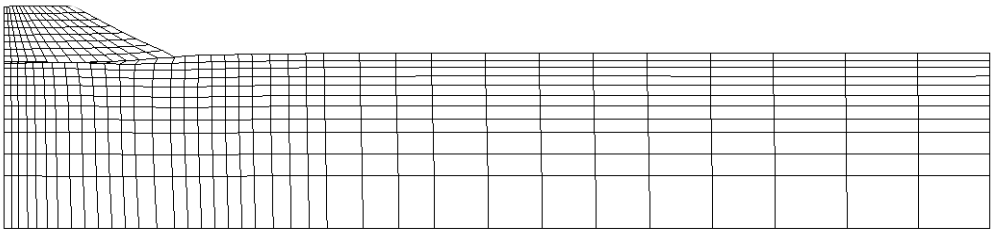

*(b)*

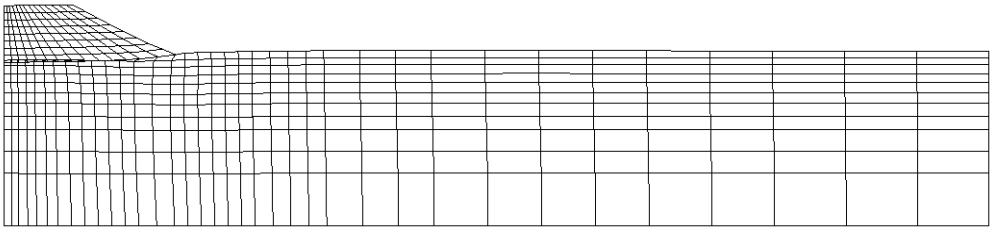

*(c)*

*Figure 2.17. Deformed meshes after 1000 days of consolidation for the different cases: (a) Case 1, (b) Case 2, and (c) Case 3 (deformations have been enlarged 10 times).*

#### 2.4.4.4. Lode Angle

The variation of Lode angle within the embankment and ground layer is presented in Figure 2.18, for Case 3. All the cases demonstrate quite similar features in the variation of Lode angle. As explained in Section 2.2, the variation of the stress ratio is considered here as a function of Lode angle according to the Mohr-Coulomb's failure criterion with zero cohesion. Lode angle alters from $\theta = 0^{\circ}$, representing the triaxial compression mode, to $\theta = 60^{\circ}$ indicating the extension mode of loading. The construction of the embankment leads to slightly rotations of the underneath ground layers which emerge as the lateral movement in the ground layers with the ground level heave near the toe of the embankment. This fact is clearly observed in the results during the construction (Figures 2.18(a) to 2.18(d)) as the increase of the Lode angle values mostly in the lower layers of the embankment, in underneath ground layers, and in the area around the toe. After the end of the construction (Figures 2.18(e) and 2.18(f)), as the consolidation proceeds, the larger values of Lode angle are developed in the upper layers of the embankment around the centreline following the ground deformations.

#### 2.4.4.5. Viscoplastic Shear Strain

The accumulated viscoplastic shear strain is determined by the viscoplastic deviatoric stain rate, as $\gamma^{vp} = \int \sqrt{de_{ij}^{vp}\, de_{ij}^{vp}}$ . The results of the accumulated viscoplastic shear strain contours at each construction stage and during consolidation are presented in Figures 2.19, 2.20, and 2.21 for Cases 1, 2, and 3, respectively. As an elastic model is employed for the embankment layers, viscoplastic strain develops only in the subsurface layer. The maximum shear strain is distributed mostly in the upper part of the soft clay foundation close to the embankment. The shear strain distributions during construction are similar for Cases 1 and 2, but the differences become more evident during consolidation. In Case 2, with structural degradation parameters, extensive strain localization can be observed just beneath the embankment with larger amounts of viscoplastic shear strain than that in Case 1. Considering the strain dependency of the shear modulus in Case 3, however, larger strain is localized during construction and consolidation. The maximum value of accumulated viscoplastic shear strain in Cases 1 and 2, from 0.6% after the end of construction, as shown in Figures 2.19(d) and 2.20(d), increases to 9.57% in Case 1 and 28.1% in Case 2 after 1000 days of consolidation, as shown in Figures 2.19(f) and 2.20(f). In Case 3, the maximum value of the accumulated viscoplastic shear strains at the end of the construction, after 40 days, is 0.84% which increases to 30.7% after 1000 days of consolidation, as shown in Figure 2.21(f).

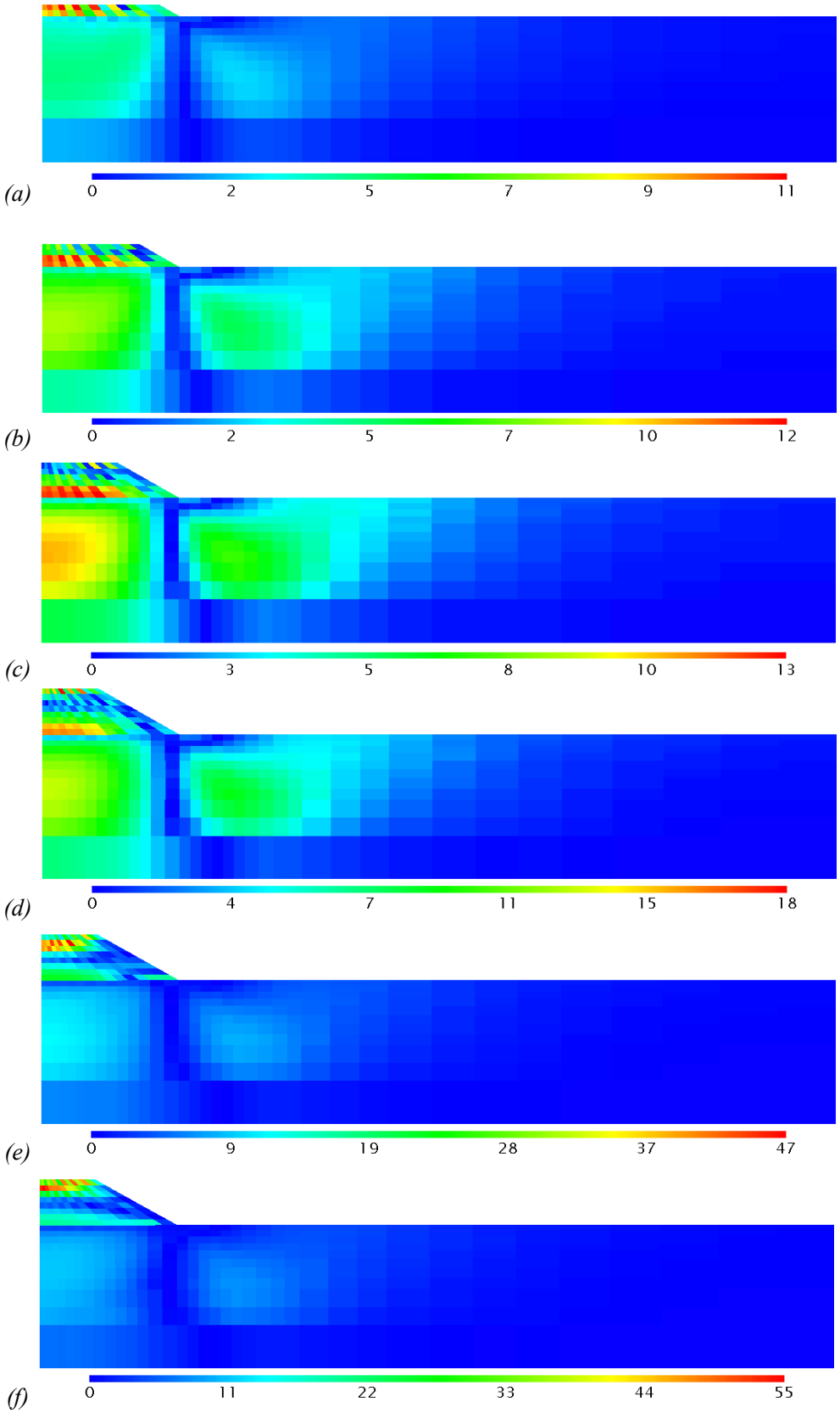


*Figure 2.18. Lode angle contours for Case 3 on various days: (a) 10 days, (b) 20 days, (c) 30 days, (d) 40 days, (e) 100 days, and (f) 1000 days (legend unit: degree).*

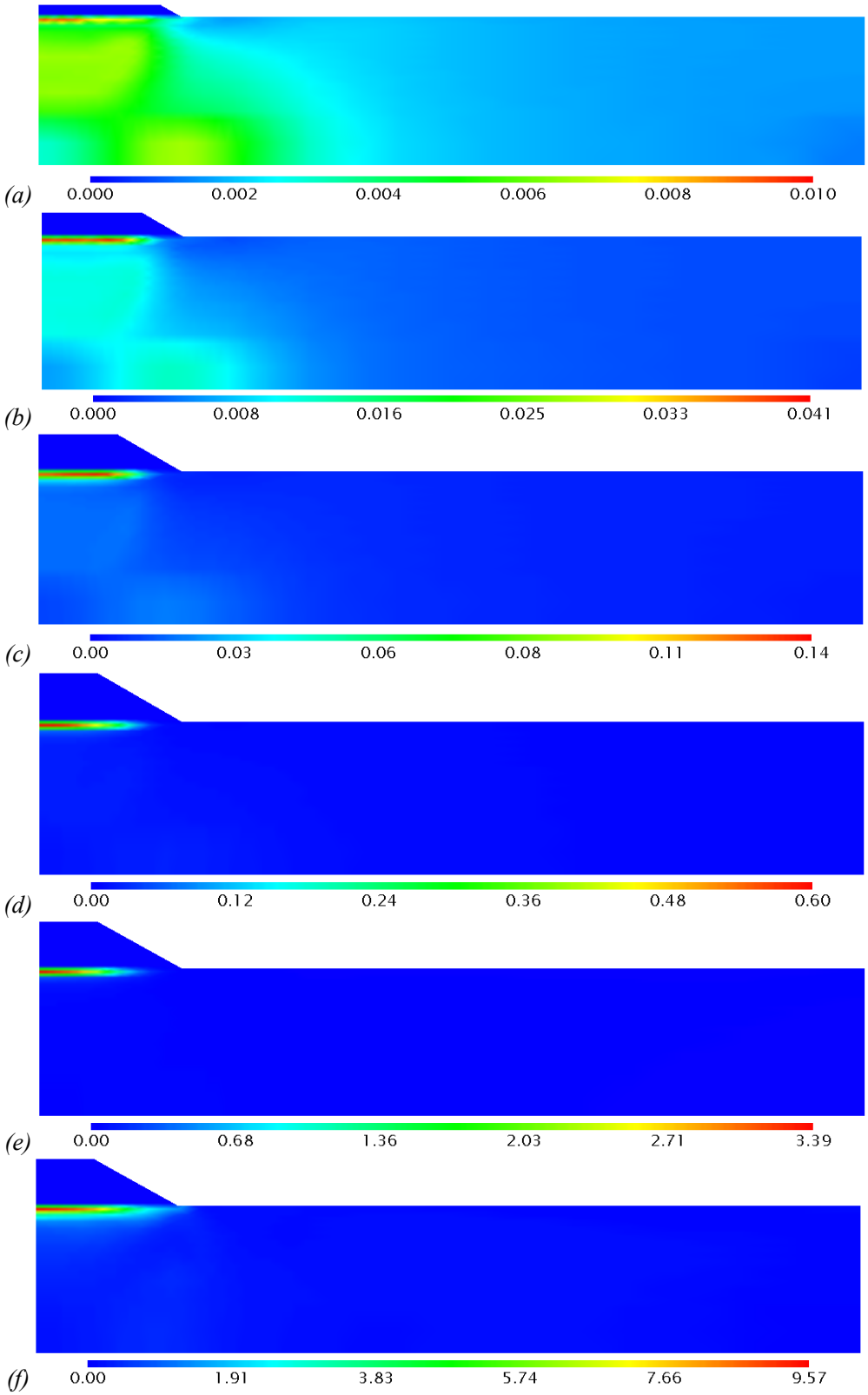


*Figure 2.19. Viscoplastic shear strain contours for Case 1 on various days: (a) 10 days, (b) 20 days, (c) 30 days, (d) 40 days, (e) 100 days, and (f) 1000 days (legend unit: %).*

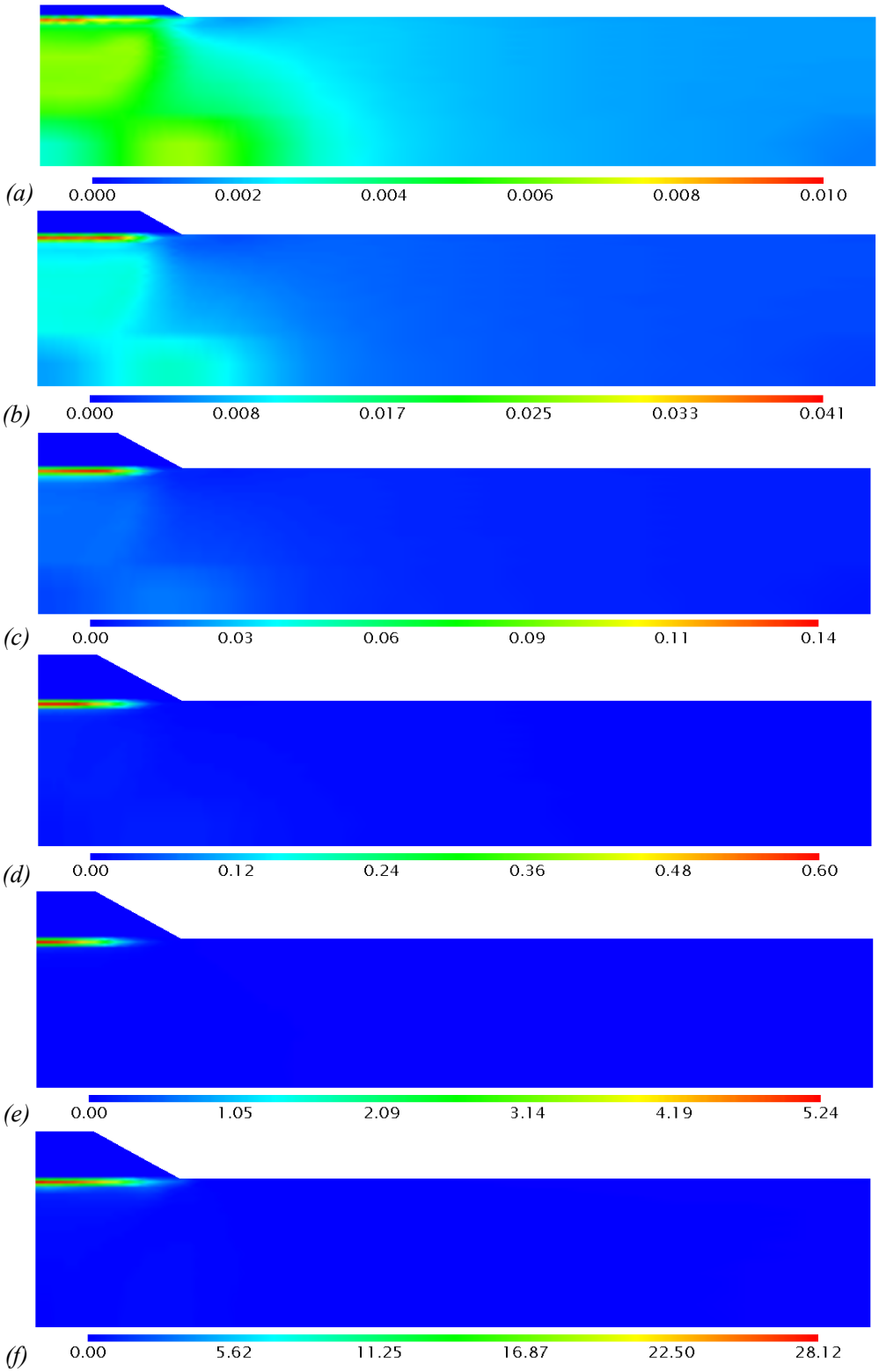


*Figure 2.20. Viscoplastic shear strain contours for Case 2 on various days: (a) 10 days, (b) 20 days, (c) 30 days, (d) 40 days, (e) 100 days, and (f) 1000 days (legend unit: %).*

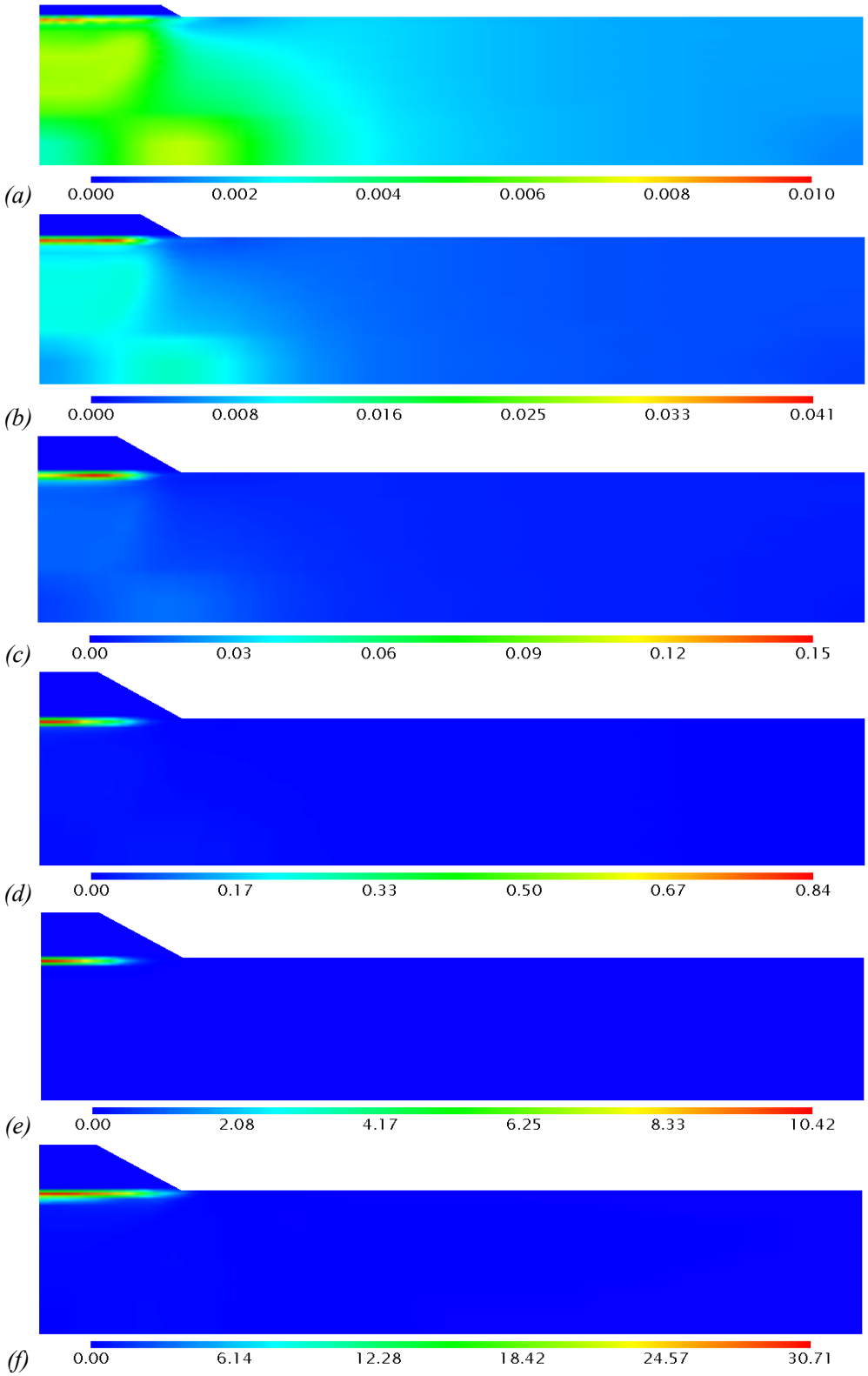


*Figure 2.21. Viscoplastic shear strain contours for Case 3 on various days: (a) 10 days, (b) 20 days, (c) 30 days, (d) 40 days, (e) 100 days, and (f) 1000 days (legend unit: %).*

#### 2.4.4.6. Excess Pore Water Pressure

The general features of the excess pore water pressure distribution are presented in Figure 2.22, which shows the excess pore pressure contours during construction and consolidation for Case 1. The excess pore water pressure is generated in the ground layer in the whole depth below the filling zone with a maximum value of 36 kPa immediately after the end of the construction and then dissipates during the consolidation and reaches about 30 kPa after 1000 days (Figure 2.22(f)). As the permeability of the clay layer is rather low and the drainage boundary is located only at the top, the dissipation rate during the consolidation is not so high. The other cases exhibit approximately the same excess pore pressure distribution as Case 1. Figure 2.23 presents the contours of excess pore pressure for Case 3 at several construction steps. The variations in the pore pressure in Case 3 during the construction process, within 40 days, shown in Figures 2.23(a) to 2.23(d) are the same as those in Case 1, shown in Figures 2.22(a) to 2.22(d). Nevertheless, after the completion of loading, Case 3 demonstrates different responses, particularly in the strain-localized region beneath the embankment. Figures 2.23(e) and 2.23(f) indicate the concentration of pore pressure contour lines just beneath the embankment in Case 3. This implies higher excess pore water pressure in that region compared with that in Case 1, as shown in Figures 2.22(e) and 2.22(f), respectively.

In order to clarify the effect of destructuration on the pore pressure response in the strain-localized region, the variations in excess pore pressure versus time at four reference points beneath the embankment are presented in Figure 2.24 in a logarithmic scale for the three cases. These points are located at different levels where large strain occurs. All the cases produce rather similar amounts of excess pore water pressure during construction, but different amounts during consolidation. For Cases 2 and 3, temporary increases in pore water pressure are observed at 100 days, during consolidation, because of the consideration given to the structural parameters. As a larger structural parameter $\beta$ is employed in Case 3, a higher secondary generation is observed. Although the amounts of regenerated excess pore pressure at various points are less in Case 2 than those in Case 3, the effect of structural degradation is clearly observed. Comparing the variations in excess pore pressure at different points in Case 3, shown in Figure 2.24(c), the secondary generated pore pressure at Points C and D, located in the area with strain localization, are higher than those at Points A and B.

It should be mentioned that the consideration of the strain-dependent shear modulus affects the pore water pressure response by changing structural parameter $\beta$ to a larger value. The anomalous build-up of pore water pressure after loading is observed; this is similar to the field- measured evidence reported by Mesri and Choi (1979), Leroueil et al. (1979), Mitchell (1986), etc. This indicates the extensive microstructural changes in the clay layer in the localization area, which causes the unstable behavior during consolidation. In sensitive soft clays, the pore pressure increases or becomes stagnant following the completion of the embankment construction, due to the collapse or

the rearrangement of the initial clay structure. This is associated with the increase in viscoplastic strain.

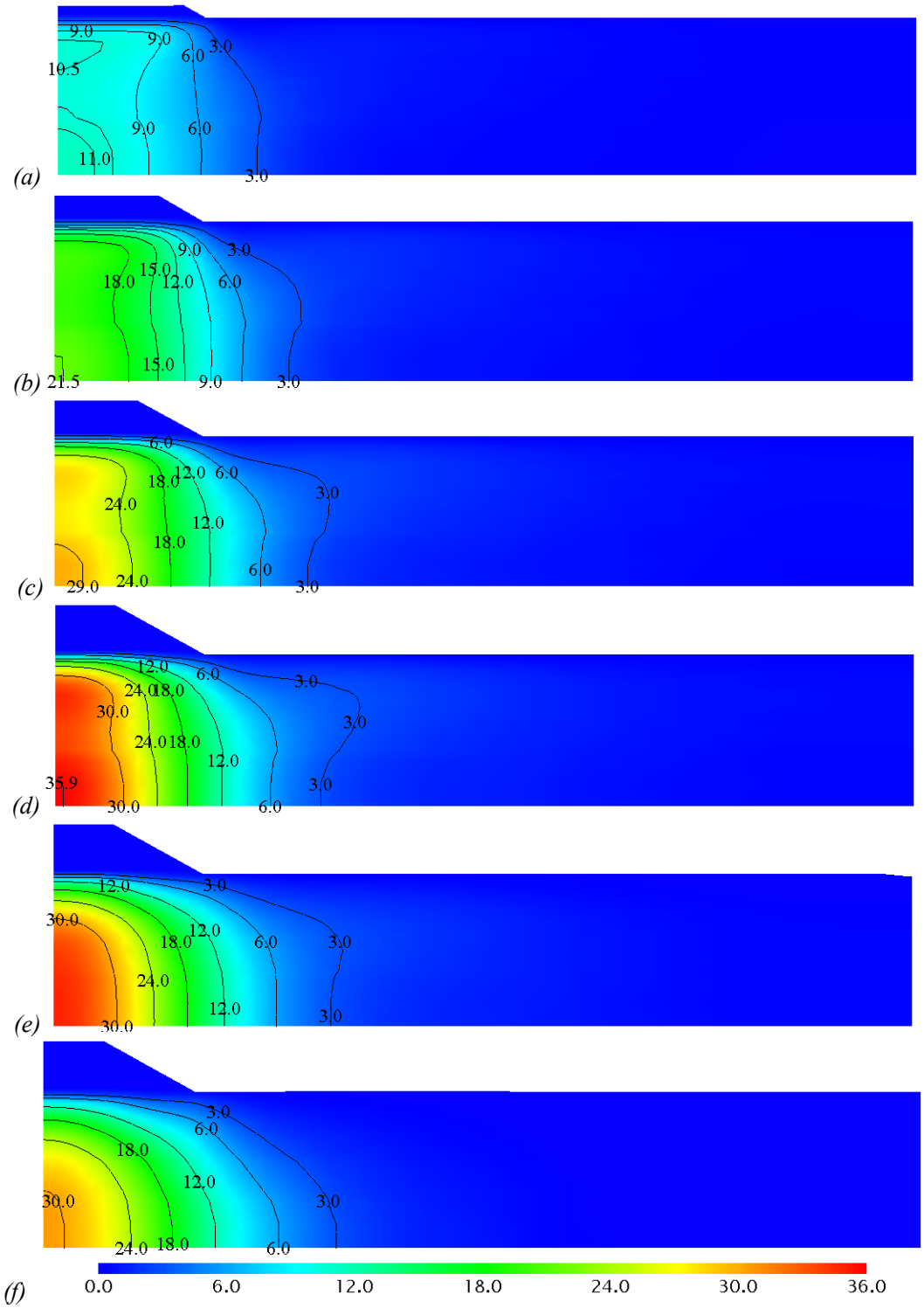


*Figure 2.22. Excess pore water pressure contours for Case 1 on various days: (a) 10 days, (b) 20 days, (c) 30 days, (d) 40 days, (e) 100 days, and (f) 1000 days (legend unit: kPa).*

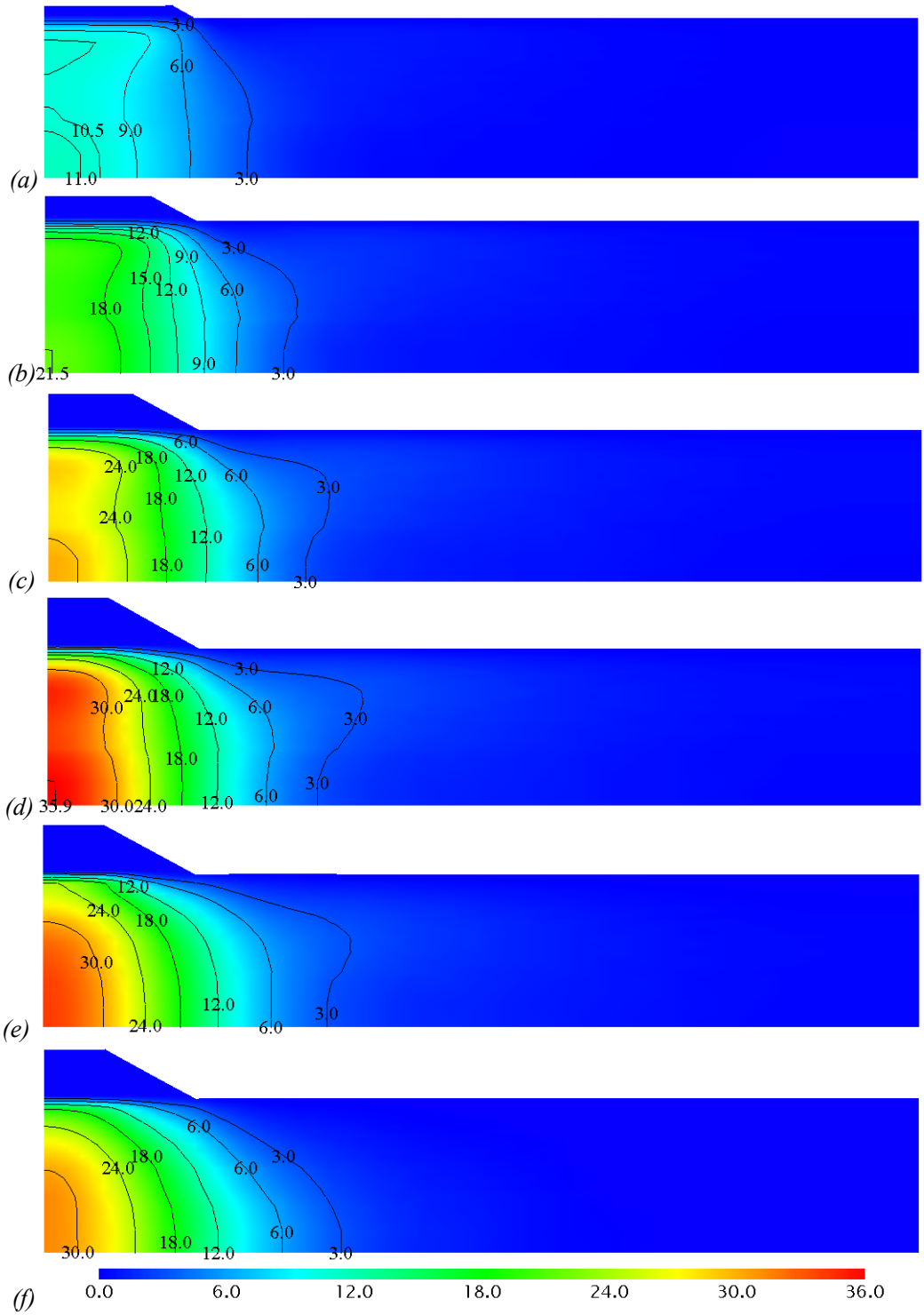


*Figure 2.23. Excess pore water pressure contours for Case 3 on various days: (a) 10 days, (b) 20 days, (c) 30 days, (d) 40 days, (e) 100 days, and (f) 1000 days (legend unit: kPa).*

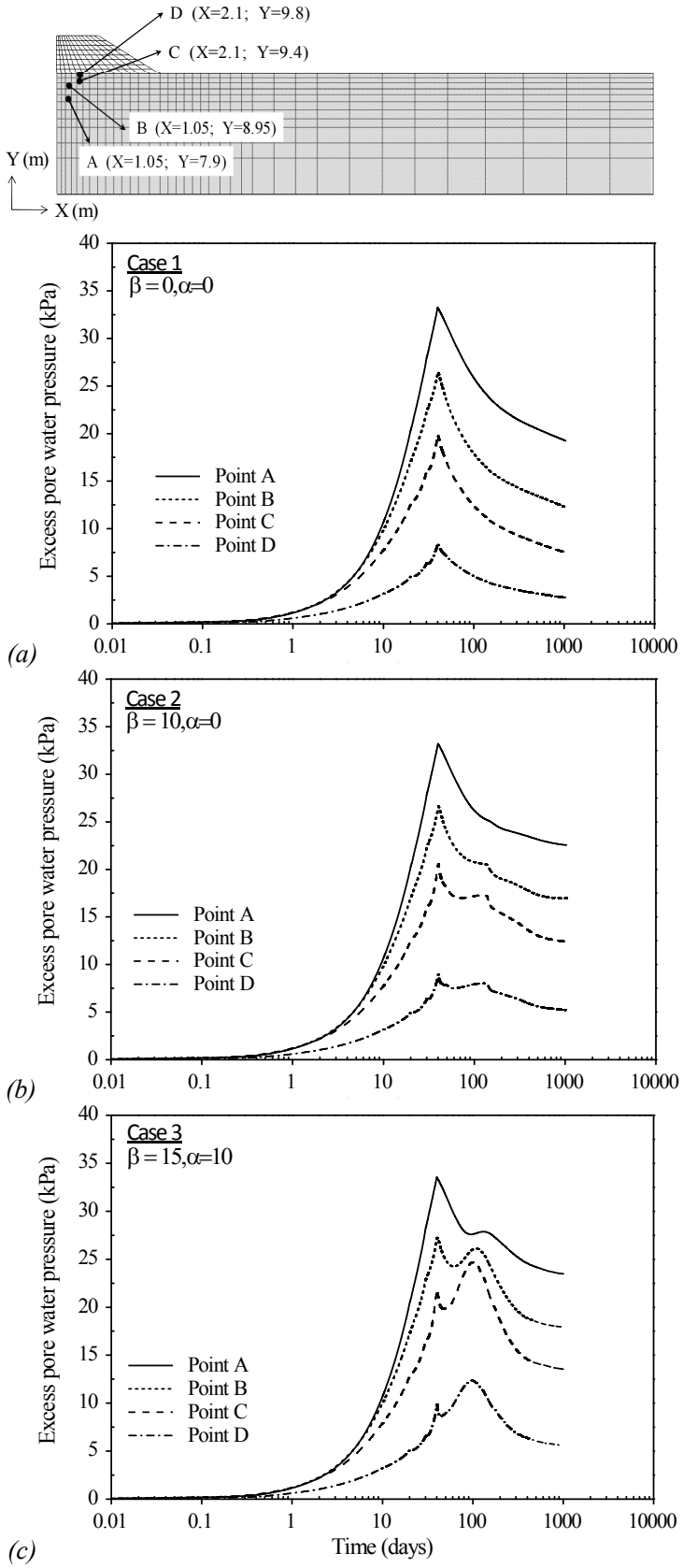


*Figure 2.24. Excess pore water pressure versus time for the different cases.*

## 2.5. Concluding Remarks

The behavior of Osaka soft clay was modeled via an elasto-viscoplastic constitutive model. The effect of destructuration on the behavior of Osaka soft clay was studied. The destructuration was considered by both viscoplastic structural degradation and a strain-dependent elastic shear modulus. The comparison of the predicted results with the laboratory test data under undrained triaxial compression conditions, exhibited the significant influence of both destructuration aspects on the soft clay response. Structural degradation includes the unstable behavior during consolidation due to the microstructural changes in the soft clay skeleton which lead to the softening behavior after the peak point along the stress-strain relation curve, a rapid increase in the strain rate, and a temporary increase in pore water pressure during consolidation. The strain dependency of the elastic shear modulus is related to the non-linear behavior of the shear modulus, which is a function of the viscoplastic shear strain and the variation in mean effective stress. In order to predict the behavior of sensitive soft clay more accurately, it is necessary to take into account the strain dependency of the shear modulus in addition to the structural degradation parameters. The predicted results presented a good agreement with the corresponding experimental values. This agreement emphasizes the capability of the elasto-viscoplastic model to reproduce the behavior of sensitive soft clay.

The influence of the destructuration aspects was then evaluated in a two-dimensional boundary value problem. The consolidation analysis of an embankment construction on a soft clay foundation was conducted by the finite element method through three cases. The results clarified the effects of these considerations of which large strain and consequent deformations developed due to the structural degradation during consolidation. Moreover, the generation of pore pressure after the completion of the construction was observed in the narrow zone close to the embankment. Considering the strain dependency of the shear modulus, however, larger strain and larger displacements developed not only during the consolidation, but also during the construction of the embankment.

# Chapter 3

# CONSOLIDATION ANALYSIS OF A LARGE-SCALE LEVEE CONSTRUCTION ON SOFT SOIL DEPOSITS

## 3.1. Introduction

In this chapter, the consolidation analysis of the Torishima super levee construction on soft soil deposits is carried out. The ground layers at the Torishima super levee site consist of alluvial sandy layers and soft clay layers, which were locally improved before the construction of the levee, by the Deep Mixing Method (DMM) beneath the normal levee and a combination of Sand Drains (SD) and Sand Compaction Piles (SCP) under the extended back slope. The elasto-viscoplastic constitutive model, proposed by Kimoto and Oka (2005), is adopted to simulate the behavior of clay layers in the two-dimensional finite element consolidation analysis. The embankments of the super levee are properly modeled in the finite element mesh so that the stiffness and the consolidation of the embankments can be considered in addition to the embankment loading. The construction sequence for the embankments is included in the numerical simulation by implementing the simulation in several stages based on the real loading profile of the embankment construction. The consolidation analysis is divided into two phases. The first phase is the consolidation analysis of the super levee construction on the natural (unimproved) ground in which the characteristic behavior of the clay layers in particular is studied by considering the effects of destructuration, namely, the structural degradation and the strain dependency of the elastic shear modulus, on the long-term consolidation

response. The second phase is the consolidation analysis of the improved ground case. The improved parts of the ground are modeled in the finite element simulation. In order to obtain material parameters after the ground improvement, the existing ground settlement data during the preloading procedure, before construction of the super levee, are used to verify the assumptions and to calibrate the material parameters of the improved layers. The results of each phase, such as deformations and excess pore water pressure responses, are presented and discussed. Comparisons are made through the results of each phase to evaluate the consolidation mechanism and the effect of the ground-improvement techniques.

## 3.2. Site Description

The cross section of the super levee with subsurface layers and ground-improvement details are schematically presented in Figure 3.1. The general stratigraphic profile of the Torishima area is composed of alluvial sandy layers and soft clay layers overlying a dense gravelly layer, and subsequently, a rather stiff clay layer at a depth of about 35 m. Em1 and Em2 represent the embankment fill materials of the main levee and of the extended back slope, respectively. B1 represents the topsoil material with a thickness of about 2.25 m. As2 is the upper alluvial sand layer, which has a thickness of approximately 8.5 m, Ac2 is the alluvial soft clay layer, which has a thickness of 12 m, As1 is the lower alluvial sand layer, which has a thickness of 5.5 m, and Ac1 is the alluvial clay deposit. Dg and Dc indicate the diluvium sandy gravel and the rather stiff clay deposits, respectively.

As shown in Figure 3.1, deep mixing (DM) was performed up to 10 and 14 m in depth beneath the main levee to improve the whole thickness of layers B1 and As2, respectively, and slightly improve the upper part of layer Ac2. The deep mixing was performed as DM walls (DMW), 1.6 m in thickness, by overlapping the soil-cement columns with a diameter of 0.9 m. DMWs were designed in a grid pattern of 5.8 by 4.8 m, which provides an average improvement ratio of 50% in the DM-improved area. The vertical sand drains were installed beneath the back slope extension in different diameters and patterns according to the design requirements, to accelerate the rate of consolidation in the Ac2 clay layer by shortening the drainage path. In the current cross section shown in Figure 3.1, the sand drains were installed in two zones, namely, Zone 1 sand drains in a 2.0×2.0 m square grid with a diameter of 0.3 m, and Zone 2 sand drains in a 2.76×2.76 m square grid with a diameter of 0.43 m. The sand drains were installed up to a depth of about 24.0 m. At the upper part of the sand drains, sand compaction piles (SCP) were positioned up to a depth of 6.7 m, covering the entire depth of layer B1 and half the depth of layer As2, mostly to prevent the liquefaction failure of these layers. The SCPs were arranged in smaller square patterns within SD grids, of which the SCPs were alternately

installed over the sand drains. In the current cross section, SCPs were formed with a diameter of 0.5 m in a square grid of 1.4×1.4 m for Zone 1 and with a diameter of 0.7 m in a square pattern of 1.95×1.95 m for Zone 2.

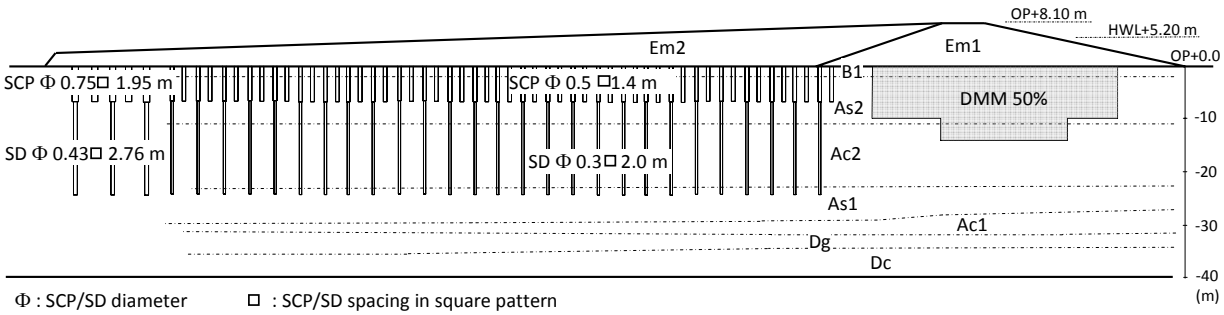


*Figure 3.1. Cross section of the Torishima super levee, soil profile, and ground-improvement techniques.*

## 3.3. Development of the Numerical Model

In order to study the long-term consolidation behavior of the super levee construction on the soft clay strata, two-dimensional numerical analyses are developed under fully saturated conditions. The behavior of the clay layers is simulated using an elasto-viscoplastic model as explained in Section 2.2, while the elastic behavior is applied for the sand and the gravel layers. The finite element formulations for large deformation analysis of the water-saturated medium are adopted. The construction procedure for the super levee and the loading profile are presented here in addition to the model geometry and the boundary conditions.

### 3.3.1. Construction Procedure and Loading Profile

The linearized construction sequence for the super levee is schematically shown in Figure 3.2. In this figure, the symbols show the assumed construction layer/stage of each embankment. The rate of loading is simulated following the procedure as explained in Section 2.5.3. The rate of loading was simulated by the successive addition of elements corresponding to each stage of embankment construction. For a particular construction stage, the elements to be constructed were added and given a constitutive model appropriate to the material behavior during placing. The nodal forces due to the self-weight body forces of the constructed material were calculated and applied to the corresponding nodes. The global stiffness matrix and all the other boundary conditions were assembled for the stage, and the FEM analysis was implemented. Before applying the next stage, the incremental

displacements of any nodes, which are only connected to the constructed elements, were zeroed. The procedure for the construction of the other stages follows similar steps. The final results are obtained by the accumulated results of each stage of the analysis.

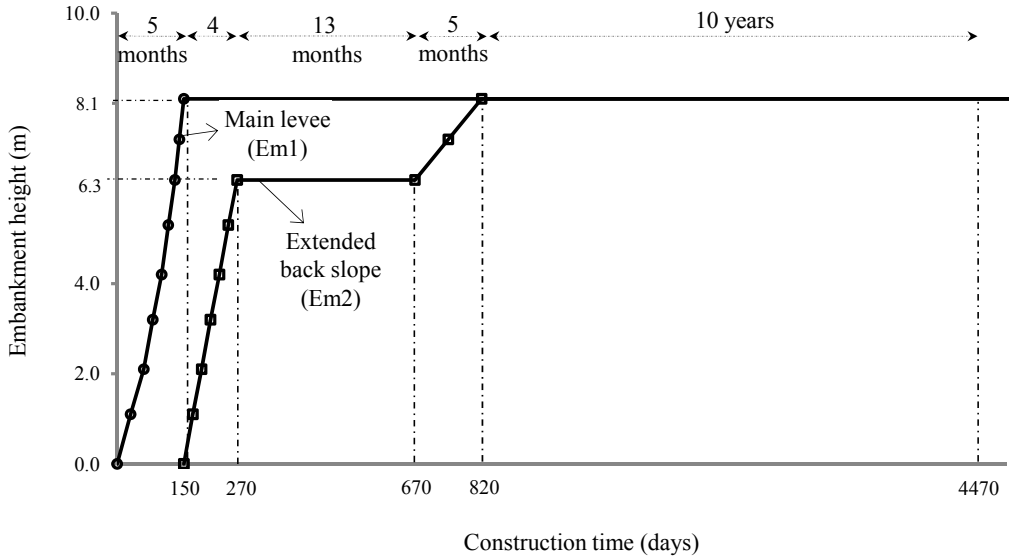


*Figure 3.2. Construction sequence for the super levee and consolidation time after its completion.*

The construction of the super levee was begun by placing the main levee fill material in eight layers consecutively within 5 months. The construction was carried out by extending the back slope immediately after the completion of the main levee in six layers up to a maximum height of 6.3 m during a period of 4 months. After the construction was suspended for 13 months, and time was allowed for a short-time consolidation, the procedure was then followed through to the final level by the placing of two layers in 5 months. Hence, the super levee was completed in a total of 27 months. As shown in Figure 3.2, the consolidation analyses are continued for 10 years after the completion of the super levee in order to consider the long-term behavior of such embankments on soft clay deposits.

### 3.3.2. Problem Geometry and Boundary Conditions

The geometry and the boundary conditions of the finite element analyses are presented in Figure 3.3. The size of the model domain is determined so that the boundary effect can be minimized. Fully saturated conditions are assumed with a drainage boundary only at the top. The displacement boundary at the bottom of the domain is fixed in both horizontal and vertical directions, while the two side boundaries are fixed only in the horizontal direction. The initial effective stress conditions of the

ground layers are assigned at the outset of the analysis based on the unit weight of the subsurface layers. The embankment layers are directly simulated in the finite element analyses following the construction sequence presented in Figure 3.2.

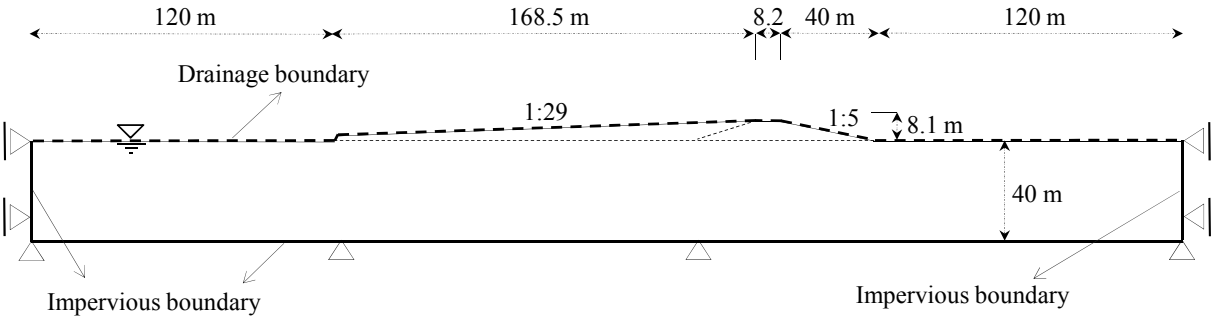


*Figure 3.3. Geometry and boundary conditions of the finite element model (final shape after completing the construction).*

## 3.4. Consolidation Analysis of the Natural (Unimproved) Ground Case

The consolidation analysis of the super levee construction on a natural ground (unimproved) is performed to study the effect of destructuration, demonstrated as the structural degradation and the strain-dependent elastic shear modulus, on the long-term consolidation behavior. The destructuration is delineated by the structural degradation in the elasto-viscoplastic constitutive model. The structural degradation has been expressed as strain softening with respect to the accumulation of viscoplastic strain, so that the model can describe the instability not only around the failure stress, but also during the compressive deformation. On the other hand, the non-linearity of the elastic shear modulus as another aspect of destructuration is taken into consideration as explained in Section 2.2.5.

Evaluating the effects of soft clay destructuration on the super levee consolidation analysis, three cases are simulated on the natural ground, namely, Case N1 without any consideration given to either the structural degradation or the strain dependency of the shear modulus, Case N2 with consideration given only to the structural degradation, and Case N3 with consideration given to both the structural degradation and the strain dependency of the shear modulus. All the cases assume the same initial conditions, in which only structural parameter $\beta$ and strain-dependent parameter $\alpha$ are subjected to change. The material parameters summarized in Table 3.1 are used in the simulations of which the elastic behavior is assumed for the sand and the gravel layers and the elasto-viscoplastic constitutive model is applied for the clay layers.

*Table 3.1. Material parameters for the natural ground case.*

| | $k$ (m/s) | $\gamma_t$ (kN/m$^3$) | $e_0$ | $G_0$ (1) (kPa) | $\lambda$ | $\kappa$ | $M^*_{mc}$ | $m'$ | $C_1, C_2$ (1/s) | $n$ | $\beta$ | $\alpha$ | $OCR$ |
|---|---|---|---|---|---|---|---|---|---|---|---|---|---|
| Em2 | $1.00\times10^{-5}$ | 18.0 | 0.8 | 5385 | | | | | | | | | |
| Em1 | $1.00\times10^{-5}$ | 17.5 | 0.8 | 4310 | | | | | | | | | |
| B1 | $1.00\times10^{-5}$ | 17.5 | 0.93 | 3300 | | | | | | | | | |
| As2 | $7.37\times10^{-6}$ | 18.0 | 0.84 | 5375 | | | | | | | | | |
| Ac2-U | $5.75\times10^{-10}$ | 17.0 | 1.25 | 3760 | 0.341 | 0.019 | 1.24 | 24.68 | $3.83\times10^{-11}$ | 0.83 | 5,10 (2) | 20 | 2.0 |
| Ac2-M | $3.85\times10^{-10}$ | 16.0 | 1.65 | 3930 | 0.593 | 0.027 | 1.18 | 28.2 | $1.85\times10^{-11}$ | 0.67 | 10,15 (2) | 10 | 1.6 |
| Ac2-L | $2.69\times10^{-10}$ | 16.6 | 1.42 | 5995 | 0.652 | 0.014 | 1.12 | 21.25 | $8.99\times10^{-11}$ | 0.60 | 15,20 (2) | 10 | 1.7 |
| As1 | $5.55\times10^{-6}$ | 18.0 | 0.9 | 6465 | | | | | | | | | |
| Ac1 | $1.60\times10^{-9}$ | 16.0 | 1.30 | 3540 | 0.326 | 0.0326 | 1.12 | 20.0 | $3.00\times10^{-12}$ | 0.70 | 10,10 (2) | 10 | 1.2 |
| Dg | $1.00\times10^{-5}$ | 19.0 | 0.9 | 40920 | | | | | | | | | |
| Dc | $5.30\times10^{-10}$ | 18.0 | 1.20 | 7695 | 0.217 | 0.0217 | 1.30 | 20.0 | $1.16\times10^{-13}$ | 0.70 | 10,10 (2) | 10 | 1.9 |

*(1) Based on the mean effective stress at depth of each layer.*
*(2) Modified values after strain-dependent shear modulus consideration*

## 3.5. Consolidation Analysis of the Improved Ground Case

The consolidation analysis of the super levee on the improved foundation is conducted based on the improvement techniques performed at the Torishima site, namely, deep mixing walls, sand drains, and sand compaction piles. The temporary effects of each improvement technique during the installation procedure, such as changes in stress in the surrounding soil and the development of excess pore water pressure, are disregarded in this study. Efforts are made to simulate each improvement technique inasmuch as its substantial function can be represented effectively in the two-dimensional (2D) analysis. The simulation for this case is conducted by considering the effect of both the structural degradation and the strain dependency of the shear modulus on the clayey layers, so the results can be compared with those in Case N3 for the natural (unimproved) ground.

### 3.5.1. Simulation of Deep Mixing Walls Under Plane Strain Conditions

Deep mixing is an *in situ* ground-improvement technique which mixes *in situ* soil with a cementitious agent (mainly cement slurry or powder) by augers to improve the engineering characteristics of the

soil. This technique has been used to mitigate potential damage to levees by enhancing the overall stiffness and reducing the permeability of the soil.

In the two-dimensional plane strain model, deep mixing walls are directly modeled in the finite element mesh based on the actual size and spacing, whilst for the surrounding parts in between the DM walls, the equivalent material parameters are estimated and assigned. The characteristics of the composite ground treated with deep mixing walls can be well represented by the estimated equivalent parameters. Figure 3.4 shows the conversion of the 3D deep mixing wall pattern into the equivalent plane strain model. The equivalent stiffness of the soil-DM composite is calculated using the stiffness of the deep mixing walls and the stiffness of the natural soil with the respective area improvement ratio as

$$E_{composite,DM} = E_{DM} \times a_{s,DM} + E_{soil} \times (1 - a_{s,DM}) \tag{3.1}$$

where $E_{composite,DM}$ is the equivalent stiffness of the soil-DM composite, $E_{DM}$ is the DM wall stiffness, $E_{soil}$ is the natural soil stiffness, and $a_{s,DM}$ is the area improvement ratio for the surrounding parts amid the DM walls. The deep mixing walls have been installed mainly in the sandy layers, as shown in Figure 3.1. Therefore, the equivalent permeability is estimated based on Darcy's law as

$$k_{v,composite} = k_{DM} \times a_{s,DM} + k_{soil} \times (1 - a_{s,DM}) \tag{3.2}$$

in which $k_{v,composite}$ is the equivalent vertical permeability of the soil-DM composite, $k_{DM}$ is the permeability of the deep mixing walls, and $k_{soil}$ is the permeability of the natural soil. In the same manner, the equivalent horizontal permeability of the soil-DM composite is assumed to be equal to the permeability of the DM walls as the part with lower permeability, namely, $k_{h,composite} = k_{DM}$.

According to the DM wall pattern in the Torishima super levee project, respective area improvement ratio $a_{s,DM}$, for the composite parts amid the DM walls, is obtained as 30%. Following Equations (3.1) and (3.2), the characteristic parameters of the soil-DM composite zone can be determined. The properties of the DM walls are subsequently obtained from the existing data in a similar case study conducted by Oka et al. (2002b).

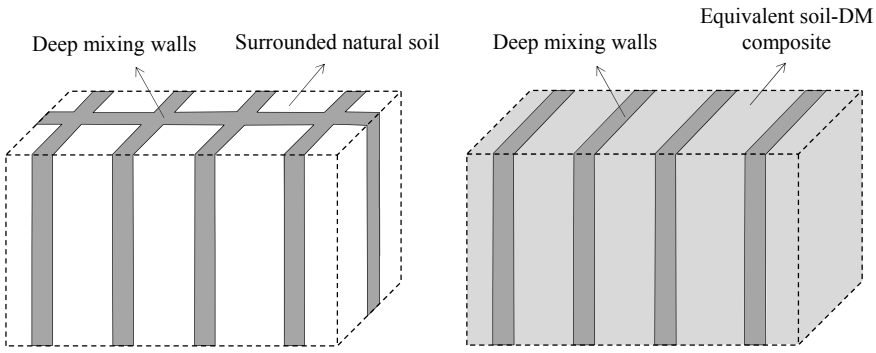


(a) Deep mixing walls in 3D pattern (b) Plane strain model of deep mixing walls and composite parts

*Figure 3.4. Conversion of the deep mixing walls in a 3D pattern into the plane strain model.*

### 3.5.2. Simulation of Sand Drains Under Plane Strain Conditions

Vertical drains have been employed for almost half a century to promote more rapid consolidation of rather thick deposits of soft fine-grained soil. Vertical drains are installed by placing high-permeability material columns such as sand, gravel, and prefabricated materials, into low-permeability soft deposits. Vertical drains accelerate the dissipation of construction-induced pore water pressure within low-permeability soil by allowing radial drainage to the high-permeability drains connected to underlying permeable strata or overlying drainage blankets. The drains speed up the construction time of the embankments and reduce the long-term maintenance costs by accelerating the rate of settlement and reducing the excess pore water pressure which may cause a risk to the stability of the embankment slopes. Since the stiffness of vertical drains is insignificant, the drains may be used in conjunction with other stabilizing techniques.

The consolidation behavior of a sand drain foundation can usually be predicted by analytical theories (e.g., Barron 1948 and Hansbo 1981), which deal with a single drain surrounded by a soil cylinder in a unit cell. The unit cell analysis assumes that consolidation takes place in uniform soil with linear compressibility characteristics in the absence of lateral movement. The consolidation around vertical drains is basically three-dimensional; therefore, such restrictive conditions are not likely to be realized in soil under embankment loading. The numerical techniques based on the finite element method provide essential means for the analysis and the design of multi-drain systems. The three-dimensional finite element modeling of vertical drain systems is very sophisticated and requires a large computational effort, especially when applied to a real super size embankment project over a large number of sand drains. In practice, drainage within the soil may take place in both vertical and radial directions, although it is often reasonable to assume that radial flow predominates. The three-dimensional radial flow into vertical drains can be approximated by simplified 2D plane strain models.

An appropriate mapping method, which represents the typical arrangement of vertical drains, can be used for effectively modeling the vertical drains in plane strain finite element analyses. Several methods have been proposed for the simulation of sand drains in plane strain models by using the concept of analytical theories (e.g., Cheung et al. 1991, Hird et al. 1992, Indraratna and Redana 1997, and Chai et al. 2001). Hird et al. (1992) developed a matching procedure which can be achieved by adjusting the drain spacing (geometry) and/or the permeability of the soil. The proposed method includes the effects of smear zones around the drains without any requirement for separate discretization. A smear zone is created during the auger drilling of sand drains or during the mandrel driving of prefabricated vertical drains, where the soil in the vicinity of the drain is remolded and its hydraulic conductivity is reduced. Here, the geometry and the hydraulic conductivity matching procedures, developed by Hird et al. (1992), are employed to simulate the sand drains.

In order to employ a realistic 2D finite element analysis for vertical drains, equivalence between the plane strain analysis and the 3D axisymmetric analysis needs to be established. The spatial vertical drain system with effective drainage radius $R$ should be converted into the equivalent infinitely parallel drain wells located at a spacing of $2B$, for which $B$ is the half width of a plane strain unit cell. Drainage radius $R$ is determined by *in situ* drain spacing $S$ based on the drain installation pattern, while $R = 0.564 \times S$ for a square pattern and $R = 0.525 \times S$ for a triangular grid pattern. The conversion of an axisymmetric sand drain unit into the plane strain approximation is schematically shown in Figure 3.5, where $l$ is the length of a drain unit cell, and $r_w$ and $r_s$ are the radius of the drain and the radius of the smear zone in an axisymmetric unit, respectively. $b_w$ is the half width of the sand drain under plane strain conditions. Following the Hird et al. (1992) method, to match the rate of consolidation in the plane strain and the axisymmetric unit cells, the equality of the average degree of consolidation is required each time and at every level in the cell. Hence,

$$\overline{U}_{hax} = \overline{U}_{hpl} \tag{3.3}$$

where $\overline{U}_{hax}$ is the average degree of consolidation for the axisymmetric cell and $\overline{U}_{hpl}$ is the average degree of consolidation for the equivalent plane strain conditions achieved by horizontal drainage. According to Hansbo (1981), under instantaneous steps of loading, the average degree of consolidation $\overline{U}_h$ on a horizontal plane at depth $z$ and time $t$ is predicted as

$$\overline{U}_h = 1 - \exp\left(-8T_h / \mu\right) \tag{3.4}$$

in which $T_h$ is the time factor for the radial drainage and $\mu$ represents the effect of the smear zone and the well resistance as

$$\mu = \ln\left(\frac{n}{s}\right) + \left(\frac{k}{k_s}\right)\ln(s) - 0.75 + \pi\left(2lz - z^2\right)\frac{k}{q_w} \tag{3.5}$$

where $n = R/r_w$ and $s = r_s/r_w$ . $k$ and $k_s$ are the horizontal permeability outside and inside the smear zone, respectively. $q_w$ is the discharge capacity of the drain representing the well resistance of the sand drains. Combining Equations (3.3) to (3.5) and disregarding the effect of the well resistance, the relationship between the horizontal permeability of plane strain condition $k_{hpl}$ and the horizontal permeability of axisymmetric unit cell $k_{hax}$, is given by

$$\frac{k_{hpl}}{k_{hax}} = \left(R^2/B^2\right) \times \left(\frac{2}{3\left[\ln\left(n/s\right) + \left(k_{hax}/k_s\right)\ln(s) - 0.75\right]}\right) \tag{3.6}$$

The modified horizontal permeability of the soil within the sand drains in the plane strain model is obtained based on the *in situ* horizontal permeability of the soil and considering the size and the permeability of the smear zone. By setting *B* to a desired value in Equation (3.6), a different geometry for the sand drain can be assigned under the plane strain conditions. This becomes useful when keeping similar drain spacing between the two systems and leads to an excessively large number of elements in the finite element analysis.

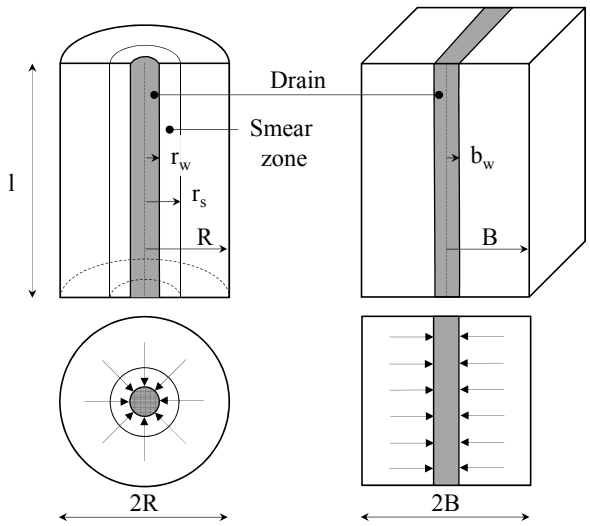


*Figure 3.5. Conversion of the axisymmetric sand drain unit into the plane strain model.*

In the present study, the sand drains are represented in the plane strain model by applying additional drainage boundary conditions to the nodes of the mesh at the locations of the sand drains instead of including separate elements to represent the sand material $\left(b_w = 0\right)$. This method is adopted to prevent any computational instability which may easily occur by putting the narrow elements as sand drain material in the finite element mesh. Representing the sand drains as boundary conditions implies that the sand drains provide ideal drains with no additional resistance to embankment loading. Concerning the permeability matching procedure described in Equation (3.6), the plane strain drain spacing is assumed as $B = 2R$ and the size of the smear zone is assumed as $s = r_s / r_w = 2$. The permeability of the smear zone as term $k_{hax} / k_s$ is considered to be determined from the preloading process results.

### 3.5.3. Simulation of Sand Compaction Piles Under Plane Strain Conditions

The sand compaction pile (SCP) method has been widely used in construction to form compacted sand piles by vibration, dynamic impact, or static excitation in a soft ground. Originally developed in Japan to improve stability or compressibility and to prevent liquefaction failure in loose sand, the SCP method is now often applied to soft clay grounds to ensure stability and to reduce ground settlement. The principle of this ground improvement technique is the densification of the ground which leads to an increase in soil density as well as lateral effective stress. Besides the strengthening effect of SCP, the drainage function of sand compaction piles is considered to enhance the resistibility of soft clay deposits by accelerating the rate of consolidation.

In the current study, as sand compaction piles have been installed only in the sandy layers, the drainage effect of SCP by itself is disregarded. For the locations in which the sand compaction piles are installed on the top of the sand drains, the drainage effect is preserved by substituting the sand compaction piles with sand drains that are connected underneath. In order to include the strengthening effect of SCP in the finite element simulation, the simplified homogenization method is adopted to avoid a large number of elements which may be produced by directly modeling the SCP as discrete elements. The basic concept of the simplified homogenization method is to describe the SCP-improved ground as a homogenized composite material with equivalent material properties, by which the improved area can be analyzed in the same mesh as that for the unimproved area.

According to the standard penetration test (SPT) results from the geotechnical site investigation before and after the SCP installation, the stiffness of the SCP improved zones is approximated as 2.5 times the stiffness of the unimproved soils in the As2 layer. The equivalent permeability matching

procedure is applied in the SCP improved zones based on the corresponding sand drain size and pattern. The others characteristic parameters are kept the same as for the unimproved soil.

### 3.5.4. Parameter Calibration Based on the Preloading Monitored Data

The excess preloading procedure has been carried out by temporarily placing the fill material over the zones of installed sand drains to improve the properties of the subsurface layers, particularly thick soft clay layer Ac2. The preloading procedure has been initiated prior to the construction of the super levee, in two stages. At first, the fill material has been placed in the whole area of preloading at a height of 1.0 m within 10 days. After a suspension of 100 days, the fill height has risen to 3.0 and 7.0 m, according to the expected embankment height of a super levee. The preloading scheme and profiles are plotted schematically in Figure 3.6 within the sketch of the super levee cross section. During the preloading procedure, the settlements at ground level have been observed at several points simultaneously. The locations of the recorded points for the current cross section are also depicted in Figure 3.6 with the distances from the left toe of the main levee.

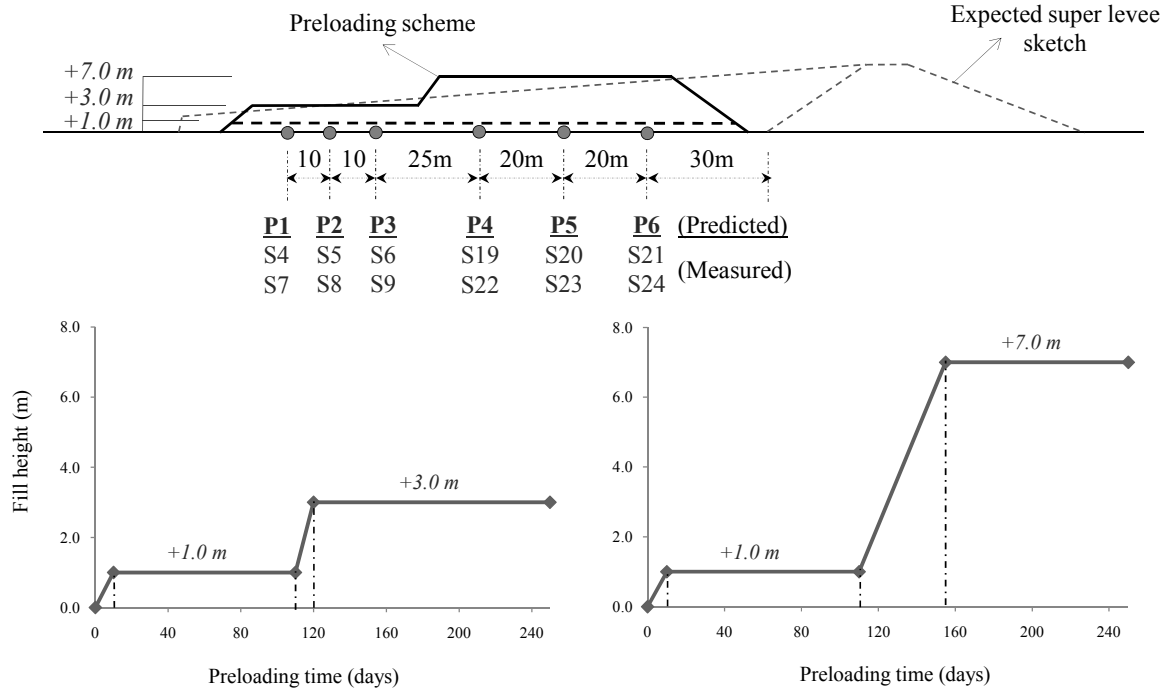


*Figure 3.6. Preloading scheme and profiles with the locations of the settlement observing points during the preloading procedure.*

Based on the preloading profiles, finite element simulations are conducted for the consolidation analyses during the preloading process. The equivalent material parameters for the improved zones are calculated using the proposed methods to model the ground-improvement techniques under plane strain conditions. For the clay materials the parameters after the strain-dependent shear modulus consideration, are allocated. Since the preloading procedure has been performed mainly to improve the characteristics of the clay layers within the sand drains by pre-consolidation, efforts are made to approximate the appropriate properties of the Ac2 layers after the sand drain installation and the preloading procedure. Two main factors are determined herein, namely, the permeability of the smear zone as $k_{hax}/k_s$ and viscoplastic parameters $C_1$ and $C_2$ in the Ac2 sub-layers within the sand drains.

By progressing the consolidation and the discharge of excess pore water pressure through the sand drains, the performance of the sand drains may be reduced in time due to the fine particles entering the drainage channel known as the clogging. This effect is speculated here by changing the permeability of the smear zone. On the other hand, the viscoplastic parameters obtained from the laboratory test data may be different from the actual field values. Several reasons can be given for this, such as the disturbance and the stress release of the soil specimens during the sampling procedure, the higher applied stress rate in the laboratory tests, and the different stress histories which the soil has experienced in the field. In addition, the installation of the sand drains and the consequent fabric changes in the clay layer can particularly affect the viscoplastic parameters. Considering the uncertainty of the viscoplastic parameter values obtained from the experimental results and the effect of the sand drain installation, changes in the viscoplastic parameters are expressed by the *CI* index. Viscoplastic parameters $C_1$ and $C_2$ are obtained to be identical in this study; therefore, the *CI* index is defined as $CI = C_1^{Improved}/C_1^{Natural}$.

Comparisons are made through the settlement profiles at the ground level with the field observed data to calibrate the soil parameters within the sand-drained zones. Figure 3.7 shows the settlement-time profiles under a preloading of +3.0 m, at the field monitored points and the corresponding points in the simulations. The field observed data are displayed by symbols and the predicted ones are shown by lines. As illustrated in Figure 3.7(a), the analysis is initiated with $CI = 1$ and $k_{hax}/k_s = 5$, wherein the predicted results are larger than the field observed data. Therefore, the analysis is carried out by reducing the viscoplastic parameter index as $CI = 0.1$, shown in Figure 3.7(b). Taking a smaller viscoplastic parameter for soft clay layers Ac2 results in a better agreement with the field observed data, since the pre-consolidation of the clay layers subjected to preloading is in progress. In the analyses under a preloading of +7.0 m, and following the same +3.0m preloading analyses, at first reduced viscoplastic parameter $CI = 0.01$ is adopted with $k_{hax}/k_s = 5$. However, as shown in Figure 3.8(a), the predicted results exhibit rather larger values than the field data. Therefore, the permeability

of the smear zone is adjusted to $k_{hax}/k_s = 10$, in order to achieve more precise values in the prediction results by slightly reducing the rate of consolidation-induced settlement, as shown in Figure 3.8(b).

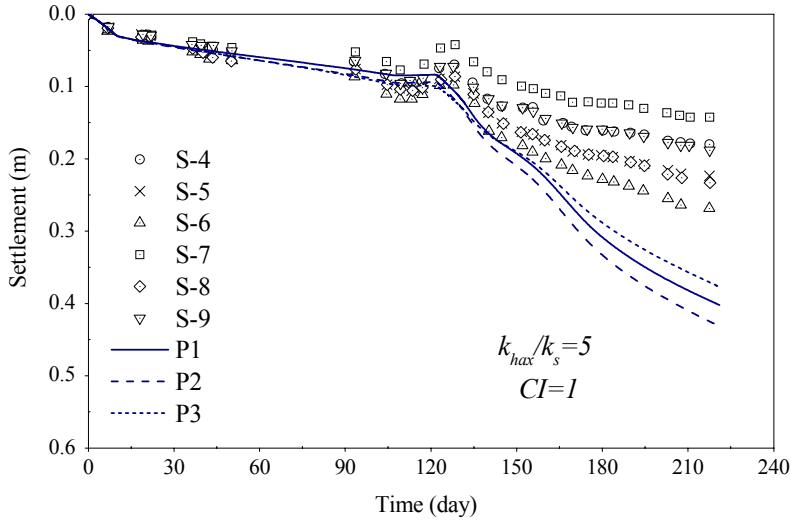


*(a)*

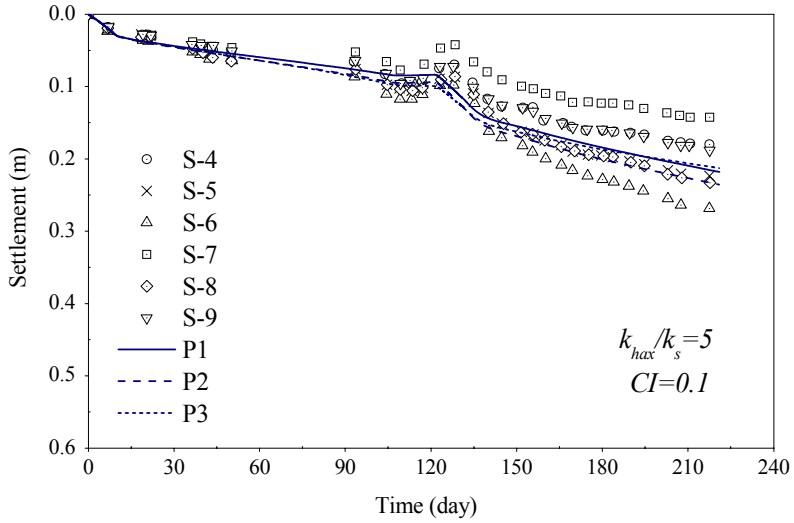


*(b)*

*Figure 3.7. Settlement-time profiles at the ground level for the points under +3.0 m preloading; (a) $CI = 1$, and (b) $CI = 0.1$, (S4-S9 the field data points, P1-P3 the predicted data points).*

As the main deformation under the super levee construction is expected to occur with the high embankment level, and also considering the long-term behavior of the super levee, the results of the +7.0m preloading analysis are assigned for further analyses of the improved ground case. Accordingly,

the final material parameters for the subsurface layers are obtained by assuming $k_{hax}/k_s = 10$ and $CI = 0.01$. Table 2 presents the additional material parameters which are used for the improved case analysis. As presented in the table, the effect of sand drains is applied by taking equivalent values for the horizontal permeability.

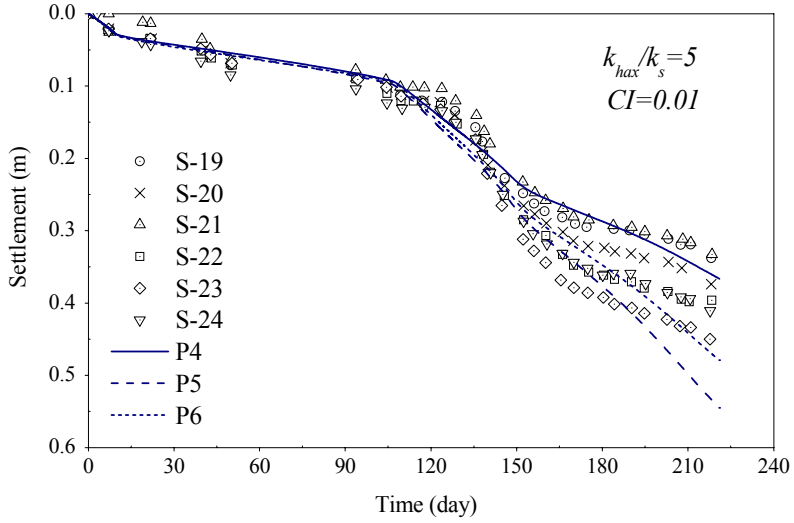


*(a)*

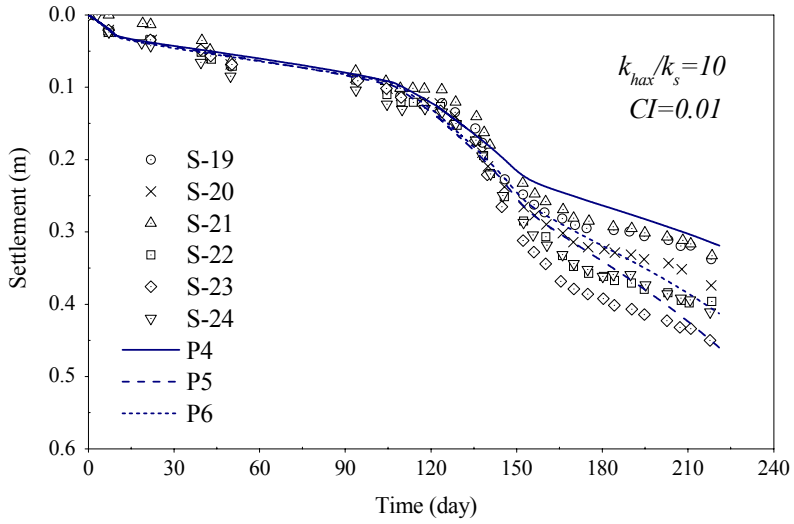


*(b)*

*Figure 3.8. Settlement-time profiles at the ground level for the points under +7.0 m preloading; (a) $k_{hax}/k_s = 5$, and (b) $k_{hax}/k_s = 10$, (S19-S24 the field data points, P4-P6 the predicted data points).*

*Table 3.2. Additional material parameters for the ground layers for the improved ground case after the preloading process calibration.*

| Layers | $k$ (m/s) | $\gamma_t$ (kN/m$^3$) | $e_0$ | $G_0$ (kPa) | $\lambda$ | $\kappa$ | $M^*_{mc}$ | $m'$ | $C_1, C_2$ (1/s) | $n$ | $\beta$ | $\alpha$ |
|---|---|---|---|---|---|---|---|---|---|---|---|---|
| DMW /Sand | $9.80\times10^{-9}$ | 20.0 | 0.72 | 81155 | | | | | | | | |
| DMW/Clay | $5.75\times10^{-11}$ | 20.0 | 0.72 | 81155 | | | | | | | | |
| B1-DM | $7.00\times10^{-6}$ | 18.75 | 0.8 | 27040 | | | | | | | | |
| B1-SCP | $k_x$: $3.55\times10^{-6}$ | 17.5 | 0.93 | 13430 | | | | | | | | |
| As2-DM | $5.16\times10^{-6}$ | 19.0 | 0.72 | 28065 | | | | | | | | |
| As2-SCP | $k_x$: $2.62\times10^{-6}$ | 18.0 | 0.84 | 13430 | | | | | | | | |
| As2-SD | $k_x$: $2.62\times10^{-6}$ | 18.0 | 0.84 | 5375 | | | | | | | | |
| Ac2-U-DM | $4.20\times10^{-10}$ | 18.5 | 1.25 | 26980 | | | | | | | | |
| Ac2-U-SD | $k_x$:$2.04\times10^{-10}$ | 17.0 | 1.25 | 3760 | 0.341 | 0.019 | 1.24 | 24.68 | $3.83\times10^{-13}$ | 0.83 | 10 | 20 |
| Ac2-M-SD | $k_x$:$1.37\times10^{-10}$ | 16.0 | 1.65 | 3930 | 0.593 | 0.027 | 1.18 | 28.2 | $1.85\times10^{-13}$ | 0.67 | 15 | 10 |
| Ac2-L-SD | $k_x$:$9.55\times10^{-11}$ | 16.6 | 1.42 | 5995 | 0.652 | 0.014 | 1.12 | 21.25 | $8.99\times10^{-13}$ | 0.60 | 20 | 10 |
| As1-SD | $k_x$: $1.97\times10^{-6}$ | 18.0 | 0.9 | 6465 | | | | | | | | |

*$k_x$: Equivalent horizontal permeability.*
*OCR is applied based on the highest overconsolidation pressure at each layer due to the preloading process.*

## 3.6. Simulation Results and Discussion

The results of the analyses, including the three cases of the natural ground (i.e., Cases N1, N2, and N3) and the improved ground case are presented in this section. Comparisons are made through the deformations and the excess pore water pressure responses. The vertical displacements are presented as the settlement at the ground level, the settlement atop the super levee, and the settlement profiles at different depths of ground layers. The lateral displacements are exhibited for the ground layers at the left- and the right-side toes of the main levee. The volumetric strain, the accumulated viscoplastic shear strain, the Lode angle, and the excess pore water pressure are shown as contours of the variations at several steps of the simulation.

### 3.6.1. Vertical Displacements

In Figure 3.9, the overall vertical displacements at the ground level are presented in various stages, during and after construction, for both natural ground and improved ground cases. The vertical displacements are plotted as settlements versus $X$ coordinate from the left-side boundary. In general, all the cases present quite similar features. The trough-shaped settlements beneath the main levee with

upward heaves adjacent to the main levee are observed at an earlier stage of construction. Continuing the construction in the back slope, the settlements develop beneath that part and increase during consolidation. The surface heaves around the toe of the embankments have an upward movement during construction, which turns downward after completing the construction.

Comparing the vertical displacements for the natural ground cases at the end of the construction (EOC) in 27 months, Cases N1 (without destructuration) and N2 (with structural degradation) demonstrate almost similar settlements, while Case N3 (with structural degradation and strain dependency of the shear modulus) exhibits relatively larger settlements. The maximum value of the settlements after 27 months is observed at $X$ = 280 m with a value of about 0.20 m equally for Cases N1 and N2, and about 0.22 m for Case N3. This fact indicates the effect of the strain dependency of the shear modulus on the deformations during the loading process. During consolidation, however, as the structural degradation is taken into account for Cases N2 and N3, larger settlements are developed because of strain softening in the soft clay layers. The maximum overall settlements in 10 years after EOC occur at $X$ = 280 m with a value of 0.26 m in Case N1, and at $X$ = 260 m with values of approximately 0.32 m and 0.40 m in Case N2 and Case N3, respectively. In Case N3, larger structural parameters are applied; thereby larger settlements are predicted compared with those in Case N2.

Comparing the vertical displacements for the improved ground case and Case N3, the improved ground case exhibits the same features in terms of the ground level settlement, although the predicted surface heave around the embankment toes is quite small. The settlements beneath the main levee become smaller than those in Case N3, as DM walls have been installed underneath. The effect of SCP/SD is observed as accelerating the rate of consolidation by shortening the drainage paths, in which the generated excess pore water pressure and subsequent deformations are reduced. The overall maximum settlements in 10 years after EOC for the natural ground case is about 0.29 m at the location of $X$ = 265 m. The settlement versus time at $X$ = 260 m, which represents the location of the maximum overall settlement in most of the cases, is plotted in Figure 3.10 in a logarithmic scale. The effect of the structural degradation and the strain dependency of the shear modulus can be clearly observed among the natural ground case results. The displacement rate in Case N3 starts with larger values in the surface heave and the settlement, compared with those in Cases N1 and N2, which have similar displacement rates during the construction process. After that, the rates of displacement in Case N2 and Case N3 increase due to the structural degradation during the consolidation and result in larger settlements. In the improved ground case, the vertical displacement appears as settlement in an earlier stage of construction, despite the surface heave in the natural ground cases. Furthermore, the effect of the sand drain installation at this location is observed as a higher rate of displacement during the construction, which is reduced during the long-term consolidation and results in smaller settlement compared with those in Case N3.

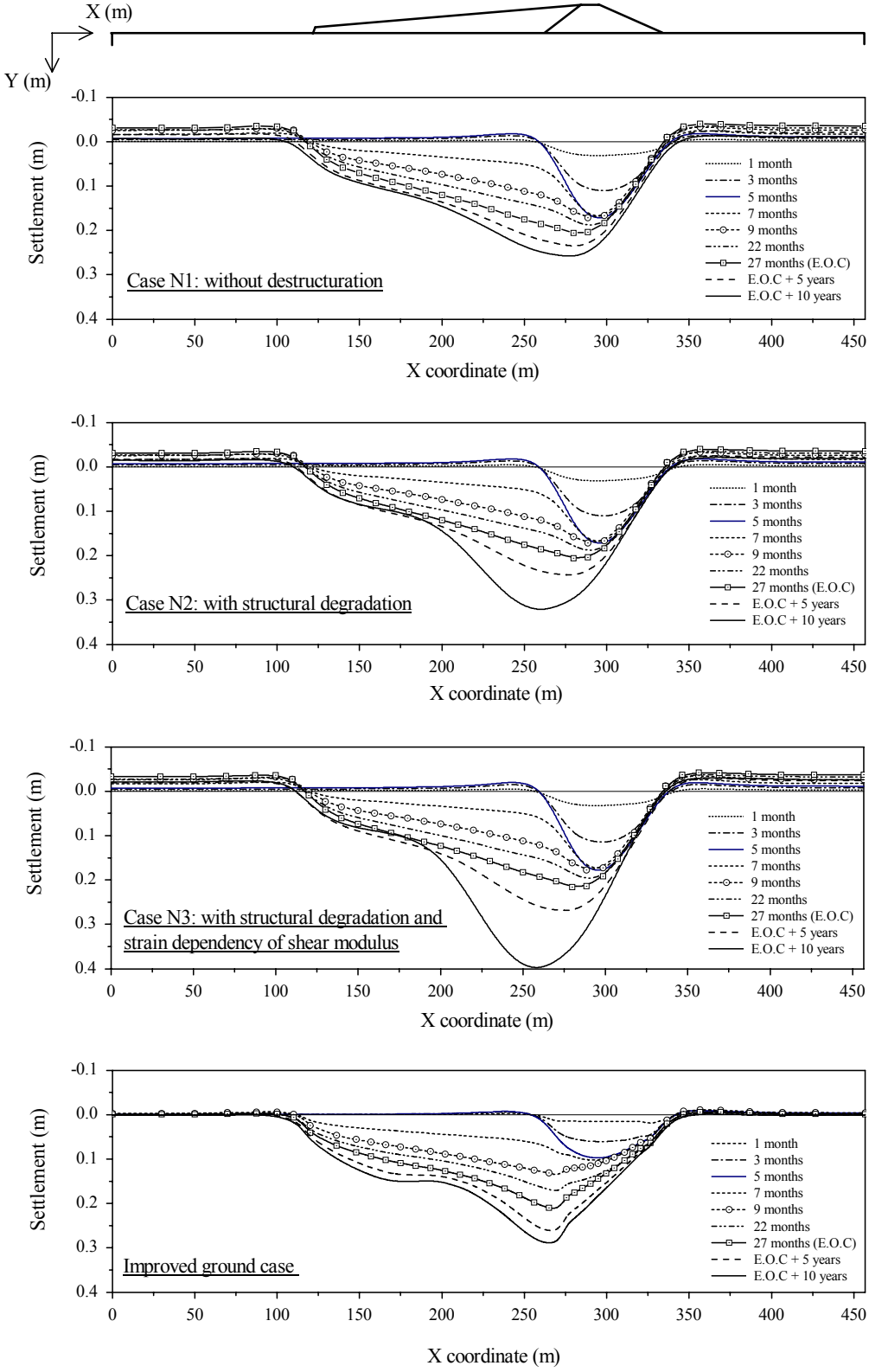


*Figure 3.9. Ground level settlement profiles during loading and consolidation for the natural ground cases (Cases N1, N2, and N3) and the improved ground case.*

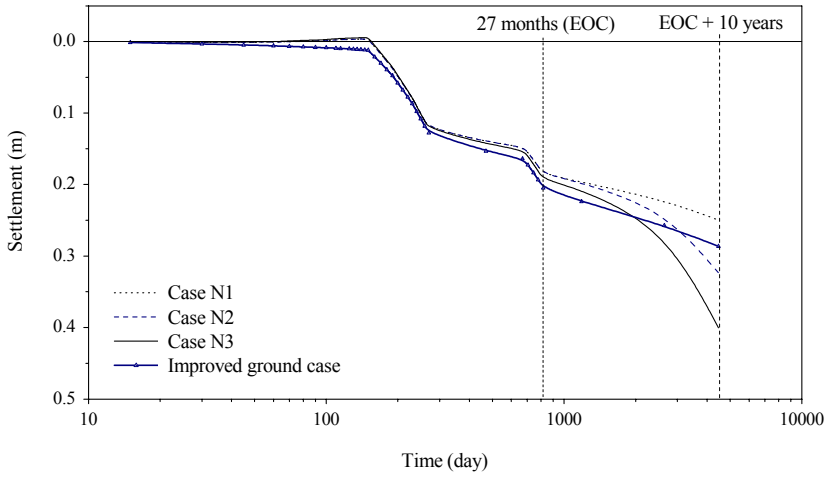


*Figure 3.10. Ground level settlement versus time at X= 260 m for the natural ground cases (Cases N1, N2, and N3) and the improved ground case.*

The overall vertical displacement profiles at different depths of ground layers are presented in Figures 3.11 and 3.12 for Case N3 and the improved ground case, respectively. The vertical displacement profiles at the ground level are depicted along the settlement profiles atop the As2 layer at a depth of 2.2 m, atop the Ac2 layer at a depth of 10.95 m, atop the As1 layer at a depth of 22.95 m, and atop the Dg layer at a depth of 32.05 m. The settlement profiles at various depths show similar features to the corresponding settlements at the ground level, but with smaller values. At the deeper layers, the values of the vertical displacement decrease due to the smaller influence of the embankment loading at those layers. Comparing the settlement profiles at each depth for Case N3 and the improved ground case, the effect of ground improvement is clearly observed as smaller vertical displacements. At depths of 22.95 m and 32.05 m, however, the improved ground case shows slightly larger settlements than those for Case N3, since the stiffness of the upper layers has been improved and the deformations under embankment loading have been distributed to the deeper layers.

The predicted vertical displacements atop the super levee after the end of the construction are presented in Figure 3.13 for different cases. The vertical displacement on top of the super levee appears in trend similar to that for the ground level settlements, but with smaller values in general. The locations of the maximum settlement atop the super levee in different cases nearly corresponded with the locations of the settlements in the ground level. For the natural ground cases, the settlements in 1 year after EOC are almost similar for Cases N1, N2, and N3. Afterwards, however, the effect of structural degradation within the consolidation process becomes more evident and leads to relatively larger settlements in Cases N2 and N3. In the improved ground case, as pre-consolidation with sand drain installation has been carried out, a smaller settlement develops compared with that in Case N3. Nonetheless, the notable relative settlement is still observed throughout the surface of the super levee.

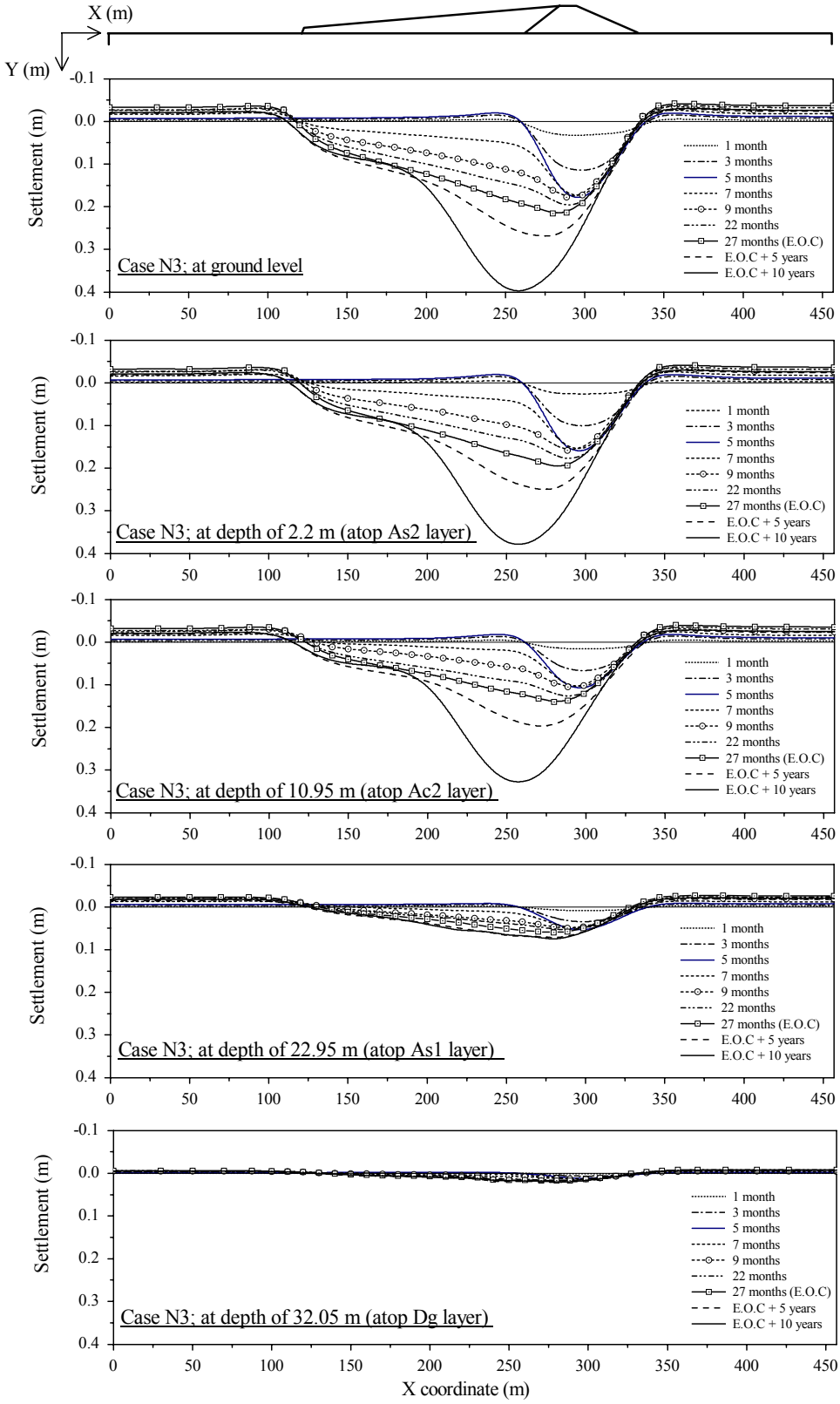


*Figure 3.11. Vertical displacement profiles for the natural ground, Case N3, at ground level and at different depths.*

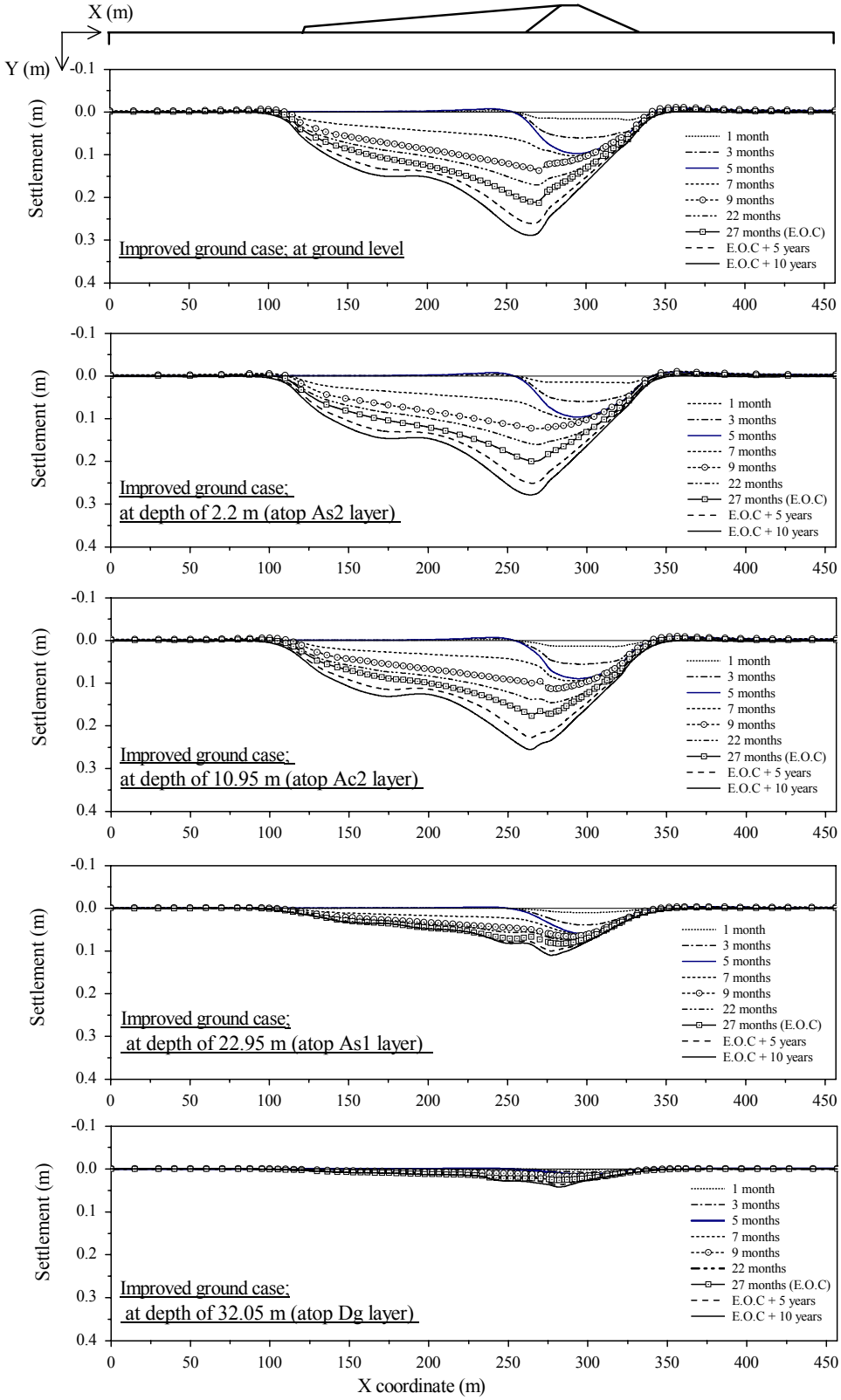


*Figure 3.12. Vertical displacement profiles for the improved ground case at ground level and at different depths.*

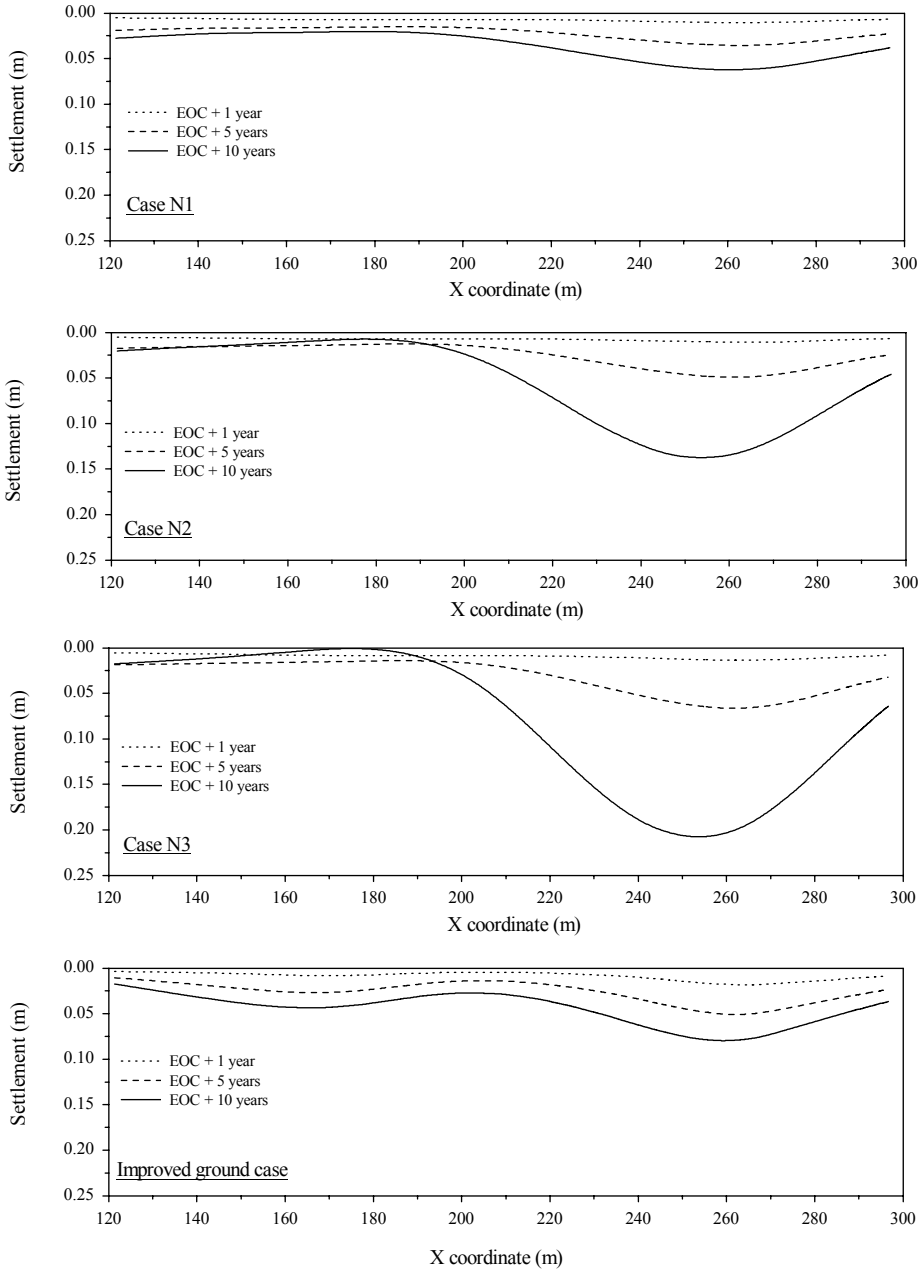


*Figure 3.13. Settlement profiles atop the super levee after the end of the construction (EOC), for the natural ground cases (Cases N1, N2, and N3) and the improved ground case.*

### 3.6.2. Lateral Displacements

The lateral displacements at the left- and the right-side toes of the main levee along the ground layers are illustrated in Figure 3.14 for Case N3 and the improved ground case. The other natural ground cases demonstrate variations nearly similar to those of Case N3; therefore, the results for Case N3 are only presented here to evaluate the effect of the ground-improvement techniques on the lateral displacements. In consolidation of the embankment construction, the lateral displacement along the

toe follows the process of excess pore pressure generation and dissipation under the embankment by forward and backward movements.

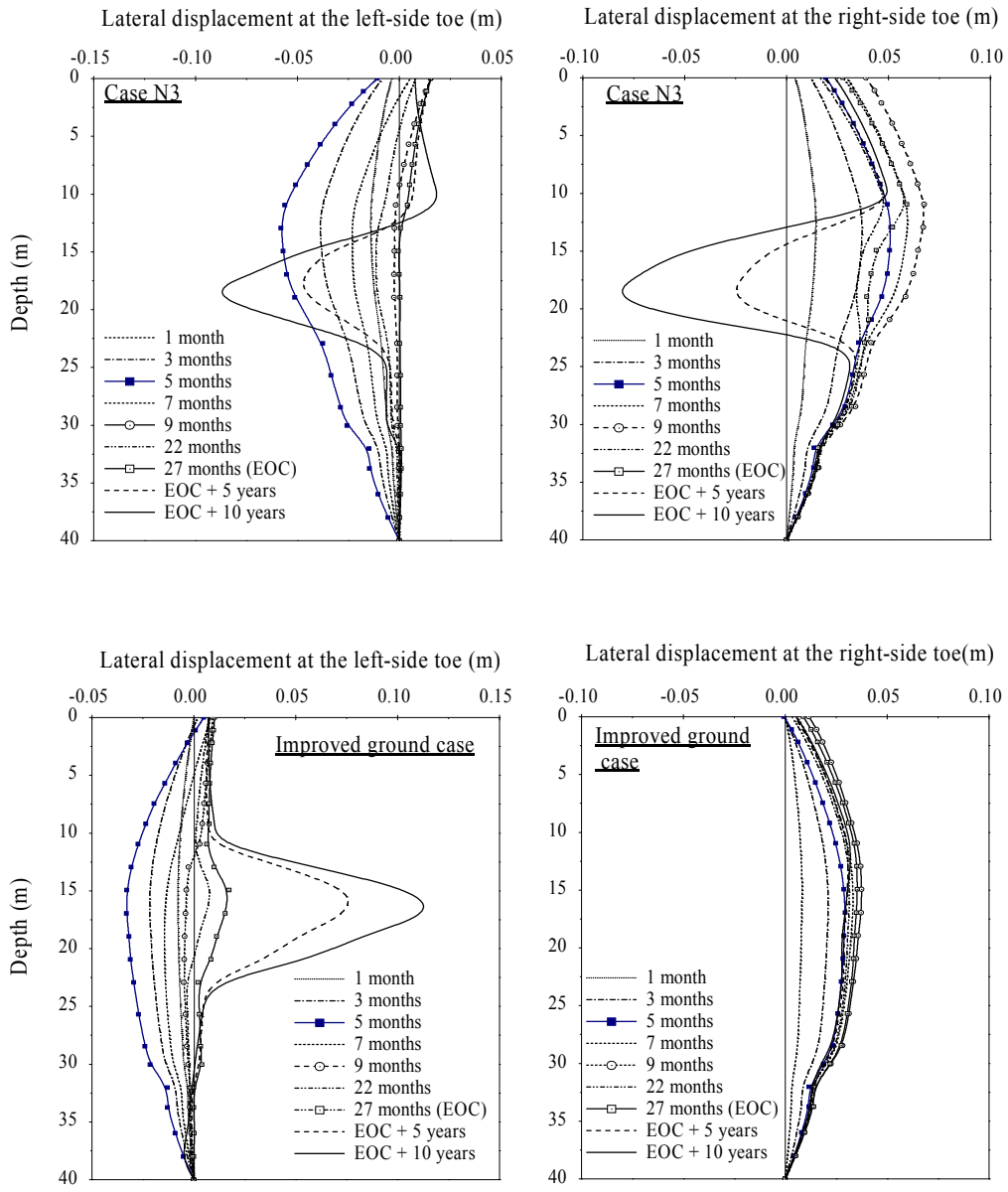


*Figure 3.14. Lateral displacement profiles at the main levee toes along the ground depth for the natural ground, Case N3, and the improved ground case.*

For Case N3, the lateral displacement at the right-side toe of the main levee is increased toward the right for 9 months with its maximum value at a depth of 11 m. Then it moves toward the left during the suspension of construction and consequent short-time consolidation. This sequence is continued by starting the next phase of construction and the following consolidation period. The maximum lateral displacement along the depth during the consolidation is observed at a depth of

about 18 m, which is located in the Ac2 clay layer. At the left-side toe section, however, the lateral displacement presents rather different behavior, since the construction is carried out on both sides of this section. At first, by constructing the main levee, it shows the lateral movement toward the left. However, by continuing the construction to the back slope, which is located on the left side of this section, rightward movements appear slightly. During the long-term consolidation, the lateral displacement in this section follows the dissipation process of the generated excess pore pressure beneath the back slope, by showing leftward movements with its maximum value at a depth of about 18 m.

For the improved ground case, at the right-side toe, the lateral displacement follows the same tendency as that for Case N3, but with smaller displacements due to the installation of the DM walls. At the left-side toe, similar movements occurred with smaller values while the surrounding soil is treated by the improvement techniques. During the long-term consolidation, the lateral displacement profile along the depth moves toward the right, following the dissipation of the generated excess pore pressure beneath the main levee.

### 3.6.3. Volumetric Strain

The volumetric strain, which is calculated by the summation of the vertical and the horizontal strain, is shown in Figures 3.15, 3.16, 3.17, and 3.20 for the three natural ground cases and the improved ground case, respectively. The volumetric strain contours at different stages of construction, namely, 9, 22, and 27 months, and 10 years after EOC are presented. As the volumetric strain changes over a wide range during the analysis, different legend scales are adopted in each case, accordingly.

After 9 months, Cases N1, N2, and N3 demonstrate nearly similar distributions of volumetric strain, with the strain localization mainly in the area just beneath the embankments and slightly at the upper part of the Ac2 clay layer. After 22 months, despite the similarity in the results for Cases N1 and N2, Case N3 shows a larger zone of strain localization in the Ac2 layer. 10 years after EOC, the volumetric strain localization is clearly observed in the Ac2 clay layers beneath the back slope for the three cases. A larger volumetric strain develops in Case N2 in comparison to that for Case N1, and the values of localized volumetric strain in Case N3 become even larger, because the strain dependency of the shear modulus is considered. The levels of volumetric strain in the improved ground case, shown in Figure 3.18, develop beneath the filling zones with smaller overall values compared with those in Case N3. However, significant strain localization is observed in the upper part of layer Ac2 in between the DM walls and the SCP/SD installation zones, in which about 5% of the volumetric strain is localized after 10 years of consolidation.

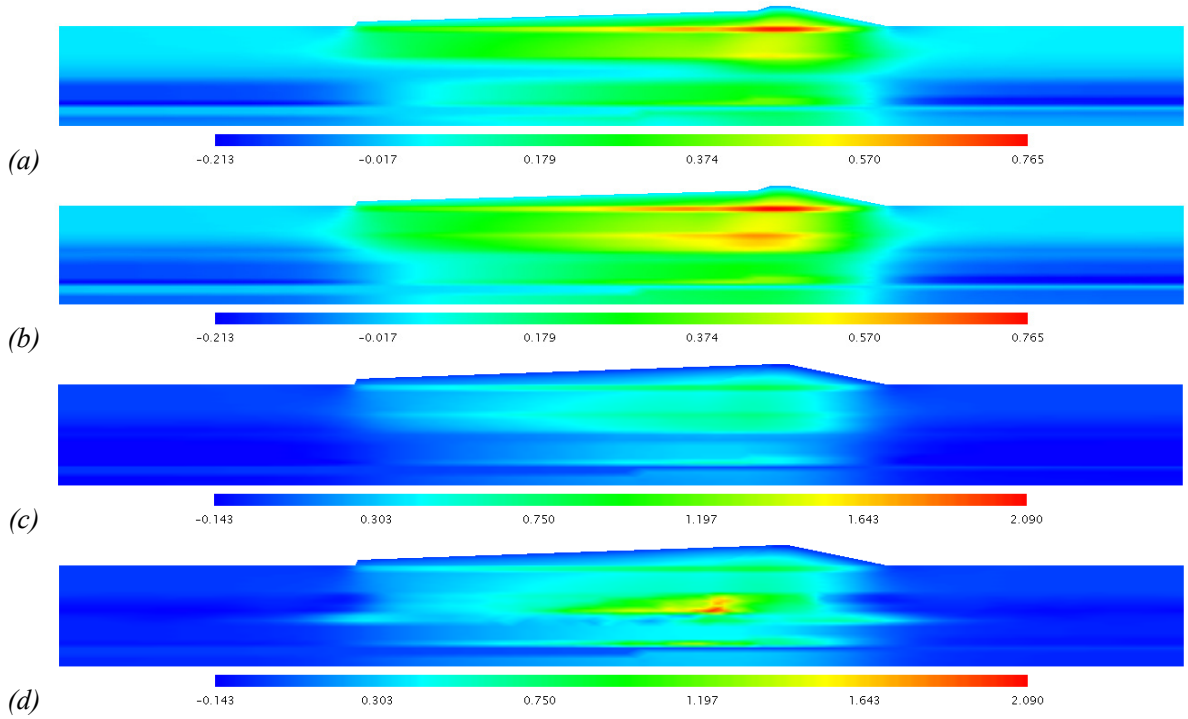


*Figure 3.15. Volumetric strain contours for Case N1 at various steps; (a) 9 months, (b) 22 months, (c) 27 months (EOC), and (d) 10 years after EOC (legend unit: %).*

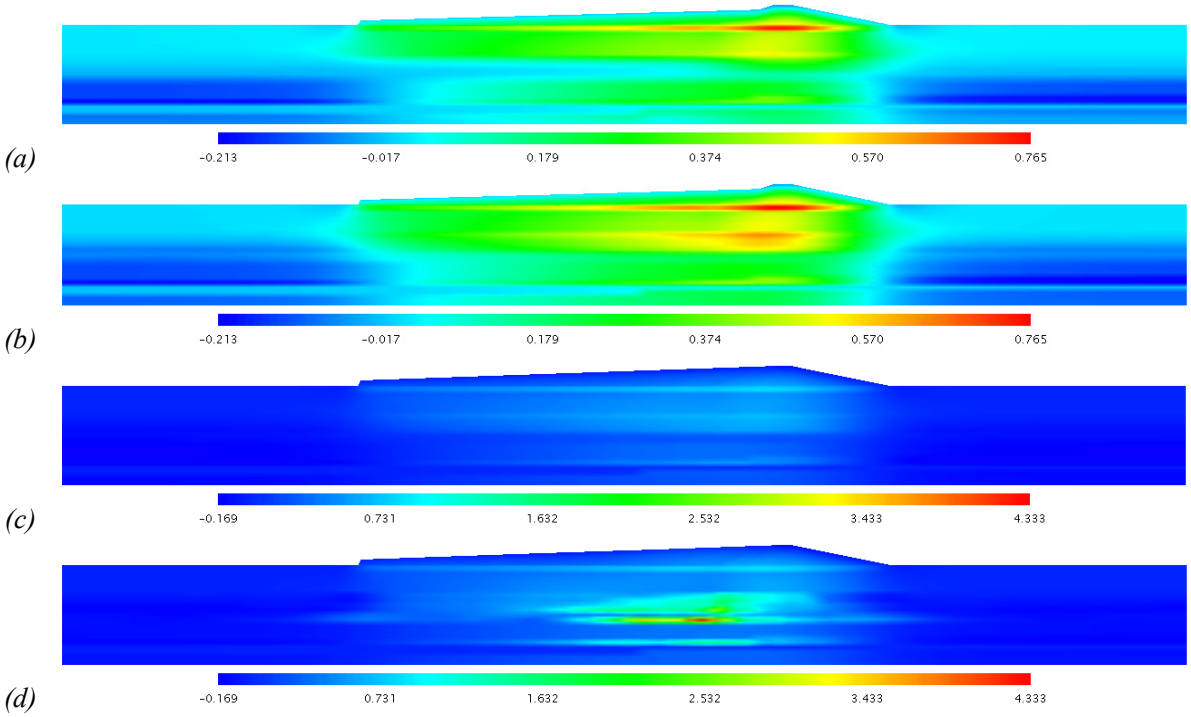


*Figure 3.16. Volumetric strain contours for Case N2 at various steps; (a) 9 months, (b) 22 months, (c) 27 months (EOC), and (d) 10 years after EOC (legend unit: %).*

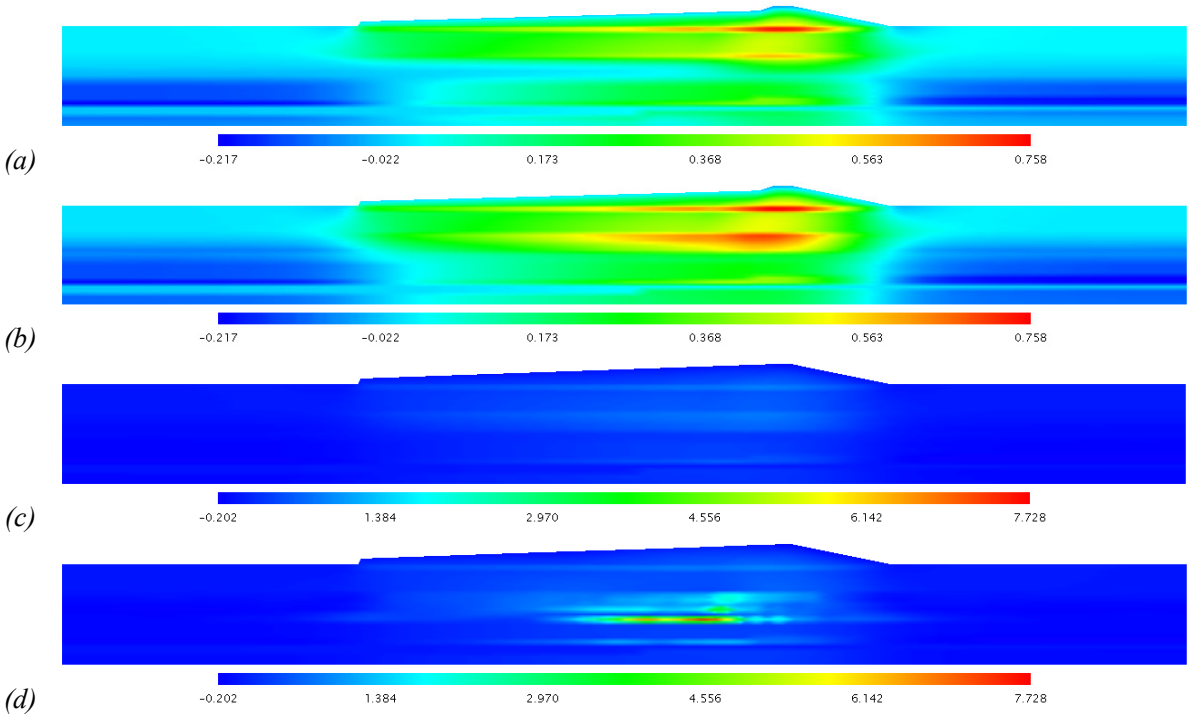


*Figure 3.17. Volumetric strain contours for Case N3 at various steps; (a) 9 months, (b) 22 months, (c) 27 months (EOC), and (d) 10 years after EOC (legend unit: %).*

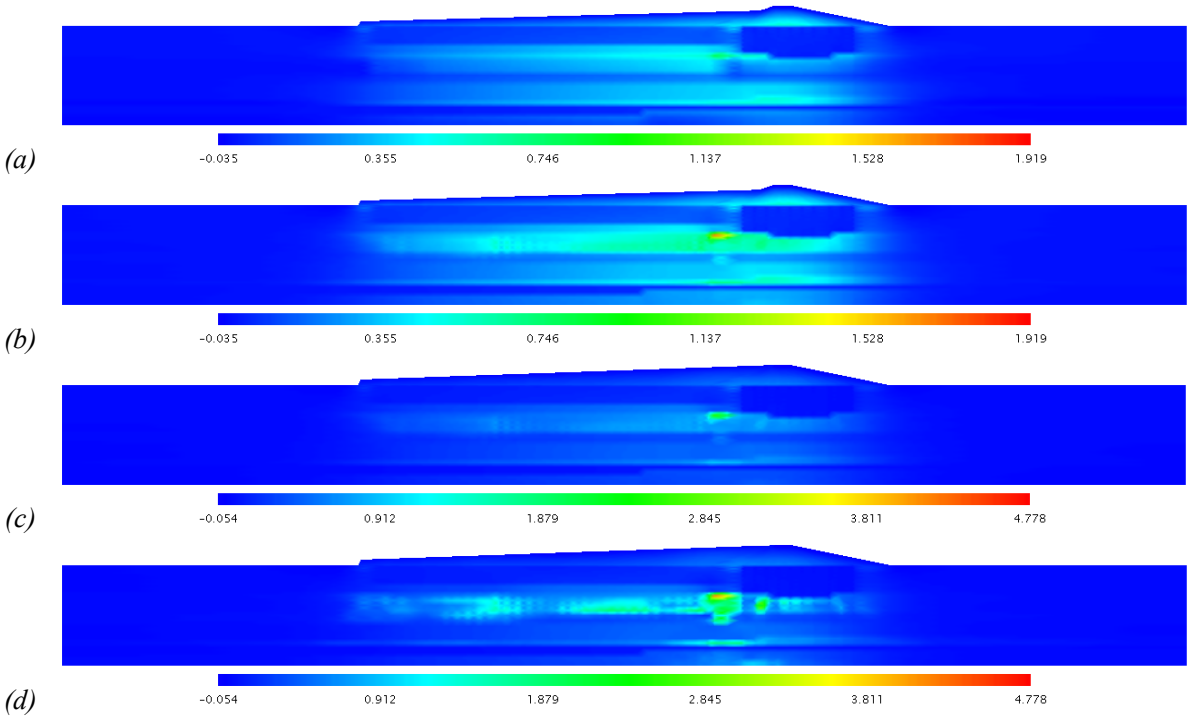


*Figure 3.18. Volumetric strain contours for the improved ground case at various steps; (a) 9 months, (b) 22 months, (c) 27 months (EOC), and (d) 10 years after EOC (legend unit: %).*

### 3.6.4. Accumulated Viscoplastic Shear Strain

The accumulated viscoplastic strain is developed only in clay layers since the elasto-viscoplastic constitutive model is assigned for these layers and the elastic behavior is considered for the sand and gravel layers. The accumulated viscoplastic shear strain contours in 10 years after EOC are shown in Figure 3.19 for all cases. Among the natural ground cases, the accumulated viscoplastic shear strain in Case N1 is distributed in a whole area of the Ac2-L layer beneath the filling zone with a maximum value of about 4%, with no apparent localization, as shown in Figure 3.19(a). For Case N2, however, the application of structural degradation parameters leads to evident strain localization with a maximum value of about 11%, as shown in Figure 3.19(b). This value increases to about 18% for Case N3, as can be seen in Figure 3.19(c), in the same area as for Case N2. For the improved ground case, in general, smaller levels of viscoplastic shear strain develop compared with those in the natural ground case, N3, even though significant strain localization is already observed in layer Ac2 beneath the back slope with a maximum value of about 6%, as illustrated in Figure 3.19(d).

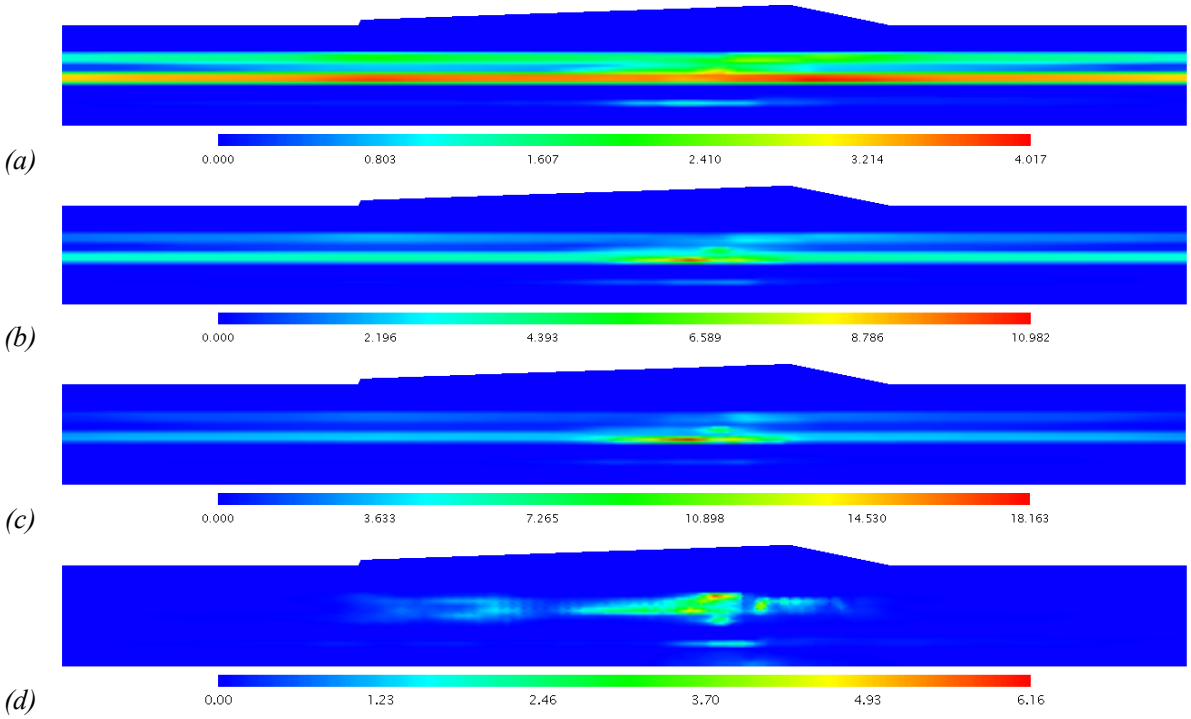


*Figure 3.19. Viscoplastic shear strain contours 10 years after EOC for different cases; (a) Case N1, (b) Case N2, (c) Case N3, and (d) the improved ground case (legend unit: %).*

### 3.6.5. Lode Angle

The variations of Lode angle for natural ground case N3 and the improved ground case at various stages of construction are presented in Figures 3.20 and 3.21. All the natural ground cases indicate similar feature in the distribution of Lode angle. In general, the large value of Lode angle corresponds to the location of the large surface settlement, which implies the high risk of failure under the extension mode. For the natural ground case N3 after 9 months, as shown in Figure 3.20(a), the large value of Lode angle is developed around the right hand side of the super levee demonstrating the ground level heave nearby. After the short-term consolidation, 22 months, the larger value of Lode angle is observed on the top of the super levee indicating the location of the large settlement, as shown in Figure 3.20(b). In 10 years of consolidation after EOC, the large value of the Lode angle is seen on the upper layer of the super levee corresponding to the location of the maximum settlement atop the super levee, as shown in Figure 3.20(d). For the improved ground case, however, since the improvement techniques are employed, the large value of lode angle is developed in a quite smaller zone on the top of the super levee after the long-term consolidation within 10 years, as shown in Figure 3.21(d).

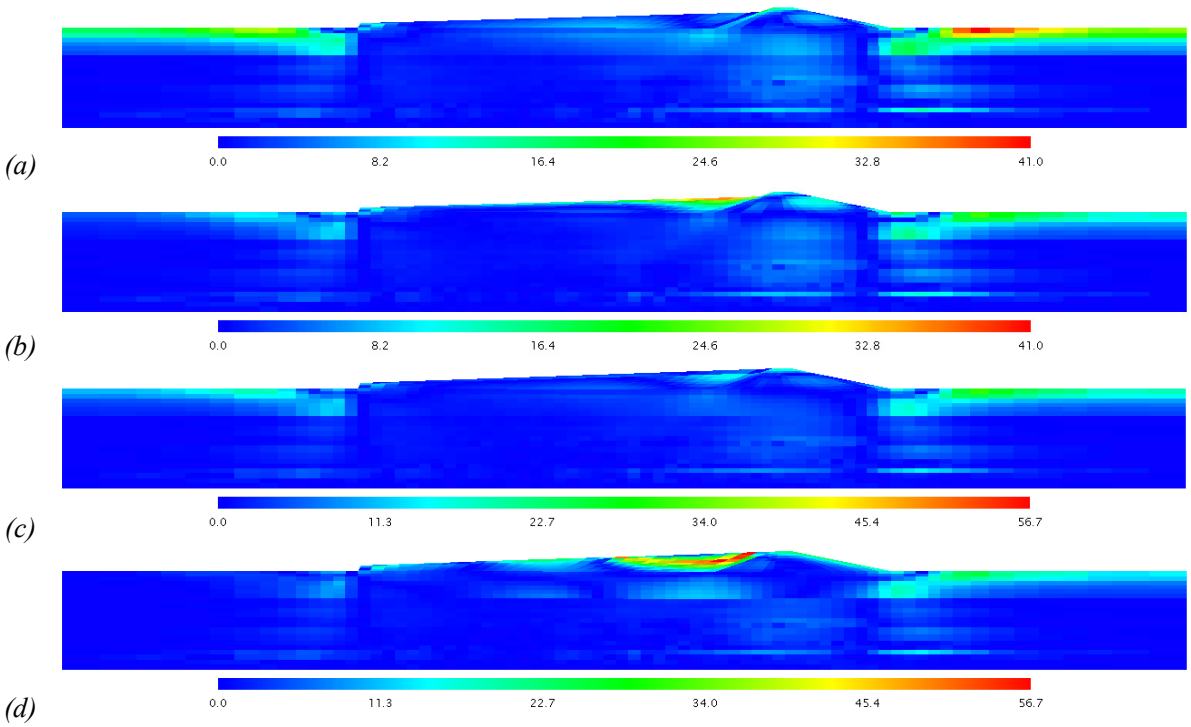


*Figure 3.20. Lode angle for Case N3 at various steps; (a) 9 months, (b) 22 months, (c) 27 months (EOC), and (d) 10 years after EOC (legend unit: degree).*

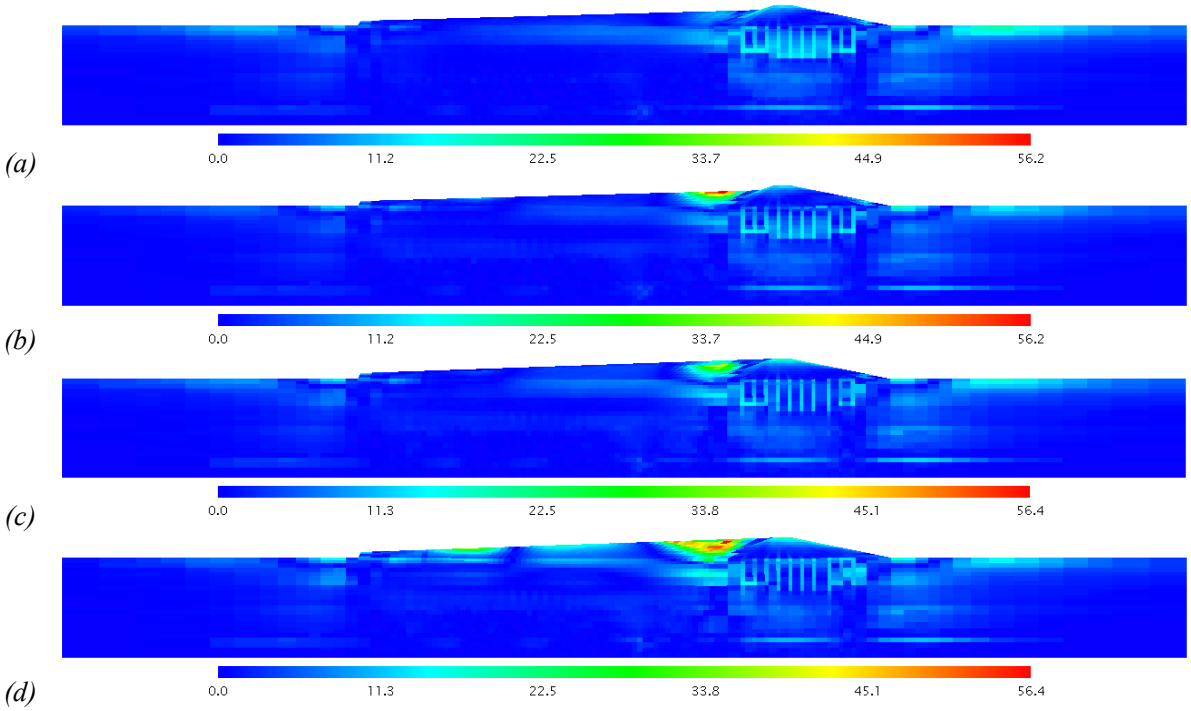


*Figure 3.21. Lode angle for the improved ground case at various steps; (a) 9 months, (b) 22 months, (c) 27 months (EOC), and (d) 10 years after EOC (legend unit: degree).*

### 3.6.6. Excess Pore Water Pressure

The excess pore water pressure distribution contours are presented in Figures 3.22 to 3.25 for natural ground cases N1, N2, and N3 and the improved ground case at various stages of construction. Due to the high permeability of the embankment materials and also the upper layers of the ground, the excess pore water pressure mostly develops in the clay layers beneath the super levee. For the natural ground cases, all three cases present rather similar excess pore water pressure variations during the construction period, namely, 27 months. In these cases, the excess pore water pressure is generated with a maximum value of approximately 87 kPa in 9 months, mainly in the Ac2 layer and slightly in the lower clay layer, Ac1, as shown in Figures 3.22(a), 3.23(a), and 3.24(a). After the short-time consolidation, the excess pore water pressure slowly dissipates to a maximum value of about 50 kPa in 22 months at the deeper layers, as shown in Figures 3.22(b), 3.23(b), and 3.24(b). Following the construction, the excess pore pressure builds up to a maximum value of about 50 kPa in 27 months, as illustrated in Figures 3.22(c), 3.23(c), and 3.24(c). During the long-term consolidation, however, different responses are observed among the natural ground cases. In Case N1, as shown in Figure 3.22(d), after 10 years of consolidation the excess pore water pressure reaches down to a value of about 25 kPa, which is widely distributed in layer Ac2 and the layers below it. For Case N2, as shown in Figure 3.23(d), giving consideration to the structural degradation of soft clay layers results in the

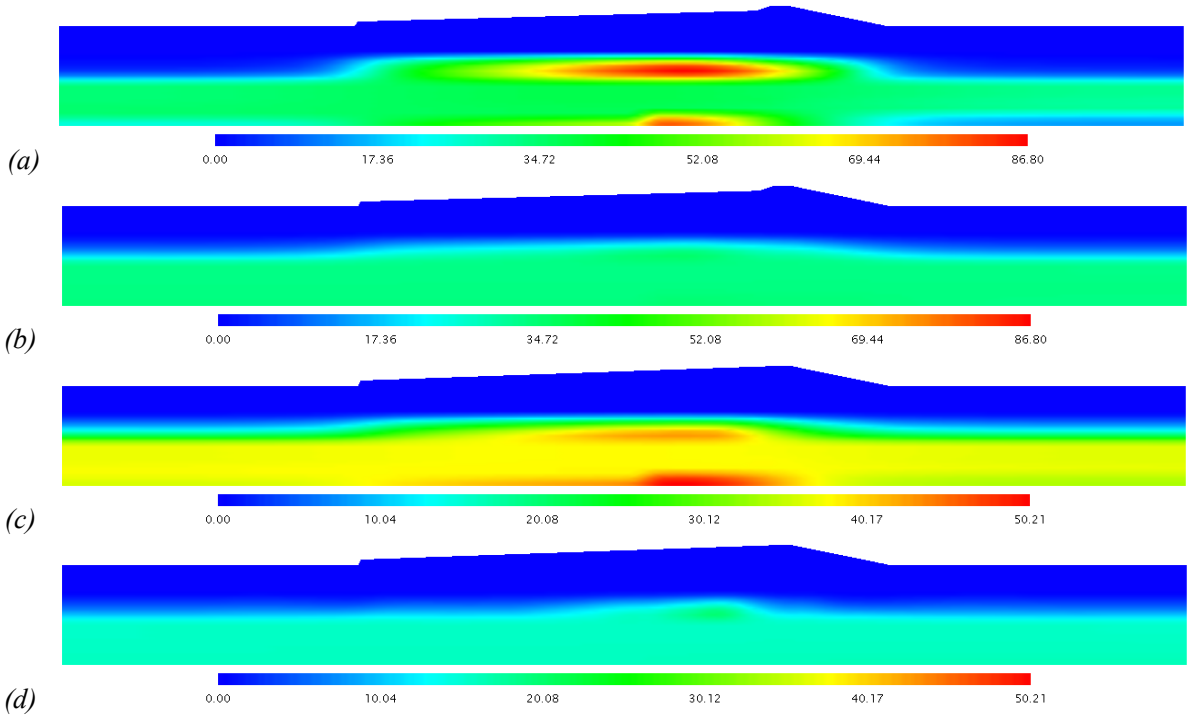


*Figure 3.22. Excess pore water pressure contours for Case N1 at various steps; (a) 9 months, (b) 22 months, (c) 27 months (EOC), and (d) 10 years after EOC (legend unit: kPa).*

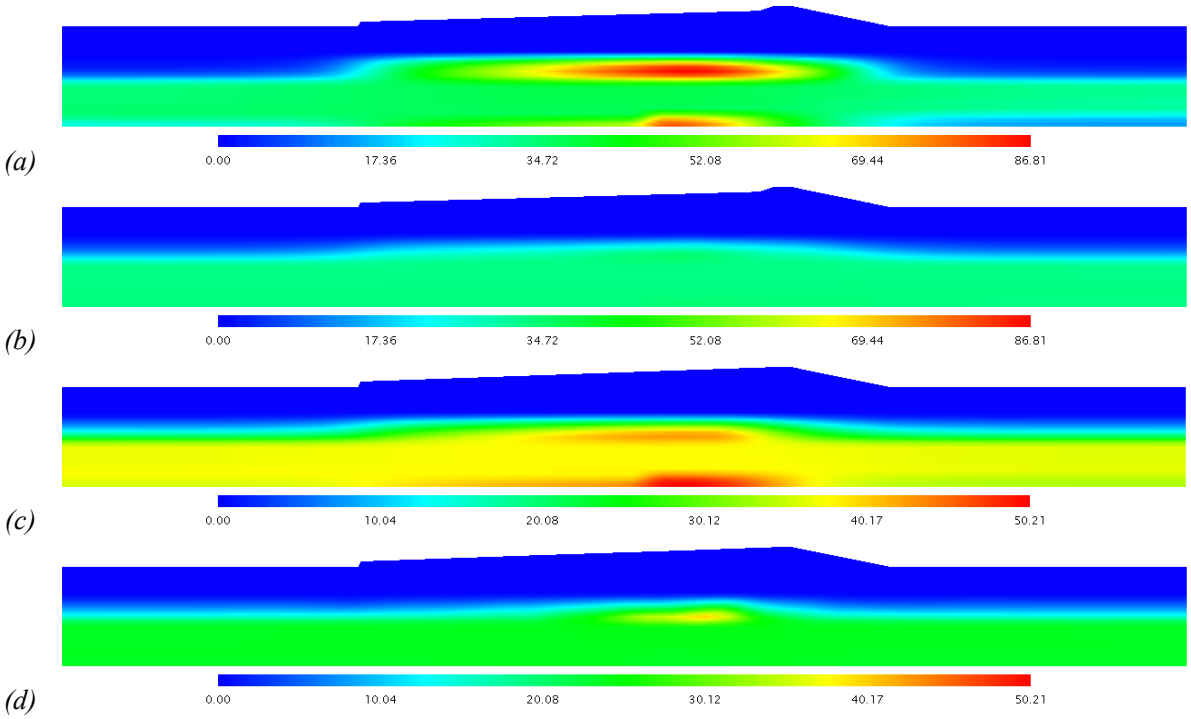


*Figure 3.23. Excess pore water pressure contours for Case N2 at various steps; (a) 9 months, (b) 22 months, (c) 27 months (EOC), and (d) 10 years after EOC (legend unit: kPa).*

buildup of excess pore pressure after the construction, in the area corresponding to the strain-localized region. The amount of the generated excess pore water pressure after the construction in the strain-localized region for Case N3 becomes even higher (Figure 3.24(d)), since the larger structural degradation parameters are assigned. In sensitive soft clay, the pore water pressure increases or becomes stagnant after the completion of the embankment construction, due to the collapse or the rearrangement of the initial clay structure. This anomalous buildup of pore water pressure is associated with the increase in viscoplastic strain and subsequent localization.

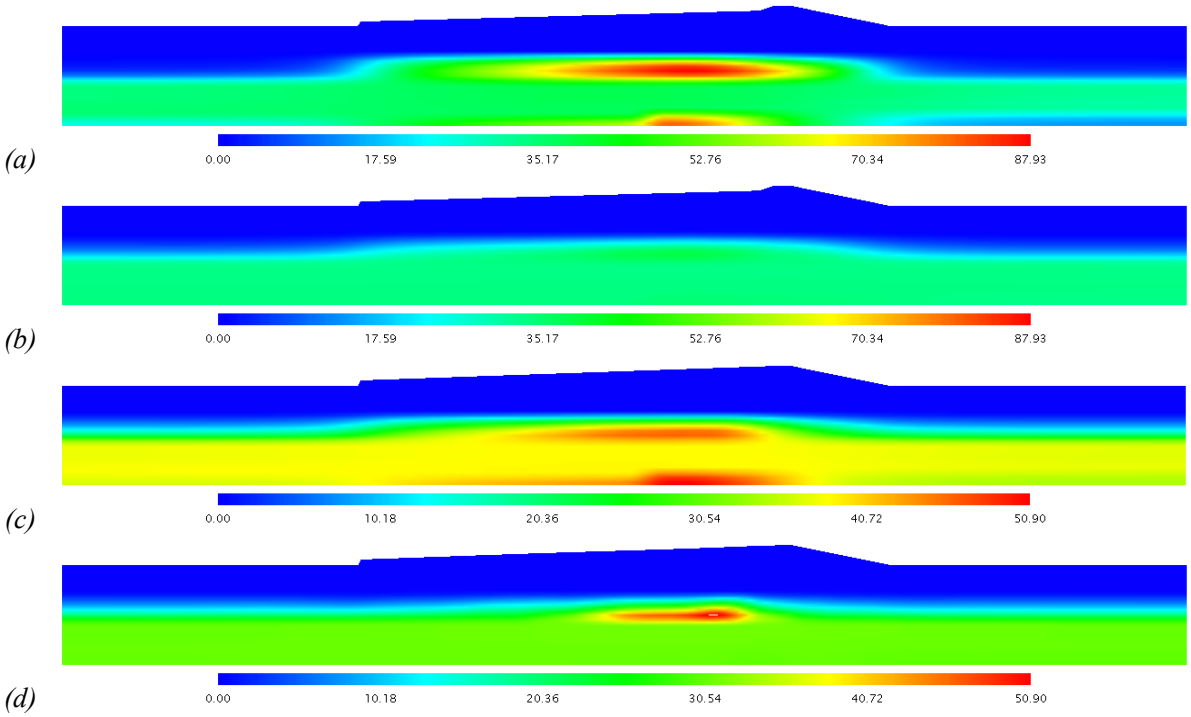


*Figure 3.24. Excess pore water pressure contours for Case N3 at various steps; (a) 9 months, (b) 22 months, (c) 27 months (EOC), and (d) 10 years after EOC (legend unit: kPa).*

In the improved ground case, the excess pore water pressure distribution is changed by the sand drains and the DM-wall installation. After the first phase of construction in 9 months, as shown in Figure 3.25(a), excess pore water pressure is only generated beneath the super levee with a maximum value of about 78 kPa. Due to the sand drain installation, the excess pore water pressure is only generated under the embankment construction zone. The presence of sand drains significantly prevents the spreading of the generated pore water pressure to other parts located outside the embankment loading zone. On the other hand, the installation of DM walls under the main levee provides a low-permeability zone over the clay layers, which prolongs the drainage paths and

decelerates the dissipation times in that region. During the short-time consolidation, the generated amount is somewhat dissipated and reaches a maximum value of about 30 kPa, as shown in Figure 3.25(b). Continuing the construction, this value increases to about 34 kPa, as can be seen in Figure 3.25(c), and after 10 years of consolidation the excess pore water pressure almost dissipates completely, as illustrated in Figure 3.25(d). In the improved ground case, as the characteristics of the clay layers have been improved by the pre-loading process, almost no build-up of pore water pressure is observed after the construction of the embankment.

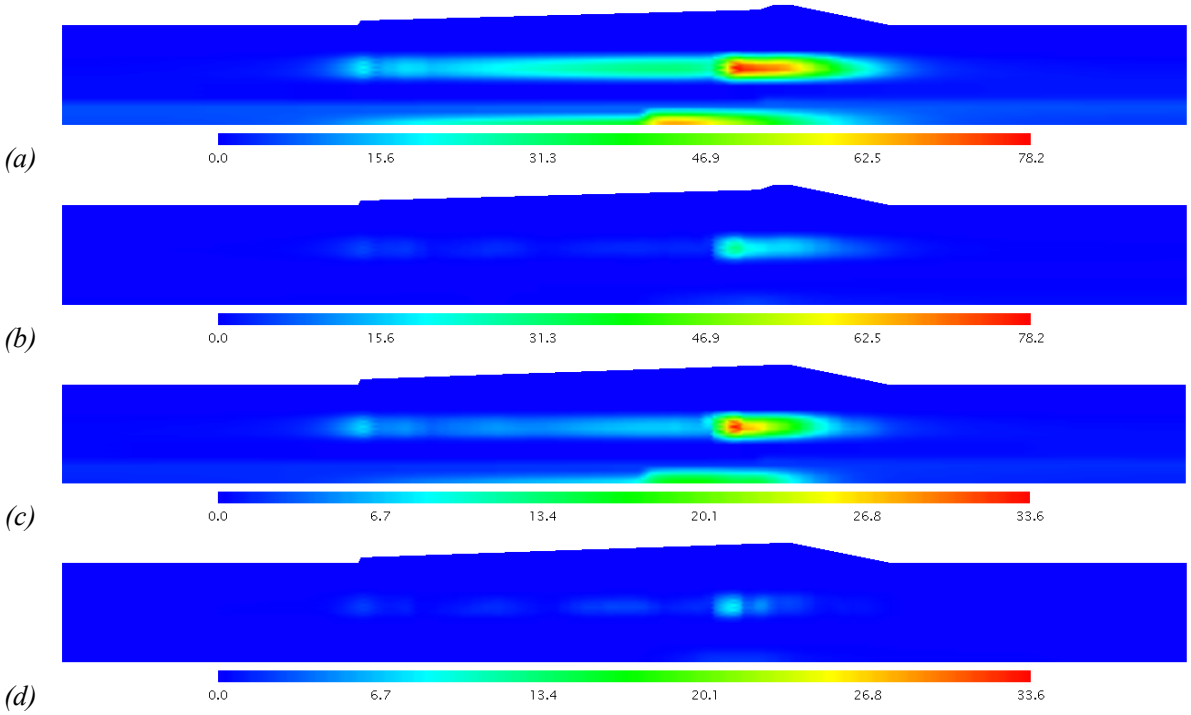


*Figure 3.25. Excess pore water pressure contours for the improved ground case at various steps; (a) 9 months, (b) 22 months, (c) 27 months (EOC), and (d) 10 years after EOC (legend unit: kPa).*

## 3.7. Concluding Remarks

The consolidation analysis of a super levee construction project in Torishima, Osaka City, Japan was conducted using an elasto-viscoplastic constitutive model. As the first phase, the effect of the destructuration of sensitive soft clay, by structural degradation and the strain dependency of the shear modulus, were studied in terms of the consolidation behavior of the super levee construction on a natural (unimproved) ground through three cases. The structural degradation was found to have an excessive effect on the after-construction responses of the pore water pressure and the associated

strain localization. On the other hand, the strain dependency of the elastic shear modulus, as another aspect of destructuration in soft clay, was found to affect the behavior at an earlier stage of loading which appears as relatively large deformations during the construction process, and therefore, during consolidation.

In the second phase of the analysis, the consolidation analysis of the super levee construction was carried out on an improved ground, according to the details of the ground-improvement techniques which have been performed on the site of the project. The field monitored data during the preloading process, prior to super levee construction, was used to obtain the appropriate soil parameters after the improvement. The performance of sand drains, in shortening the drainage paths and accelerating the consolidation rates, was clearly observed through the settlement profiles and the excess pore water pressure contours. The effect of DM walls was observed as reducing the overall settlements beneath the main levee, and also as creating a low-permeability top layer over the clay layers which decelerate the dissipation rate beneath the main levee. It was found that even after ground improvements, large relative displacements are observed in the ground level and atop the super levee. The predicted large relative settlements atop the super levee in the improved case were found to be consistent to the recent field observed data after the construction (Oka 2009), in terms of the location and the approximation of the settlement quantities. In addition, the rather large strain localization mainly occurred in the area of the SCP/SD installation, where it is under the highest influence of embankment loading. Consequently, the unevenness of the ground-improvement techniques under the two parts of the super levee, and also the inadequacy of the preloading process in terms of the height/location of temporary fill material and the preloading duration, can be expressed as the main cause of subsidence in this case even after ground improvements were made. In order to construct a large-scale river embankment for the mitigation of flood disaster, it is necessary to carefully estimate unequal settlement of ground.

# Chapter 4

# CYCLIC ELASTO-VISCOPLASTIC MODEL AND SIMULATION OF SOFT CLAY UNDER CYCLIC TRIAXIAL CONDITIONS

## 4.1. Introduction

The behavior of soft clay under cyclic loading conditions is of considerable importance in the dynamic analysis of multilayered ground. This behavior includes the interaction between the sand layer and the clay layer, the total settlement of both layers, and the effect of the clay layer on liquefaction. In order to accurately predict the behavior of the natural ground foundation during earthquakes, ocean wave storm, traffic vibrations, and any other similar phenomena, it is necessary to employ the constitutive models which properly reproduce the dynamic behavior of clay layers. The prediction of soft clays is rather complex due to the time-dependent and cyclic behaviors. This becomes even more complicated as the destructuration and microstructural changes in the soil particles are taken into consideration. Several viscoplastic constitutive models have been proposed to describe the rheological behavior of clay under static loading conditions (e.g., Adachi and Oka 1982, Dafalias 1982, Katona 1984, Matsui and Abe 1985, Kaliakin and Dafalias 1990, Kimoto and Oka 2005). However, few viscoplastic constitutive models are available for the analysis under dynamic loading conditions (e.g., Oka 1992, Modaressi nad Laloui 1997, Oka et al. 2004a, Maleki and Cambou 2009). Oka (1992) developed a cyclic elasto-viscoplastic constitutive model for clay based on nonlinear kinematic hardening rule (Chaboche and Rousselier 1983). Later on, Oka et al. (2004a)

proposed a cyclic viscoelastic-viscoplastic model by incorporating the viscoelastic feature into the constitutive equations, in which the behavior of clay can be described not only in the range of middle to high level of strain, but also in the range of low level of strain. Despite the ability of these models to explain the deformation characteristics under cyclic loading conditions, the effect of structural degradation of clay particles was disregarded. Taking into account the structural degradation and microstructural changes, a cyclic elasto-viscoplastic model was developed based on the nonlinear kinematic hardening rules for the changes in both the stress ratio and the mean effective stress (Hoizumi 1996, Watanabe et al. 2007). In order to improve the prediction of the behavior during cyclic loading process, the nonlinear kinematic hardening rule for changes in viscoplastic volumetric strain was included into the model (Sawada 2008).

In this chapter, a cyclic elasto-viscoplastic constitutive model for water-saturated soils is presented. The element test simulations are conducted by integration of the constitutive equations on soft clay specimen characterized by the material parameters of Nakanoshima clay, and the results are compared with the experimental data from the cyclic and the monotonic triaxial tests. Then, the parametric studies are performed to evaluate the performance of the constitutive model. Finally, modeling of Osaka soft clay samples (Torishima clay) is carried out under undrained cyclic triaxial conditions to obtain the material parameters for the future dynamic analyses.

## 4.2. Cyclic Elasto-Viscoplastic Model for Water-Saturated Soils

The cyclic elasto-viscoplastic constitutive model is derived following the concept of structural degradation in the elasto-viscoplastic model (Kimoto and Oka 2005) incorporated with the nonlinear kinematic hardening rules (Armstrong and Frederick 1966, Chaboche and Rousselier 1983). The model considers the structural degradation of the soil skeleton by the shrinkage of both the overconsolidation boundary surface and the static yield surface with respect to the accumulation of viscoplastic strain. The model is derived based on an overstress type of viscoplasticity theory and the non-associated flow rule. The nonlinear kinematic hardening rule is adopted in addition to the viscoplastic strain dependency of elastic shear modulus.

The model is modified here from the preceding formulations, presented in Sawada (2008), in terms of the inclusion of the kinematic hardening rule for volumetric strain. This term appears in the definition of the static yield function and consequently in the material function. In the current reformulation, the volumetric strain hardening has been appropriately included in the definition of the static yield function by replacing $\sigma'_{mb}$ with $\sigma'_{ma}$. Moreover, a new formulation is introduced here for

the degradation of the elastic shear modulus as a function of the mean effective stress and the accumulated viscoplastic shear strain from the initial state.

In the adopted constitutive model, Terzaghi's effective stress for water-saturated soil is used as

$$\sigma_{ij} = \sigma'_{ij} + p\delta_{ij} \tag{4.1}$$

where $\sigma_{ij}$ is the total stress tensor, $\sigma'_{ij}$ is the effective stress tensor, $p$ is the pore water pressure, and $\delta_{ij}$ is Kronecker's delta. In addition, total strain rate tensor $\dot{\varepsilon}_{ij}$ is assumed to be divided into two parts, namely,

$$\dot{\varepsilon}_{ij} = \dot{\varepsilon}^{e}_{ij} + \dot{\varepsilon}^{vp}_{ij} \tag{4.2}$$

where $\dot{\varepsilon}^{e}_{ij}$ denotes the elastic strain rate tensor and $\dot{\varepsilon}^{vp}_{ij}$ is the viscoplastic strain rate tensor. The elastic strain rate tensor is expressed as

$$\dot{\varepsilon}^{e}_{ij} = \frac{1}{2G}\dot{S}_{ij} + \frac{\kappa}{3(1+e)}\frac{\dot{\sigma}'_{m}}{\sigma'_{m}}\delta_{ij} \tag{4.3}$$

in which $G$ is the elastic shear modulus, $S_{ij}$ is the deviatoric stress tensor ($S_{ij} = \sigma'_{ij} - \sigma'_{m}\delta_{ij}$), $\sigma'_{m}$ is the mean effective stress, and the superimposed dot denotes the time differentiation. $\kappa$ is the swelling index and $e$ is the void ratio. The degradation of elastic shear modulus $G$ as a function of strain will be presented in the next section. In the present study, the initial void ratio $e_0$ is used in Equation (4.3) for simplicity.

### 4.2.1. Overconsolidation Boundary Surface

An overconsolidation boundary surface $f_b$ is defined as the boundary in the stress space between the normally consolidated (NC) region and the overconsolidated (OC) region by

$$f_b = \overline{\eta}^{*}_{(0)} + M^{*}_{m}\ln\left(\sigma'_{m}/\sigma'_{mb}\right) = 0 \tag{4.4}$$

where $f_b < 0$ indicates the overconsolidated region and $f_b \geq 0$ shows the normally consolidated region. $\overline{\eta}^{*}_{(0)}$ is the relative stress ratio defined by

$$\bar{\eta}^{*}_{(0)} = \left\{ \left( \eta^{*}_{ij} - \eta^{*}_{ij(0)} \right) \left( \eta^{*}_{ij} - \eta^{*}_{ij(0)} \right) \right\}^{\frac{1}{2}} \tag{4.5}$$

in which subscript (0) denotes the initial state before deformation and $\eta^{*}_{ij}$ is the stress ratio tensor. $\sigma'_{mb}$ controls the size of the OC boundary surface. $M^{*}_{m}$ is the value of $\eta^{*} = \sqrt{\eta^{*}_{ij}\eta^{*}_{ij}}$ when the volumetric strain increment changes from compression to swelling. The stress ratio at triaxial compression state $M^{*}_{mc}$ and the stress ratio at the extension state $M^{*}_{me}$ can be obtained by the internal frictional angle $\phi$ as

$$M^{*}_{mc} = \sqrt{\frac{2}{3}} \frac{6\sin\phi}{3-\sin\phi} \tag{4.6}$$

$$M^{*}_{me} = \sqrt{\frac{2}{3}} \frac{6\sin\phi}{3+\sin\phi} \tag{4.7}$$

To describe the structural degradation of clay, strain softening with the accumulated viscoplastic strain is introduced in addition to strain hardening with the viscoplastic volumetric strain as

$$\sigma'_{mb} = \sigma'_{ma} \exp\left(\frac{1+e_0}{\lambda-\kappa}\varepsilon^{vp}_{v}\right) \tag{4.8}$$

where $\sigma'_{ma}$ is assumed to decrease with an increase in viscoplastic strain with

$$\sigma'_{ma} = \sigma'_{maf} + \left(\sigma'_{mai} - \sigma'_{maf}\right)\exp(-\beta z) \tag{4.9}$$

in which $z$ is the accumulation of the second invariant of the viscoplastic strain rate given by

$$z = \int_0^t \dot{z}\,dt \quad ; \quad \dot{z} = \sqrt{\dot{\varepsilon}^{vp}_{ij}\dot{\varepsilon}^{vp}_{ij}} \tag{4.10}$$

In Equation (4.9), $\sigma'_{mai}$ and $\sigma'_{maf}$ are the initial and the final values for $\sigma'_{ma}$, respectively. $\beta$ is a parameter that stands for the changing rate of $\sigma'_{ma}$, while the proportion of $n = \sigma'_{maf} / \sigma'_{mai}$ provides the degree of possible collapse of the soil structure at the initial state.

### 4.2.2. Static Yield Function

Static yield function is obtained by considering the nonlinear kinematic hardening rule for the changes in the stress ratio, in the mean effective stress, and in the viscoplastic volumetric strain, as

$$f_y = \bar{\eta}_\chi^* + \tilde{M}^* \left( \ln \frac{\sigma'_{mk}}{\sigma'^{(s)}_{my}} + \left| \ln \frac{\sigma'_m}{\sigma'_{mk}} - y^*_{m1} \right| \right) = 0 \tag{4.11}$$

$$\bar{\eta}_\chi^* = \left\{ \left( \eta_{ij}^* - \chi_{ij}^* \right) \left( \eta_{ij}^* - \chi_{ij}^* \right) \right\}^{\frac{1}{2}} \tag{4.12}$$

in which $\sigma'_{mk}$ is the unit value of the mean effective stress, $y^*_{m1}$ is the scalar kinematic hardening parameter, and $\sigma'^{(s)}_{my}$ denotes the static hardening parameter. $\chi^*_{ij}$ is so-called back stress parameter, which has the same dimensions as stress ratio $\eta^*_{ij}$.

Incorporating the strain softening for the structural degradation, the hardening rule of $\sigma'^{(s)}_{my}$ can be expressed as

$$\sigma'^{(s)}_{my} = \frac{\sigma'_{maf} + \left( \sigma'_{mai} - \sigma'_{maf} \right) \exp(-\beta z)}{\sigma'_{mai}} \sigma'^{(s)}_{myi} \tag{4.13}$$

### 4.2.3. Viscoplastic Potential Function

In the same manner as for the static yield function, viscoplastic potential function $f_p$ is given by

$$f_p = \bar{\eta}_\chi^* + \tilde{M}^* \left( \ln \frac{\sigma'_{mk}}{\sigma'_{mp}} + \left| \ln \frac{\sigma'_m}{\sigma'_{mk}} - y^*_{m1} \right| \right) = 0 \tag{4.14}$$

The dilatancy coefficient $\tilde{M}^*$ is defined separately for the normally consolidated region (NC) and the overconsolidated region (OC) as

$$\tilde{M}^* = \begin{cases} M_m^* & \text{:NC region} \\ \left( \sigma_m^* / \sigma'_{mc} \right) M_m^* & \text{:OC region} \end{cases} \tag{4.15}$$

where $\sigma'_{mc}$ is the mean effective stress at the intersection of the overconsolidation boundary surface and $\sigma'_m$ axis, which is defined by

$$\sigma'_{mc} = \sigma'_{mb} \exp\left( \frac{\sqrt{\eta^*_{ij(0)} \eta^*_{ij(0)}}}{M^*_m} \right) \tag{4.16}$$

in addition, $\sigma^*_m$ denotes the mean effective stress at the intersection of the surface, which has the same shape as $f_b$, and is given by

$$\sigma^*_m = \sigma'_m \exp\left( \frac{\bar{\eta}^*_\chi}{M^*_m} \right) \tag{4.17}$$

### 4.2.4. Kinematic Hardening Rules

The evolution equation for the nonlinear kinematic hardening parameter $\chi^*_{ij}$ is given by

$$d\chi^*_{ij} = B^* \left( A^* de^{vp}_{ij} - \chi^*_{ij} d\gamma^{vp} \right) \tag{4.18}$$

where $A^*$ and $B^*$ are material parameters, $de^{vp}_{ij}$ is the viscoplastic deviatoric strain increment tensor, and $d\gamma^{vp} = \sqrt{de^{vp}_{ij} de^{vp}_{ij}}$ is the viscoplastic shear strain increment tensor. $A^*$ is related to the stress ratio at failure, namely, $A^* = M^*_f$, and $B^*$ is proposed to be dependent on the viscoplastic shear strain as

$$B^* = \left( B^*_{\max} - B^*_1 \right) \exp\left( -C_f \gamma^{vp*}_{(n)} \right) + B^*_1 \tag{4.19}$$

in which $B^*_1$ is the lower boundary of $B^*$, $C_f$ is the parameter controlling the amount of reduction, $\gamma^{vp*}_{(n)}$ is the accumulated value of the viscoplastic shear strain between two sequential stress reversal points in the previous cycle. $B^*_{\max}$ is the maximum value of parameter $B^*$, which is defined following the proposed method by Oka et al (1999) as

$$B^*_{\max} = \begin{cases} B^*_0 & \text{:Before reaching failure line} \\ \dfrac{B^*_0}{1 + \gamma^{vp*}_{(n)\max} \big/ \gamma^{vp*}_{(n)r}} & \text{:After reaching failure line} \end{cases} \tag{4.20}$$

where $B_0^*$ is the initial value of $B^*$, $\gamma_{(n)\max}^{vp*}$ is the maximum value of $\gamma_{(n)}^{vp*}$ in past cycles, and $\gamma_{(n)r}^{vp*}$ is the viscoplastic reference strain.

In order to improve the predicted results under cyclic loading conditions, the scalar nonlinear kinematic hardening parameter $y_{m1}^*$ is introduced as

$$dy_{m1}^* = B_2^* \left( A_2^* d\varepsilon_v^{vp} - y_{m1}^* \left| d\varepsilon_v^{vp} \right| \right) \tag{4.21}$$

where $A_2^*$ and $B_2^*$ are material parameters, $d\varepsilon_v^{vp}$ is the increment of the viscoplastic volumetric strain tensor. The values of $A_2^*$ and $B_2^*$ are determined by data-adjusting method from the laboratory test data.

The degradation of the elastic shear modulus from the beginning of loading can be expressed by its dependency on the accumulated viscoplastic shear strain $\gamma^{vp}$ as

$$G = \frac{G_0}{\left(1 + \alpha \left(\gamma^{vp}\right)^r\right)} \sqrt{\frac{\sigma_m'}{\sigma_{m0}'}} \tag{4.22}$$

where $r$ and $\alpha$ are the strain-dependent parameters, which can be determined from the laboratory test results. In this study, based on the experimental results, $r = 0.4$ is chosen.

### 4.2.5. Viscoplastic Flow Rule

Based on the overstress type of viscoplastic theory first adopted by Perzyna (1963), viscoplastic strain rate tensor $\dot{\varepsilon}_{ij}^{vp}$ is defined as

$$\dot{\varepsilon}_{ij}^{vp} = C_{ijkl} \left\langle \Phi\left(f_y\right) \right\rangle \frac{\partial f_p}{\partial \sigma_{kl}'} \tag{4.23}$$

$$\left\langle \Phi\left(f_y\right) \right\rangle = \begin{cases} \Phi\left(f_y\right) & : f_y > 0 \\ 0 & : f_y \le 0 \end{cases} \tag{4.24}$$

$$C_{ijkl} = a\delta_{ij}\delta_{kl} + b\left(\delta_{ik}\delta_{jl} + \delta_{il}\delta_{jk}\right) \tag{4.25}$$

where $\langle\ \rangle$ are Macaulay's brackets, $\Phi\left(f_y\right)$ is the rate-sensitive material function, and $C_{ijkl}$ is a fourth order isotropic tensor. *a* and *b* in Equation (4.25) are material constants. The material function $\Phi\left(f_y\right)$ is determined as

$$\Phi\left(f_y\right)=\sigma'_m\ \exp\left\{m'\left(\bar{\eta}^*_\chi+\tilde{M}^*\left(\ln\frac{\sigma'_{mk}}{\sigma'_{ma}}+\left|\ln\frac{\sigma'_m}{\sigma'_{mk}}-y^*_{m1}\right|\right)\right)\right\} \tag{4.26}$$

in which $m'$ is the viscoplastic parameter. Finally, by combining Equations (4.23) to (4.26) viscoplastic deviatoric strain rate $\dot{e}^{vp}_{ij}$ and viscoplastic volumetric strain rate $\dot{\varepsilon}^{vp}_{ij}$ can be expressed as

$$\dot{e}^{vp}_{ij}=C_1\ \exp\left\{m'\left(\bar{\eta}^*_\chi+\tilde{M}^*\left(\ln\frac{\sigma'_{mk}}{\sigma'_{ma}}+\left|\ln\frac{\sigma'_m}{\sigma'_{mk}}-y^*_{m1}\right|\right)\right)\right\}\frac{\eta^*_{ij}-\chi^*_{ij}}{\bar{\eta}^*_\chi} \tag{4.27}$$

$$\dot{\varepsilon}^{vp}_{kk}=C_2\ \exp\left\{m'\left(\bar{\eta}^*_\chi+\tilde{M}^*\left(\ln\frac{\sigma'_{mk}}{\sigma'_{ma}}+\left|\ln\frac{\sigma'_m}{\sigma'_{mk}}-y^*_{m1}\right|\right)\right)\right\}\left\{\tilde{M}^*\frac{\ln\frac{\sigma'_m}{\sigma'_{mk}}-y^*_{m1}}{\left|\ln\frac{\sigma'_m}{\sigma'_{mk}}-y^*_{m1}\right|}-\frac{\eta^*_{mn}\left(\eta^*_{mn}-\chi^*_{mn}\right)}{\bar{\eta}^*_\chi}\right\} \tag{4.28}$$

where $C_1=2b$ and $C_2=3a+2b$ are the viscoplastic parameters for the deviatoric and the volumetric strain components, respectively.

## 4.3. Simulation of Triaxial Behavior of Nakanoshima Clay

### 4.3.1. Material Parameters

In the proposed constitutive model, the material parameters can be determined by conventional tests, physical-property tests, or triaxial compression tests. For some parameters, as will describe later, the data-adjusting method can be employed. The initial void ratio can be calculated with the specific gravity of the soil particles, the water contents, and the bulk density based on the results of tests conducted on undisturbed samples. The compression index and swelling index can be calculated as the slope of the $e$-ln $p$ relation during the isotropic consolidation and swelling tests, respectively. The initial elastic shear modulus is calculated from the slope of stress-strain relation curve at the early stage of loading. The stress ratios at the compression and the extension state are calculated from the internal friction angle using Equations (4.6) and (4.7). Viscoplastic parameters $m'$ is determined from undrained triaxial compression tests conducted at different strain rates. By having $m'$, the other viscoplastic parameters, $C_1$ and $C_2$, are obtained from Equations (4.27) and (4.28) in the monotonic triaxial stress state. In the lack of the adequate laboratory test data, the viscoplastic parameters $C_1$ and $C_2$ are determined by date-adjusting method from the existing experimental results. The rest of the parameters are conventionally determined by the data-adjusting method through the comparison of the simulated results with the experimental values. However, there are often some empirical relations which can be used to determine the parameters for the first trial. Following the procedures and using the proposed cyclic elasto-viscoplastic constitutive model, the material parameters of the Nakanoshima clay are determined and listed in Table 4.1.

The soil samples, which are used for the cyclic triaxial test and the monotonic test, appear to be slightly different. Therefore, different sets of parameters are obtained for each sample. Comparing the initial void ratio of the samples, the cyclic sample has smaller void ratio, which emphasizes the stiffer behavior compared with the sample for monotonic test. Accordingly, the values of the hardening parameter and the structural parameters have been determined in a manner that more softening behavior can be reproduced for the monotonic sample.

The results of the stress-strain relation and stress path for the simulation and for the cyclic triaxial test are presented in Figure 4.1. The stress-strain relations of the simulated results demonstrate a good tendency with the experimental data, in terms of the strain levels in both compression and extension sides and the number of cycles. The simulated result of stress paths, on the other hand, does not show such a good agreement with the experimental data. This might be attributed to the different mechanism of measurement for the pore water pressure during the experiments, which is based on the average values of the whole specimen, while in the simulation the results of the one-point response is considered.

*Table 4.1. Material parameters of Nakanoshima clay, for the cyclic and the monotonic test conditions.*

| | | Cyclic test | Monotonic test |
|---|---|---|---|
| Initial void ratio | $e_0$ | 1.373 | 1.573 |
| Compression index | $\lambda$ | 0.2173 | |
| Swelling index | $\kappa$ | 0.0344 | |
| Initial elastic shear modulus *(kPa)* | $G_0$ | 22670 | |
| Initial mean effective stress *(kPa)* | $\sigma'_{m0}$ | 200 | |
| Stress ratio at compression | $M^*_{mc}$ | 1.143 | |
| Stress ratio at extension | $M^*_{me}$ | 1.061 | |
| Viscoplastic parameter | $m'$ | 22.7 | |
| Viscoplastic parameter *(1/s)* | $C_1$ | $1.00\times10^{-5}$ | |
| Viscoplastic parameter *(1/s)* | $C_2$ | $3.30\times10^{-6}$ | |
| Structural parameter | $n=\sigma'_{maf}/\sigma'_{mai}$ | 0.325 | |
| Structural parameter | $\beta$ | 3.7 | 5.7 |
| Hardening parameter | $B^*_0$ | 105 | |
| Hardening parameter | $B^*_1$ | 1.0 | |
| Hardening parameter | $C_f$ | 5 | 75 |
| Reference value of viscoplastic strain *(%)* | $\gamma^{vp*}_{(n)r}$ | 3.5 | |
| Strain-dependent parameter | $\alpha$ | 10 | 1 |
| Scalar hardening parameter | $A^*_2$ | 5.1 | |
| Scalar hardening parameter | $B^*_2$ | 2.6 | |

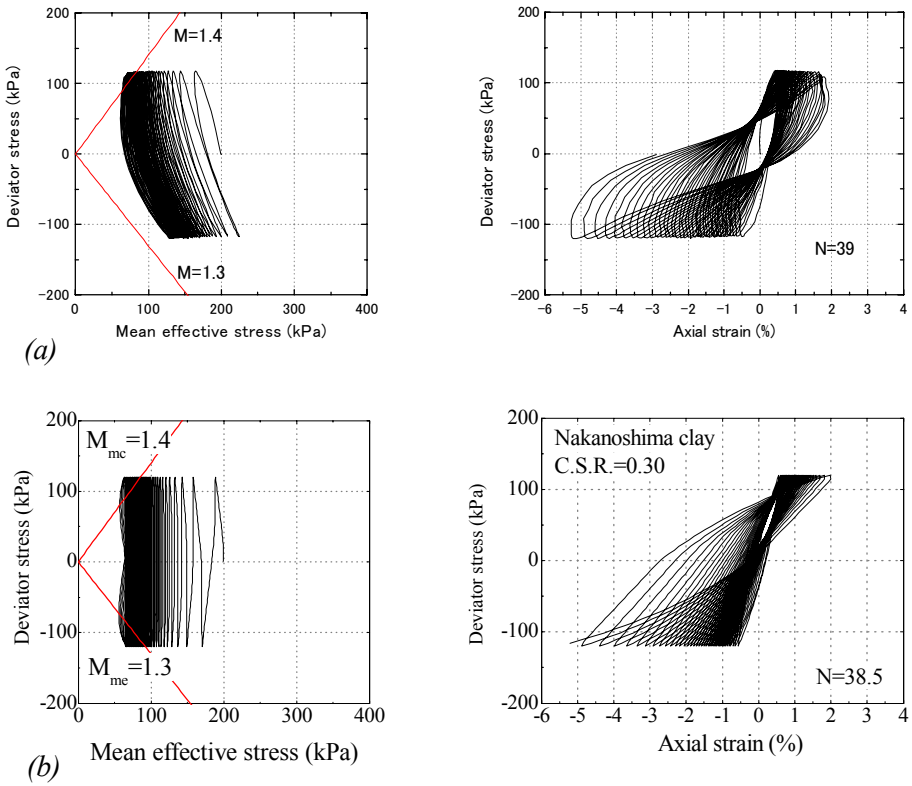


*Figure 4.1. Stress paths and stress-strain relations under cyclic triaxial conditions: (a) experimental results, (b) simulated results.*

The results of the simulation under monotonic triaxial conditions are illustrated in Figure 4.2, in which the symbols show the experimental values and the solid lines represent the simulated results. The simulated results for stress-strain relation and stress path provide good agreement with the experimental data. Efforts are made for adjusting the parameters such as the structural parameters, the hardening parameters, and the strain-dependent parameter, so that the best possible agreement can be achieved between the simulation and the experimental results.

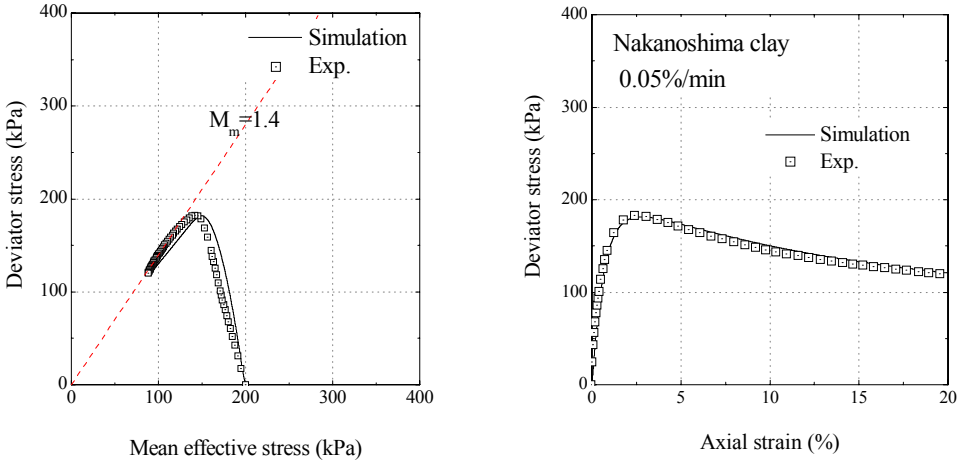


*Figure 4.2. Stress paths and stress-strain relations under the monotonic triaxial conditions.*

### 4.3.2. Effect of the Current Reformulation

As mentioned earlier, the constitutive equations are reformulated here from the previous ones presented in Sawada (2008). In Sawada's formulation the hardening rule of $\sigma'^{(s)}_{my}$ has been given by

$$\sigma'^{(s)}_{my} = \frac{\sigma'_{ma}\left(\exp(\frac{1+e_0}{\lambda-\kappa}\varepsilon_v^{vp})\right)}{\sigma'_{mai}}\sigma'^{(s)}_{myi} \tag{4.29}$$

By which, the definition of the material function becomes as

$$\Phi\left(f_y\right)=\sigma'_m \exp\left\{m'\left(\bar{\eta}^*_\chi+\tilde{M}^*\left(\ln\frac{\sigma'_{mk}}{\sigma'_{mb}}+\left|\ln\frac{\sigma'_m}{\sigma'_{mk}}-y^*_{m1}\right|\right)\right)\right\} \tag{4.30}$$

This formulation includes the effect of volumetric strain twice, as in the $\sigma'_{mb}$ and in the kinematic hardening parameter $y^*_{m1}$. This additional inclusion has been corrected in the new formulation by

eliminating the term of $\exp(\frac{1+e_0}{\lambda-\kappa}\varepsilon_v^{vp})$ from Equation (4.29) which leads to the replacement of $\sigma'_{mb}$ with $\sigma'_{ma}$, in the material function formulation, as presented in Equation (4.13) and (4.26).

The effect of the new correction of the kinematic hardening rule for the volumetric strain is studied using the material parameters of Nakanoshima clay as listed in Table 4.1. The results of the simulation are shown in Figure 4.3 for the cyclic triaxial conditions and in Figure 4.4 for the monotonic triaxial loading. For the cyclic triaxial loading, the correction of the constitutive equations leads to notable changes in the stress-strain relations, of which more softening behavior is observed after the correction. When the effect of viscoplastic volumetric strain is considered in the material function as term of $\sigma'_{mb}$, the value $\Phi\left(f_y\right)$ reduces and smaller values are obtained for strain components at a specific level of stress. Subsequently, the accumulative strain decreases and more hardening behavior achieves at the same stress level. For the monotonic loading, the application of the new correction results in less changes compared with the cyclic results, although slightly softening behavior with reduction in the values of peak stress are observed in both stress-strain relations and stress paths.

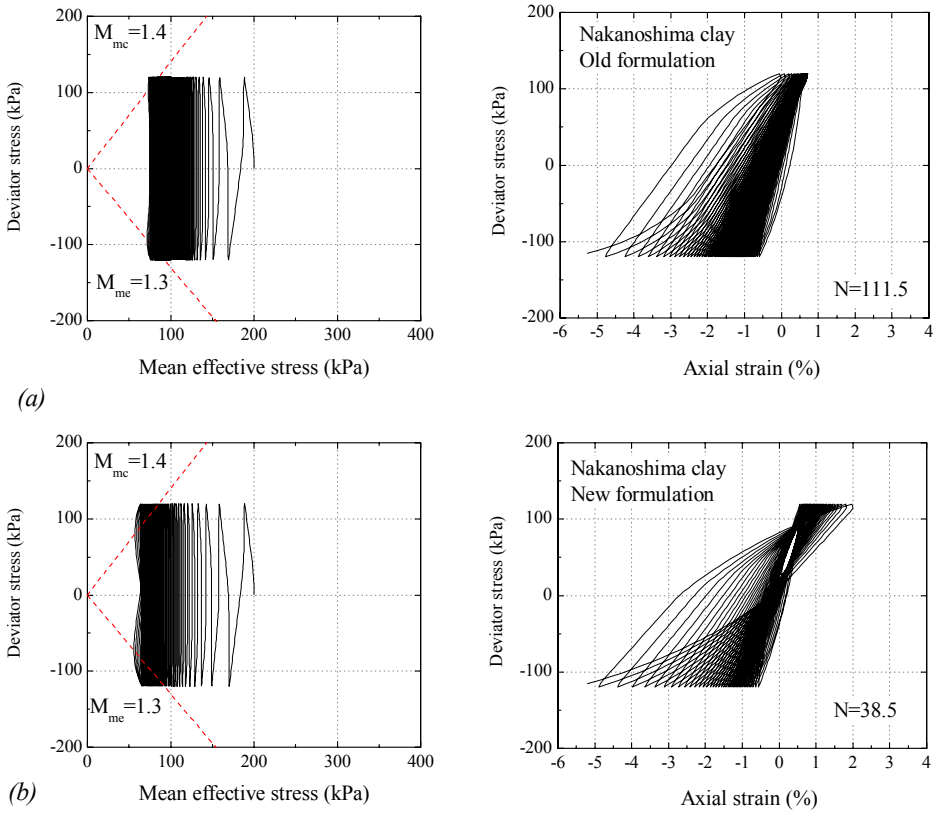


*Figure 4.3. The simulated results for stress paths and stress-strain relations under cyclic triaxial conditions: (a) Sawada's formulation, (b) current formulation.*

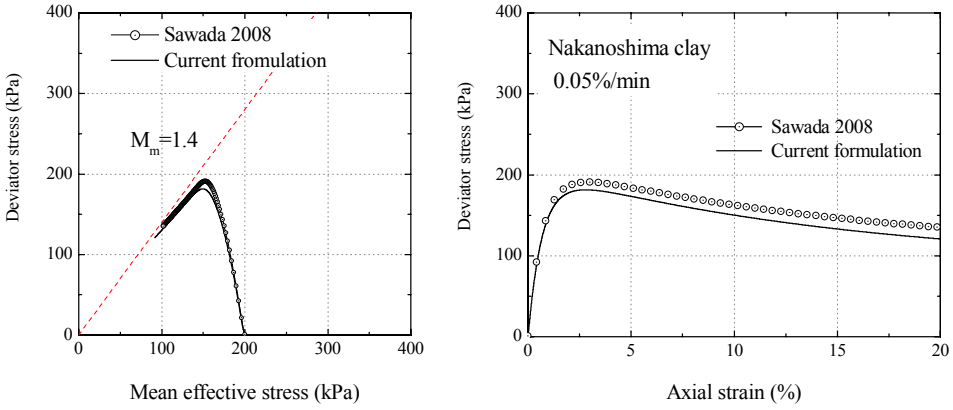


*Figure 4.4. Stress paths and stress-strain relations under monotonic triaxial conditions for Sawada's formulation and the current formulation.*

### 4.3.3. Effect of the Linear Evolution Equation for $y^*_{m1}$

In the adopted formulation, the nonlinear equation has been applied for the scalar kinematic hardening rule for the changes in the viscoplastic volumetric strain. However, the linear evolution equation for the scalar kinematic hardening parameter $y^*_{m1}$ can be expressed as

$$dy^*_{m1} = B^*_2 \left( A^*_2 d\varepsilon^{vp}_v \right) \tag{4.31}$$

In order to evaluate the effect of nonlinearity of evolution equation for $y^*_{m1}$, the undrained cyclic and monotonic triaxial simulations are conducted by the material parameters of Nakanoshima clay. The results of the linear and the nonlinear evolution equations for $y^*_{m1}$ are presented in Figure 4.5 for the cyclic and monotonic triaxial conditions. For the stress-strain relation and stress path under the monotonic loading, the effect of the linear evolution equation is insignificant as the results for both linear and nonlinear cases are exactly the same. For the stress-strain relation of cyclic specimen, the linear equation results in one cycle more at similar level of strain in the stress-strain relation, which implies the slightly higher hardening effect for the linear case.

The variations of the scalar kinematic hardening rule $y^*_{m1}$ , for the linear and nonlinear evolution equations, are presented in Figures 4.6 and 4.7 for the cyclic and monotonic cases, respectively. The variations of $y^*_{m1}$ for the cyclic loading case are slightly larger for the linear evolution equation, but for the monotonic case, the results are nearly similar for both linear and nonlinear evolution equations.

The variations of viscoplastic volumetric strain versus $y^*_{m1}$ are plotted in Figure 4.8 for the cyclic and monotonic loading conditions. It is seen that the effect of the linear evolution equation of $y^*_{m1}$ on the viscoplastic volumetric strain is insignificant for both cases under undrained loading conditions.

In order to assess the effect in the drained loading conditions, a simple drained consolidation test with one reloading process is simulated using the linear and the nonlinear evolution equations. The material parameters of the Nakanoshima cyclic sample are used in the simulation. Figure 4.9 shows the variation of the total volumetric strain versus the mean effective stress for the linear and the nonlinear evolution equations. In the drained conditions, the influence of the nonlinear evolution equation of $y^*_{m1}$ becomes more distinct, inasmuch as larger volumetric strain is developed by taking the nonlinear equation compared to the linear evolution equation.

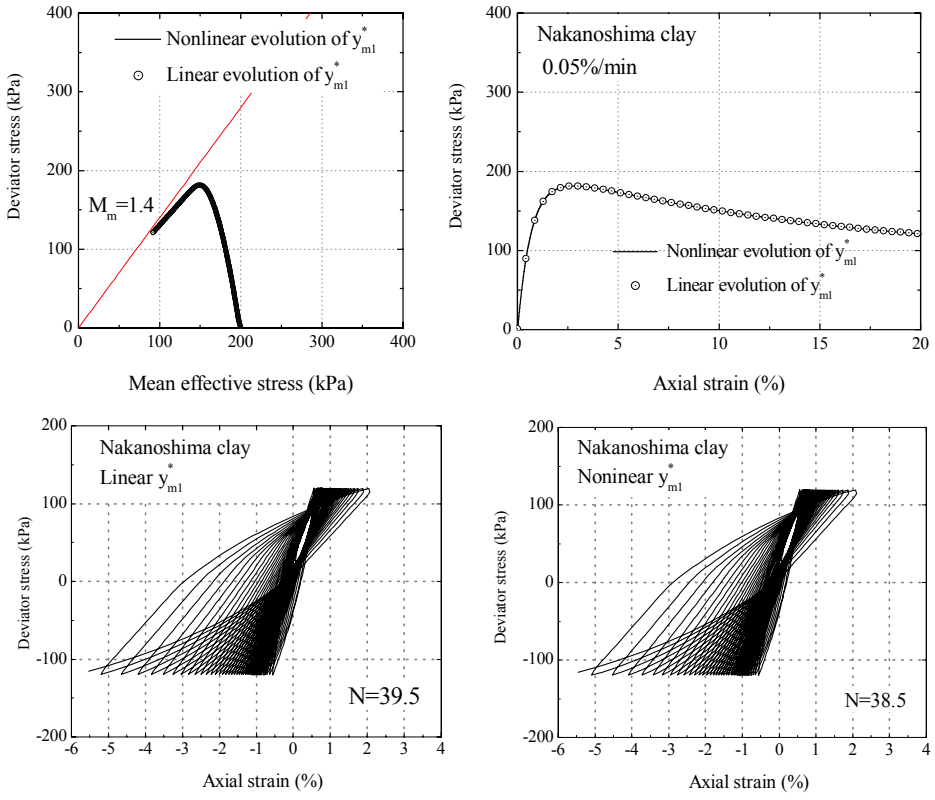


*Figure 4.5. The simulated results for the linear and the nonlinear evolution equations of $y^*_{m1}$, for the monotonic loading (above) and the cyclic triaxial loading conditions (below).*

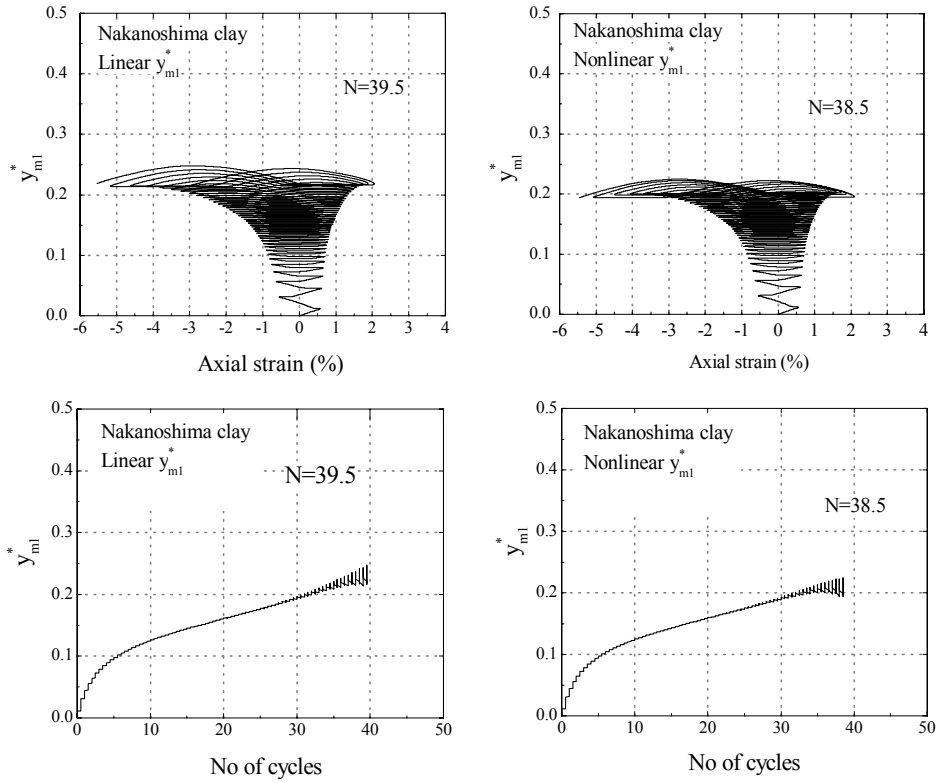


*Figure 4.6. The variation of $y^*_{m1}$ for the linear and the nonlinear evolution equations, under cyclic triaxial loading conditions.*

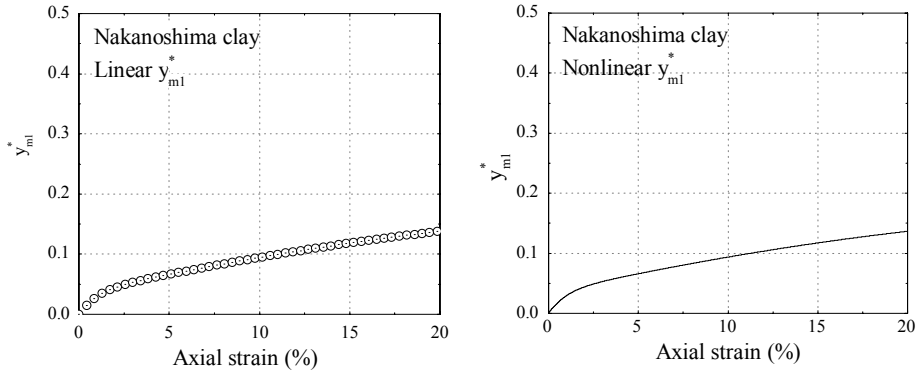


*Figure 4.7. The variation of $y^*_{m1}$ for the linear and the nonlinear evolution equation, under monotonic loading conditions.*

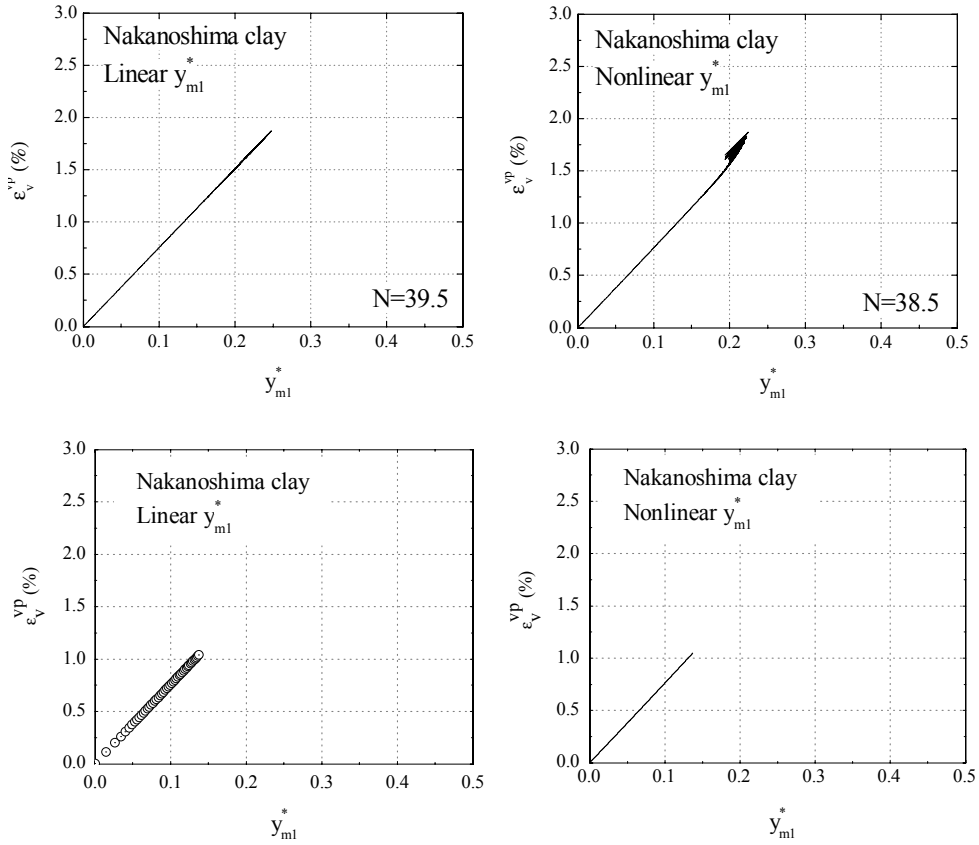


*Figure 4.8. Viscoplastic volumetric strain vs. $y^*_{m1}$ for the linear and the nonlinear evolution equations, under cyclic loading (above) and under monotonic loading conditions (below).*

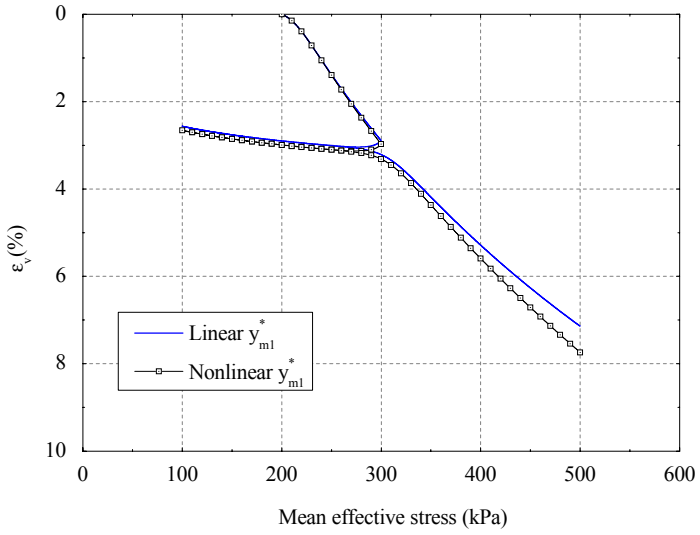


*Figure 4.9. The variations of volumetric strain under drained consolidation for the linear and the nonlinear evolution equations.*

### 4.3.4. Effect of the Hardening Parameter $C_f$

The Nakanoshima clay sample, which is used for the monotonic loading case, demonstrated rather more softer behavior compared with the cyclic test sample. Therefore different value for the hardening parameters, in particular $C_f$, is allocated for the monotonic sample. Three cases are considered herein with different values of the hardening parameter $C_f$ equal to 5, 45, and 75. For the other material parameters the values as listed in Table 4.1 are assigned. The simulated results of the stress-strain relations and stress paths for the monotonic and the cyclic loading conditions are presented in Figures 4.10 and 4.11, respectively. By taking the larger values for $C_f$, more softening behavior in stress-strain relations is observed for both cyclic and monotonic loading cases, which results in a better agreement between the simulated results and the experimental values under monotonic loading conditions.

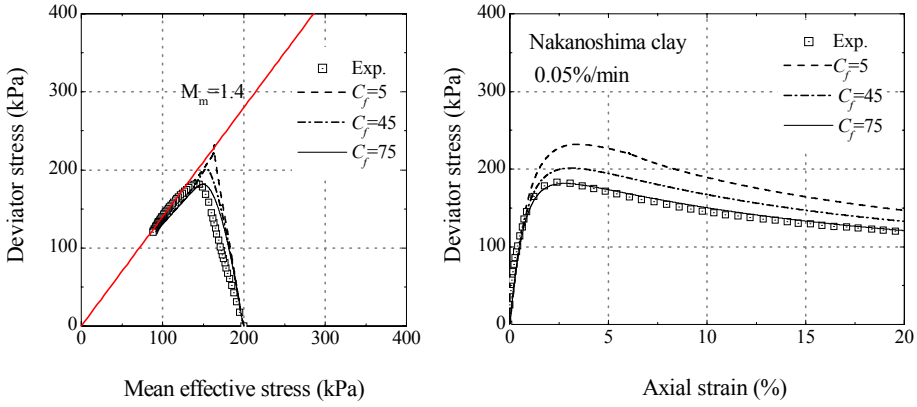


*Figure 4.10. Stress paths and stress-strain relations under monotonic loading for different values of $C_f$.*

The variations of $B^*$ for the different values of $C_f$, under the monotonic and the cyclic loading conditions, are illustrated in Figures 4.12 and 4.13, respectively. The variation in $B^*$ for the monotonic case is quite smooth, while for the cyclic loading case the variations in $B^*$ has more perturbation following the variation of the viscoplastic shear strains. However in both loading cases, by increasing the $C_f$ the reduction rate of $B^*$ increases which results in more softening behavior and consequently larger deformations.

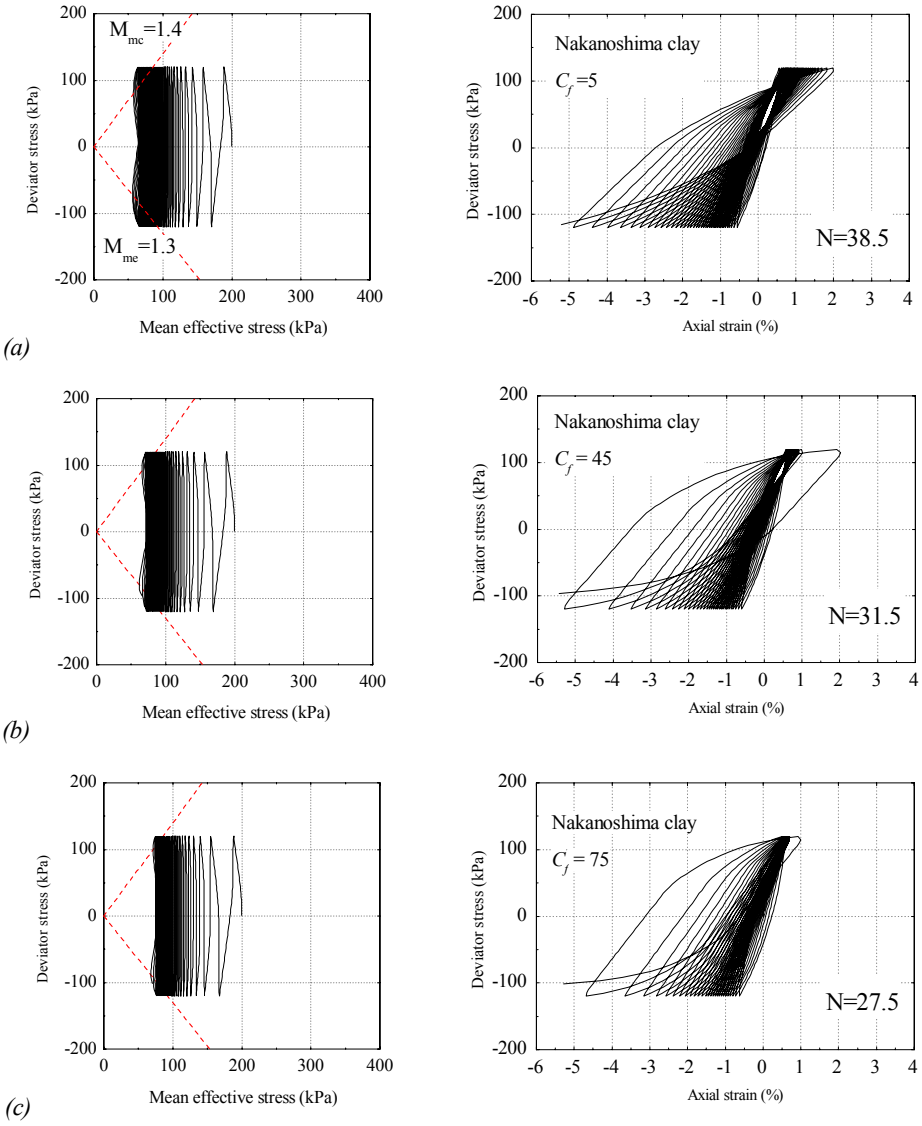


*Figure 4.11. Stress paths and stress-strain relations under cyclic loading for different values of $C_f$.*

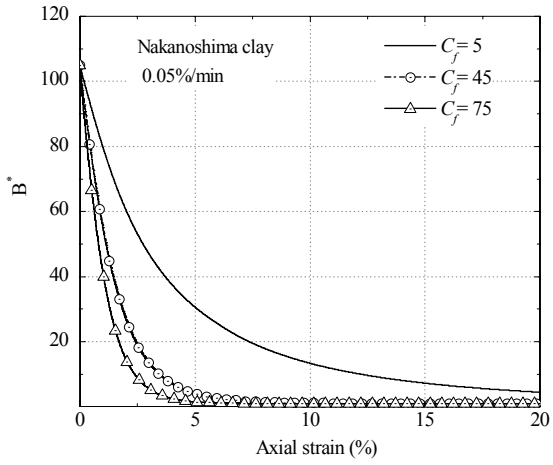


*Figure 4.12. The variation of $B^*$ under monatomic loading for different values of $C_f$.*

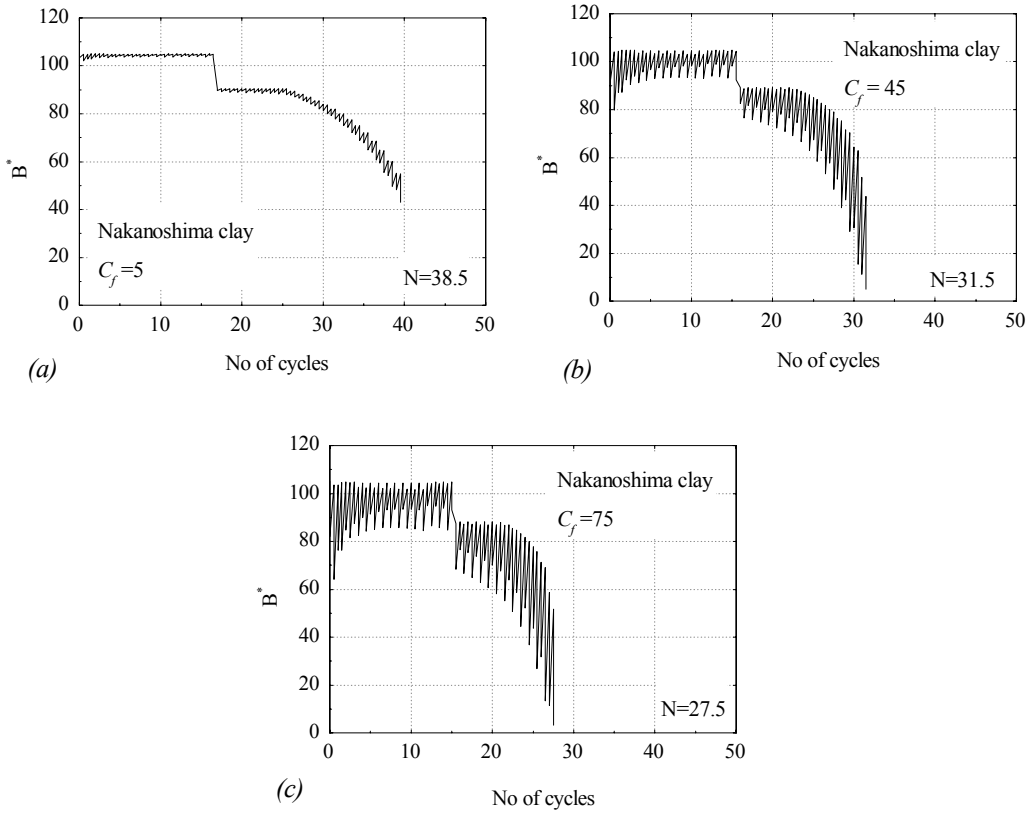


*Figure 4.13. The variation of $B^*$ under cyclic loading for different values of $C_f$.*

### 4.3.5. Effect of the Strain-Dependent Parameter $\alpha$

In the constitutive equations, the degradation of the elastic shear modulus $G$ is introduced as the function of the mean effective stress and the accumulated viscoplastic shear strain from the initial state, given by

$$G = \frac{G_0}{\left(1+\alpha\left(\gamma^{vp}\right)^r\right)}\sqrt{\frac{\sigma'_m}{\sigma'_{m0}}} \tag{4.32}$$

in which the strain-dependent parameter $\alpha$ is determined from the experimental results by data-adjusting method. To evaluate the effect of the strain-dependent parameter $\alpha$, three cases are considered using the material parameters as listed in Table 4.1. For parameter $\alpha$, however, three different values equal to 1, 10, and 20 are assigned. The simulation results for monotonic and cyclic loading conditions are illustrated in Figures 4.14 and 4.15 as stress paths and stress-strain relations. The effect of the variation of $\alpha$ on the stress path results is insignificant for the monotonic case, while for the cyclic case slightly changes in observed due to the variation of $\alpha$. For stress-strain relations, the larger values of $\alpha$ results in faster degradation of $G$ and softer behavior. Of course this influence is more evident for the cyclic case as the values of the accumulated shear strain is higher compared with those of monotonic case.

Figures 4.16 and 4.17 demonstrate the variation of $G$ for different values of $\alpha$ under both the cyclic and monotonic loading conditions. The larger values of $\alpha$ leads to higher degradation of the elastic shear modulus and consequently larger deformations at similar level of shearing.

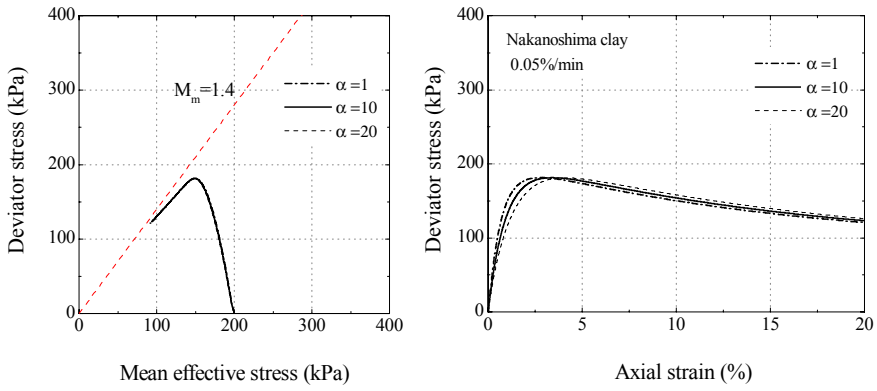


*Figure 4.14. Stress paths and stress-strain relations under monotonic loading for different values of $\alpha$.*

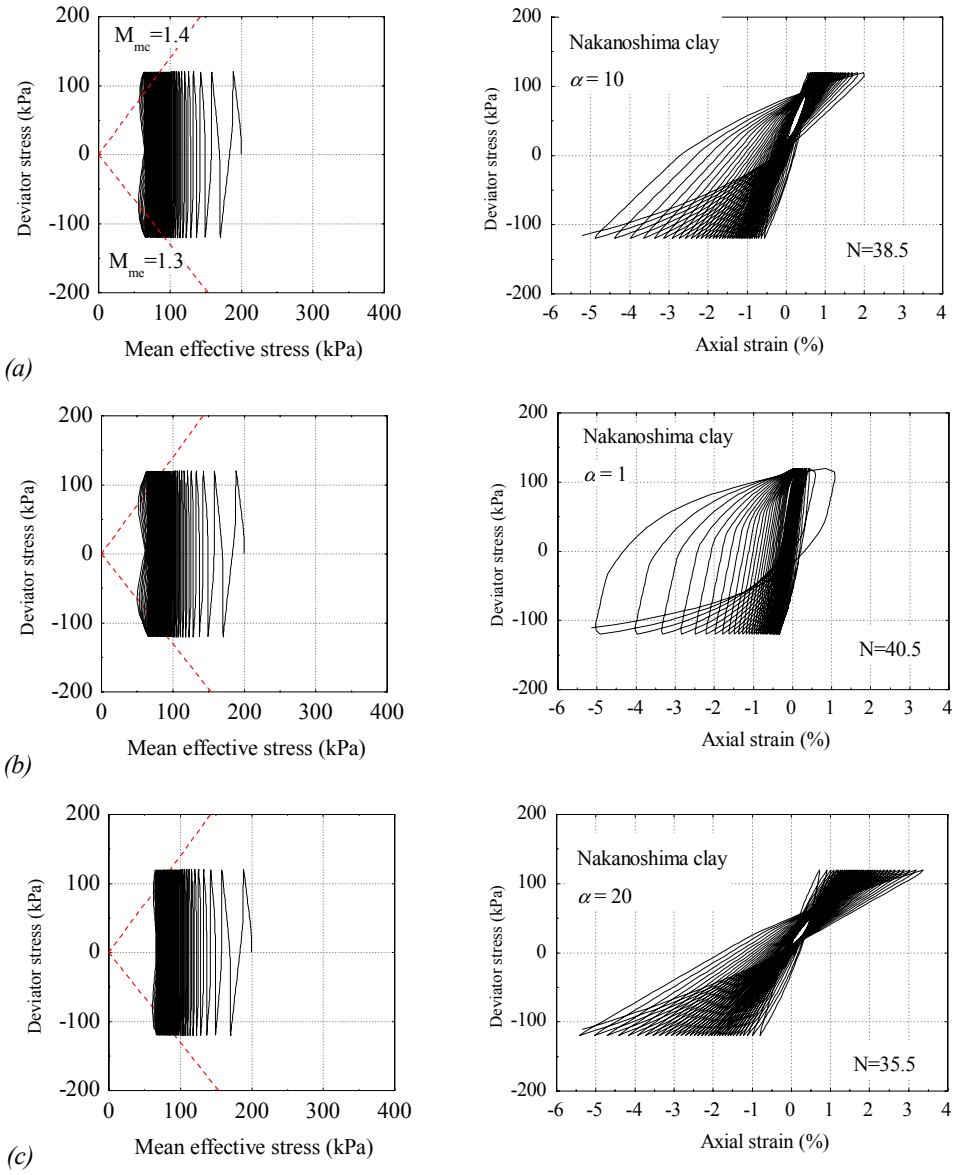


*Figure 4.15. Stress paths and stress-strain relations under cyclic loading for different values of $\alpha$ .*

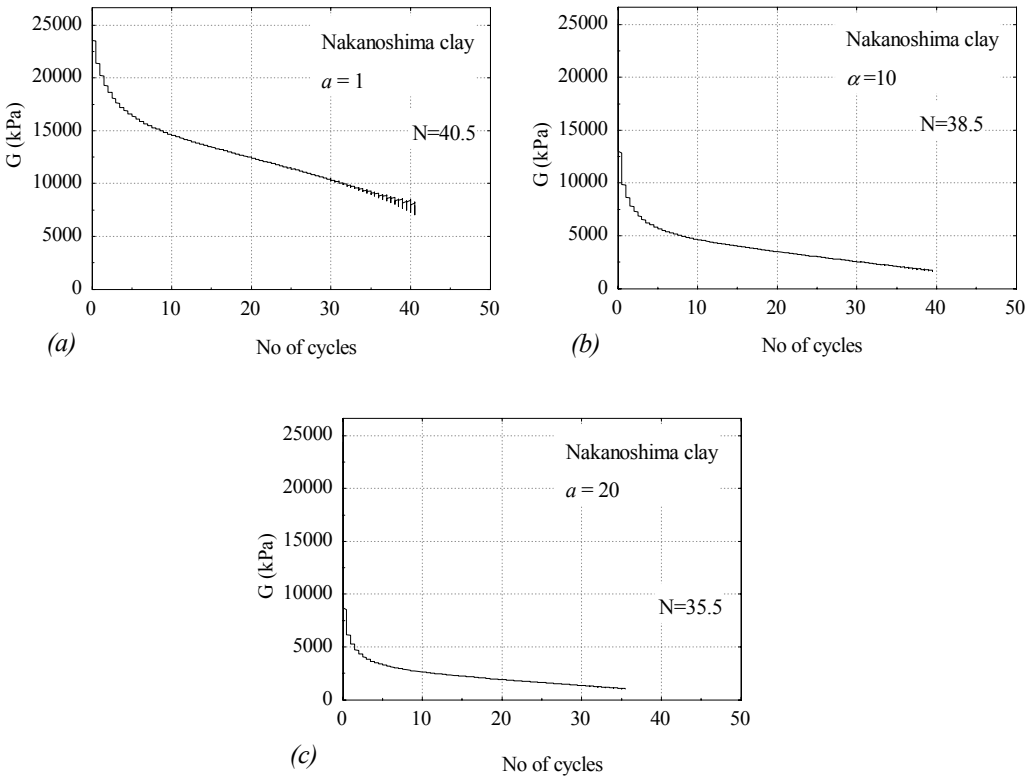


*Figure 4.16. The variation of G under cyclic triaxial conditions for different values of $\alpha$.*

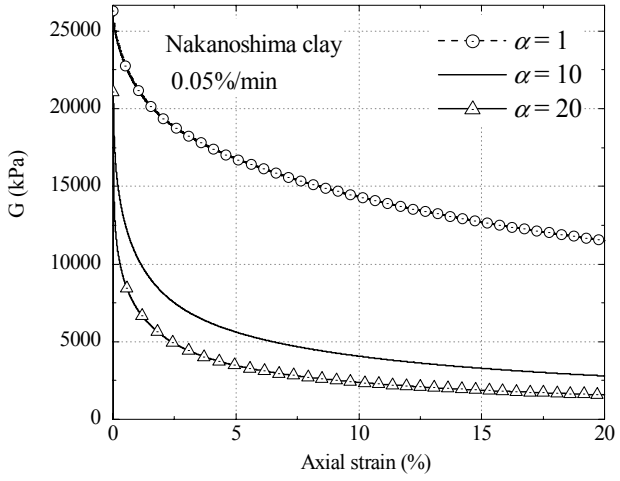


*Figure 4.17. The variation of G under monotonic triaxial conditions for different values of $\alpha$.*

## 4.4. Simulation of Cyclic Triaxial Behavior of Osaka Soft Clay

In order to obtain the dynamic characteristics of Osaka soft clay layer at Torishima super levee site (see Section 3.2 for further details), cyclic triaxial tests have been performed on the soft clay specimen from Ac2 layer. One borehole has been drilled with 86 mm diameter reaching down to about 20m below the ground surface. Undisturbed samplings have been obtained from the Ac2-U and Ac2-M sub-layers. The undrained cyclic triaxial tests were accomplished on the soft clay specimens with different cyclic stress ratios $\left(CSR = q/2\sigma'_{m0}\right)$ equal to 0.370, 0.311, and 0.250. Figure 4.18 shows the experimental results of the undrained cyclic triaxial tests on the samples from Ac2-U layer, named as T-1, with different cyclic stress ratios. The results for the samples obtained from Ac2-M layer, which are named as T-2, are presented in Figure 4.19 for different cyclic stress ratio as the stress-strain relations and stress paths.

The simulations of the cyclic triaxial tests are conducted to obtain the material parameters of the soft clay specimens using the cyclic elasto-viscoplastic constitutive model. The material parameters of soft clay specimens are listed in Table 4.2. The conventional characteristic parameters such as the initial void ratio, the swelling index, the compression index, and the viscoplastic parameter *m'* are obtained from the representative material parameters of the corresponding layer as presented in Chapter 2. While for the rest of the parameters, the data-adjusting method and comparison of the simulated results with the cyclic triaxial test data are utilized. The simulated results for the Ac2-U layer specimens are presented in Figure 4.20, and for the Ac2-M layer specimens are shown in Figure 4.21. Efforts were made to determine the parameters so that the simulated results provide the closest trend to the experimental data under different level of cyclic shearing in terms of the strain amplitude and number of cycles in the stress-strain relations. Nonetheless, the simulated results show some dissimilarity with the experimental results, particularly in the higher level of cyclic shearing. This might be attributed to the differences between the loading conditions in the laboratory tests and in the simulation. Furthermore, the simulated results represent the behavior of a realistic clay sample regardless of the boundary effect and size, while the experimental data show the response of the samples which may have been disturbed during the sampling process, and also have an inherent heterogeneity. Therefore, it is inevitable to have such dissimilarity between the simulated results and experiments, particularly when an individual set of parameters are employed for the samples under different cyclic stress ratios.

The cyclic shear ratio versus number of cycles curve which provides the cyclic resistibility of clay samples at a specific level of double strain amplitude, i.e., *DA*= 5% or *DA*= 10%, are plotted in Figure 4. 22 and the values are listed in Table 4.3 for both experimental and simulation results. The simulation results demonstrate rather higher number of cycles at the same shearing level compared

with the experimental results. However, considering the overall shape and curve slope, the simulated results present good agreement with the experimental data.

*Table 4.2. Material parameters of soft clay layer Ac2 in Torishima.*

| | | T-1(Ac2-U) | T-2 (Ac2-M) |
|---|---|---|---|
| Test No. | | #1: CSR=0.370<br>#2: CSR=0.250<br>#4: CSR=0.311 | #1: CSR=0.370<br>#2: CSR=0.250<br>#4: CSR=0.311 |
| Initial void ratio | $e_0$ | 1.25 | 1.65 |
| Compression index | $\lambda$ | 0.341 | 0.593 |
| Swelling index | $\kappa$ | 0.019 | 0.027 |
| Normalized initial shear modulus | $G_0/\sigma'_m$ | 75.2 | 58.95 |
| Stress ratio at compression | $M^*_{mc}$ | 1.24 | 1.18 |
| Stress ratio at extension | $M^*_{me}$ | 0.94 | 0.915 |
| Viscoplastic parameter | $m'$ | 24.68 | 28.2 |
| Viscoplastic parameter *(1/s)* | $C_1$ | $1.00\times10^{-5}$ | $1.00\times10^{-5}$ |
| Viscoplastic parameter *(1/s)* | $C_2$ | $3.83\times10^{-6}$ | $1.85\times10^{-6}$ |
| Structural parameter | $n=\sigma'_{maf}/\sigma'_{mai}$ | 0.30 | 0.325 |
| Structural parameter | $\beta$ | 3.6 | 3.8 |
| Hardening parameter | $B^*_0$ | 100 | 180 |
| Hardening parameter | $B^*_1$ | 40 | 3 |
| Hardening parameter | $C_f$ | 10 | 3 |
| Reference value of viscoplastic strain *(%)* | $\gamma^{vp*}_{(n)r}$ | 1.25 | 1.25 |
| Strain-dependent parameter | $\alpha$ | 10 | 20 |
| Scalar hardening parameter | $A^*_2$ | 5.9 | 5.9 |
| Scalar hardening parameter | $B^*_2$ | 1.8 | 1.8 |

*Table 4.3. Number of cycles at DA= 5% and DA=10% at different CSR, for Torishima soft clays.*

| | | T-1(Ac2-U) | | T-2(Ac2-M) | |
|---|---|---|---|---|---|
| | | *DA*=5% | *DA*=10% | *DA*=5% | *DA*=10% |
| Experiment: | | | | | |
| | CSR= 0.370 | 0.5 | 1.5 | 3 | 5 |
| | CSR= 0.311 | 2 | 4 | 17 | 25 |
| | CSR= 0.250 | 36 | 43 | 135 | 154 |
| Simulation: | | | | | |
| | CSR= 0.370 | 2.5 | 4 | 6 | 8 |
| | CSR= 0.311 | 7 | 9.5 | 18 | 24 |
| | CSR= 0.250 | 26 | 38.5 | 125 | 142 |

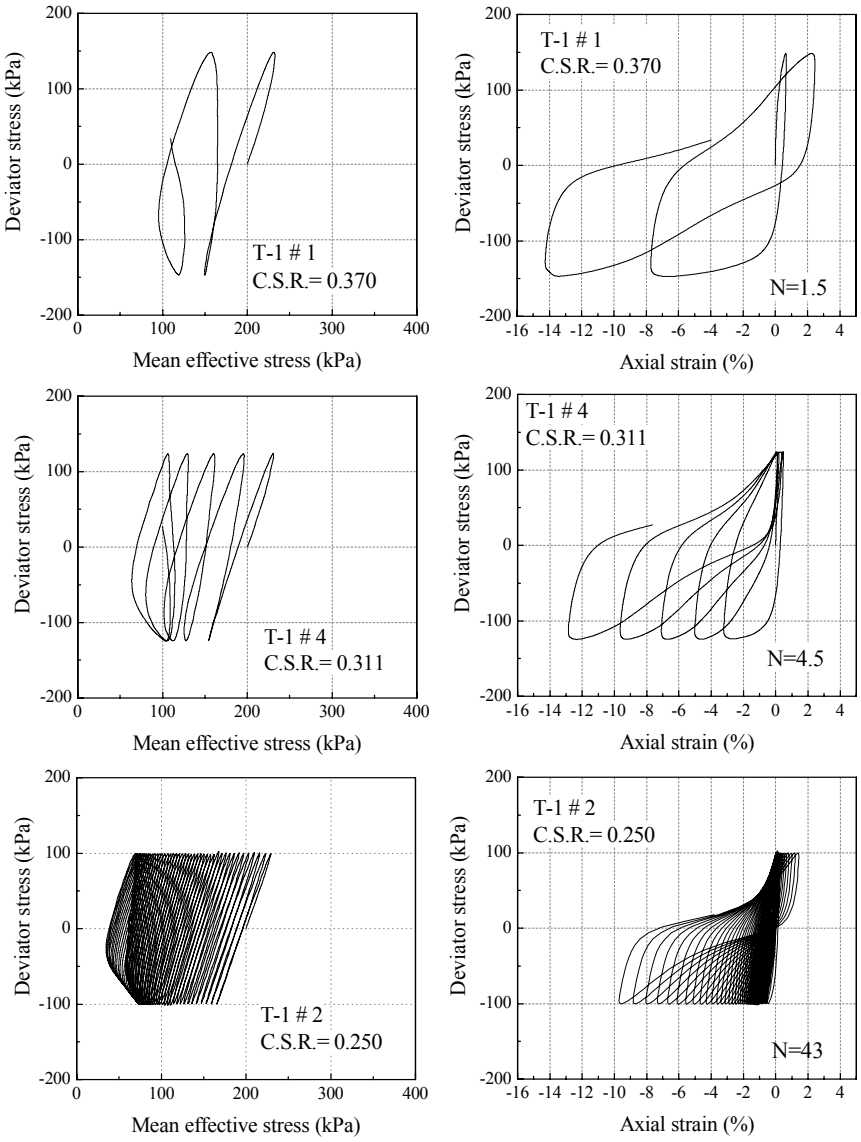


*Figure 4.18. Cyclic triaxial test results as stress-strain relations and stress paths for Ac2-U samples (T-1) under different cyclic stress ratios.*

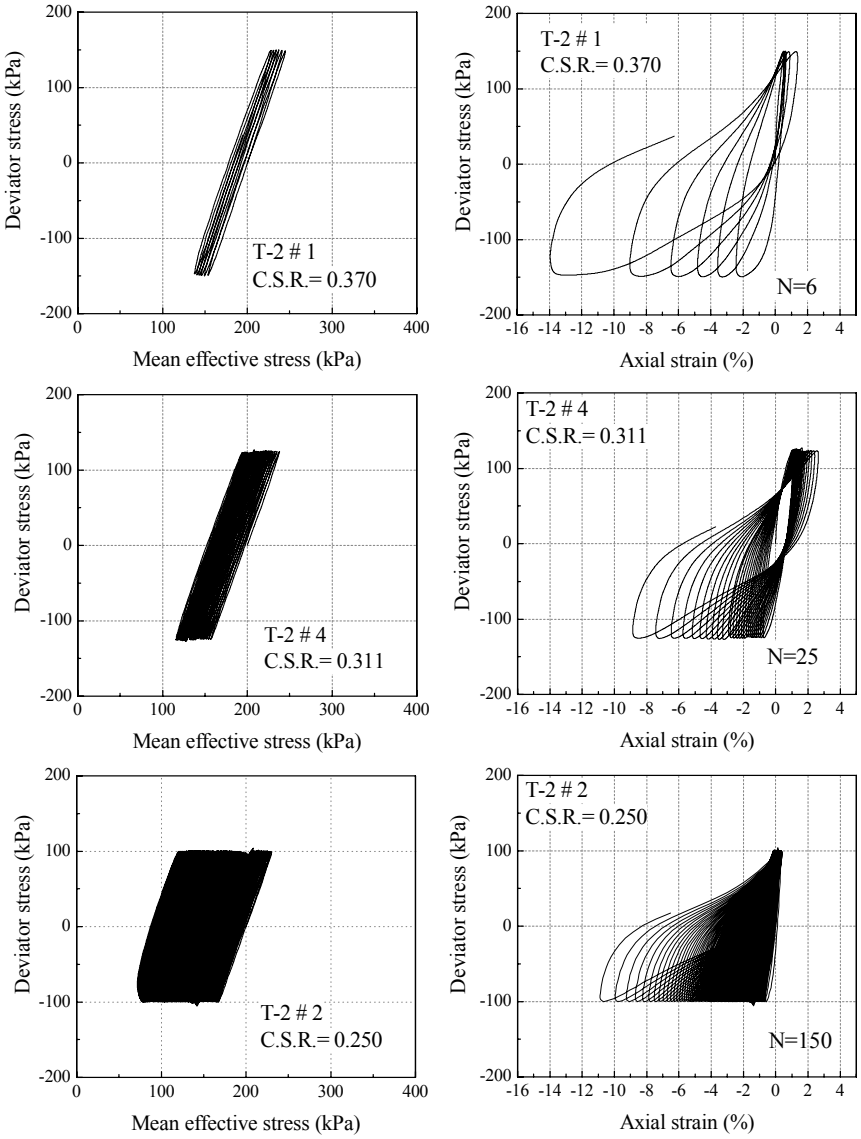


*Figure 4.19. Cyclic triaxial test results as stress-strain relations and stress paths for Ac2-M samples (T-2) under different cyclic stress ratios.*

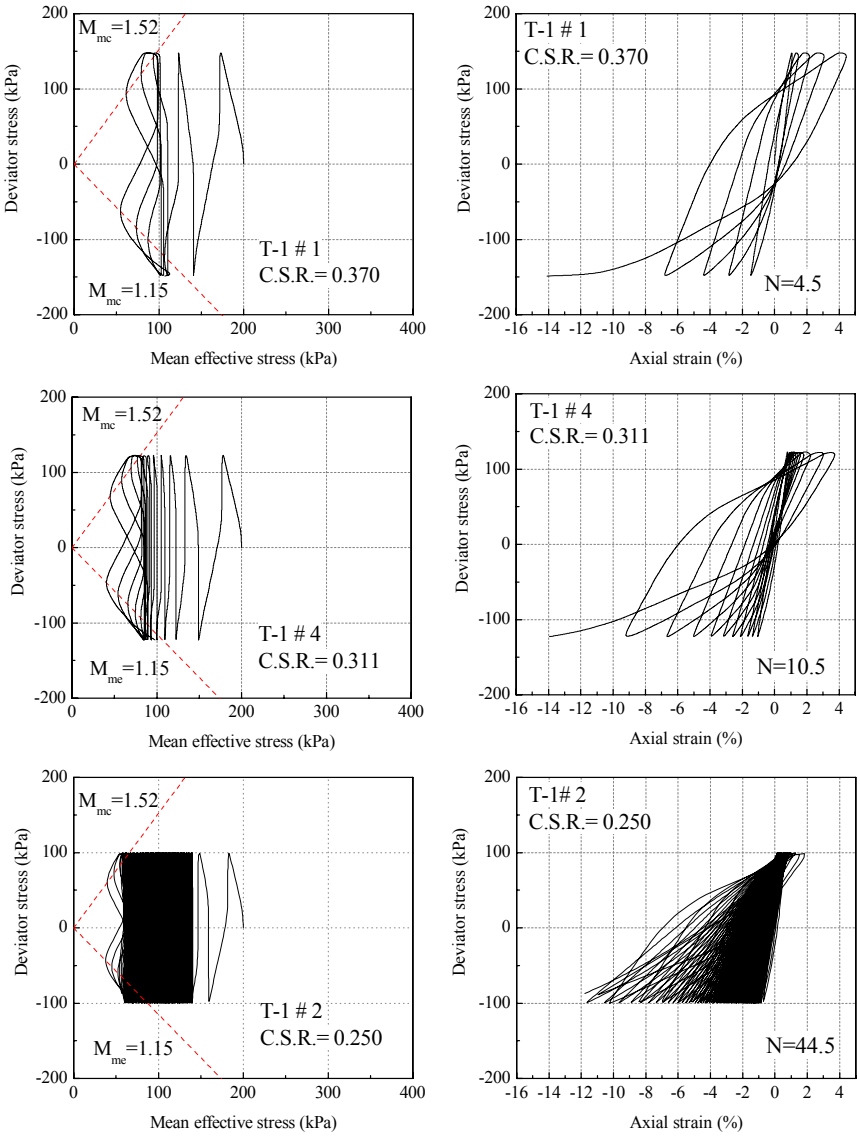


*Figure 4.20. Simulated results of stress-strain relations and stress paths for Ac2-U samples (T-1), under different cyclic stress ratios.*

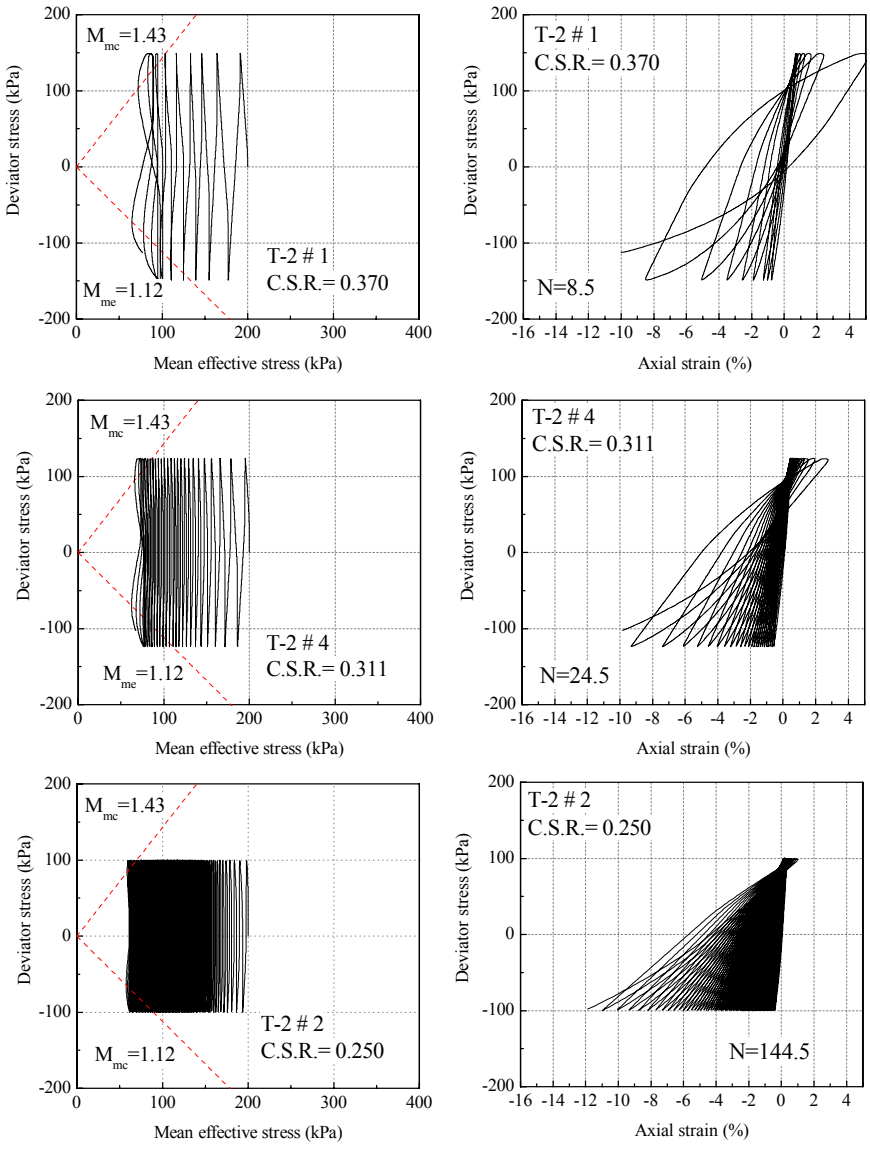


*Figure 4.21. Simulated results of stress paths and stress-strain relations for Ac2-M samples (T-2), under different cyclic stress ratios.*

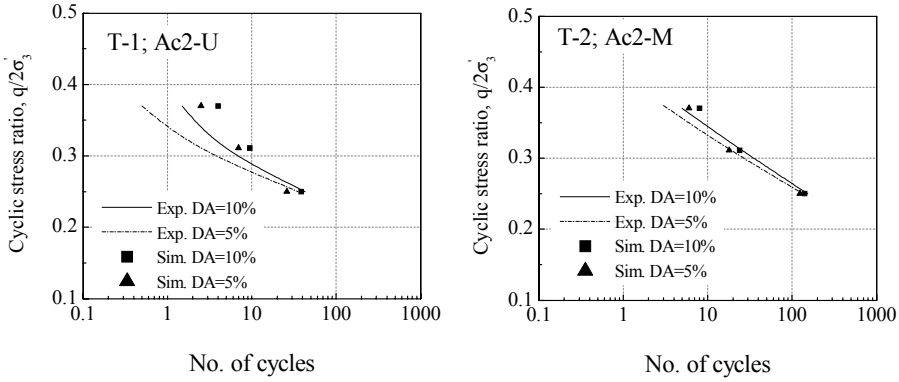


*Figure 4.22. CSR-N curves for the experimental and the simulation results for Ac2-U and Ac2-M samples.*

## 4.5. Concluding Remarks

A cyclic elasto-viscoplastic constitutive model was presented in this chapter following the nonlinear kinematic hardening rules and considering the effect of the structural degradation. The model was modified here from the preceding formulations, presented in Sawada (2008), in terms of the inclusion of the kinematic hardening rule for volumetric strain. The effect of the reformulation was found to be as more softening behavior in the stress-strain relations and thus more deformation at the same shearing level. The performance of the model was then verified through the modeling of soft clay specimens under undrained cyclic and monotonic triaxial conditions. Furthermore, the effect of the linear and nonlinear evolution equations for the kinematic hardening parameter $y_{m1}^{*}$ was studied. The consideration of linear evolution equation has shown insignificant influence in the simulated results using the material parameter of Nakanoshima clay under undrained loading condition. However, the effects appeared to be more significant under drained loading conditions such as cyclic compression test. From the parametric study on the hardening parameter $C_f$ and the strain-dependent parameter $\alpha$, it was found that by increasing $C_f$ the reduction rate of $B^{*}$ increases, which results in more softening behavior and consequently larger deformations. Moreover, the larger values of $\alpha$ leads to higher degradation of the elastic shear modulus and consequently larger deformations at the same level of shearing.

# Chapter 5

# DYNAMIC ANALYSIS OF SOFT SOIL DEPOSITS USING FINITE DEFORMATION THEORY

## 5.1. Introduction

Large deformations often take place during the strong ground motions, which may bring about extensive damages to the infrastructures and overlying buildings. In the dynamic analysis of a multilayered ground, besides the presence of sand layers and susceptibility to liquefaction, the large deformations of soft clay layers need to be considered as a possible cause to failure. In order to obtain precise results in the finite element analysis of such problems, which involve the geometric nonlinearity, the formulation based on the finite deformation theory should be employed. Several numerical codes have been developed for the analysis of large deformation problems induced by liquefaction, which have been equipped with robust constitutive models for sand. However, the influence of soft clay layers in the dynamic analysis of such problems has been either omitted, or considered insufficiently by adopting a simple constitutive model for representing the clay behavior.

In this study, the numerical program entitled LIQCA3D-FD (Oka et al. 2001), which has been developed for three-dimensional analysis of dynamic problems in the context of large deformations, is extended to include a cyclic elasto-viscoplastic constitutive model for analysis of clayey materials under dynamic loading conditions. For that purpose, the cyclic elasto-viscoplastic model, as presented

in Chapter 4, is applied. In addition, the preceded finite element formulations (Oka 2002) are modified for the viscoplastic materials within the framework of finite deformation theory. The new numerical program, entitled COMVI3D-DY10, is used for the analysis of strain localization under dynamic loading conditions on soft clay specimen characterized by the cyclic elasto-viscoplastic constitutive model parameters. Several cases are considered to study the effects of the mesh size and the drainage boundaries on the shear band development. Furthermore, the dynamic analysis of the Torishima super levee on a stratified ground, which consists of sandy layers and soft clay layers, is conducted using the developed numerical program. In order to obtain the material parameters of upper sand layer in Torishima site, the simulation of sand specimens is carried out using the cyclic elasto-plastic constrictive model (Oka et al. 1999). The cyclic elasto-viscoplastic constitutive model is assigned for the clay layers, while the cyclic elasto-plastic constitutive model is applied for the sandy layers. An input wave based on an earthquake record is applied in the horizontal direction and the behavior of the system is studied in terms of liquefaction potential and deformation responses through two different cases as the natural ground case and the improved ground case.

## 5.2. Dynamic FEM Formulations Based on Finite Deformation Theory

The dynamic finite element formulation for a Biot's type mixture is presented within the framework of the finite deformation theory and updated Lagrangian method. The equations are modified here from the preceded formulations, presented by Oka (2002), to include the viscoplastic-related configurations such as the tangent stiffness method and the relaxation stress tensor.

For the dynamic analysis of a coupled scheme based on the Biot's type two phase mixture theory, there are several methods according to the nature and number of unknown variables, such as; *u-p* (displacement-pore water pressure) formulation, *u-w-p* (displacement-relative acceleration-pore water pressure) formulation, and etc. (Zienkiewicz et al. 1980). In the *u-p* formulation method, acceleration of soil skeleton and pore pressure are taken as independent variables, while in the *u-w-p* formulation, acceleration of soil skeleton, relative acceleration as difference between accelerations of soil skeleton and pore fluid, and pore pressure are independent variables. In the cases with low permeability and low frequency for input motion, the relative acceleration is negligible and the *u-p* formulation can be sufficiently applied for the analysis (Zienkiewicz and Bettes 1982). Barends (1991) concluded that the relative acceleration could be negligible in the case with permeability lower than 1 cm/sec.

### 5.2.1. General Setting

In the current study, the *u-p* formulation in updated-Lagrangian frame is employed with the Jaumann rate of Cauchy stress rate tensor. The grain particles in the soil skeleton are assumed to be incompressible. The distribution of porosity in the soil and the distribution of body force in space are assumed to be smooth. An isoparametric 20-node hexahedron element with a reduced Gaussian (2×2×2) integration is adopted for displacement, velocity, and acceleration of the solid skeleton in three-dimensional analysis, while the pore water pressure is defined at the eight corner nodes of the element. Figure 5.1 shows the 20-node hexahedron elements with numbering order and Gauss points for the soil skeleton and the pore water pressure.

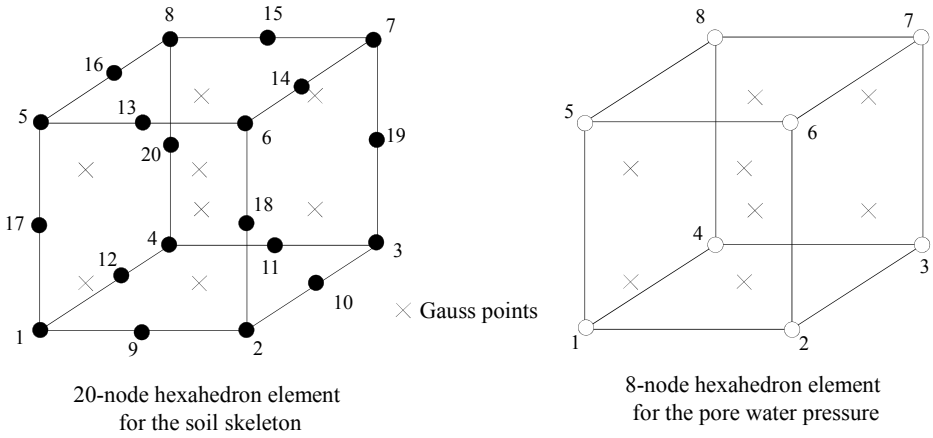


*Figure 5.1. Isoparametric 3D elements for the soil skeleton and the pore water pressure.*

### 5.2.2. Definition of Partial Stresses for a Two-Phase Mixture

In the theory of the two-phase mixture, the mixture is expressed by the superposition of two phases, namely, the solid phase and the fluid phase. The solid phase and the fluid phase represent the soil skeleton and the distributed pore fluid, respectively. The apparent densities of the soil and the fluid phases are given by the following relations

$$\rho = \overline{\rho}^S + \overline{\rho}^F \tag{5.1}$$

$$\rho = (1-n)\rho^S + n\rho^F \tag{5.2}$$

$$\overline{\rho}^S = (1-n)\rho^S \tag{5.3}$$

$$\overline{\rho}^F = n\rho^F \tag{5.4}$$

where $\rho$ is the density of the fluid saturated soil, $\rho^S$ is the density of the soil particles, $\rho^F$ is the density of the pore fluid, $\overline{\rho}^S$ and $\overline{\rho}^F$ are the apparent densities of the solid and the fluid phases, respectively, and $n$ is the porosity.

The total Cauchy's stress is given by

$$T_{ij} = T_{ij}^S + T_{ij}^F \tag{5.5}$$

where $T_{ij}^S$ is the partial stress of solid phase, and $T_{ij}^F$ is the partial stress of the fluid phase. Based on the principle of effective stress by Terzaghi and by considering that extension is positive even for the pressure $p$ , the effective Cauchy's stress tensor is obtained as

$$T_{ij} = T_{ij}' + p\delta_{ij} \tag{5.6}$$

where $\delta_{ij}$ is the Kronecker's delta, $p$ is the pore water pressure and

$$T_{ij}^F = np\delta_{ij} \tag{5.7}$$

Hence, from Equations (5.5) and (5.6),

$$T_{ij}^S = T_{ij}' + (1-n)p\delta_{ij} \tag{5.8}$$

### 5.2.3. Equations of Motion for a Two-Phase Mixture Theory

The equations of motion for solid and fluid phases are given by

$$\overline{\rho}^S a_i^S = \frac{\partial T_{ji}^S}{\partial x_j} + \frac{n^2\gamma_w}{k}(v_i^F - v_i^S) + \overline{\rho}^S b_i \tag{5.9}$$

$$\overline{\rho}^F a_i^F = \frac{\partial T_{ji}^F}{\partial x_j} - \frac{n^2\gamma_w}{k}(v_i^F - v_i^S) + \overline{\rho}^F b_i \tag{5.10}$$

in which $v_i^S$ is the velocity of soil skeleton, $v_i^F$ is the velocity of pore fluid, $b_i$ is the body force, $k$ is the coefficient of permeability and $\gamma_w$ is the unit density of pore fluid.

By summation of Equations (5.9) and (5.10), we obtain

$$\overline{\rho}^S a_i^S + \overline{\rho}^F a_i^F = \frac{\partial T_{ji}^S}{\partial x_j} + \frac{\partial T_{ji}^F}{\partial x_j} + \left(\overline{\rho}^S + \overline{\rho}^F\right) b_i \tag{5.11}$$

Using Equations (5.1), (5.4) and (5.9), the above equation becomes

$$\rho a_i^S - n\rho^F \left(a_i^S - a_i^F\right) = \frac{\partial T_{ji}}{\partial x_j} + \rho b_i \tag{5.12}$$

Considering the u-p formulation, the term $a_i^S - a_i^F$ can be disregarded. Therefore, the equations of motion for two-phase mixture are obtained as

$$\rho a_i^S = \frac{\partial T_{ji}}{\partial x_j} + \rho b_i \tag{5.13}$$

### 5.2.4. Continuity Equation of Pore Fluid

Mass of material $M(t)$ in domain $V$ at time $t$ is given by

$$M(t) = \int_V \rho\left(x_i, t\right) dV \tag{5.14}$$

where $\rho\left(x_i, t\right)$ is the density at time $t$, and $x_i$ is the position vector of the material point of domain $V$.

Outflow $J_S$ of the mass from closed surface $S$ at time $t$ is

$$J_S = \int_S \rho\left(x_i, t\right) v\left(x_i, t\right) dS \tag{5.15}$$

in which $v\left(x_i, t\right)$ is the velocity vector.

From the mass conservation law, $J_S$ in Equation (5.15) is equal to the change in $M(t)$ in Equation (5.14). Hence,

$$\frac{d}{dt}\left\{\int_V \rho\left(x_i, t\right) dV\right\} = -\int_S \rho\left(x_i, t\right) v\left(x_i, t\right) \tilde{n} dS \tag{5.16}$$

Using the Gauss's theorem, Equation (5.16) can be rewritten in a local form, namely,

$$\frac{\partial \rho(x_i,t)}{\partial t} + \nabla\{\rho(x_i,t)v(x_i,t)\} = 0 \tag{5.17}$$

which is a general mass conservation law.

Applying Equation (5.17) to the solid and the fluid phases of the mixture, we obtain

$$\frac{\partial \overline{\rho}^S}{\partial t} + \frac{\partial\left(\overline{\rho}^S v_i^S\right)}{\partial x_i} = 0 \tag{5.18}$$

$$\frac{\partial \overline{\rho}^F}{\partial t} + \frac{\partial\left(\overline{\rho}^F v_i^F\right)}{\partial x_i} = 0 \tag{5.19}$$

From Equation (5.3), Equation (5.18) becomes

$$\rho^S \frac{\partial(1-n)}{\partial t} + (1-n)\frac{\partial \rho^S}{\partial t} + \rho^S \frac{\partial\left\{(1-n)v_i^S\right\}}{\partial x_i} + \left\{(1-n)v_i^S\right\}\frac{\partial \rho^S}{\partial x_i} = 0 \tag{5.20}$$

and from Equation (5.4), Equation (5.19) becomes

$$\rho^F \frac{\partial n}{\partial t} + n\frac{\partial \rho^F}{\partial t} + \rho^F \frac{\partial\left\{n\, v_i^F\right\}}{\partial x_i} + \left(n\, v_i^F\right)\frac{\partial \rho^F}{\partial x_i} = 0 \tag{5.21}$$

Multiplying Equation (5.17) by $\rho^F / \rho^S$ and by the addition of Equation (5.21), we obtain

$$\begin{aligned} &\rho^F\left\{\frac{\partial(1-n)}{\partial t} + \frac{\partial n}{\partial t}\right\} + \rho^F \frac{\partial\left\{n\left(v_i^F - v_i^S\right)\right\}}{\partial x_i} + \rho^F \frac{\partial v_i^S}{\partial x_i} \\ &+ n\left(\frac{\partial \rho^F}{\partial t} + v_i^F \frac{\partial \rho^F}{\partial x_i}\right) + (1-n)\frac{\rho^F}{\rho^S}\left(\frac{\partial \rho^S}{\partial t} + v_i^S \frac{\partial \rho^S}{\partial x_i}\right) = 0 \end{aligned} \tag{5.22}$$

Upon dividing Equation (5.22) by $\rho^F$, we obtain

$$\frac{\partial \dot{w}_i}{\partial x_i} + D_{ii}^S + \frac{n}{\rho^F}\left(\frac{\partial \rho^F}{\partial t} + v_i^F \frac{\partial \rho^F}{\partial x_i}\right) + \frac{(1-n)}{\rho^S}\left(\frac{\partial \rho^S}{\partial t} + v_i^S \frac{\partial \rho^S}{\partial x_i}\right) = 0 \tag{5.23}$$

where

$$D_{ii}^S = \frac{\partial v_i^S}{\partial x_i} \tag{5.24}$$

$$\dot{w}_i = n\left(v_i^F - v_i^S\right) \tag{5.25}$$

By assuming the incompressibility of the grain particles in the soil and the pore water, $\dot{\rho}^S$ and $\dot{\rho}^F$ are equal to zero. The assumption of smooth distribution of the porosity in the soil leads to $\partial n/\partial x_i = 0$. Therefore, Equation (5.25) is rewritten as

$$\frac{\partial \dot{w}_i}{\partial x_i} + D_{ii}^S = 0 \tag{5.26}$$

From Equation (5.4), Equation (5.10) becomes

$$\overline{\rho}^F a_i^F = \frac{\partial T_{ij}^F}{\partial x_j} - \frac{n\gamma_w}{k}\dot{w}_i + \overline{\rho}^F b_i \tag{5.27}$$

Since

$$\frac{\partial T_{ij}^F}{\partial x_j} = \frac{\partial (np)}{\partial x_i} \tag{5.28}$$

holds from Equation (5.7), Equation (5.27) can be rewritten from Equations (5.1) and (5.28) by following the assumptions, as

$$\rho^F a_i^S = \frac{\partial p}{\partial x_i} - \frac{\gamma_w}{k}\dot{w}_i + \rho^F b_i \tag{5.29}$$

By taking the derivative of Equation (5.29), with respect to $x_i$,

$$\rho^F \frac{\partial a_i^S}{\partial x_i} = \frac{\partial^2 p}{\partial x_i^2} - \frac{\gamma_w}{k}\frac{\partial \dot{w}_i}{\partial x_i} + \rho^F \frac{\partial b_i}{\partial x_i} \tag{5.30}$$

From Equations (5.26) and (5.30), we obtain

$$\rho^F \frac{\partial a_i^S}{\partial x_i} = \frac{\partial^2 p}{\partial x_i^2} + \frac{\gamma_w}{k} D_{ii}^S + \rho^F \frac{\partial b_i}{\partial x_i} \tag{5.31}$$

Considering the smooth distribution of the body force in space, $\partial b_i/\partial x_i = 0$. Therefore, the continuity equation of pore fluid is resulted as

$$\rho^F \frac{\partial a_i^S}{\partial x_i} - \frac{\partial^2 p}{\partial x_i^2} - \frac{\gamma_w}{k} D_{ii}^S = 0 \tag{5.32}$$

### 5.2.5. Discretization of the Equations of Motion for the Two-Phase Mixture

The following simple expressions are used without notice: $a_i = a_i^S$, $v_i = v_i^S = \dot{u}_i^S$, and $D_{ij} = D_{ij}^S$. In the present study, an updated-Lagrangian method is employed to discretize the governing equations. The equations of motion for two-phase mixture, Equation (5.13), are expressed by the nominal stress with respect to the reference time state as

$$\rho\left(a_i - b_i\right) - \Pi_{ji,j} = 0 \tag{5.33}$$

where $\Pi_{ij}$ is the total nominal stress tensor with respect to the reference configuration, such as the area and the normal vector of the reference surface, and the reference configuration is now taken at time *t*.

The boundary conditions for the solid and fluid phases are assumed as follows:

- For the solid skeleton:
  - ${}_0t_i = {}_0\,\overline{t}_i$ on the stress boundary $\Gamma_1$,
  - $u = \overline{u} = 0$ on the displacement boundary $\Gamma_2$.
- For the pore fluid:
  - $p = \overline{p}$ on the boundary $\Gamma_3$,
  - $\partial p / \partial x_i = 0$ on the boundary $\Gamma_4$.

in which $t_i$ stands for the nominal stress vector and $-$ indicates the prescribed value. The total boundary is obtained as $\Gamma = \Gamma_1 + \Gamma_2 = \Gamma_3 + \Gamma_4$.

It is worth to mention that the utilization of the rate form of the equations of motion may lead to divergent results because of the accumulation of the digitizing errors within the calculation steps. Therefore, unlike the quasi-static case formulations as in Chapter 2, the total form of the equations is adopted here.

From the virtual work theorem, a weak form of Equation (5.33) can be given by multiplying the virtual velocity by the equation. Hence,

$$\int_{V_0}\left\{\rho\left(a_i-b_i\right)-\Pi_{ji,j}\right\}\delta v_i dV+\int_{\Gamma_0}\left({}_0t_i-{}_0\overline{t}_i\right)\delta v_i d\Gamma=0 \tag{5.34}$$

By integrating in parts and using Gauss's divergence theorem, we obtain

$$\int_{V_0}\Pi_{ji,j}\delta v_i dV=\int_{V_0}\left(\Pi_{ji}\delta v_i\right)_{,j}dV-\int_{V_0}\Pi_{ji}\delta v_{i,j}dV=\int_{\Gamma_0}\Pi_{ji}n_j\delta v_i d\Gamma-\int_{V_0}\Pi_{ji}\delta v_{i,j}dV \tag{5.35}$$

where $n_j$ is an outward unit normal vector of the surface $\Gamma$. Surface traction ${}_0t_i$ can be expressed by nominal stress $\Pi_{ij}$ as

$${}_0t_i=\Pi_{ji}n_j \tag{5.36}$$

and by definition of velocity gradient tensor, we obtain

$$\delta L_{ij}=\delta v_{i,j} \tag{5.37}$$

Hence, from Equations (5.35) to (5.37), Equation (5.34) becomes

$$\int_{V_0}\rho_0 a_i\delta v_i dV+\int_{V_0}\Pi_{ji}\delta L_{ij}dV=\int_{\Gamma_0}{}_0\overline{t}_i\delta v_i d\Gamma+\int_{V_0}\rho_0 b_i\delta v_i dV \tag{5.38}$$

Then by transferring the configuration to the current one at time $t+\Delta t$ , we have

$$\int_{V}\rho a_i\delta v_i dV+\int_{V}\Pi_{ji|t+\Delta t}\delta L_{ij}dV=\int_{\Gamma}{}_0\overline{t}_i\delta v_i d\Gamma+\int_{V}\rho b_i\delta v_i dV \tag{5.39}$$

where $\Pi_{ji|t+\Delta t}$ is the nominal stress at time $t+\Delta t$ expressed by

$$\Pi_{ji|t+\Delta t}=\Pi_{ji|t}+\Delta\Pi_{ji}=\Pi_{ji|t}+\left(\Delta t\right)\dot{\Pi}_{ji} \tag{5.40}$$

Moreover, from the time derivation of Nanson's theorem we have

$$\dot{\Pi}_{ji}=J\frac{\partial X_j}{\partial x_k}\hat{\dot{S}}_{ki} \tag{5.41}$$

$$\hat{\dot{S}}_{ki}=\dot{T}_{ki}-T_{kp}L_{ip}+L_{pp}T_{ki} \tag{5.42}$$

in which, $J$ is the Jacobean. $T_{ij}$ is the Cauchy stress tensor, $\dot{T}_{ij}$ is the rate type of the Cauchy stress tensor, and $L_{ij}$ is the velocity gradient tensor.

The relation between the Cauchy stress tensor and the Cauchy's effective stress tensor is given as

$$T_{ij} = T'_{ij} + p\delta_{ij} \tag{5.43}$$

The time rate of the Cauchy stress tensor is given as

$$\dot{T}_{ij} = \dot{T}'_{ij} + \dot{p}\delta_{ij} \tag{5.44}$$

By substituting the above equations in to Equation (5.41), we have

$$\begin{aligned}\hat{\dot{S}}_{ji} &= \left(\dot{T}'_{ij} + \dot{p}\delta_{ij}\right) + L_{kk}\left(T'_{ij} + p\delta_{ij}\right) - \left(T'_{ik} + p\delta_{ik}\right)L_{jk} \\ &= \left(\dot{T}'_{ij} + L_{kk}T'_{ij} - T'_{ik}L_{jk}\right) + \dot{p}\delta_{ij} + L_{kk}p\delta_{ij} - p\delta_{ik}L_{jk} \\ &= \hat{\dot{S}}'_{ji} + \dot{p}\delta_{ij} + \left(L_{kk}p\delta_{ij} - p\delta_{ik}L_{jk}\right)\end{aligned} \tag{5.45}$$

in which, effective nominal stress rate tensor $\hat{\dot{S}}'_{ij}$, is defined as

$$\hat{\dot{S}}'_{ji} = \dot{T}'_{ij} + L_{kk}T'_{ij} - T'_{ik}L_{jk} \tag{5.46}$$

The following relations are obtained by substituting Equation (5.40) into Equation (5.39)

$$\int_V \rho a_i \delta v_i dV + \int_V \Pi_{ji|t}\delta L_{ij} dV + (\Delta t)\int_V \dot{\Pi}_{ji}\delta L_{ij} dV = \int_\Gamma {}_0\bar{t}_i \delta v_i d\Gamma + \int_V \rho b_i \delta v_i dV \tag{5.47}$$

Considering Equation (5.41), when time $t$ tends to time $t + \Delta t$, the term $J\dfrac{\partial X_j}{\partial x_k}$ becomes identity matrix; therefore,

$$\int_V \dot{\Pi}_{ji}\delta L_{ij} dV = \int_V J\frac{\partial X_j}{\partial x_k}\hat{\dot{S}}_{ki}\delta L_{ij} dV = \int_V \hat{\dot{S}}_{ki}\delta L_{ij} dV \tag{5.48}$$

Replacing the above equation into Equation (5.47), we obtain

$$\int_V \rho a_i \delta v_i dV + \int_V \Pi_{ji|t}\delta L_{ij} dV + (\Delta t)\int_V \hat{\dot{S}}_{ji}\delta L_{ij} dV = \int_\Gamma {}_0\bar{t}_i \delta v_i d\Gamma + \int_V \rho b_i \delta v_i dV \tag{5.49}$$

by substituting Equation (5.45) into the above equation, we have

$$\int_V \rho a_i \delta v_i dV + \int_V \Pi_{ji|t} \delta L_{ij} dV + (\Delta t)\int_V \dot{T}'_{ij} \delta L_{ij} dV - (\Delta t)\int_V T'_{ik} L_{jk} \delta L_{ij} dV + (\Delta t)\int_V T'_{ij} L_{kk} \delta L_{ij} dV$$
$$+(\Delta t)\int_V \dot{p}\delta_{ij} \delta L_{ij} dV + (\Delta t)\int_V \left(L_{kk} p\delta_{ij} - p\delta_{ik} L_{jk}\right) \delta L_{ij} dV \tag{5.50}$$
$$= \int_\Gamma {}_0\overline{t}_i \delta v_i d\Gamma + \int_V \rho b_i \delta v_i dV$$

Since $\dot{T}'_{ij}\ \delta W_{ij} = 0$, we have

$$\dot{T}'_{ij}\ \delta L_{ij} = \dot{T}'_{ij}\ \delta D_{ij} \tag{5.51}$$

$$\delta_{ij} \delta L_{ij} = \delta D_{ii} \tag{5.52}$$

From the above equations, we obtain

$$\rho\int_V a_i \delta v_i dV + (\Delta t)\int_V \dot{T}'_{ij}\ \delta D_{ij} dV - (\Delta t)\int_V T'_{ik} L_{jk} \delta L_{ij} dV + (\Delta t)\int_V T'_{ij} L_{kk} \delta L_{ij} dV$$
$$+(\Delta t)\int_V \dot{p}\delta D_{kk} dV + (\Delta t)\int_V \left(L_{kk} p\delta_{ij} - p\delta_{ik} L_{jk}\right) \delta L_{ij} dV \tag{5.53}$$
$$= \int_\Gamma {}_0\overline{t}_i \delta v_i d\Gamma + \rho\int_V b_i \delta v_i dV - \int_V T_{ij} \delta L_{ij} dV$$

Taking acceleration vector $\{a_N\}$, velocity vector $\{v_N\}$, and pore water pressure $\{p_N\}$ as three unknown variables at nodal points, Equation (5.53) can be written in matrix form as

$$\rho\int_V \{\delta v\}^T \{a\} dV + (\Delta t)\int_V \{\delta D\}^T \{\dot{T}'\} dV + (\Delta t)\int_V \{\delta L\}^T [D_S]\{L\} dV$$
$$+(\Delta t)\int_V \{\delta L\}^T \{T'\} dV\,(trD) + (\Delta t)\int_V (tr\delta D)^T\ \dot{p} dV + (\Delta t)\int_V \{\delta L\}^T [U]\{L\} dV \tag{5.54}$$
$$= \int_\Gamma \{\delta v\}^T \{{}_0\overline{t}\} d\Gamma + \rho\int_V \{\delta v\}^T \{b\} dV - \int_V \{\delta L\}^T \{T\} dV$$

where $[D_S]\{L\} = -T'_{ik}\ L_{jk}$, and $[U]\{L\} = L_{kk} p\delta_{ij} - p\delta_{ik} L_{jk}$.

The following definitions can be set as

$$\{D\} = [B]\{v_N\} \tag{5.55}$$

$$\{v\} = [N]\{v_N\} \tag{5.56}$$

$$\{L\} = [N_L]\{v_N\} \tag{5.57}$$

$$\{a\} = [N]\{a_N\} \tag{5.58}$$

$$trD = \{B_v\}^T \{v_N\} \tag{5.59}$$

$$\dot{p} = \{N_h\}^T \{\dot{p}_N\} \tag{5.60}$$

The Jaumann rate of effective Cauchy's stress tensor $\hat{T}'_{ij}$ is objective and is given by

$$\hat{T}'_{ij} = \dot{T}'_{ij} + T'_{ik} W_{kj} - W_{ik} T'_{kj} \tag{5.61}$$

in which $W_{ij}$ is spin tensor.

For the elasto-viscoplastic materials, the constitutive equation is described using the Jaumann rate of Cauchy stress tensor $\hat{T}'_{ij}$ and stretching tensor $D_{ij}$ as

$$\hat{T}'_{ij} = C^e_{ijkl}(D_{kl} - D^{vp}_{kl}) \tag{5.62}$$

where $C^e_{ijkl}$ is the elastic tangential stiffness matrix and $D^{vp}_{ij}$ is the viscoplastic stretching tensor, which is related to the total stretching tensor as

$$D_{ij} = D^e_{ij} + D^{vp}_{ij} \tag{5.63}$$

where $D^e_{ij}$ is the elastic stretching tensor defined as

$$D^e_{ij} = \frac{1}{2G}\dot{S}_{ij} + \frac{\kappa}{3(1+e)}\frac{\dot{T}'_m}{T'_m}\delta_{ij} \tag{5.64}$$

in which $\dot{S}_{ij}$ is the deviatoric stress tensor rate ( $\dot{S}_{ij} = \dot{T}'_{ij} - \dot{T}'_m \delta_{ij}$ ). Viscoplastic stretching tensor $D^{vp}_{ij}$ is given by

$$D^{vp}_{ij} = C_{ijkl}\left\langle \Phi\left(f_y\right)\right\rangle \frac{\partial f_p}{\partial T'_{kl}} \tag{5.65}$$

where $\langle\ \rangle$ are Macaulay's brackets; $\left\langle \Phi\left(f_y\right)\right\rangle = \Phi\left(f_y\right)$, if $f_y > 0$ and $\left\langle \Phi\left(f_y\right)\right\rangle = 0$, if $f_y \le 0$.

The tangent stiffness method (Pierce et al. 1984) is implemented here to determine the viscoplastic stretching tensor. Hence, Equation (5.62) can be rewritten in matrix form as

$$\{\hat{T}'\} = [C]\{D\} - \{Q\} \tag{5.66}$$

where $[C]$ is the tangential stiffness matrix and $\{Q\}$ is the relaxation stress vector.

The substitution of Equation (5.61) into Equation (5.66) gives

$$\{\dot{T}'\} = [C]\{D\} - \{Q\} + \{W'\} \tag{5.67}$$

in which $\{W'\}$ is the vector defined as $\{W'\} = W_{ik}T'_{kj} - T'_{ik}W_{kj}$.

Therefore, the Equation (5.54) can be written as

$$\begin{aligned} &[M]\{a_N\} + (\Delta t)([K] + [K_L])\{v_N\} + (\Delta t)[K_v]\{\dot{p}_N\} \\ &= \{F\} - \{S^*\}_t - (\Delta t)\{T_W\} + (\Delta t)\{T_Q\} \end{aligned} \tag{5.68}$$

where

$$[M] = \rho \int_V [N]^T [N] dV \tag{5.69}$$

$$[K] = \int_V [B]^T [C][B] dV \tag{5.70}$$

$$[K_L] = \int_V [N_L]^T [D_S][N_L] dV + \int_V [N_L]^T [U][N_L] dV + \int_V [N_L]^T \{T'\}\{B_v\}^T dV \tag{5.71}$$

$$[K_v] = \int_V \{B_v\}\{N_h\}^T dV \tag{5.72}$$

$$\{T_W\} = \int_V [B]^T \{W'\} dV \tag{5.73}$$

$$\{T_Q\} = \int_V [B]^T \{Q\} dV \tag{5.74}$$

$$\{F\} = \int_\Gamma [N]^T \{{}_0\bar{t}\} d\Gamma + \rho \int_V [N]^T \{b\} dV \tag{5.75}$$

$$\{S^*\}_t = \int_V [N_L]^T \{T\} dV \tag{5.76}$$

The Rayleigh damping $[R]$, which is proportional to nodal velocity vector, is applied in the formulation. The Rayleigh damping can be described by the linear combination of mass matrix $[M]$ and stiffness matrix $[K]$ as

$$[R] = \alpha_0 [M] + \alpha_1 [K] \tag{5.77}$$

in which $\alpha_0$ and $\alpha_1$ are the constant values. Using the Rayleigh damping $[R]$, the discretized equations of motion are obtained as

$$\begin{aligned} [M]\{a_N\} + \{\Delta t([K]+[K_L]) + [R]\}\{v_N\} + (\Delta t)[K_v]\{\dot{p}_N\} \\ = \{F\} - \{S^*\}_t - (\Delta t)\{T_W\} + (\Delta t)\{T_Q\} \end{aligned} \tag{5.78}$$

### 5.2.6. Discretization of the Continuity Equations

Using the relation $\partial a_i / \partial x_i = \dot{D}_{ii}$ in the continuity equation for pore fluid leads to

$$\rho^F \dot{D}_{ii} - p_{,ii} - \frac{\gamma_w}{k} D_{ii} = 0 \tag{5.79}$$

By multiplying Equation (5.79) by a Galerkin weighted function as $\bar{W} = \{N_h\}$, a weak for of the continuity equation is obtained as

$$\int_V \rho^F \dot{D}_{ii} \bar{W}\, dV - \int_V p_{,ii} \bar{W}\, dV - \frac{\gamma_w}{k} \int_V D_{ii} \bar{W}\, dV = 0 \tag{5.80}$$

Using Gauss's divergence theorem, we have

$$\int_V p_{,ii} \bar{W}\, dV = \int_\Gamma p_{,i} \bar{W}\, n_i d\Gamma - \int_V p_{,i} \bar{W}_{,i} dV \tag{5.81}$$

Hence, Equation (5.80) in the matrix form becomes

$$\rho^F \int_V \bar{W}^T \dot{D}_{ii} dV + \int_V \{\bar{W}_{,i}\}^T \{p_{,i}\} dV - \frac{\gamma_w}{k} \int_V \bar{W}^T D_{ii} dV = \int_{\Gamma_3+\Gamma_4} \bar{W}^T \{n\}^T \{p_{,i}\} d\Gamma \tag{5.82}$$

Herein, the right-hand side of Equation (5.82) becomes zero in the case of either impermeable or drained boundary conditions. Definitions include the following:

$$p = \{N_h\}^T \{p_N\} \tag{5.83}$$

$$\{p_{,i}\} = \left[N_{h,i}\right]\{p_N\} \tag{5.84}$$

$$D_{ii} = \{B_v\}^T \{v_N\} \tag{5.85}$$

$$\dot{D}_{ii} = \{B_v\}^T \{a_N\} \tag{5.86}$$

Finally, the discretized form of the continuity equation for pore fluid is given by

$$\rho^F [K_v]^T \{a_N\} - \left(\frac{\gamma_w}{k}\right)[K_v]^T \{v_N\} + [K_h]\{p_N\} = 0 \tag{5.87}$$

in which

$$[K_v]^T = \int_V \{N_h\}\{B_v\}^T \, dV \tag{5.88}$$

$$[K_h] = \int_V \left[N_{h,i}\right]^T \left[N_{h,i}\right] dV \tag{5.89}$$

### 5.2.7. Time Discretization of the Governing Equations by Newmark's $\beta$ Method

Using Newmark's $\beta$ method, the displacement and the velocity of the soil skeleton can be approximated as

$$\{u_N\}_{t+\Delta t} = \{u_N\}_t + (\Delta t)\{v_N\}_t + \frac{(\Delta t)^2}{2}\{a_N\}_t + \overline{\beta}(\Delta t)^2\left(\{a_N\}_{t+\Delta t} - \{a_N\}_t\right) \tag{5.90}$$

$$\{v_N\}_{t+\Delta t} = \{v_N\}_t + (\Delta t)\{a_N\}_t + \overline{\gamma}\,\Delta t\left(\{a_N\}_{t+\Delta t} - \{a_N\}_t\right) \tag{5.91}$$

where $\Delta t$ is the time increment and $\overline{\beta}$ and $\overline{\gamma}$ are the Newmark's parameters.

For the rate of pore pressure, a backward finite difference method is used as

$$\{\dot{p}_N\}_{t+\Delta t} = \frac{\{p_N\}_{t+\Delta t} - \{p_N\}_t}{\Delta t} \tag{5.92}$$

Considering the equations of motion and continuity at time $t+\Delta t$, and applying Equations (5.90) and (5.91) to Equations (5.79) and (5.87), the discretized governing equations are

$$\left[\begin{array}{c|c} \dfrac{[M]_{t+\Delta t}+\overline{\gamma}(\Delta t)\left\{\Delta t\left([K]_{t+\Delta t}+[K_L]_{t+\Delta t}\right)+[R]_{t+\Delta t}\right\}}{\gamma_w\left\{\dfrac{1}{g}-\dfrac{\overline{\gamma}\,\Delta t}{k}\right\}[K_v]^T{}_{t+\Delta t}} & \dfrac{[K_v]_{t+\Delta t}}{[K_h]_{t+\Delta t}} \end{array}\right] \left\{\begin{array}{c} \{a_N\}_{t+\Delta t} \\ \{p_N\}_{t+\Delta t} \end{array}\right\}$$

$$= \left\{\begin{array}{l} \{F\}_{t+\Delta t}-\{S^*\}_t-\left\{\Delta t\left([K]_{t+\Delta t}+[K_L]_{t+\Delta t}\right)+[R]_{t+\Delta t}\right\}\left\{\Delta t(1-\overline{\gamma})\{a_N\}_t+\{v_N\}_t\right\} \\ +[K_v]_{t+\Delta t}\{p_N\}_t-(\Delta t)\{T_W\}_t+(\Delta t)\{T_Q\}_t \\ \hline \left(\dfrac{\gamma_w}{k}\right)[K_v]^T{}_{t+\Delta t}\left\{\Delta t(1-\overline{\gamma})\{a_N\}_t+\{v_N\}_t\right\} \end{array}\right\} \tag{5.93}$$

where the acceleration vector and the pore water pressure at the nodal points are unknown variables.

### 5.2.8. Tangent Stiffness Method

In this section, the nonlinear relation between the Jaumann rate of Cauchy's stress and the stretching tensor for elasto-viscoplastic materials is derived using the tangent stiffness method proposed by Pierce et al. (1984). The tangent stiffness method was developed for rate dependent materials based on a one-step forward gradient time integration scheme. This method results in more stability and accuracy for step sizes much larger than that can be employed with the Euler method. A parameter, termed $\theta$, has been introduced in this method, which can range from 0 to 1, with $\theta = 0$ corresponding to a simple Euler time integration scheme. Through the numerical examples on materials ranging from elastic-nonlinearly viscous behavior to nearly rate independent behavior, Pierce et al. (1984) found that the method is stable and accurate for the values of $\theta$ between 0.5 and 1.0.

As shown earlier, the total stretching tensor is divided to the elastic stretching tensor $D_{ij}^e$ and the viscoplastic stretching tensor $D_{ij}^{vp}$, in which the viscoplastic stretching tensor is given by

$$D_{ij}^{vp} = C_{ijkl}\left\langle \Phi\left(f_y\right)\right\rangle \frac{\partial f_p}{\partial T'_{kl}} \tag{5.94}$$

Material function $\Phi\left(f_y\right)$ is assumed to dependent on the effective Cauchy stress tensor $T'_{ij}$, and the kinematic hardening parameters $y^*_{m1}$ and $\chi^*_{ij}$. Therefore, the time derivative of material function is written as

$$\dot{\Phi}\left(f_y\right)=\frac{\partial\Phi}{\partial T'_{ij}}\dot{T}'_{ij}+\frac{\partial\Phi}{\partial y^*_{m1}}\dot{y}^*_{m1}+\frac{\partial\Phi}{\partial\chi^*_{ij}}\dot{\chi}^*_{ij} \tag{5.95}$$

The rate of effective Cauchy stress is related to the Jaumann rate of Cauchy stress as

$$\hat{T}'_{ij}=\dot{T}'_{ij}+T'_{ik}W_{kj}-W_{ik}T'_{kj} \tag{5.96}$$

where $W_{ij}$ is the spin vector.

Using two arbitrary scalars, $A$ and $B$, and a symmetric tensor $U_{ij}$, we can write

$$\begin{aligned}\frac{\partial\Phi}{\partial T'_{ij}}\hat{T}_{ij}&=\frac{\partial\Phi}{\partial T'_{ij}}\left(\dot{T}'_{ij}+T'_{ik}W_{kj}-W_{ik}T'_{kj}\right)\\&=\frac{\partial\Phi}{\partial T'_{ij}}\dot{T}'_{ij}+\frac{\partial\Phi}{\partial T'_{ij}}\left(T'_{ik}W_{kj}-W_{ik}T'_{kj}\right)\\&=\frac{\partial\Phi}{\partial T'_{ij}}\dot{T}'_{ij}+\left(AU_{ij}+B\delta_{ij}\right)\left(T'_{ik}W_{kj}-W_{ik}T'_{kj}\right)\end{aligned} \tag{5.97}$$

in which, $AU_{ij}\left(-W_{ik}T'_{kj}+T'_{ik}W_{kj}\right)=0$ and $B\delta_{ij}\left(-W_{ik}T'_{kj}+T'_{ik}W_{kj}\right)=0$, therefore

$$\frac{\partial\Phi}{\partial T'_{ij}}\hat{T}_{ij}=\frac{\partial\Phi}{\partial T'_{ij}}\dot{T}'_{ij} \tag{5.98}$$

Finally, by substituting Equation (5.98) into Equation (5.95), we have

$$\dot{\Phi}\left(f_y\right)=\frac{\partial\Phi}{\partial T'_{ij}}\hat{T}'_{ij}+\frac{\partial\Phi}{\partial y^*_{m1}}\dot{y}^*_{m1}+\frac{\partial\Phi}{\partial\chi^*_{ij}}\dot{\chi}^*_{ij} \tag{5.99}$$

Using the tangent stiffness parameter $\theta$ yields

$$\Phi=\left(1-\theta\right)\Phi_t+\theta\,\Phi_{t+\Delta t} \tag{5.100}$$

in which

$$\Phi_{t+\Delta t} = \Phi_t + \Delta\Phi = \Phi_t + \Delta t\ \dot{\Phi}_t \tag{5.101}$$

Applying Equations (5.99), (5.100), and (5.101), we obtain

$$\Phi = (1-\theta)\Phi_t + \theta\ \left\{ \Phi_t + \frac{\partial \Phi}{\partial T'_{ij}} \hat{T}'_{ij}\ \Delta t + \frac{\partial \Phi}{\partial y^*_{m1}} \dot{y}^*_{m1}\ \Delta t + \frac{\partial \Phi}{\partial \chi^*_{ij}} \dot{\chi}^*_{ij}\ \Delta t \right\} \tag{5.102}$$

The constitutive equation is described using the Jaumann rate of Cauchy stress tensor $\hat{T}'_{ij}$ and stretching tensor $D_{ij}$ as

$$\begin{aligned} \hat{T}'_{ij} &= C^e_{ijkl}\left(D_{kl} - D^{vp}_{kl}\right) \\ &= C^e_{ijkl}\left(D_{kl} - C_{klmn}\Phi \frac{\partial f_p}{\partial T'_{mn}}\right) \end{aligned} \tag{5.103}$$

And, the kinematic hardening parameters, $y^*_{m1}$ and $\chi^*_{ij}$, are given by

$$\dot{y}^*_{m1} = B^*_2\left(A^*_2 D^{vp}_{kk} - y^*_{m1}\left|D^{vp}_{kk}\right|\right) \tag{5.104}$$

$$\dot{\chi}^*_{ij} = B^*\left\{A^* D'^{vp}_{ij} - \chi^*_{ij}\left(D'^{vp}_{mn} D'^{vp}_{mn}\right)^{\frac{1}{2}}\right\} \tag{5.105}$$

where $D'^{vp}_{ij}$ is the viscoplastic deviatoric stretching tensor, and $D^{vp}_{kk}$ is the viscoplastic volumetric stretching tensor. According to the cyclic elasto-viscoplastic constitutive equations and if we assume $C_{ijkl}$ is a fourth order isotropic tensor, the viscoplastic volumetric and deviatoric stretching tensor are obtained as

$$D^{vp}_{kk} = C_{kkij}\Phi \frac{\partial f_p}{\partial T'_{ij}} \tag{5.106}$$

$$D'^{vp}_{ij} = D^{vp}_{ij} - \frac{1}{3} D^{vp}_{kk}\delta_{ij} = C_{ijkl}\Phi \frac{\partial f_p}{\partial S_{kl}} \tag{5.107}$$

Substituting the above equations into Equation (5.102) results in

$$\Phi = (1-\theta)\Phi_t + \theta \left\{ \Phi_t + \frac{\partial \Phi}{\partial T'_{ij}} C^e_{ijkl} \left( D_{kl} - D^{vp}_{kl} \right) \Delta t + \frac{\partial \Phi}{\partial y^*_{m1}} B^*_2 \left( A^*_2 D^{vp}_{kk} - y^*_{m1} \left| D^{vp}_{kk} \right| \right) \Delta t + \frac{\partial \Phi}{\partial \chi^*_{ij}} B^* \left\{ A^* D'^{vp}_{ij} - \chi^*_{ij} \left( D'^{vp}_{mn} D'^{vp}_{mn} \right)^{\frac{1}{2}} \right\} \Delta t \right\} \tag{5.108}$$

$$\Phi = \Phi_t + \theta \ \frac{\partial \Phi}{\partial T'_{ij}} C^e_{ijkl} D_{kl} \Delta t - \theta \ \Delta t \Phi \frac{\partial \Phi}{\partial T'_{ij}} C^e_{ijkl} C_{klmn} \frac{\partial f_p}{\partial T'_{mn}} + \theta \ \Delta t \Phi \frac{\partial \Phi}{\partial y^*_{m1}} B^*_2 \left( A^*_2 C_{kkij} \frac{\partial f_p}{\partial T'_{ij}} - y^*_{m1} \left| C_{kkij} \frac{\partial f_p}{\partial T'_{ij}} \right| \right) + \theta \ \Delta t \Phi \frac{\partial \Phi}{\partial \chi^*_{ij}} B^* \left\{ A^* C_{ijkl} \frac{\partial f_p}{\partial S_{kl}} - \chi^*_{ij} \left( C_{mnpq} \frac{\partial f_p}{\partial S_{pq}} C_{mnrs} \frac{\partial f_p}{\partial S_{rs}} \right)^{\frac{1}{2}} \right\} \tag{5.109}$$

and finally

$$\Phi = \frac{1}{1+\xi'} \left\{ \Phi_t + \left( \theta \ \Delta t \right) \frac{\partial \Phi}{\partial T'_{ij}} C^e_{ijkl} D_{kl} \right\} \tag{5.110}$$

in which,

$$\xi' = \left( \theta \ \Delta t \right) \left\{ \frac{\partial \Phi}{\partial T'_{ij}} C^e_{ijkl} C_{klmn} \frac{\partial f_p}{\partial T'_{mn}} - \frac{\partial \Phi}{\partial y^*_{m1}} B^*_2 \left( A^*_2 C_{kkij} \frac{\partial f_p}{\partial T'_{ij}} - y^*_{m1} \left| C_{kkij} \frac{\partial f_p}{\partial T'_{ij}} \right| \right) - \frac{\partial \Phi}{\partial \chi^*_{ij}} B^* \left( A^* C_{ijkl} \frac{\partial f_p}{\partial S_{kl}} - \chi^*_{ij} \left( C_{mnpq} \frac{\partial f_p}{\partial S_{pq}} C_{mnrs} \frac{\partial f_p}{\partial S_{rs}} \right)^{\frac{1}{2}} \right) \right\} \tag{5.111}$$

Thus, substituting Equation (5.111) into Equation (5.94) results in

$$D^{vp}_{ij} = C_{ijkl} \frac{1}{1+\xi'} \left\{ \Phi_t + \left( \theta \ \Delta t \right) \frac{\partial \Phi}{\partial T'_{pq}} C^e_{pqrs} D_{rs} \right\} \frac{\partial f_p}{\partial T'_{kl}} \tag{5.112}$$

Combining Equations (5.103) and (5.112), we obtain

$$\begin{aligned} \hat{T}'_{ij} &= C^e_{ijkl} \left( D_{kl} - C_{klmn} \frac{1}{1+\xi'} \left\{ \Phi_t + \left( \theta \ \Delta t \right) \frac{\partial \Phi}{\partial T'_{pq}} C^e_{pqrs} D_{rs} \right\} \frac{\partial f_p}{\partial T'_{mn}} \right) \\ &= \left[ C^e_{ijkl} - C^e_{ijrs} C_{rsmn} \frac{\partial f_p}{\partial T'_{mn}} \frac{1}{1+\xi'} \left( \theta \ \Delta t \right) \frac{\partial \Phi}{\partial T'_{pq}} C^e_{pqkl} \right] D_{kl} - C^e_{ijkl} C_{klmn} \frac{\partial f_p}{\partial T'_{mn}} \frac{1}{1+\xi'} \Phi_t \end{aligned} \tag{5.113}$$

Thereby, tangential stiffness matrix $C_{ijkl}^{\tan}$ and relaxation stress $Q_{ij}$ are defined as

$$C_{ijkl}^{\tan} = C_{ijkl}^{e} - C_{ijrs}^{e} C_{rsmn} \frac{\partial f_p}{\partial T'_{mn}} \frac{1}{1+\xi'} \left(\theta\ \Delta t\right) \frac{\partial \Phi}{\partial T'_{pq}} C_{pqkl}^{e} \tag{5.114}$$

$$Q_{ij} = C_{ijkl}^{e} C_{klmn} \frac{\partial f_p}{\partial T'_{mn}} \frac{1}{1+\xi'} \Phi_t \tag{5.115}$$

Then, the Equation (5.113) can be rewritten as

$$\hat{T}'_{ij} = C_{ijkl}^{\tan} D_{kl} - Q_{ij} \tag{5.116}$$

#### 5.2.8.1. Differential Components

The differential components of material function derivation are calculated according to the material function definition and chain rule. As explained earlier, material function is determined as

$$\Phi\left(f_y\right) = \sigma'_m \exp\left\{m'\left(f_y\right)\right\} \tag{5.117}$$

$$\Phi\left(f_y\right) = \sigma'_m \exp\left\{m'\left(\overline{\eta}_{\chi}^{*} + \tilde{M}^{*}\left(\ln\frac{\sigma'_{mk}}{\sigma'_{ma}} + \left|\ln\frac{\sigma'_m}{\sigma'_{mk}} - y_{m1}^{*}\right|\right)\right)\right\} \tag{5.118}$$

Hence,

$$\frac{\partial \Phi}{\partial \sigma'_{ij}} = \frac{\partial \Phi}{\partial \sigma'_m}\frac{\partial \sigma'_m}{\partial \sigma'_{ij}} + \frac{\partial \Phi}{\partial f_y}\frac{\partial f_y}{\partial \sigma'_{ij}} \tag{5.119}$$

$$\frac{\partial \Phi}{\partial y_{m1}^{*}} = \frac{\partial \Phi}{\partial f_y}\frac{\partial f_y}{\partial y_{m1}^{*}} \tag{5.120}$$

$$\frac{\partial \Phi}{\partial \chi_{ij}^{*}} = \frac{\partial \Phi}{\partial f_y}\frac{\partial f_y}{\partial \chi_{ij}^{*}} \tag{5.121}$$

where

$$\frac{\partial \Phi}{\partial \sigma'_m} = \exp\left\{m'\left(f_y\right)\right\} + m'\sigma'_m \exp\left\{m'\left(f_y\right)\right\}\frac{\partial f_y}{\partial \sigma'_m} \tag{5.122}$$

$$\frac{\partial \sigma'_m}{\partial \sigma'_{ij}} = \frac{1}{3}\delta_{ij} \tag{5.123}$$

$$\frac{\partial \Phi}{\partial f_y} = m' \sigma'_m \exp\left\{ m'\left( f_y \right) \right\} \tag{5.124}$$

$$\frac{\partial f_y}{\partial \sigma'_{ij}} = \frac{\partial f_y}{\partial \sigma'_m}\frac{\partial \sigma'_m}{\partial \sigma'_{ij}} + \frac{\partial f_y}{\partial S_{kl}}\frac{\partial S_{kl}}{\partial \sigma'_{ij}} \tag{5.125}$$

$$\frac{\partial f_y}{\partial y^*_{m1}} = -\tilde{M}^* \frac{\ln \dfrac{\sigma'_m}{\sigma'_{mk}} - y^*_{m1}}{\left| \ln \dfrac{\sigma'_m}{\sigma'_{mk}} - y^*_{m1} \right|} \tag{5.126}$$

$$\frac{\partial f_y}{\partial \chi^*_{ij}} = -\frac{\eta^*_{ij} - \chi^*_{ij}}{\bar{\eta}^*_{\chi}} \tag{5.127}$$

Considering $\dfrac{\partial \eta^*_{ij}}{\partial S_{kl}} = \dfrac{1}{\sigma'_m}\delta_{ik}\delta_{jl}$ and $\dfrac{\partial \eta^*_{ij}}{\partial \sigma'_m} = -\dfrac{S_{ij}}{\left(\sigma'_m\right)^2}$, the components of Equation (5.125) are given by

$$\frac{\partial f_y}{\partial \sigma'_m} = \frac{\eta^*_{ij} - \chi^*_{ij}}{\bar{\eta}^*_{\chi}}\left\{ -\frac{S_{mn}}{\left(\sigma'_m\right)^2} \right\} + \frac{\tilde{M}^*}{\sigma'_m}\left( \frac{\ln \dfrac{\sigma'_m}{\sigma'_{mk}} - y^*_{m1}}{\left| \ln \dfrac{\sigma'_m}{\sigma'_{mk}} - y^*_{m1} \right|} \right) = \frac{1}{\sigma'_m}\left\{ \tilde{M}^* \frac{\ln \dfrac{\sigma'_m}{\sigma'_{mk}} - y^*_{m1}}{\left| \ln \dfrac{\sigma'_m}{\sigma'_{mk}} - y^*_{m1} \right|} - \frac{\eta^*_{st}\left( \eta^*_{st} - \chi^*_{st} \right)}{\bar{\eta}^*_{\chi}} \right\} \tag{5.128}$$

$$\frac{\partial f_y}{\partial S_{ij}} = \frac{1}{\sigma'_m}\frac{\eta^*_{ij} - \chi^*_{ij}}{\bar{\eta}^*_{\chi}} \tag{5.129}$$

$$\frac{\partial S_{kl}}{\partial \sigma'_{ij}} = \frac{\partial\left( \sigma'_{kl} - \sigma'_m \delta_{kl} \right)}{\partial \sigma'_{ij}} = \delta_{ki}\delta_{lj} - \frac{1}{3}\delta_{ij}\delta_{kl} \tag{5.130}$$

Substituting Equation (5.123) and Equations (5.128) to (5.130) into Equation (5.125)

$$\frac{\partial f_y}{\partial \sigma'_{ij}} = \frac{\delta_{ij}}{3\sigma'_m}\left\{ \tilde{M}^* \frac{\ln \dfrac{\sigma'_m}{\sigma'_{mk}} - y^*_{m1}}{\left| \ln \dfrac{\sigma'_m}{\sigma'_{mk}} - y^*_{m1} \right|} - \frac{\eta^*_{st}\left( \eta^*_{st} - \chi^*_{st} \right)}{\bar{\eta}^*_{\chi}} \right\} + \frac{\delta_{ik}\delta_{jl} - \dfrac{1}{3}\delta_{ij}\delta_{kl}}{\sigma'_m}\frac{\eta^*_{kl} - \chi^*_{kl}}{\bar{\eta}^*_{\chi}} \tag{5.131}$$

in which the second term of right-hand side equation can be rewritten as

$$\frac{\delta_{ik}\delta_{jl}-\frac{1}{3}\delta_{ij}\delta_{kl}}{\sigma'_m}\frac{\eta^*_{kl}-\chi^*_{kl}}{\overline{\eta}^*_\chi}=\frac{1}{\sigma'_m}\frac{\eta^*_{ij}-\chi^*_{ij}+\frac{\delta_{ij}\left(\chi^*_{pp}-\eta^*_{pp}\right)}{3}}{\overline{\eta}^*_\chi} \tag{5.132}$$

Since $\eta^*_{kk}=\frac{S_{kk}}{\sigma'_m}=0$ and from the definition of the kinematic hardening parameter, we have

$$\dot{\chi}^*_{ij}=B^*\left\{A^*D'^{vp}_{ij}-\chi^*_{ij}\left(D'^{vp}_{mn}D'^{vp}_{mn}\right)^{\frac{1}{2}}\right\} \tag{5.133}$$

Considering $D'^{vp}_{kk}=0$

$$\dot{\chi}^*_{pp}=-B^*\chi^*_{pp}\left(D'^{vp}_{mn}D'^{vp}_{mn}\right)^{\frac{1}{2}} \tag{5.134}$$

When $\chi^*_{pp}=0$ at initial state, $\chi^*_{pp}$ is constantly zero. Therefore, Equation (5.131) becomes

$$\frac{\partial f_y}{\partial\sigma'_{ij}}=\frac{\delta_{ij}}{3\sigma'_m}\left\{\tilde{M}^*\frac{\ln\frac{\sigma'_m}{\sigma'_{mk}}-y^*_{m1}}{\left|\ln\frac{\sigma'_m}{\sigma'_{mk}}-y^*_{m1}\right|}-\frac{\eta^*_{st}\left(\eta^*_{st}-\chi^*_{st}\right)}{\overline{\eta}^*_\chi}\right\}+\frac{1}{\sigma'_m}\frac{\eta^*_{ij}-\chi^*_{ij}}{\overline{\eta}^*_\chi} \tag{5.135}$$

Since the static yield function $f_y$ and the viscoplastic potential function $f_p$ have the same shape, we have

$$\frac{\partial f_y}{\partial\sigma'_{ij}}=\frac{\partial f_p}{\partial\sigma'_{ij}} \tag{5.136}$$

$$\frac{\partial f_y}{\partial\sigma'_m}=\frac{\partial f_p}{\partial\sigma'_m} \tag{5.137}$$

$$\frac{\partial f_y}{\partial S_{ij}}=\frac{\partial f_p}{\partial S_{ij}} \tag{5.138}$$

## 5.3. Dynamic Strain Localization of Osaka Soft Clay

Strain localization or shear banding is a phenomenon in materials under shearing, in which plastic deformations localize into finite narrow bands of intense straining. The phenomenon is described as a precursor to fracture and, in general, as a characteristic feature of inelastic deformations. Strain localization is observed in a wide range of materials including single-phase solids and multiphase fluid-saturated materials such as soils. The analytical solution of strain localization has been previously conducted as material instability in rate-independent solids within a theoretical framework by Hadamard (1903), Rice (1976), and others. The instability and ensuing ill-posedness of initial and boundary value problems were found to preclude meaningful analyses in rate-independent materials. Under quasi-static loading conditions, the instability appears as an ellipticity loss in the rate equilibrium equations, while under dynamic loading conditions wave speeds become imaginary. In the numerical solutions, on the other hand, the instability exhibits inherent mesh dependence and spurious length scale effects (Needleman 1988, Loret and Prevost 1991).

In order to overcome this type of difficulty, various methods have been proposed which can be summarized into three approaches as described by Oka et al. (2002a). The first approach is the introduction of viscoplastic effects in the numerical analysis. The viscoplasticity can be expressed by either assuming a viscoplastic constitutive model for material behavior, or a viscoplasticity regularization procedure within the numerical analysis, which is applied for inviscid constitutive model (e.g., Cormeau 1975, Needleman 1989, and Prevost and Loret 1990). The second method is applying higher order strain gradients into the constitutive model (e.g., Aifantis 1984, Mühlhaus and Aifantis 1991, de Borst and Sluys 1991, Aifantis et al. 1999, and Hutchinson 2001). In localization of multiphase materials, shear band development is mostly affected by the interaction between solid and fluid, in terms of time sequence of band formation and the way of their appearance. Hence, the third method is to incorporate a Darcy type of soil-fluid interaction, which can alleviate the instability problem in multiphase materials by delaying the onset of material instability (e.g., Rice 1975, Loret and Prevost 1991, Oka et al. 1995, and Schrefler et al. 1996).

The consideration of rate dependency has been found to eliminate significantly the instability and subsequent influences in the analysis of strain localization problems under both quasi-static and dynamic loading conditions. When material rate dependence or viscosity is accounted for, there is no loss of ellipticity in the incremental equilibrium equations, wave speeds remain real, and consequently, the pathological mesh size effects do not occur (Needleman 1988). Furthermore, the inelastic response of geomaterials, such as clays, is inevitably rate dependent; therefore, the viscoplasticity can be effectively employed in the analysis, providing a satisfactory framework to capture localized shear banding.

From the numerical point of view, the strain localization of geomaterials has been widely studied under quasi-static and dynamic loading conditions. Under quasi-static deformations, Oka et al. (1994, 1995, 2000, 2002a, and 2005) have studied the shear band development of water-saturated clays by using an elasto-viscoplastic constitutive model. The Biot's type two-phase mixture theory was adopted in the formulation to reduce the material instability problems. It was found that the shear band development and the following strain localization could be effectively simulated through the finite element analysis using the elasto-viscoplastic model, for both normally consolidated and over consolidated water-saturated clays.

The aim of the present study is to extend the finite element analysis of shear banding in elasto-viscoplastic clays to the analysis under dynamic transient loading conditions. The development of shear bands is examined numerically in a three-dimensional geometry without resorting to the usual bifurcation or stability analysis. The cyclic elasto-viscoplastic model is adopted to simulate the behavior of clay under dynamic loading conditions. The compelled step acceleration is applied on the upper nodes of the domain providing axial displacements pertinent to dynamic loading conditions. The finite element simulations are conducted in plane strain conditions by constraining the deformations in a three-dimensional problem. The shear band development is studied through the distributions of the strain and the mean effective stress in the specimen at various steps of shearing.

### 5.3.1. Problem Description

The finite element mesh and the boundary conditions for the localization analysis of Torishima soft clay sample are shown in Figure 5.2. The simulation is performed using a three-dimensional mesh system under plane strain conditions, for which the constrained deformation conditions are assigned for Y direction. The size of the specimen is assumed as 10 m in width by 20 m in height. As mentioned earlier in Section 5.2.1, a 20-node hexahedron element with a reduced Gaussian integration is used for the finite element analysis, by which the appearance of a spurious hourglass mode and shear locking can be eliminated. The mesh pattern of 10×20 (200 elements) is considered as the default mesh configuration in the analysis. The displacement boundary conditions are adjusted so as the symmetric conditions can be provided. The constrained boundary conditions at the corners of the specimen are applied to trigger the localization at a fixed location. All the boundaries are assumed as impermeable, while the pore fluid is allowed to flow within the specimen. The vertical nodal acceleration is applied at the top nodes of the domain providing the vertical compelled displacement atop the specimen. The applied acceleration rises from zero to a maximum value of 3.5 gal within 0.1 sec, and remains constant afterward until 12.5 sec, as illustrated in Figure 5.2. The applied acceleration results in an overall axial strain of about 13.5% within 12.5 sec.

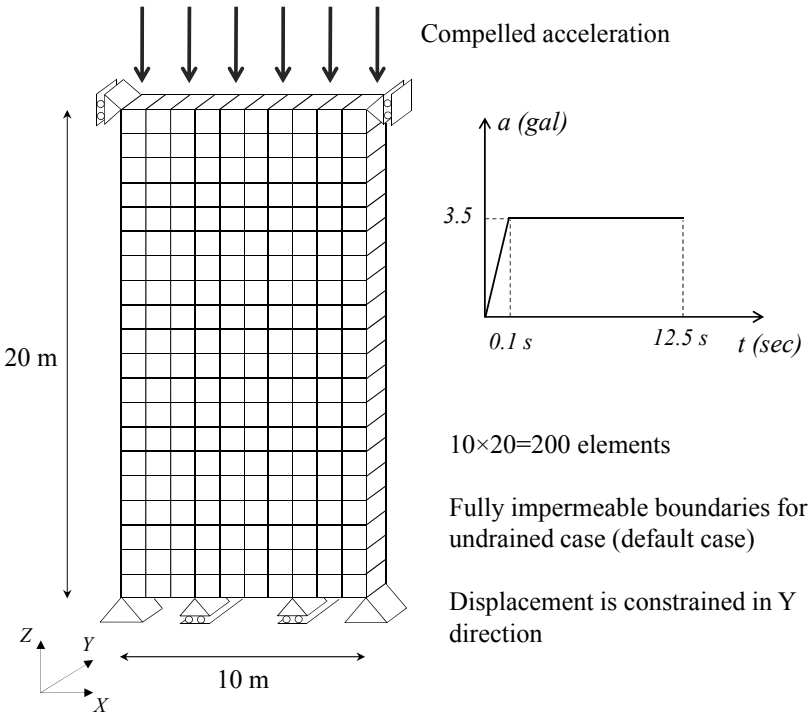


*Figure 5.2. Size of the specimen, boundary conditions, and applied acceleration profile.*

The material parameters of Torishima clay Ac2-U are used in the analysis, as listed in Table 5.1. The time increment is determined satisfying two criteria to achieve stable time steps. The first criterion is based on the stable time-step estimates (CFL condition) for explicit time-marching schemes, of which for a four-node square element with side lengths $h_1$ and $h_2$, the critical time-step estimate is obtained as

$$\Delta t \le \Delta t_{crit} = \frac{1}{c_{\max}} \min\left[h_1, h_2\right] \tag{5.139}$$

where $c_{\max}$ is the maximum wave speed. In the current study, having the 20-node hexahedron element with side lengths $l_1$, $l_2$, and $l_3$, and taking the longitudinal wave velocity $V_p$ as the maximum wave speed, the critical time step is given by

$$\Delta t \le \Delta t_{crit} = \frac{1}{V_p} \min\left[\frac{l_1}{2}, \frac{l_2}{2}, \frac{l_3}{2}\right]; \qquad V_p = \sqrt{\frac{E}{\rho}} \tag{5.140}$$

The latter criterion is from the stability of Newmark-$\beta$ method, by which the stable solution is accomplished,

$$\Delta t \ge \frac{2k}{g\left(2\overline{\gamma} - 1\right)} \tag{5.141}$$

Using both time increment constraints, the time step $\Delta t=0.001s$ is allocated for the analysis.

*Table 5.1. Material parameters of Torishima clay Ac2-U and other inputs for the analysis.*

| | | |
|---|---|---|
| Initial void ratio | $e_0$ | 1.250 |
| Coefficient of permeability | $k/\gamma_w$ | $5.87\times10^{-11}$ |
| Coefficient of earth pressure at rest | $K_0$ | 1.0 |
| Overconsolidation ratio | $OCR$ | 1.00 |
| Density *(t/m³)* | $\rho$ | 1.70 |
| Compression index | $\lambda$ | 0.341 |
| Swelling index | $\kappa$ | 0.019 |
| Initial elastic shear modulus *(kPa)* | $G_0$ | 15040 |
| Initial mean effective stress *(kPa)* | $\sigma'_{m0}$ | 200 |
| Stress ratio at compression | $M^*_{mc}$ | 1.24 |
| Viscoplastic parameter | $m'$ | 24.68 |
| Viscoplastic parameter *(1/s)* | $C_1$ | $1.00\times10^{-5}$ |
| Viscoplastic parameter *(1/s)* | $C_2$ | $3.83\times10^{-6}$ |
| Structural parameter *(kPa)* | $\sigma'_{maf}$ | 60 |
| Structural parameter | $\beta$ | 3.6 |
| Hardening parameter | $B^*_0$ | 100 |
| Hardening parameter | $B^*_1$ | 40 |
| Hardening parameter | $C_f$ | 10 |
| Reference value of plastic strain *(%)* | $\gamma^{vp*}_{(n)r}$ | 1.25 |
| Strain-dependent parameter | $\alpha$ | 10 |
| Scalar hardening parameter | $A^*_2$ | 5.9 |
| Scalar hardening parameter | $B^*_2$ | 1.8 |
| Newmark's parameter | $\overline{\beta}$ | 0.3025 |
| Newmark's parameter | $\overline{\gamma}$ | 0.6 |
| Rayleigh damping parameter | $\alpha_0$ | 0.0 |
| Rayleigh damping parameter | $\alpha_1$ | 0.01 |

## 5.3.2. Numerical Results and Discussion

### 5.3.2.1. Shear Banding Progress

The shear band development is studied through the evaluation of the results for the axial strain, the accumulated viscoplastic shear strain, the viscoplastic volumetric strain, and the mean effective stress, as well as the deformed mesh. The axial strain contours at various levels of the overall axial strain are shown in Figure 5.3, in addition to the accumulated viscoplastic shear strain and the viscoplastic volumetric strain contours. The strain localization emerges from the trigger points at the corner of the specimen, which eventually narrows to four distinct diagonal bands by increasing the compelled displacement. The shear bands occur at an angle of about 45°. This pattern is also observed in the

distribution of the accumulated viscoplastic shear strain and the viscoplastic volumetric strain. The deformed meshes at several strain levels are depicted in Figure 5.4, in which the deformation is clearly observed at the end of loading as the bulking in the specimen. The distributions of the mean effective stress and the pore water pressure are displayed in Figure 5.5 at various levels of overall strain. The mean effective stresses reduce along the shear bands by progress of the axial displacement, while the pore water pressure appears to increase along the shear bands.

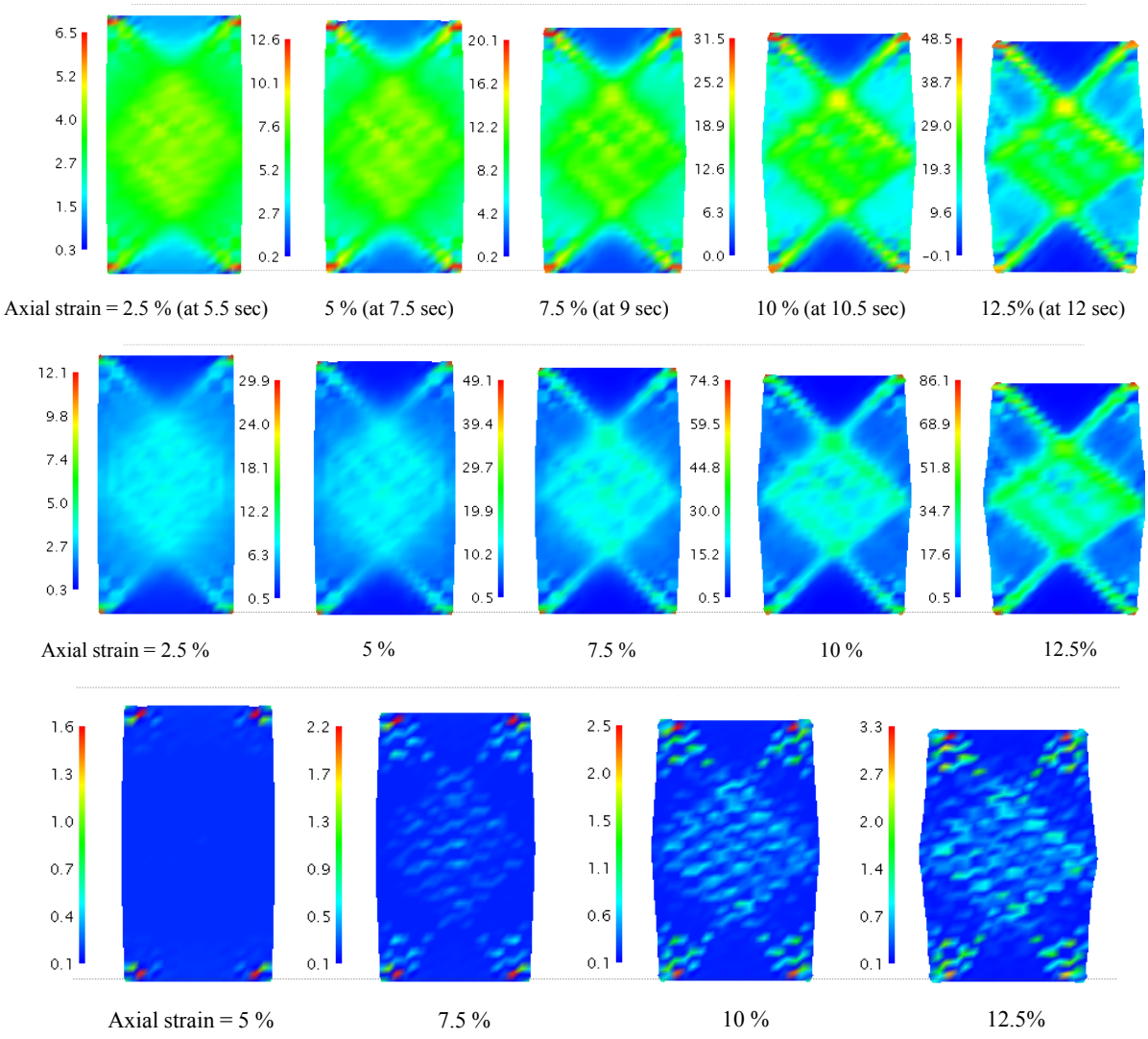


*Figure 5.3. Distributions of axial strain (above), accumulated viscoplastic shear strain (center), and viscoplastic volumetric strain (below), (legend unit: %).*

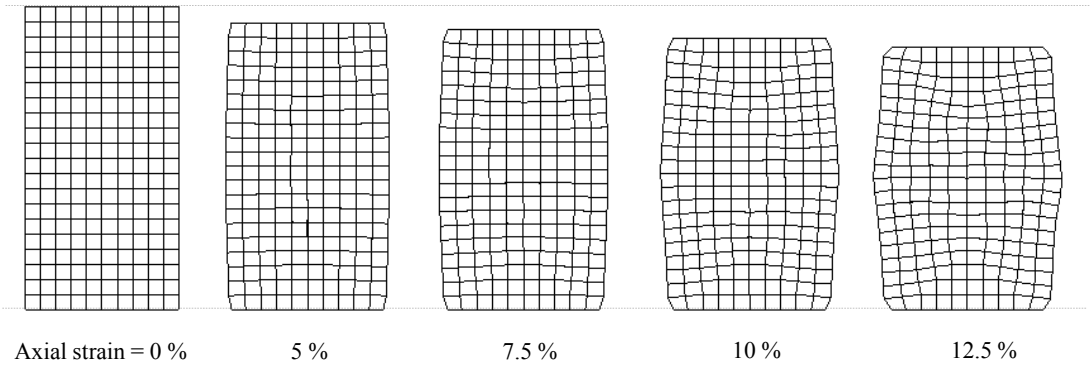


*Figure 5.4. Deformed meshes of the specimen at various strain levels.*

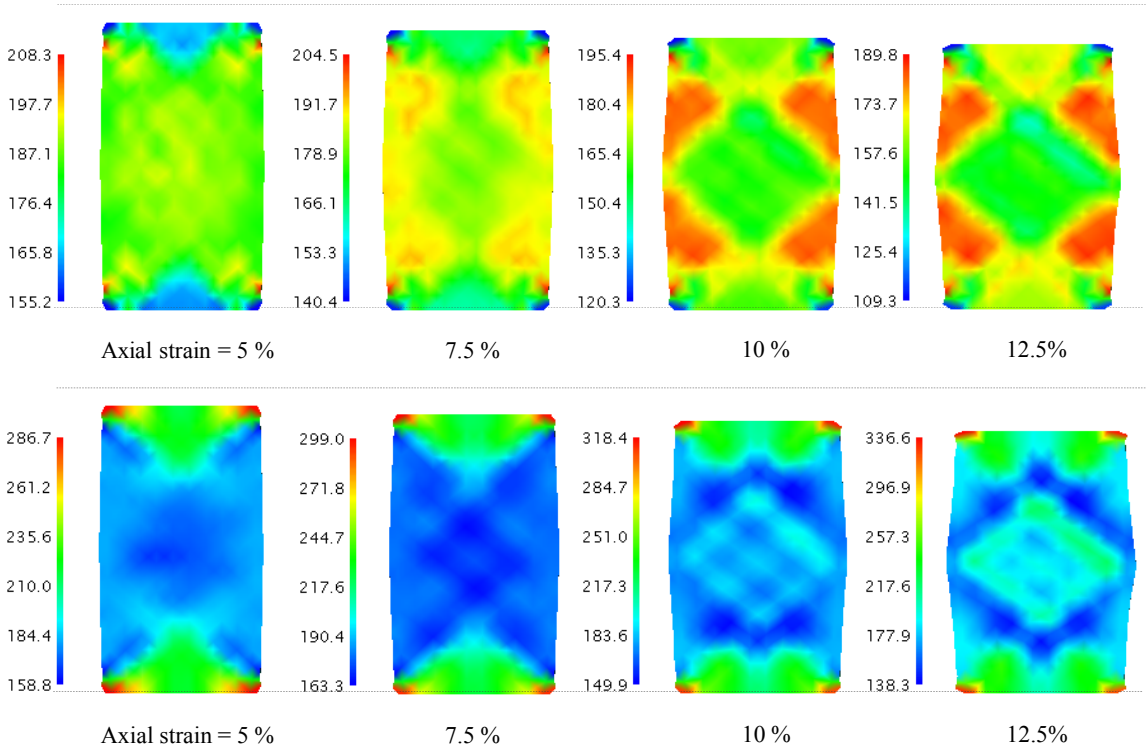


*Figure 5.5. Distributions of the mean effective stress (above), and the pore water pressure (below) at various strain levels, (legend unit: kPa).*

### 5.3.2.2. Effect of Drainage Boundary

The effect of the drainage boundaries is studied by considering a partially drained case for which the drainage boundaries are set at the top and bottom of the specimen. Figure 5.6 shows the accumulated viscoplastic shear strain contours for the partially drained case, which is compared with the undrained case results at several levels of the axial strain. Due to the rapid rate of applied loading and low permeability of the Torishima clay, the effect of drainage boundary on the strain localization appears

to be insignificant, although in the partially drained case, large viscoplastic strains are concentrated near the drainage boundary.

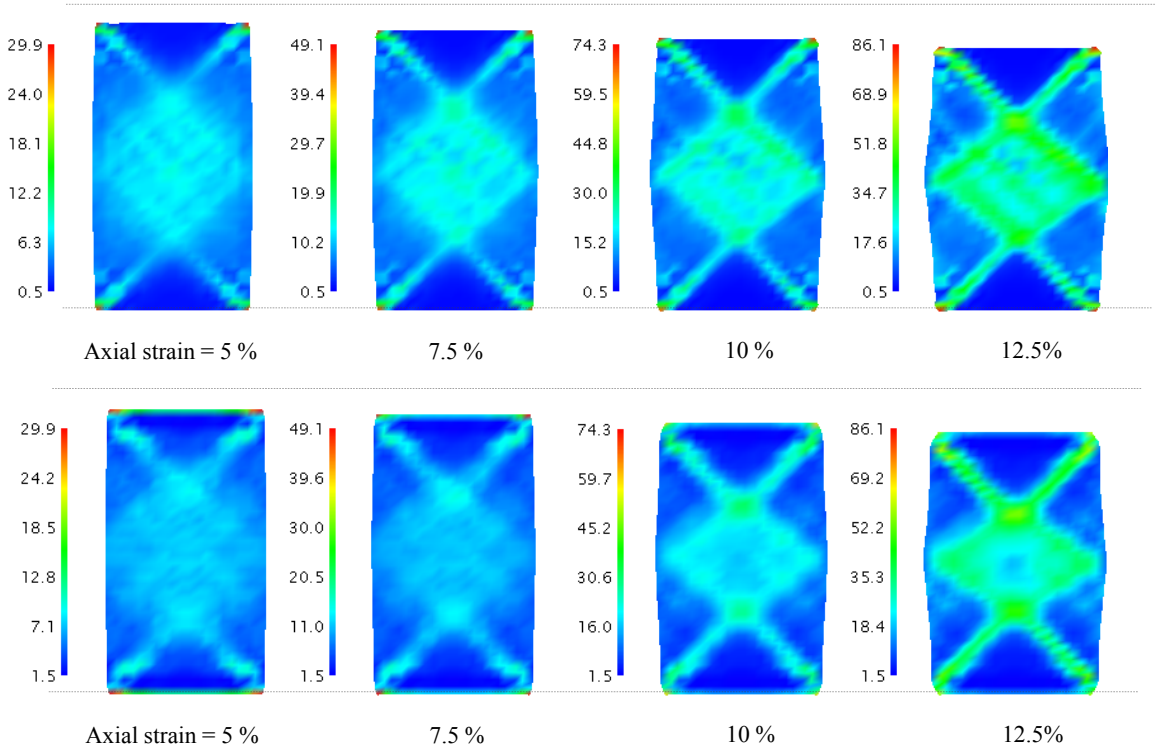


*Figure 5.6. Distributions of accumulated viscoplastic shear strain for the undrained case (above), and the partially drained case (below), (legend unit: %).*

### 5.3.2.3. Mesh-Size Dependency

In order to evaluate the mesh-size sensitivity of the numerical results, three extra square mesh patterns are considered besides the defaults mesh pattern for the localization analyses. The pattern of 5×10 (50 elements) is considered as the coarser mesh, and 20×40 (800 elements) and 25×50 (1250 elements) are assumed as the finer meshes, as illustrated in Figure 5.7. The deformed mesh and the distribution of the accumulated viscoplastic shear strain for these four cases are depicted in Figure 5.8 at the end of loading. Taking the finer mesh size leads to a higher level of strain localization, and narrows the width of the shear band since the shear bands span across the smaller elements. In the finer meshes, i.e., 800 elements and 1250 elements patterns, the shear banding is observed in the same shape and angle as for 200 elements pattern, emanating from the corners of the specimen and finally localizing into four diagonal bands. In the case with 50 elements, however, the strain is localized into a wider band across the specimen, of which a high level of localized strain is observed in the center of the specimen.

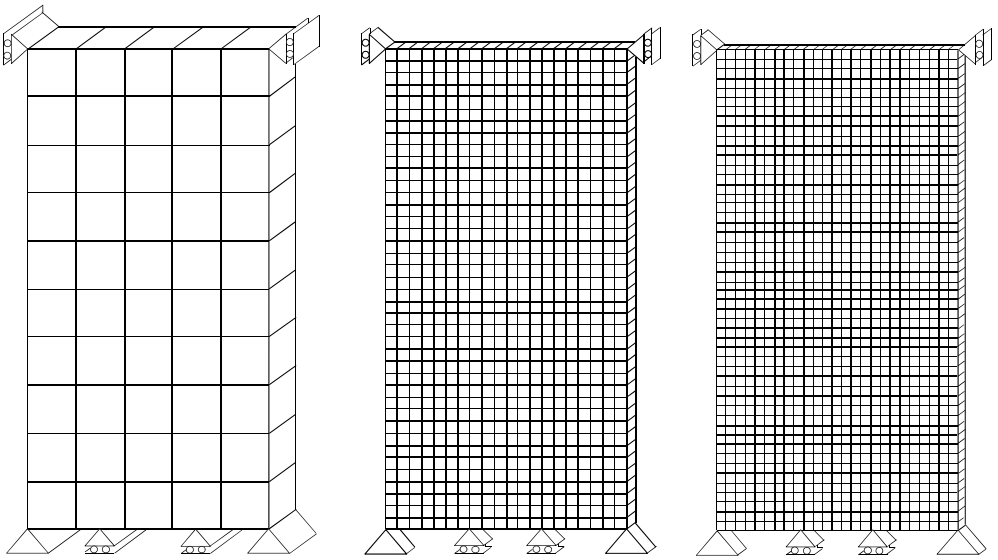


*Figure 5.7. Additional mesh patterns to study mesh-size dependency.*

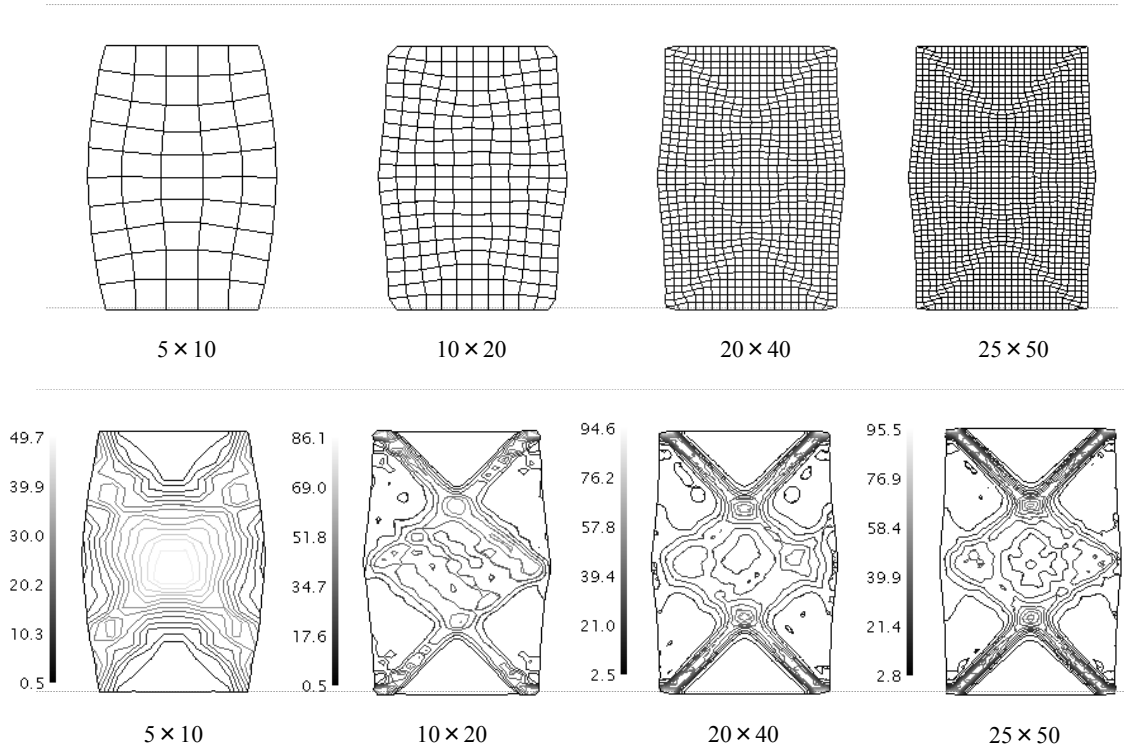


*Figure 5.8. Deformed meshes and localization of the viscoplastic shear strain for different mesh patterns at the end of loading (legend unit: %).*

The stress-strain relations and stress paths for these four cases are compared in Figure 5.9, where the average deviator stress is plotted versus the average axial strain and the average mean effective stress, respectively. The average values are obtained by computing the average of stresses over all the elements in each case. All the cases demonstrate rather similar tendency in stress-strain relations and stress paths, although slight differences are observed among stresses during softening after the peak stress point. In the coarser mesh pattern, the deviator stresses after the peak point tend to decrease more rapidly in comparison with those in the finer meshes. Nonetheless, the results appear to be convergent by mesh refinement after 200 elements, in view of the fact that the differences become smaller between the stresses in 200 elements case and 800 elements case, and also the stresses in 800 elements case and 1250 elements case are nearly the same. This fact is clearly perceived in Figure 5.10, which shows the average deviator stresses at various levels of strain versus number of the elements in the mesh configurations.

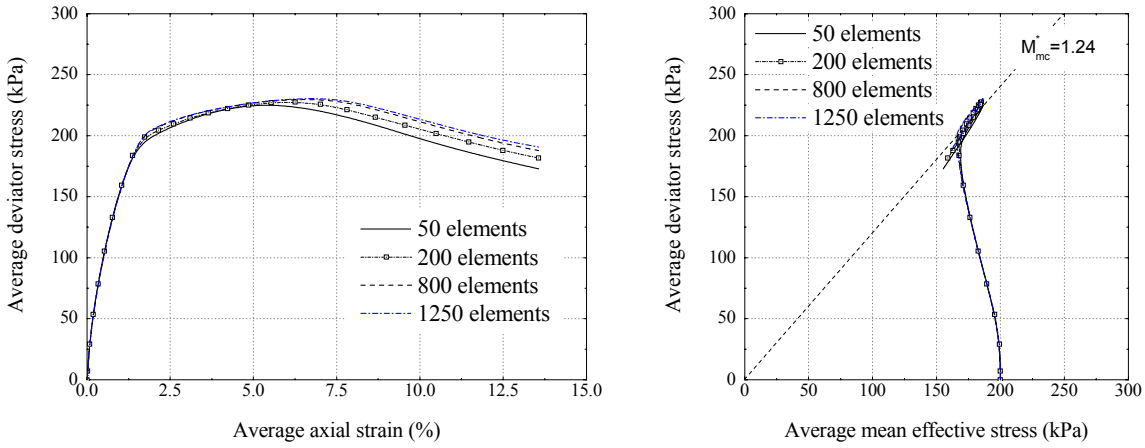


*Figure 5.9. Stress-strain relations and stress paths for different mesh patterns.*

It has been shown by many researchers that the consideration of material rate dependence substantially eliminates the pathological mesh sensitivity under quasi-static and/or dynamic loading conditions (e.g., Needleman 1988, Loret and Prevost 1991, etc.). However, the mesh-size dependency is somewhat observed in simulation results like any other finite element analyses. For the stress-strain relations of clay under quasi-static loading, Oka et al. (1995) have reported a slightly more softening response in a finer mesh configuration. In the latter work by Oka et al. (2002a), the mesh size effects were found to be insignificant on the stress-strain relations, whereas all the cases with different mesh configurations have shown identical values. In the present study, however, a slightly more hardening behavior is observed by taking a finer mesh configuration under dynamic loading conditions. Since

the constitutive model and loading conditions are different from the preceding works, this behavior might be explained. Moreover, deformation mechanism of the specimen caused by the material parameters under the current state of dynamic loadings, as well as the applied boundary conditions and constrained trigger points at the corners, might account for in this regard. The aspect ratio of the specimen, also, has a significant influence on the stress-strain behaviors in the 3D analysis of dynamic shear banding, as pointed out by Zbib and Jubran (1992). Accordingly, further studies have to be carried out to evaluate the effect of above-mentioned reasons on the dynamic strain localization of soft clays.

Despite the slight differences in stress-strain relations for different mesh configurations, convergency of the results verifies the suitability of current analysis at an acceptable level of mesh-size dependency. In addition, considering the overall shape of the shear bands and the stress-strain relations, the case with 200 elements gives results consistent with the finer meshes in a significantly shorter computation time, which implies adequacy of the 200 elements pattern to resolve the localization phenomenon for soft clay under dynamic loading conditions.

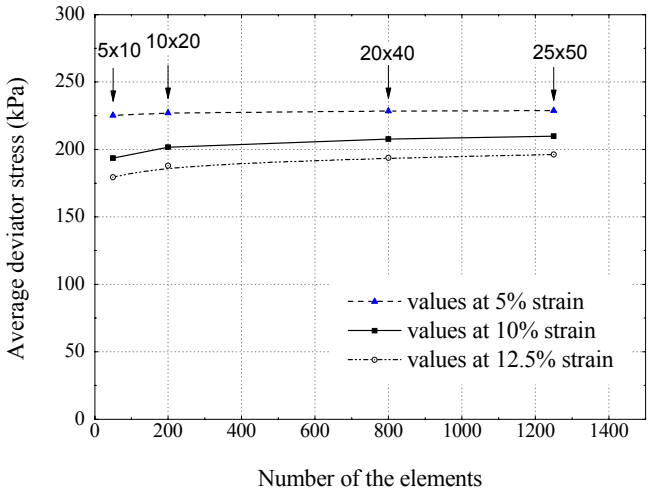


*Figure 5.10. Average deviator stresses at various strain levels for different mesh patterns.*

## 5.4. Dynamic Analysis of a Large-Scale Levee on Soft Soil Deposits

The dynamic analysis of the Torishima super levee on the multilayered ground foundation (see Section 3.2 for more details) is conducted to evaluate the behavior of such a large-scale embankment on stratified foundation during the earthquake. Due to the existence of saturated loose sand layers, liquefaction is expected to occur in the unimproved zone. Furthermore, the soft clay layers are likely to have some influences on the dynamic behavior of the system. The dynamic analyses are performed in two cases as the natural ground case and the improved ground case. For the improved ground case, the proposed procedures, as described in Section 3.5, are employed to model the improved ground techniques in plane strain conditions. The material parameters for the sand layer As2 and soft clay layer Ac2 are designated from the laboratory test results and in particular from the cyclic triaxial test simulation results. For the other layers, the parameters compatible with those used in the consolidation analysis (Chapter 3) are assigned. However, for some additional model parameters, the available values from similar sites are properly chosen.

In this section, at first the cyclic elasto-plastic model, which used for simulation of sandy layers, is presented. The simulations of the undrained cyclic triaxial tests on the sand specimens obtained from the As2 layer are then performed to determine the material parameters for the As2 layer. The dynamic simulations of the Torishima super levee are conducted under plane strain conditions using the developed numerical program. The full shape of the super levee after construction is considered for the dynamic analysis. The cyclic elasto-plastic constitutive model is adopted for the granular layers, while for the clay layers the cyclic elasto-viscoplastic constitutive model (see Section 4.2 for further details) is used.

### 5.4.1. Cyclic Elasto-Plastic Constitutive Model

The cyclic elasto-plastic model based on the nonlinear kinematic hardening rule, developed by Oka et al. (1999), is explained in this section with a modification on the dilatancy coefficient $\tilde{M}^*$. In the formulation of the present constitutive model, the following assumptions are applied:

1- Elasto-plastic theory,

2- Generalized non-associated flow rule,

3- Overconsolidation boundary surface,

4- Nonlinear kinematic hardening rule,

5- Degradation of the plastic strain-dependent shear modulus,

6- Fading memory of the initial anisotropy.

The overconsolidation boundary surface is defined in the similar way as for the cyclic elasto-viscoplastic model, with

$$f_b = \overline{\eta}^*_{(0)} + M^*_m \ln\left(\sigma'_m / \sigma'_{mb}\right) = 0 \tag{5.142}$$

$$\overline{\eta}^*_{(0)} = \left\{\left(\eta^*_{ij} - \eta^*_{ij(0)}\right)\left(\eta^*_{ij} - \eta^*_{ij(0)}\right)\right\}^{\frac{1}{2}} \tag{5.143}$$

where $\eta^*_{ij}$ is the stress ratio defined as $\eta^*_{ij} = S_{ij}/\sigma'_m$ , $\eta^*_{ij(0)}$ is the value of $\eta^*_{ij}$ at the end of consolidation, $\sigma'_m$ is the mean effective stress, $S_{ij}$ is the deviatoric stress tensor and $M^*_m$ is the value of the stress ratio expressed by $\sqrt{\eta^*_{ij}\eta^*_{ij}}$ when the maximum volumetric strain during shearing takes place and which could be called the phase transformation stress ratio. The condition $f_b < 0$ means that the stress state stays in the overconsolidated (OC) region and $f_b \geq 0$ means that the stress state is the normally consolidated (NC) region. $\sigma'_{mb}$ follows an evolutional equation as

$$\frac{d\sigma'_{mb}}{\sigma'_{mb}} = \frac{\lambda - \kappa}{1+e} d\varepsilon^p_v \tag{5.144}$$

The integration of the above equation gives

$$\sigma'_{mb} = \sigma'_{mbi} \exp\left(\frac{1+e_0}{\lambda - \kappa}\varepsilon^p_v\right) \tag{5.145}$$

where $\sigma'_{mbi}$ is the initial value of $\sigma'_{mb}$ , which is determined based on the volume change characteristics of soils by the quasi overconsolidation ratio as $OCR^* = \sigma'_{mbi}/\sigma'_{m0}$ .

Furthermore, $\sigma'_{mc}$ , which is the mean effective stress at the intersection of the overconsolidation boundary surface and $\sigma'_m$ axis, is defined as

$$\sigma'_{mc} = \sigma'_{mb} \exp\left(\frac{\eta^*_{(0)}}{M^*_m}\right) \tag{5.146}$$

$$\eta^*_{(0)} = \sqrt{\eta^*_{ij(0)}\eta^*_{ij(0)}} \tag{5.147}$$

The yield function for changes in the stress ratio is denoted as

$$f_{y1} = \bar{\eta}^*_{\chi} - k = 0 \tag{5.148}$$

$$\bar{\eta}^*_{\chi} = \left\{\left(\eta^*_{ij} - \chi^*_{ij}\right)\left(\eta^*_{ij} - \chi^*_{ij}\right)\right\}^{\frac{1}{2}} \tag{5.149}$$

where $k$ is a parameter which controls the size of the elastic region and $\chi^*_{ij}$ is the nonlinear kinematic hardening parameter which has the same dimension as the stress ratio $\eta^*_{ij}$. The evolution equation for the hardening parameter is defined by

$$d\chi^*_{ij} = B^*\left(A^* de^p_{ij} - \chi^*_{ij} d\gamma^p\right) \tag{5.150}$$

$$d\gamma^p = \sqrt{de^p_{ij}\, de^p_{ij}} \tag{5.151}$$

in which $A^*$ and $B^*$ are material parameters, $de^p_{ij}$ is the plastic deviatoric strain increment tensor, and $d\gamma^p$ is the plastic shear strain increment tensor. $A^*$ is related to the stress ratio at failure, namely, $A^* = M^*_f$, and $B^*$ is proposed to be dependent on the viscoplastic shear strain as

$$B^* = \left(B^*_{\max} - B^*_1\right)\exp\left(-C_f \gamma^{vp*}_{(n)}\right) + B^*_1 \tag{5.152}$$

in which $B^*_1$ is the lower boundary of $B^*$, $C_f$ is the parameter controlling the amount of reduction, $\gamma^{p*}_{(n)}$ is the accumulated value of the plastic shear strain between two sequential stress reversal points in the previous circle. $B^*_{\max}$ is the maximum value of parameter $B^*$, which is defined following the proposed method by Oka et al. (1999) as

$$B^*_{\max} = \begin{cases} B^*_0 & \text{:Before reaching failure line} \\ \dfrac{B^*_0}{1 + \gamma^{p*}_{(n)\max} \big/ \gamma^{p*}_{(n)r}} & \text{:After reaching failure line} \end{cases} \tag{4.153}$$

where $B^*_0$ is the initial value of $B^*$, $\gamma^{p*}_{(n)\max}$ is the maximum value of $\gamma^{p*}_{(n)}$ in past cycles, and $\gamma^{p*}_{(n)r}$ is the plastic reference strain.

In the other method proposed by Oka et al. (2004b) the definition of $B^*_{\max}$ is given by

$$B^*_{\max} = \begin{cases} B^*_0 & \text{:Before reaching failure line} \\ \dfrac{B^*_0}{1+\gamma^{p*}_{apc}\big/\gamma^{p*}_{apr}} & \text{:After reaching failure line} \end{cases} \tag{5.154}$$

in which, $\gamma^{p*}_{apc}$ is the accumulated plastic shear strain after reaching the failure line, and $\gamma^{p*}_{apr}$ is the plastic reference strain.

The same type of equation is also applied for the degradation function of the elastic shear modulus, in which $\gamma^{E*}_{(n)r}$ and $\gamma^{E*}_{apr}$ are used as the reference values instead of $\gamma^{p*}_{(n)r}$ and $\gamma^{p*}_{apr}$.

For changes in the mean effective stress, the following yield function is applied

$$f_{y2} = M^*_m \left| \ln\left(\sigma'_m / \sigma'_{mk}\right) - y^*_m \right| - R_d = 0 \tag{5.155}$$

where $y^*_m$ is the scalar kinematic hardening parameter, $\sigma'_{mk}$ is the unit value of the mean effective stress, and $R_d$ is a scalar variable. The scalar kinematic hardening parameter $y^*_m$ can be decomposed into two terms as

$$dy^*_m = dy^*_{m1} + dy^*_{m2} \tag{5.156}$$

The evolution equations for the scalar kinematic hardening parameter are assumed to be nonlinear for $y^*_{m1}$ and linear for $y^*_{m2}$, which are given by

$$dy^*_{m1} = B^*_2 \left( A^*_2 d\varepsilon^p_v - y^*_{m1} \left| d\varepsilon^p_v \right| \right) \tag{5.157}$$

$$dy^*_{m2} = H^*_2 d\varepsilon^p_v \tag{5.158}$$

where $A^*_2$, $B^*_2$ and $H^*_2$ are the material parameters. For cyclic behavior under undrained condition, the changes in the mean effective stress are insignificant; hence, the second yield function can be disregarded for simplicity.

The plastic potential function is assumed as follow:

$$g = \bar{\eta}^*_\chi + \tilde{M}^* \ln\left(\sigma'_m / \sigma'_{mp}\right) = 0 \tag{5.159}$$

The dilatancy coefficient $\tilde{M}^*$ is defined separately for the normally consolidated region (NC) and the overconsolidated region (OC). According to the new modification, the dilatancy coefficient is obtained as

$$\tilde{M}^* = \begin{cases} M_m^* & \text{:NC region} \\ \left(\sigma_m^* / \sigma'_{mc}\right) M_m^* & \text{:OC region} \end{cases} \tag{5.160}$$

where $\sigma_m^*$ denotes the mean effective stress at the intersection of the surface, given by

$$\sigma_m^* = \sigma'_m \ \exp\left(\frac{\bar{\eta}_\chi^*}{M_m^*}\right) \tag{5.161}$$

The generalized flow rule for the constitutive model using a fourth rank isotropic tensor $H_{ijkl}$, is expressed as

$$d\varepsilon_{ij}^p = H_{ijkl} \frac{\partial g}{\partial \sigma'_{kl}} \tag{5.162}$$

$$H_{ijkl} = a\delta_{ij}\delta_{kl} + b\left(\delta_{ik}\delta_{jl} + \delta_{il}\delta_{jk}\right) \tag{5.163}$$

where $d\varepsilon_{ij}^p$ is the plastic strain increment tensor and $d\sigma'_{kl}$ is the effective stress increment tensor. *a* and *b* in Equation (5.163) are material constants.

The stress-dilatancy relation is obtained from the generalized flow rule as

$$\frac{d\varepsilon_v^p}{d\gamma_v^p} = D^*\left(\tilde{M}^* - \bar{\eta}_\chi^*\right) \tag{5.164}$$

in which $D^* = 3a/2b + 1$ is the dilatancy parameter which controls the ratio of the plastic deviatoric increment to the plastic deviatoric strain increment. The variation of $D^*$ is given by

$$D^* = D_0^*\left(\tilde{M}^* / M_m^*\right)^{n_0} \tag{5.165}$$

where $D^*$ and $n_0$ are the material parameters.

During the cyclic loading in soils, the effect of the initial anisotropy decreases. The overconsolidation boundary surface depends on the initial anisotropy of soil. This means that the

existence of the initial anisotropy influences the shape of the overconsolidation boundary surface. Therefore, the initial anisotropy is assumed to fade during the cyclic loading. To consider this, coefficient $\zeta$ is used in definition of $\sigma'_{mc}$ as

$$\sigma'_{mc} = \sigma'_{mb} \exp\left( \zeta \frac{\overline{\eta}^*_{(0)}}{M^*_m} \right) \tag{5.166}$$

$$\zeta = \exp\left(-C_d \gamma^*_{cum}\right) \tag{5.167}$$

where $\gamma^*_{cum}$ is the accumulative plastic shear strain from the initial condition, and $C_d$ is a constant that controls the rate of disappearance of anisotropy.

### 5.4.2. Simulation of Cyclic Triaxial Behavior of Torishima Sand Specimens

The simulation of the cyclic triaxial tests on the sand specimens from As2 layer in Torishima super levee site are carried out to find the representative model parameters. The laboratory tests were performed on the specimens obtained at two different depths within the As2 layer; thereby the layer As2 is divided into two individual sub-layers, namely, As2-U and As2-L. The samples were obtained through the undisturbed tube sampling from two boreholes drilled in the Torishima super levee site. In addition to the basic laboratory tests for physical properties, the undrained cyclic triaxial tests were conducted on the sand samples at different levels of cyclic stress ratio CSR, which is defined as $CSR = q/2\sigma'_{m0}$ .

The experimental results of the cyclic triaxial tests are plotted in Figures 5.11 and 5.12, as the stress-strain relations, stress paths, and excess pore pressure ratio versus number of cycle curves, for the As2-U layer samples and As2-L layer samples, respectively. Following the cyclic triaxial test, the cyclic test simulations are performed for different levels of cyclic stress ratio by integration of the cyclic elasto-plastic constitutive equations under undrained triaxial conditions. The material parameters are determined following the proposed method by Oka et al. (1999) and the data-adjusting method. Due to the lack of classical consolidation tests to determine the swelling and compression indexes, the following equation is used for the first approximation of the swelling index $\kappa$, based on the assumed Poisson's ratio and the initial elastic shear modulus,

$$\kappa = \frac{3(1\text{-}2\upsilon)(1+e_0)}{2(1+\upsilon)G_0}\sigma'_{m0} \tag{5.168}$$

The initial elastic shear modulus is approximated from the slope of the stress-strain relation at the earlier stage of loading. The stress ratios at compression and extension are roughly calculated from the failure line in stress path. Nonetheless, the data-adjusting method is mainly used to determine the exact value of the parameters. The representative material parameters for As2-U and As2-L layers are listed in Table 5.2.

Figures 5.13 and 5.14 show the corresponding simulated results for the specimens from As2-U and As2-L layer, respectively. Attempts are made to obtain a suitable set of parameters representing the characteristic of each layer. Although the obtained specimens from each layer are tested under similar conditions, some inconsistency emerges in the experimental results, probably due to the sample disturbance and sensitivity, which cannot be encountered in the simulations. Consequently, slightly disagreement with the experimental results is observed in the simulated results when an individual set of parameters is employed for all the specimens of each layer under different levels of CSR. For the excess pore pressure ratio in the simulated results, as the calculation of pore water pressure is not directly included in the constitutive equations, the reduction ratio of the mean effective stress is considered instead. Thereby, the simulated results show different response in the excess pore pressure ratio, particularly during the rise time before the onset of cyclic mobility.

The liquefaction resistance curves of the sand samples from As2 sub-layers are depicted in Figure 5.15 for the experiment and the simulation. The liquefaction resistance of sand is determined as the number of the cycles in which the sand is being liquefied. The liquefaction is defined by either the excess pore pressure ratio $\left(R_u = P_w / \sigma'_{m0}\right)$, or the double amplitude strain (DA) criterion. In Table 5.3, the number of cycles are presented for $DA$= 5%, $DA$= 10%, and $R_u$= 95%. The simulated results, in general, show larger number of cycles at high level of CSR, which results in a steeper liquefaction strength cure compared with the laboratory test data.

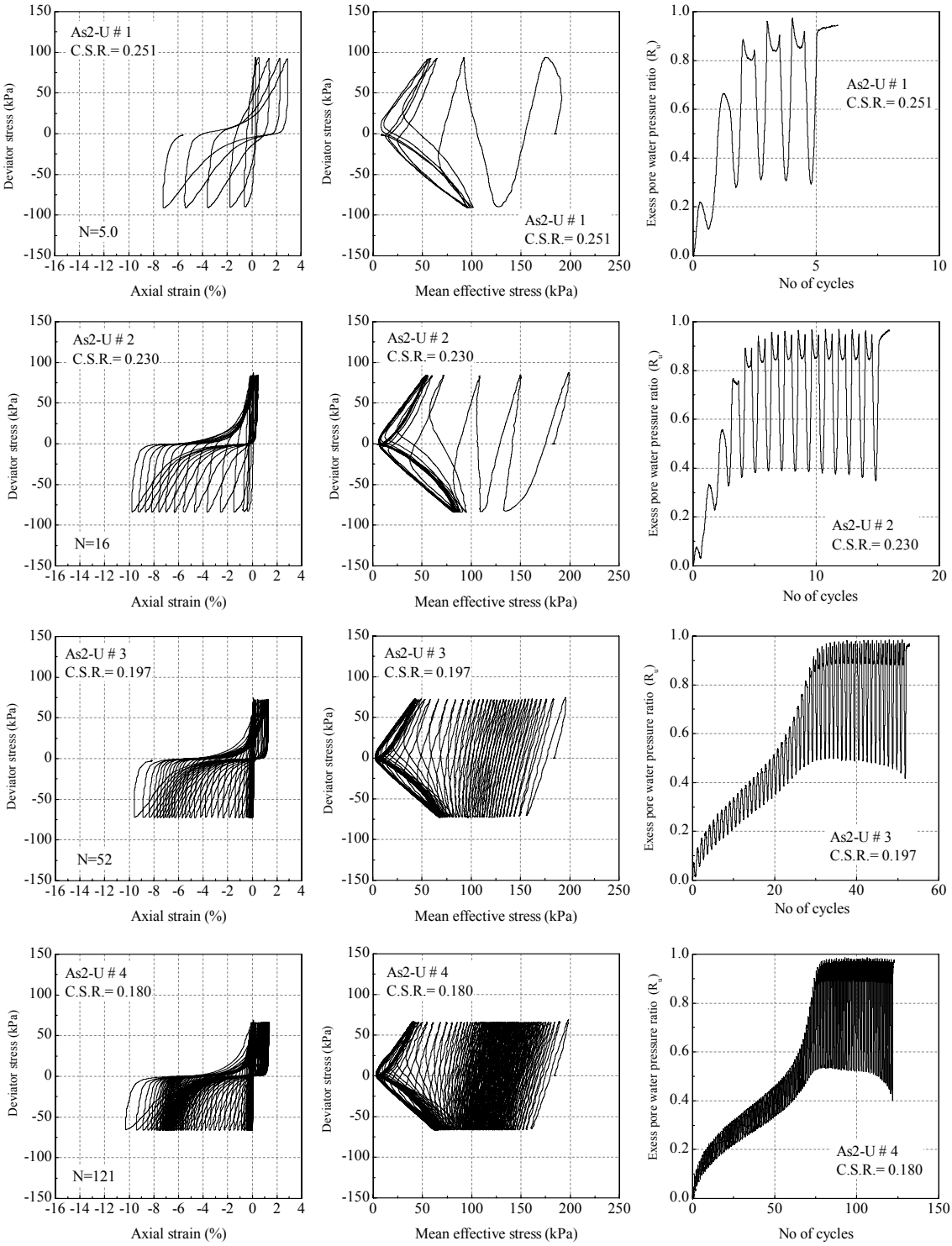


*Figure 5.11. Cyclic triaxial test results on As2-U samples under different levels of cyclic stress ratio.*

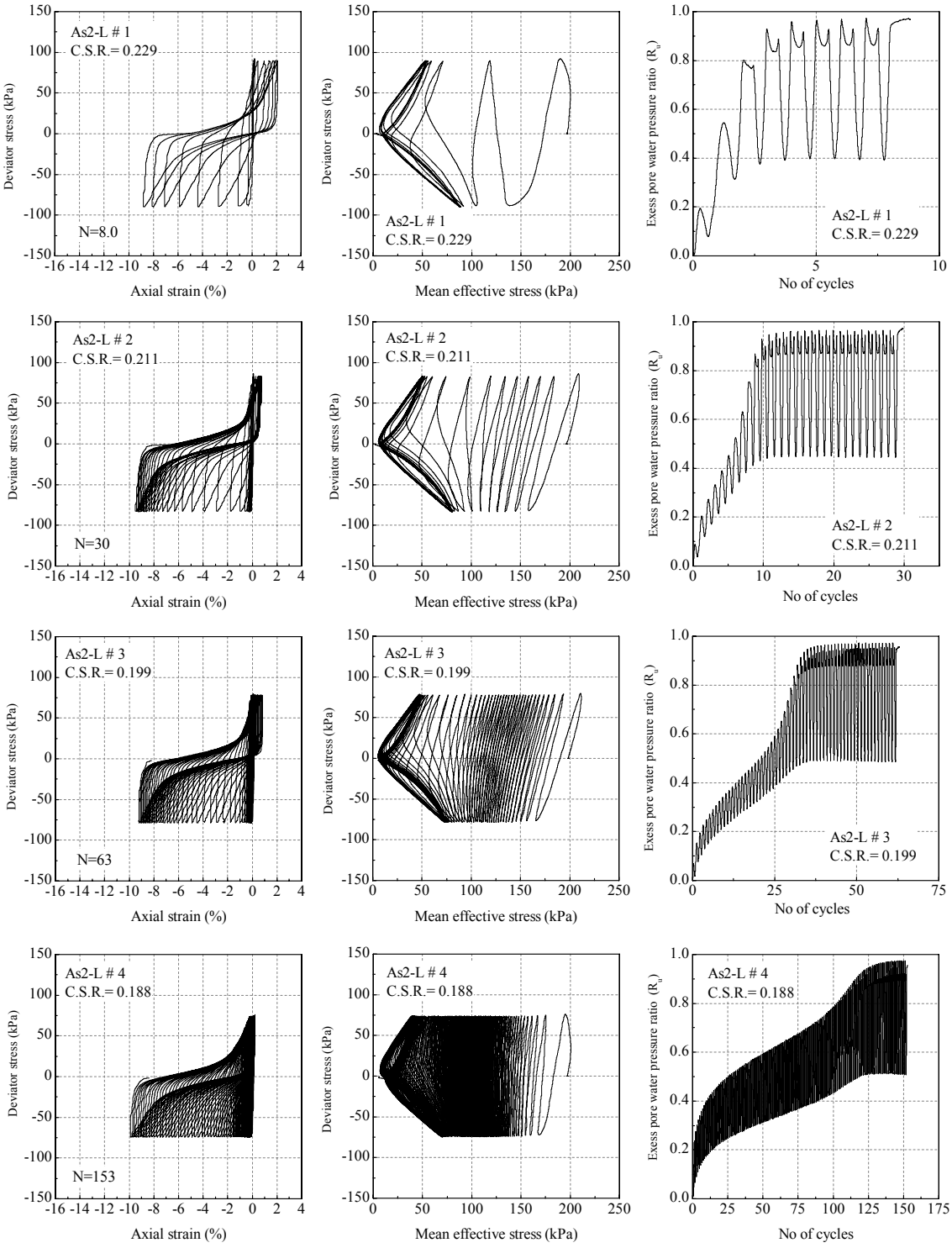


*Figure 5.12. Cyclic triaxial test results on As2-L samples under different levels of cyclic stress ratio.*

*Table 5.2. Material parameters of sand layer As2 in Torishima.*

| | | As2-U | As2-L |
|---|---|---|---|
| Test No. | | #1: CSR=0.251<br>#2: CSR=0.230<br>#3: CSR=0.197<br>#4: CSR=0.180 | #1: CSR=0.229<br>#2: CSR=0.211<br>#3: CSR=0.199<br>#4: CSR=0.188 |
| Initial void ratio | $e_0$ | 0.623 | 0.81 |
| Compression index | $\lambda$ | 0.0875 | 0.870 |
| Swelling index | $\kappa$ | 0.0068 | 0.0064 |
| Normalized initial shear modulus | $G_0/\sigma'_m$ | 175.5 | 185.5 |
| Initial mean effective stress *(kPa)* | $\sigma'_{m0}$ | 183 | 197 |
| Failure stress ratio at compression | $M^*_{fc}$ | 1.36 | 1.36 |
| Phase transformation stress ratio at compression | $M^*_{mc}$ | 1.12 | 1.12 |
| Failure stress ratio at extension | $M^*_{fe}$ | 1.0 | 1.0 |
| Phase transformation stress ratio at extension | $M^*_{me}$ | 0.81 | 0.81 |
| Anisotropy control parameter | $C_d$ | 2000 | 2000 |
| Parameter of dilatancy | $D^*_0$ | 2.75 | 1.15 |
| Parameter of dilatancy | $n_0$ | 4.75 | 5.75 |
| Hardening parameter | $B^*_0$ | 3000 | 3500 |
| Hardening parameter | $B^*_1$ | 5 | 5 |
| Hardening parameter | $C_f$ | 15 | 10 |
| Reference value of plastic strain *(%)* | $\gamma^{p*}_{(n)r}$ | 0.33 | 0.27 |
| Reference value of elastic strain *(%)* | $\gamma^{E*}_{(n)r}$ | 1.9 | 2.15 |

*Table 5.3. Number of cycles at different CSR for experiment and simulation.*

| | As2-U | | | | As2-L | | | |
|---|---|---|---|---|---|---|---|---|
| *CSR =* | *0.251* | *0.230* | *0.197* | *0.180* | *0.230* | *0.211* | *0.199* | *0.188* |
| Experiment: | | | | | | | | |
| *DA*= 5% | 3 | 7 | 36 | 83 | 4 | 12 | 38 | 129 |
| *DA*= 10% | 5 | 14 | 52 | 121 | 7 | 28 | 61 | 151 |
| $R_u$= 95% | 4 | 6 | 32 | 78 | 4 | 11 | 35 | 123 |
| Simulation: | | | | | | | | |
| *DA*= 5% | 7 | 12 | 32 | 73 | 18.5 | 29 | 62 | 109 |
| *DA*= 10% | 8 | 17 | 49 | 87 | 20.5 | 34 | 65 | 112 |
| $R_u$= 95% | 7 | 9 | 33 | 78 | 16 | 29 | 61 | 107 |

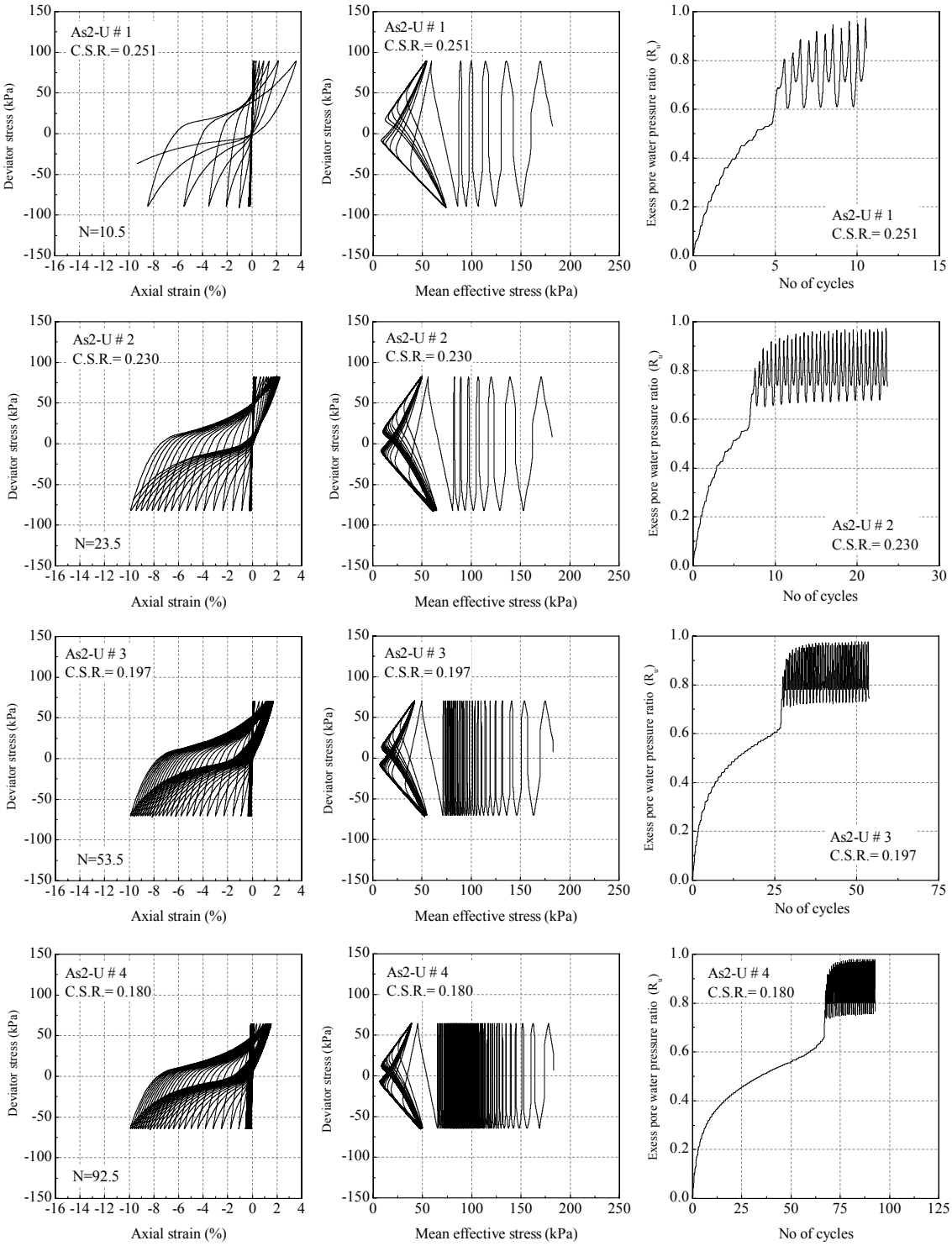


*Figure 5.13. Simulated results of As2-U samples under different levels of cyclic stress ratio.*

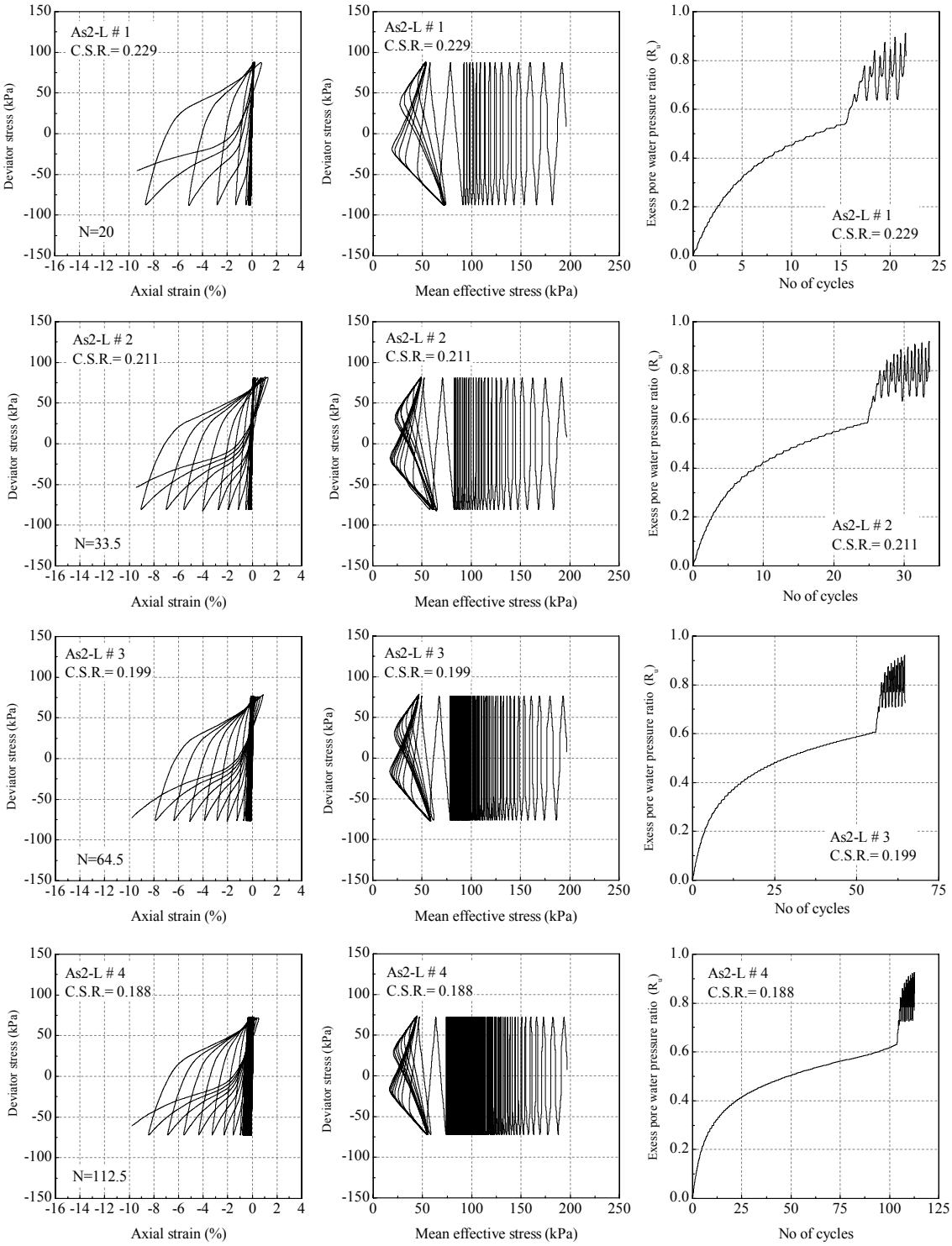


*Figure 5.14. Simulated results of As2-L samples under different levels of cyclic stress ratio.*

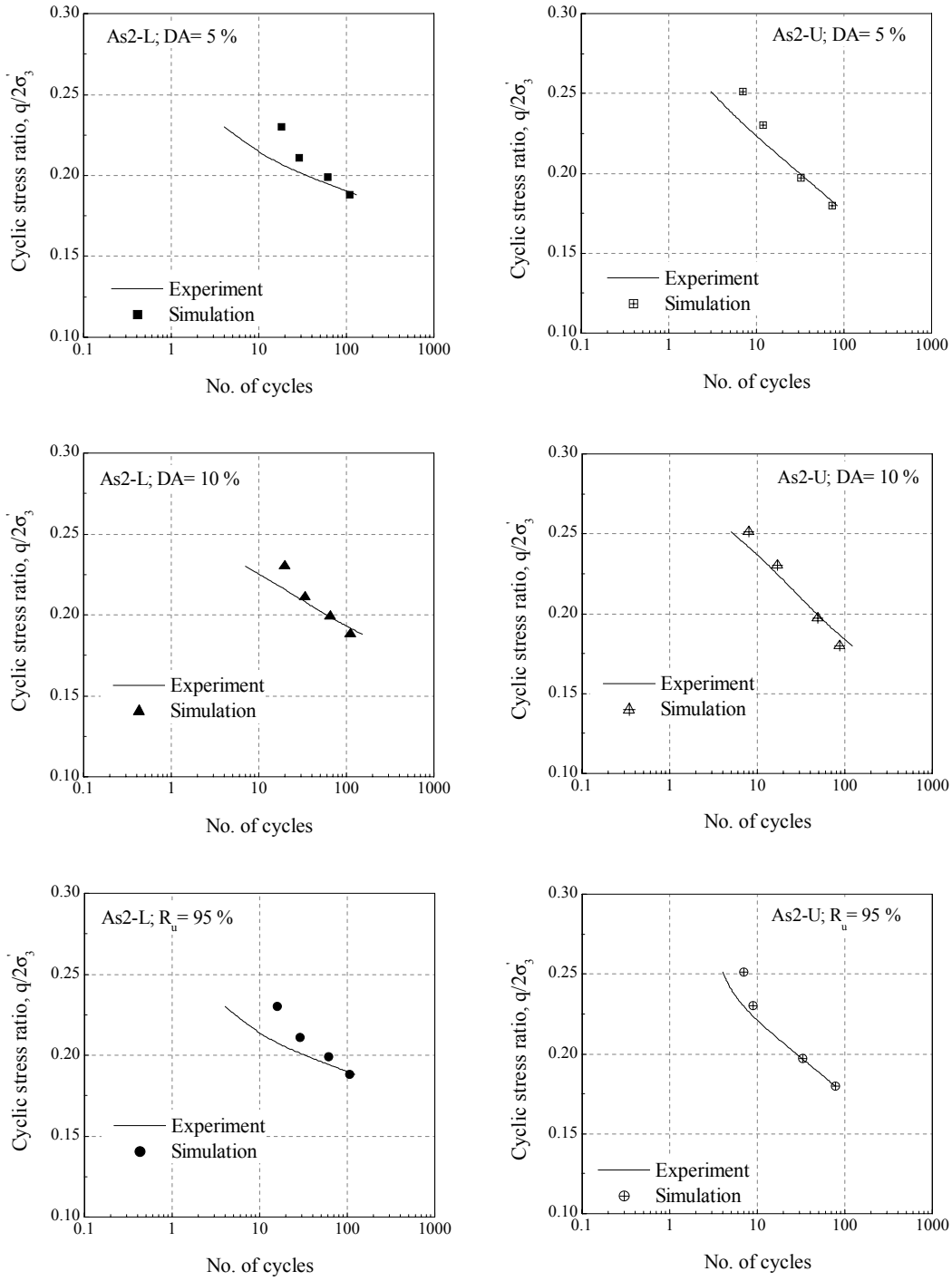


*Figure 5.15. Liquefaction resistance curves for the experimental and the simulated results based on different criteria.*

### 5.4.3. Problem Geometry and Boundary Conditions

The geometry of the FEM model and the boundary conditions are depicted in Figure 5.16. The simulations are accomplished using a three-dimensional mesh system under plane strain conditions, for which the unit length is considered in the third dimension and the deformations in that direction are restricted. Fully saturated conditions with drainage boundaries only at the top are assumed. The assumption of fully saturated conditions, for both embankment and ground layers, refers to a worst-case scenario in which earthquake occurs after the heavy rainfall. For the displacement boundaries, the displacements at the bottom are fixed in all directions assuming the rigid base at a depth of 40 m, and for the both side boundaries, the free movement conditions only in the vertical direction are assumed. The effective stress conditions immediately after the construction of the super levee are considered as the initial configuration. The initial stress state is computed by the static elasto-perfectly-plastic analysis using the Drucker-Prager type material model.

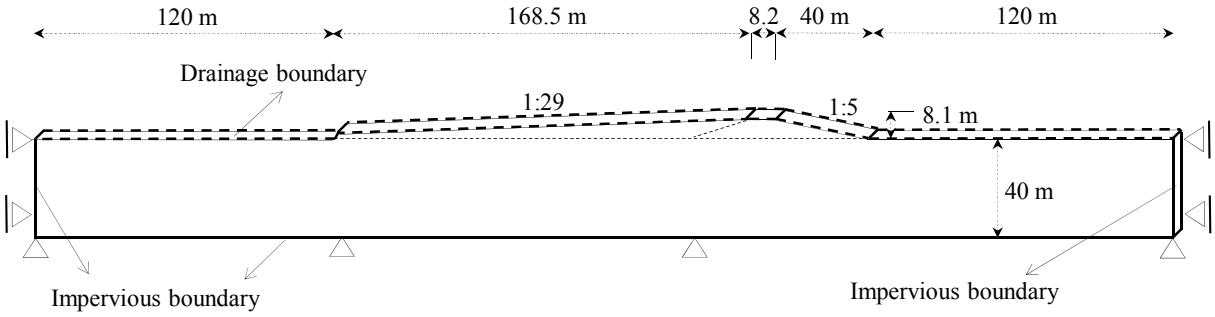


*Figure 5.16. Geometry and boundary conditions of 3D finite element model for the dynamic analysis.*

The material parameters for the natural ground case are summarized in Tables 5.4 and 5.5. The cyclic elasto-viscoplastic model is adopted for the clayey layers, while for the granular layers, including the embankment layers, the cyclic elasto-plastic constitutive model is allocated. The additional material parameters for the improved ground case are listed in Tables 5.6 and 5.7. The effect of each ground improvement technique is considered following the same procedures as those proposed for the consolidation analyses in Chapter 3. For the deep mixing parts, the linear elastic behavior is assumed and relevant parameters are assigned. For the SCP/SD installed zones, the horizontal permeability matching procedure is employed with the same assumptions as those used for the consolidation analysis after parameter calibration process. However, the drain spacing in the dynamic simulation is increased to $B = 4R$, in order to reduce the overall number of nodes in the mesh and consequently to optimize the computation time.

For the input ground motion, as illustrated in Figure 5.17, a wave with a maximum acceleration of 509 gal is assumed based on a NS component of an earthquake record on Port Island, Kobe City during the 1995 Kobe (Great Hanshin) Earthquake, and applied in the horizontal direction. The major shock occurs in 10 sec and after that, the simulation is carried on until 20 sec to evaluate the post-quake responses. In the dynamic analyses, an initial stiffness dependent type of Rayleigh damping is adopted with the attenuation constant equal to 0.9%. In addition, a direct integration scheme of the Newmark's $\beta$ method is employed, for which the values of 0.3025 and 0.6 are applied for $\overline{\beta}$ and $\overline{\gamma}$, respectively.

*Table 5.4. Material parameters of cyclic elasto-viscoplastic model for the natural ground case.*

| | Ac2-U | Ac2-M | Ac2-L (1) | Ac1 (1) | Dc (1) |
|---|---|---|---|---|---|
| Initial void ratio $e_0$ | 1.25 | 1.65 | 1.42 | 1.30 | 1.20 |
| Coefficient of permeability $k/\gamma_w$ $(m^4/kN.s)$ | $5.87\times10^{-11}$ | $3.93\times10^{-11}$ | $2.74\times10^{-11}$ | $1.63\times10^{-10}$ | $5.40\times10^{-11}$ |
| Compression index $\lambda$ | 0.341 | 0.593 | 0.652 | 0.326 | 0.217 |
| Swelling index $\kappa$ | 0.019 | 0.027 | 0.014 | 0.0326 | 0.0217 |
| Density $\rho$ $(t/m^3)$ | 1.7 | 1.6 | 1.66 | 1.6 | 1.8 |
| Normalized initial shear modulus $G_0/\sigma'_{m0}$ | 75.2 | 58.95 | 65 | 88.5 | 128.25 |
| Phase transformation stress ratio $M^*_m$ | 1.24 | 1.18 | 1.12 | 1.12 | 1.30 |
| Failure stress ratio $M^*_f$ | 1.24 | 1.18 | 1.12 | 1.12 | 1.30 |
| Viscoplastic parameter $m'$ | 24.68 | 28.2 | 21.25 | 20 | 20 |
| Viscoplastic parameter $C_1$ $(1/s)$ | $1.00\times10^{-5}$ | $1.00\times10^{-5}$ | $1.00\times10^{-5}$ | $1.00\times10^{-6}$ | $1.00\times10^{-7}$ |
| Viscoplastic parameter $C_2$ $(1/s)$ | $3.83\times10^{-6}$ | $1.85\times10^{-6}$ | $8.99\times10^{-6}$ | $3.00\times10^{-7}$ | $1.16\times10^{-8}$ |
| Structural parameter $n=\sigma'_{maf}/\sigma'_{mai}$ | 0.30 | 0.325 | 0.30 | 0.35 | 0.35 |
| Structural parameter $\beta$ | 3.6 | 3.8 | 4.0 | 3.0 | 3.0 |
| Hardening parameter $B^*_0$ | 100 | 180 | 200 | 200 | 350 |
| Hardening parameter $B^*_1$ | 40 | 3 | 5 | 5 | 50 |
| Hardening parameter $C_f$ | 10 | 3 | 5 | 5 | 5 |
| Reference viscoplastic strain $\gamma^{vp*}_{(n)r}$ (%) | 1.25 | 1.25 | 1.25 | 1.5 | -- |
| Strain-dependent parameter $\alpha$ | 10 | 20 | 20 | 10 | -- |
| Scalar hardening parameter $A^*_2$ | 5.9 | 5.9 | 5.9 | 5.9 | 5.9 |
| Scalar hardening parameter $B^*_2$ | 1.8 | 1.8 | 1.8 | 1.8 | 1.8 |
| Quasi-overconsolidation ratio $OCR^*$ | 1.00 | 1.00 | 1.00 | 1.20 | 1.9 |

*(1) The material parameters for these layers are properly chosen from the existing data due to the lack of cyclic tests.*

*(2)* $\sigma'_{mai}=\sigma'_{m0}\times OCR^*$

*Table 5.5. Material parameters of cyclic elasto-plastic model for the natural ground case.*

| | Em2 (1) | Em1(1) | B1(1) | As2-U | As2-L | As1(1) | Dg (1) |
|---|---|---|---|---|---|---|---|
| Initial void ratio $e_0$ | 0.8 | 0.8 | 0.93 | 0.623 | 0.81 | 0.9 | 0.9 |
| Coefficient of permeability $k/\gamma_w$ $(m^4/kN.s)$ | $1.0\times10^{-6}$ | $1.0\times10^{-6}$ | $1.0\times10^{-6}$ | $3.9\times10^{-7}$ | $1.1\times10^{-6}$ | $5.6\times10^{-7}$ | $1.0\times10^{-6}$ |
| Compression index $\lambda$ | 0.03 | 0.03 | 0.0025 | 0.0875 | 0.087 | 0.01 | 0.01 |
| Swelling index $\kappa$ | 0.002 | 0.002 | 0.0015 | 0.0068 | 0.0064 | 0.003 | 0.003 |
| Density $\rho$ $(t/m^3)$ | 1.8 | 1.75 | 1.75 | 1.8 | 1.8 | 1.8 | 1.9 |
| Initial shear modulus $G_0/\sigma'_{m0}$ | 251 | 215 | 150 | 175.5 | 185.5 | 512 | 541 |
| Phase transformation stress ratio $M^*_m$ | 0.909 | 0.909 | 0.99 | 1.12 | 1.12 | 0.909 | 0.909 |
| Failure stress ratio $M^*_f$ | 1.15 | 1.14 | 1.28 | 1.36 | 1.36 | 1.158 | 1.336 |
| Anisotropy control parameter $C_d$ | 2000 | 2000 | 2000 | 2000 | 2000 | 2000 | 2000 |
| Parameter of dilatancy $D^*_0$ | 1.0 | 1.0 | 2.5 | 2.75 | 1.15 | 1 | -- |
| Parameter of dilatancy $n_0$ | 4.0 | 4.0 | 4.5 | 4.75 | 5.75 | 6 | -- |
| Hardening parameter $B^*_0$ | 3000 | 2850 | 2750 | 3000 | 3500 | 3800 | 3000 |
| Hardening parameter $B^*_1$ | 7.5 | 7 | 5 | 5 | 5 | 70 | 5 |
| Hardening parameter $C_f$ | 0 | 0 | 10 | 15 | 10 | 0 | 0 |
| Reference plastic strain $\gamma^{p*}_{(n)r}$ (%) | 0.25 | 0.25 | 0.25 | 0.33 | 0.27 | 0.5 | -- |
| Reference elastic strain $\gamma^{E*}_{(n)r}$ (%) | 1.0 | 1.0 | 1.0 | 1.9 | 2.15 | 1.0 | -- |
| Quasi-overconsolidation ratio $OCR^*$ | 1.00 | 1.00 | 1.00 | 1.00 | 1.00 | 1.20 | 1.50 |

*(1) The material parameters for these layers are properly chosen from the existing data due to the lack of cyclic tests.*

*Table 5.6. Elastic model parameters of the deep mixing parts for the improved ground case.*

| | DMW/Sand | DMW/Clay | B1-DM | As2-DM | Ac2-U-DM |
|---|---|---|---|---|---|
| Initial void ratio $e_0$ | 0.72 | 0.72 | 0.8 | 0.72 | 1.25 |
| Coefficient of permeability $k/\gamma_w$ | $1.0\times10^{-9}$ | $5.87\times10^{-12}$ | $7.14\times10^{-7}$ | $5.26\times10^{-8}$ | $4.3\times10^{-11}$ |
| Lame's constant $\tilde{\lambda}$ (kPa) | 121732 | 121732 | 40560 | 42098 | 40470 |
| Lame's constant $\tilde{\mu}$ (kPa) | 81155 | 81155 | 27040 | 28065 | 26980 |
| Density $\rho$ (t/m3) | 2.0 | 2.0 | 1.875 | 1.9 | 1.85 |

*Table 5.7. Additional material parameters for the improved ground case.*

| | B1-SCP | As2-U-SCP | As2-L-SD | Ac2-U-SD | Ac2-L-SD | Ac2-L-SD | As1-SD |
|---|---|---|---|---|---|---|---|
| Initial void ratio $e_0$ | 0.93 | 0.623 | 0.81 | 1.25 | 1.65 | 1.42 | 0.9 |
| Coefficient of permeability $k_x/\gamma_w$ | $1.42\times10^{-6}$ | $5.54\times10^{-7}$ | $1.56\times10^{-6}$ | $8.3\times10^{-11}$ | $5.58\times10^{-11}$ | $3.9\times10^{-11}$ | $7.95\times10^{-7}$ |
| Compression index $\lambda$ | 0.0025 | 0.0875 | 0.087 | 0.341 | 0.593 | 0.652 | 0.01 |
| Swelling index $\kappa$ | 0.0015 | 0.0068 | 0.0064 | 0.019 | 0.027 | 0.014 | 0.003 |
| Density $\rho$ *(t/m3)* | 1.75 | 1.8 | 1.8 | 1.7 | 1.6 | 1.66 | 1.8 |
| Initial shear modulus $G_0/\sigma'_{m0}$ | 450 | 438.75 | 185.5 | 75.2 | 58.95 | 65 | 512 |
| PT stress ratio $M^*_m$ | 0.99 | 1.12 | 1.12 | 1.24 | 1.18 | 1.12 | 0.909 |
| Failure stress ratio $M^*_f$ | 1.28 | 1.36 | 1.36 | 1.24 | 1.18 | 1.12 | 1.158 |
| Viscoplastic parameter $m'$ | -- | -- | -- | 24.68 | 28.2 | 21.25 | -- |
| Viscoplastic parameter $C_1$ *(1/s)* | -- | -- | -- | $1.00\times10^{-7}$ | $1.00\times10^{-7}$ | $1.00\times10^{-7}$ | -- |
| Viscoplastic parameter $C_2$ *(1/s)* | -- | -- | -- | $3.83\times10^{-8}$ | $1.85\times10^{-8}$ | $8.99\times10^{-8}$ | -- |
| Structural parameter $n=\sigma'_{maf}/\sigma'_{mai}$ | -- | -- | -- | 0.30 | 0.325 | 0.30 | -- |
| Structural parameter $\beta$ | -- | -- | -- | 3.6 | 3.8 | 4.0 | -- |
| Anisotropy control parameter $C_d$ | 2000 | 2000 | 2000 | -- | -- | -- | 2000 |
| Parameter of dilatancy $D^*_0$ | 2.5 | 2.75 | 1.15 | -- | -- | -- | 1 |
| Parameter of dilatancy $n_0$ | 4.5 | 4.75 | 5.75 | -- | -- | -- | 6 |
| Hardening parameter $B^*_0$ | 3750 | 4000 | 3500 | 100 | 180 | 200 | 3800 |
| Hardening parameter $B^*_1$ | 5 | 5 | 5 | 40 | 3 | 5 | 70 |
| Hardening parameter $C_f$ | 5 | 5 | 10 | 10 | 3 | 5 | 0 |
| Reference plastic strain $\gamma^{p*}_{(n)r}$ *(%)* | 0.25 | 0.33 | 0.27 | 1.25 | 1.25 | 1.25 | 0.5 |
| Reference elastic strain $\gamma^{E*}_{(n)r}$ *(%)* | 1.0 | 1.9 | 2.15 | -- | -- | -- | 1.0 |
| Strain-dependent parameter $\alpha$ | -- | -- | -- | 10 | 20 | 20 | -- |
| Scalar hardening parameter $A^*_2$ | -- | -- | -- | 5.9 | 5.9 | 5.9 | -- |
| Scalar hardening parameter $B^*_2$ | -- | -- | -- | 1.8 | 1.8 | 1.8 | -- |

*$k_x$: Equivalent horizontal permeability.*

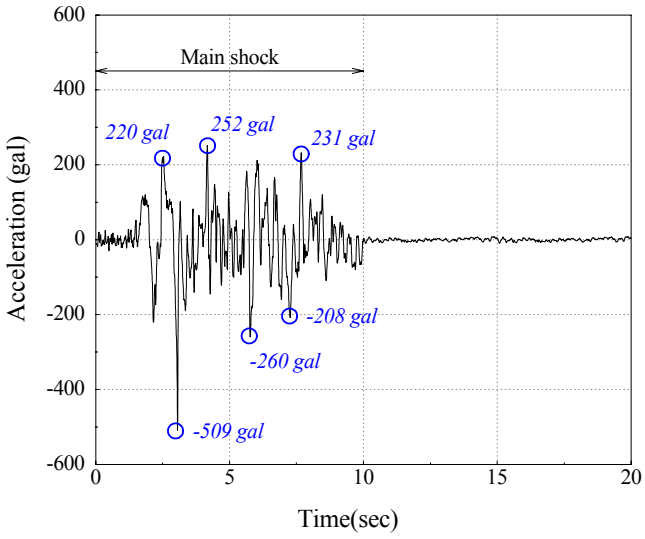


*Figure 5.17. Input earthquake wave.*

### 5.4.4. Analysis Results and Discussion

The dynamic analysis results are presented for the natural (unimproved) ground case and the improved ground case, as the time histories of displacements in both vertical and horizontal directions, the acceleration responses, and the excess pore pressure responses, at the center of each subsurface layer and some nodes over the ground level and atop the super levee. In addition, the distribution contours of the vertical strain, the accumulated plastic/viscoplastic shear strain, the excess pore water pressure, and the effective stress reduction ratio (ESDR) are exhibited at several steps of the simulation. The locations of the reference points for the nodal outputs at several sections are schematically depicted in Figure 5.18 with respect to the dimensions from the boundaries.

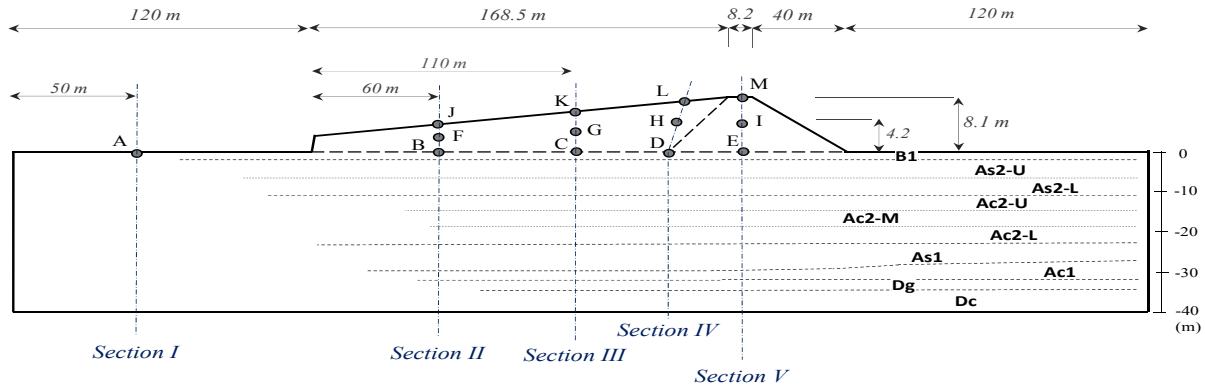


*Figure 5.18. Location of the reference points for the nodal outputs within the sketch of the super levee and ground layers.*

#### 5.4.4.1. Effective Stress Decreasing Ratio (ESDR)

The effective stress decreasing ratio is defined as $ESDR = 1 - \sigma'_m / \sigma'_{m0}$, where $\sigma'_m$ is the mean effective stress, and $\sigma'_{m0}$ is the initial mean effective stress. Liquefaction occurs when ESDR is equal to one. Figures 5.19 and 5.20 demonstrate the effective stress decreasing ratio contours at several steps of the computation, namely, at 5, 7.5, 10, and 20 sec, for the natural (unimproved) ground case and the improved ground case, respectively.

In the natural ground case, by progress of the ground motion at 5 sec, as shown in Figure 5.19(a), the values of the ESDR start to increase in the upper sandy layers, B1 and As2, beneath the super levee, and in the super levee layers. Simultaneously, the reduction of effective stress appears in the deeper layers, e.g. As1, in the areas on the left and right side of the super levee. In those areas, the

initial effective stresses are smaller than those areas underneath the super levee; therefore, the reduction of the effective stress occurs faster. The reduction of ESDR accelerates by progress of the ground motion. At the end of the major ground motion, at 10 sec as shown in Figure 5.19(c), the upper sand layers B1 and As2, and most parts of the super levee layers nearly liquefy. In addition, the deep sand layer As1 shows remarkable values of ESDR about 0.8, indicating the threshold of the liquefaction in that layer. The other layers such as Ac2-U and Ac2-L demonstrate the values of about 0.5. After the main shock, the liquefied zones develop throughout the upper layers. At the end of the analysis, at 20 sec as shown in Figure 5.19(d), the liquefaction is observed in almost the whole part of B1 and As2, and in the entire part of the super levee, as well as in As1 layer on the left and right side of the super levee. In the superficial parts of B1 layer, on the left and right side of the super levee, the value of ESDR is about 0.6 after 20 sec.

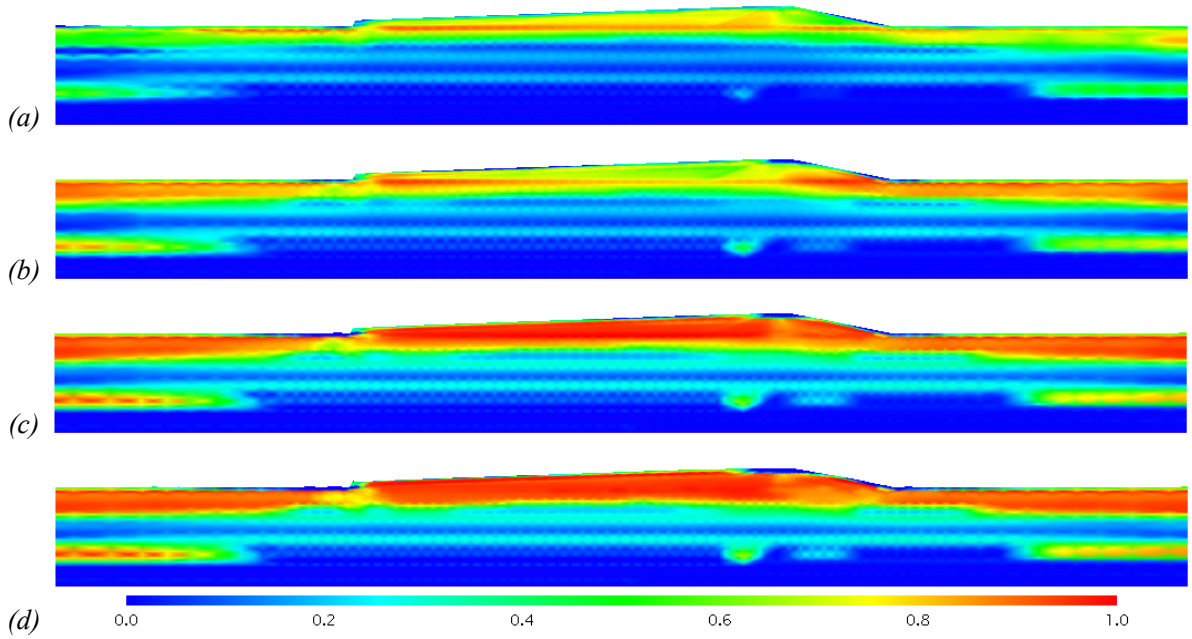


*Figure 5.19. Effective stress decreasing ratio contours for the natural ground case at several times; (a) 5 s, (b) 7.5 s, (c) 10 s, and (d) 20 s.*

In the improved ground case, as shown in Figure 5.20, the accomplishment of the ground improvement techniques significantly prevents the occurrence of liquefaction in the subsurface strata beneath the super levee. However, liquefaction is still observed in almost the whole part of the super levee due to its initial saturated conditions, and in the ground layers on the left and right side of the super levee, in the similar manner as for the natural ground case. In As2 layer in the gap between the deep mixing and the SCP/SD installation zone, the high values of the ESDR indicates high risk of

liquefaction and the resultant large deformations, which may emerge as the large relative settlements on the surface.

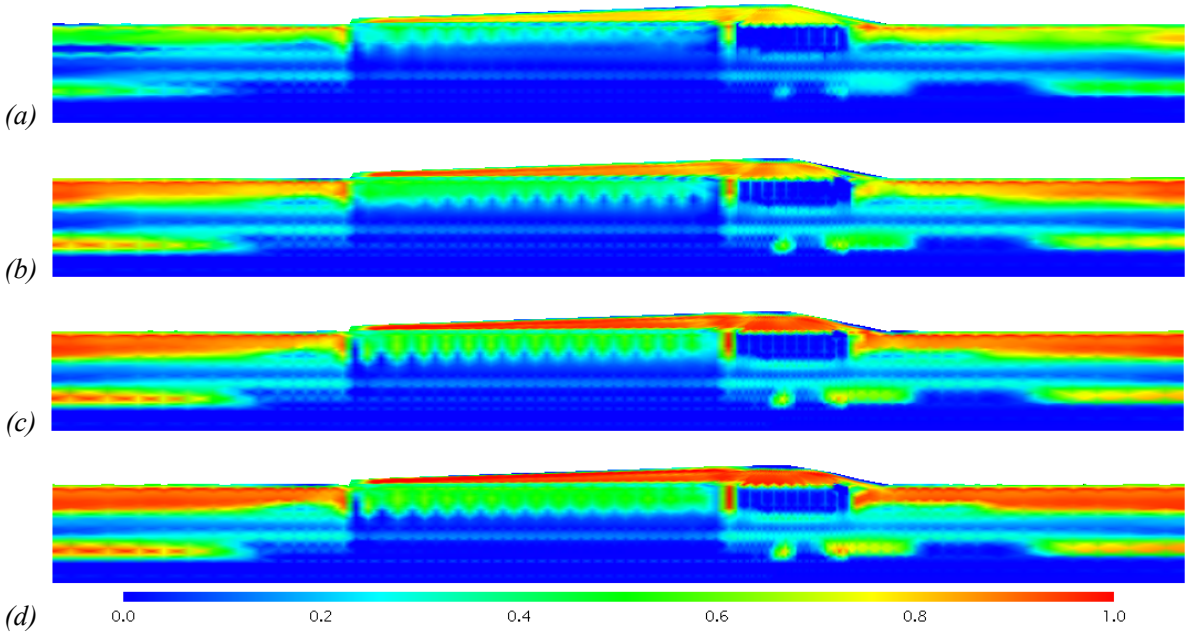


*Figure 5.20. Effective stress decreasing ratio contours for the improved ground case at several times; (a) 5 s, (b) 7.5 s, (c) 10 s, and (d) 20 s.*

#### 5.4.4.2. Excess Pore Water Pressure (EPWP) Responses

The residual EPWP contours at the end of the analysis, at 20 sec, are presented in Figure 5.21 for the natural and the improved ground cases. The contours show the value of excess pore water pressure on each element, which is determined by averaging the values at the surrounding nodes of each element. In the natural ground case, the residual EPWP is developed in the ground layers mostly under the super levee. The highest value of EPWP is observed at As1 layer beneath the main levee, and in the area away from the super levee (i.e., on the left and right side of the super levee). In the improved ground case, however, as the sand drains have been installed, the residual EPWP is reduced throughout the ground layers within the SCP/SD installation zone. Nonetheless, the similar values of EPWP, as those for the natural ground case, are observed in the As1 layer and in the adjacent clay layers, beneath the main levee as well as on the left and right side of the super levee. High level of the residual EPWP after the earthquake indicates a high potential of large deformations, which will be induced by the ensuing consolidation of the ground strata. Therefore, a relatively long-term analysis

of the system after the liquefaction must be considered for the comprehensive evaluation of the deformations.

In order to have a better comparison of the excess pore pressure responses in both cases, the time histories of the excess pore pressure responses at the corresponding nodes along Sections II and V are illustrated, respectively, for the natural ground case in Figures 5.22 and 5.23, and for the improved ground case in Figures 5.24 and 5.25. In general, the buildup of the excess pore water pressure with a positive value is observed in all the layers in both cases, except for the natural ground case in the deep layers, in which negative pore pressure is slightly generated during the motion. At Points J and M, which located on the drainage boundary, the value of the EPWP is zero. Moreover, for the improved ground case, at Point B, which coincides with the position of the sand mat on the ground level, the EPWP is equal to zero. The excess pore pressure responses show a fluctuation with an increasing trend during the quake and a while after. It nearly becomes stagnant with a residual value after about 15 sec.

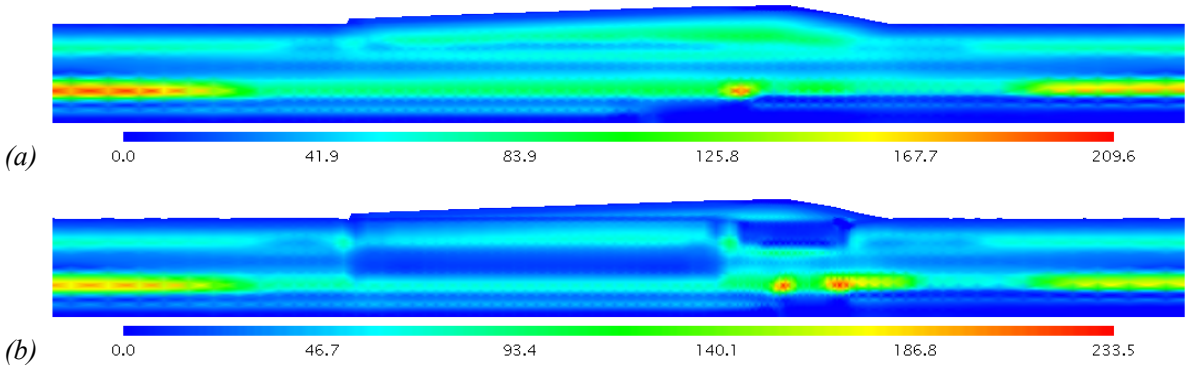


*Figure 5.21. Distribution of the residual EPWP after 20 sec, for (a) the natural ground and (b) the improved ground case, (legend unit: kPa).*

Comparing the EPWP results for the natural ground case and the improved ground case in Section II (i.e., Figures 5.22 and 5.24), which represents the SCP/SD installation zone for the improved case, the improved ground case demonstrates rather larger values of excess pore pressure at the corresponding nodal points, particularly within the sandy layers. Due to the sand drains installation and shortening the drainage paths in the lower layers, the migration of the pore water increases toward the sand drains resulting higher value of EPWP in the nearby soil layers. In addition, more fluctuation is observed at the nodes near sand drains.

For the nodes along Section V (Figures 5.23 and 5.25), which represents the deep mixing part and the underlying area, significant differences are observed in the excess pore pressure responses at the center of deeper layers, between the natural ground case and the improved ground case. In the improved ground case, as the deep mixing walls have been installed under the main levee, the generated excess pore pressure is blocked in the lower layers, which makes a higher level of pore pressure generation in those layers. Furthermore, in the layers within the deep mixing installation zone, the value of the excess pore pressure is significantly smaller compared with the corresponding nodes in the natural ground case.

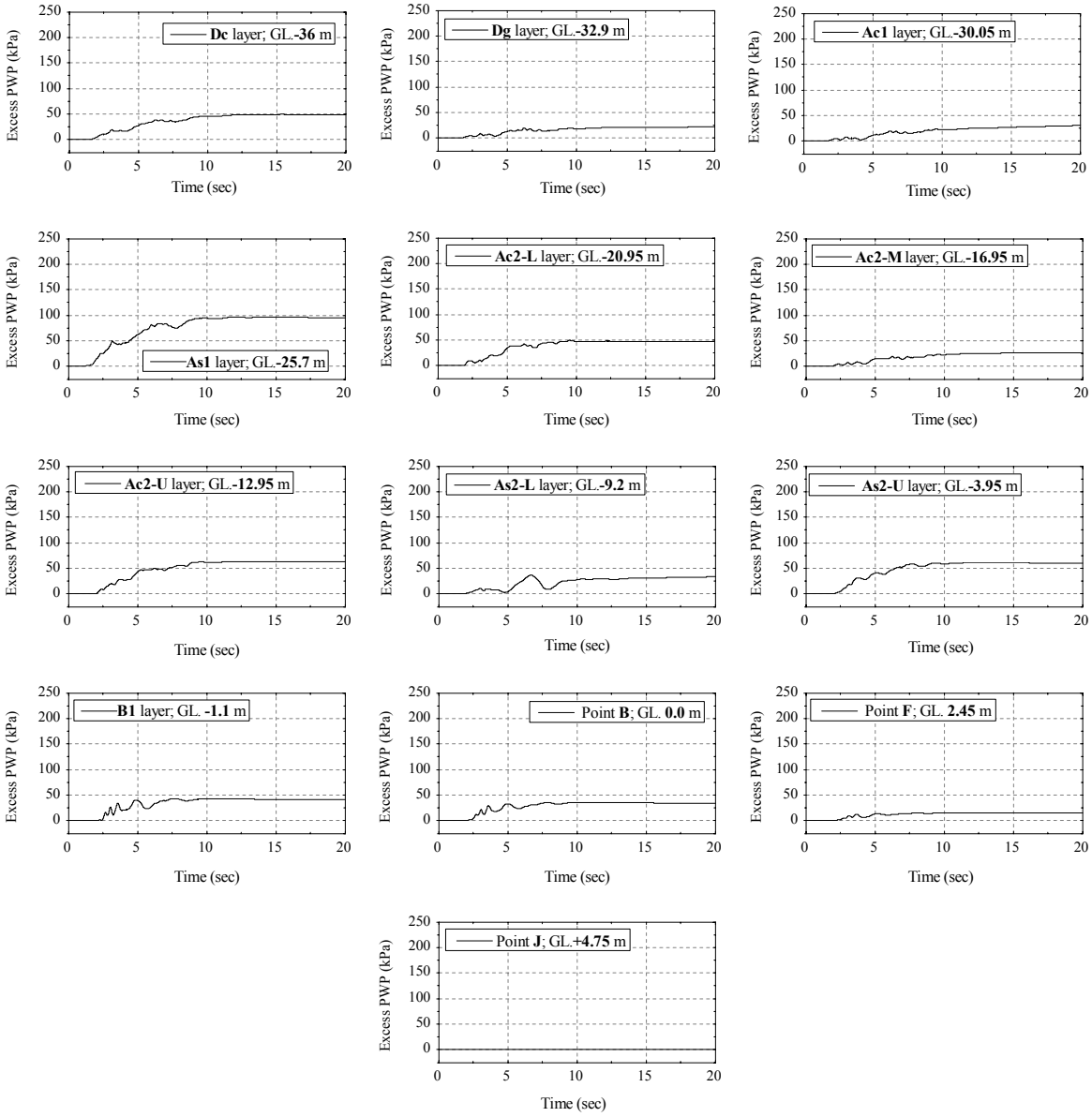


*Figure 5.22. EPWP profiles for the natural ground case along Section II at the center of each subsurface layer and at some points in the super levee.*

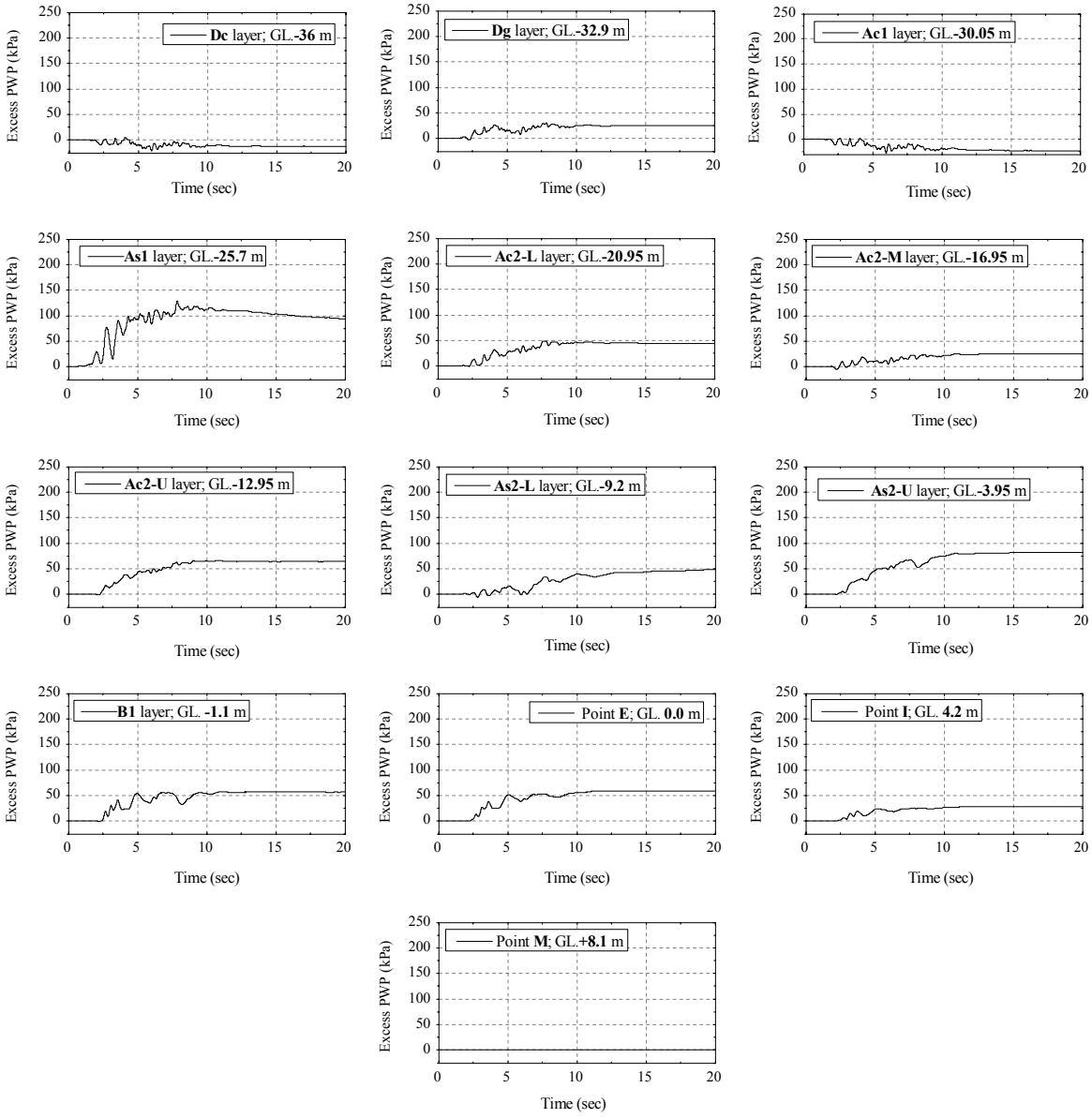


*Figure 5.23. EPWP profiles for the natural ground case along Section V at the center of each subsurface layer and at some points in the super levee.*

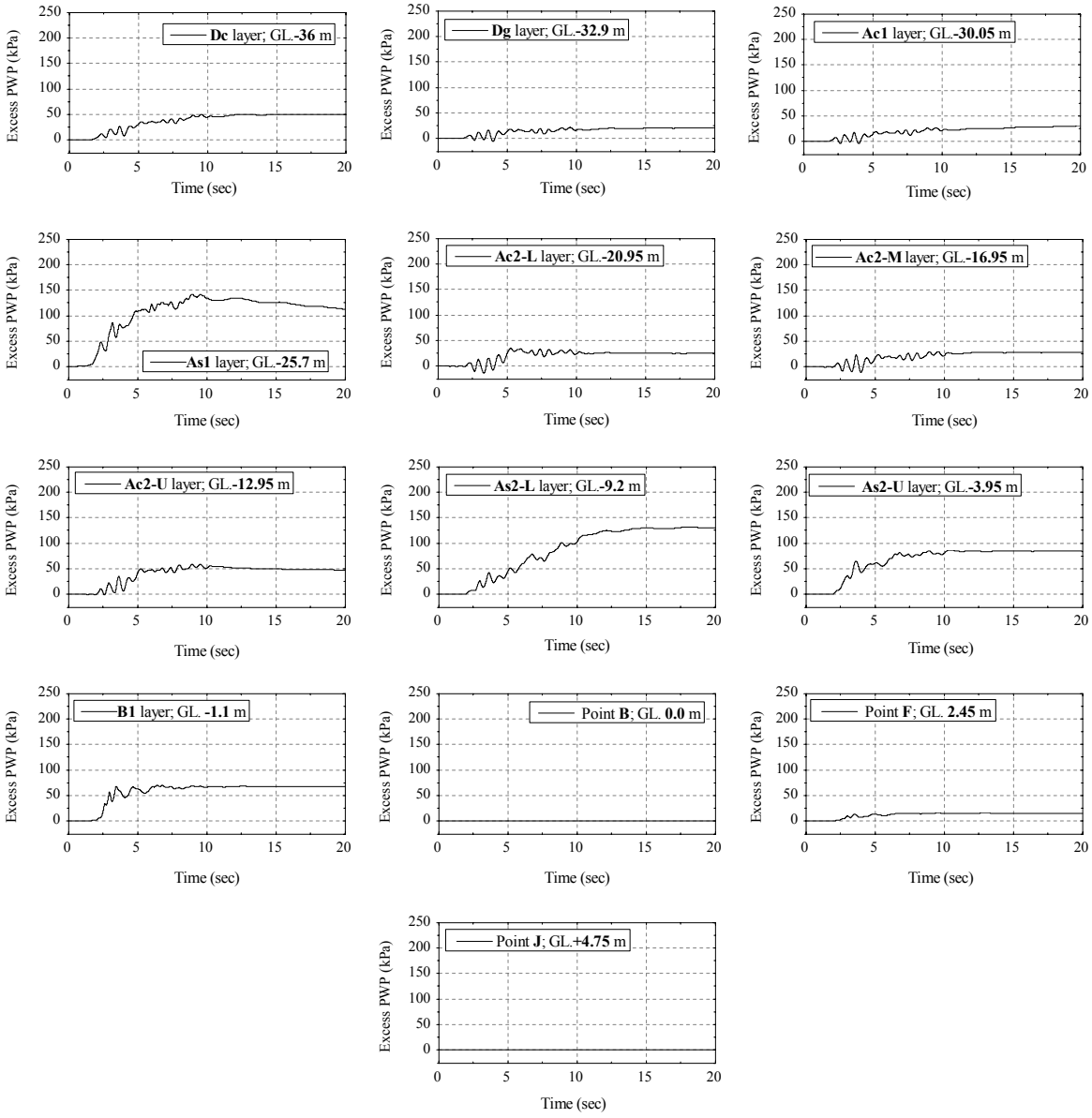


*Figure 5.24. EPWP profiles for the improved ground case along Section II at the center of each subsurface layer and at some points in the super levee.*

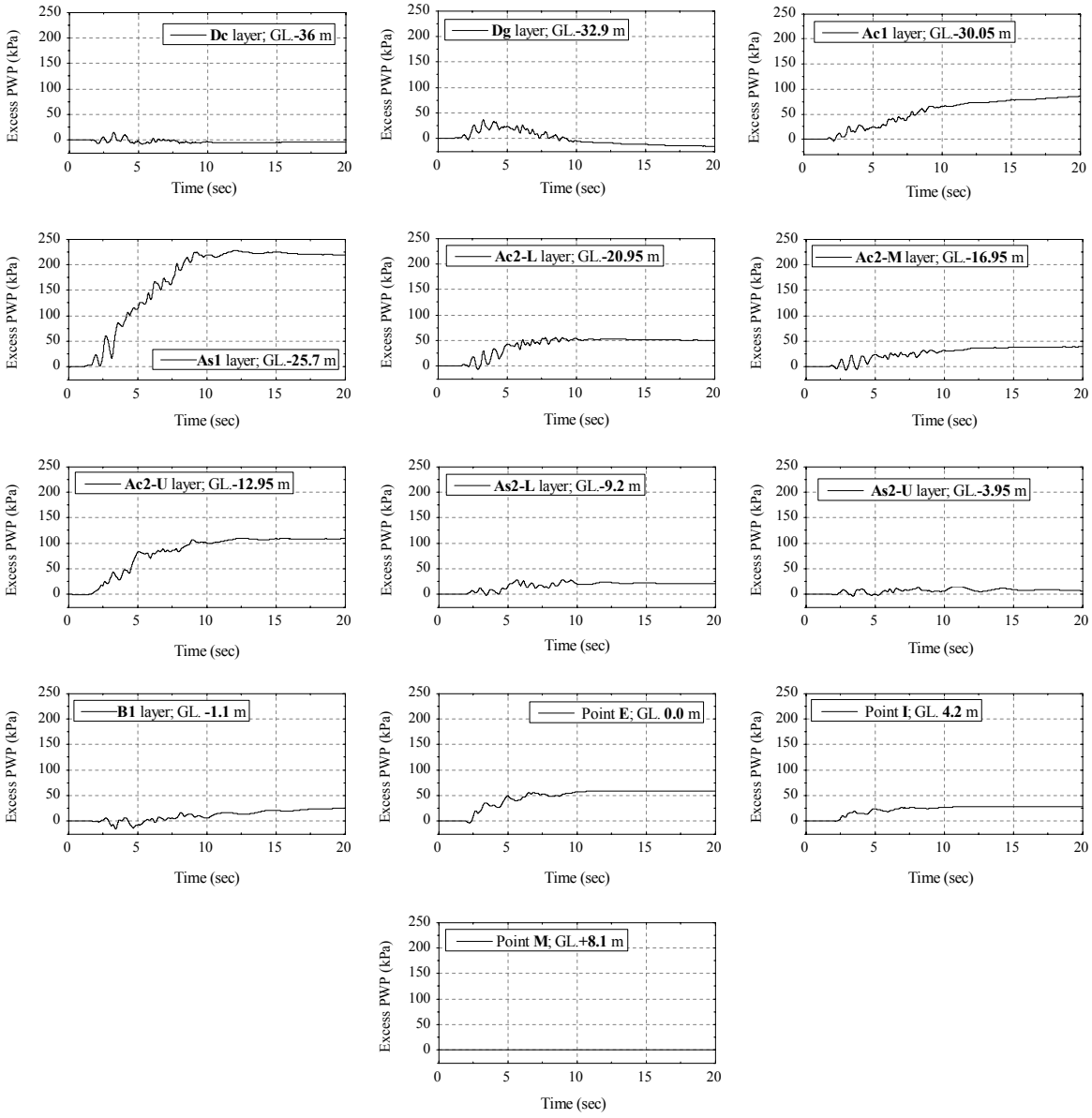


*Figure 5.25. EPWP profiles for the improved ground case along Section V at the center of each subsurface layer and some points in the super levee.*

### 5.4.4.3. Acceleration Responses

The acceleration responses at the center of each ground layer and at some reference points along Section I and III are presented respectively for the natural ground case in Figures 5.26 and 5.27, and for the improved ground case in Figures 5.28 and 5.29. In Section I, where located on the left side of the super levee, both cases exhibit exactly similar responses at the corresponding nodes. In section III, which represents the SCP/SD installation zone for the improved ground case, the results are rather similar in both cases, although slight differences are observed at the nodes nearby the sand drains. Indeed, the improved ground case has different configuration due to the partially ground improvement,

which results in different response to the input motion. At the current section, for instance, the installation of the sand drains causes slightly more attenuation in the acceleration responses, which might be attributed to the higher excess pore pressure buildup in the surrounding soil layers.

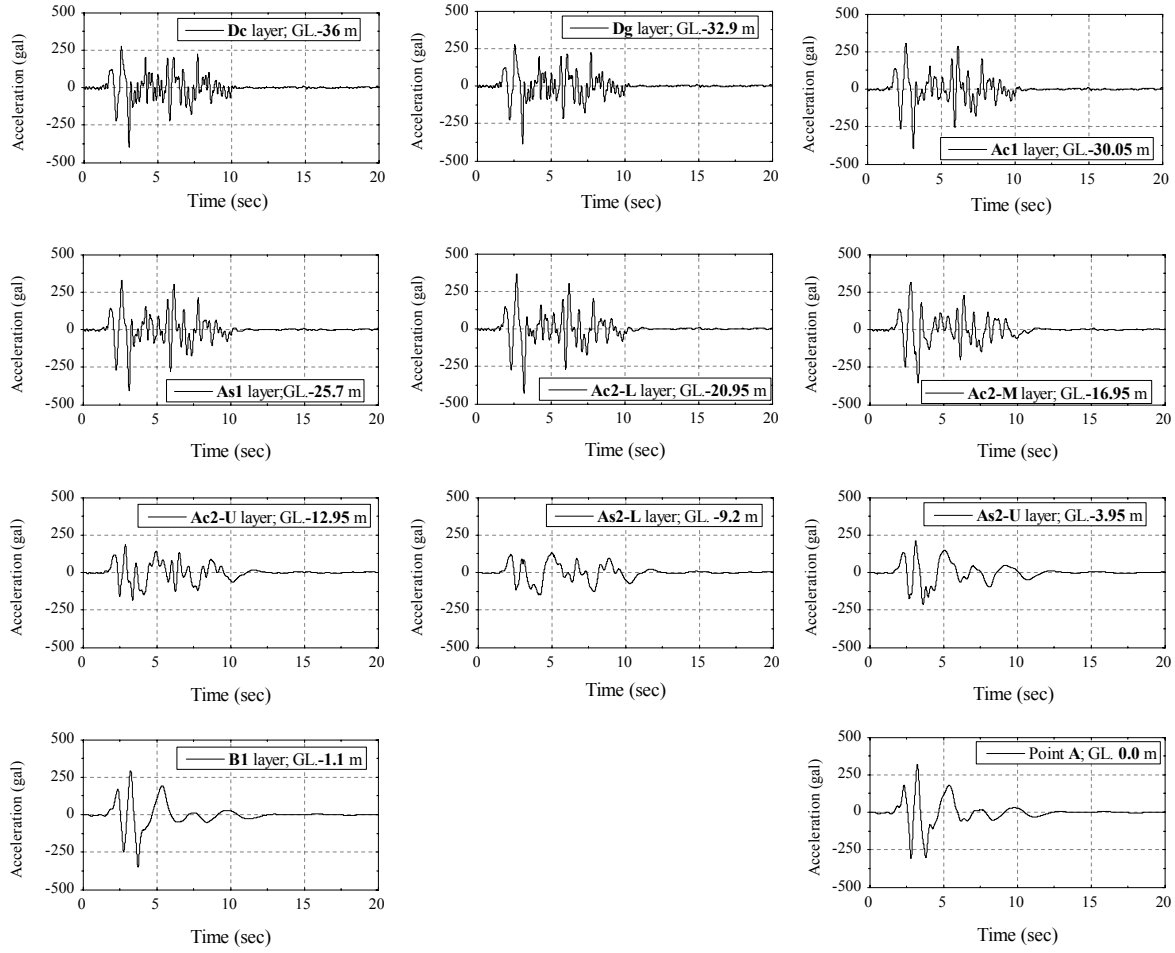


*Figure 5.26. Acceleration responses at the center of each ground layers and super levee layers for the natural ground case along Section I.*

Considering the responses along depth, the deep dense layers Dc and Dg demonstrate the same responses as the input motion. In the upper layers, i.e., Ac1, As1 and Ac2-L, the amplification during the main shock is observed, while aftershock behavior is almost without any fluctuation and similar to the input motion. In the Ac2-M layer and the above layers, the acceleration response emerges as attenuation during the main shock (within 10 sec). By comparing the acceleration responses along depth at Section I and III, as shown in Figures 5.26 and 5.27, it is found that the presence of the super levee results in more amplification in the deeper ground layers and more attenuation in the upper ground layers, due to the difference in the predominant vibrational mode at each section.

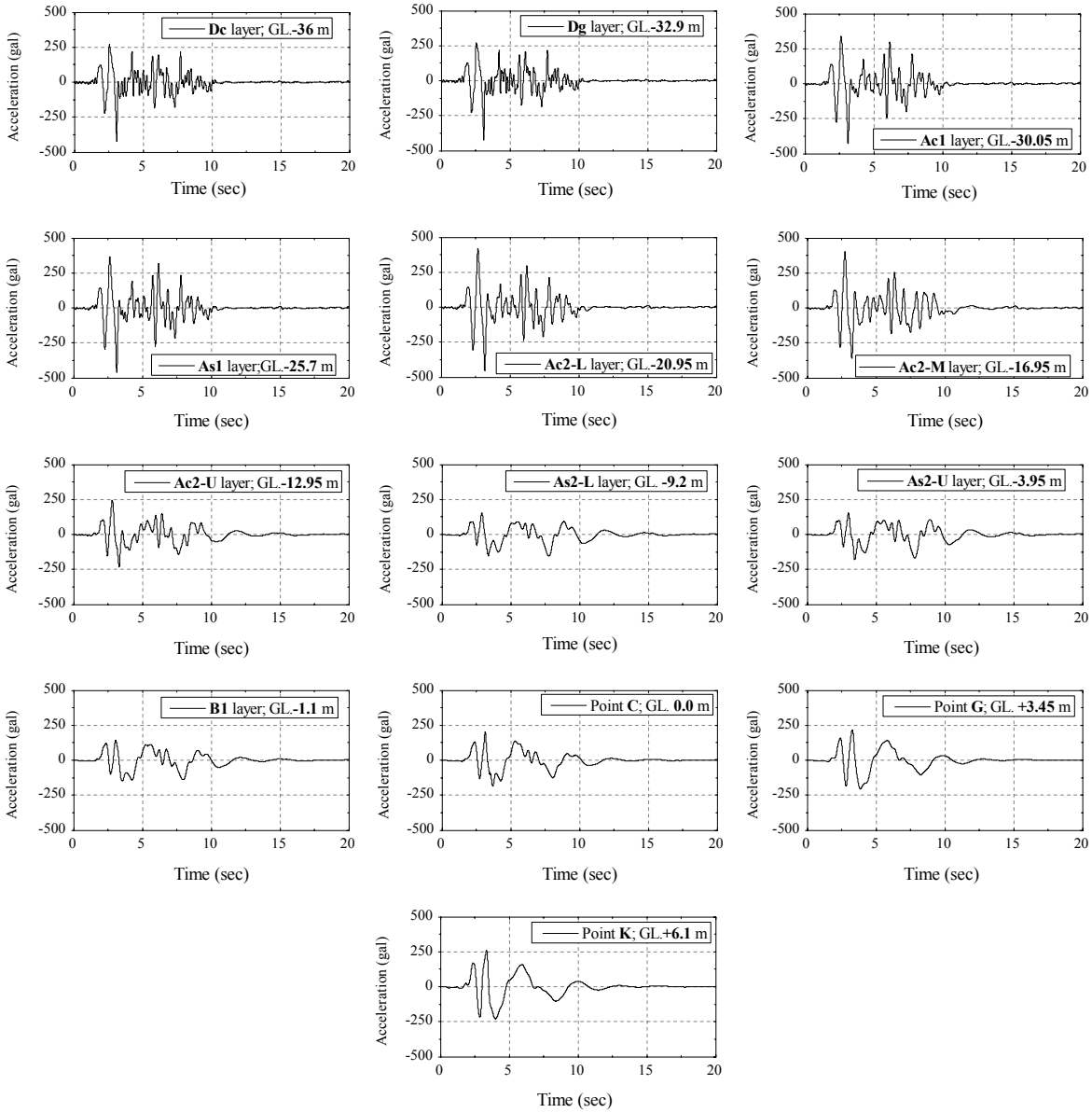


*Figure 5.27. Acceleration responses at the center of each ground layers and super levee layers for the natural ground case along Section III.*

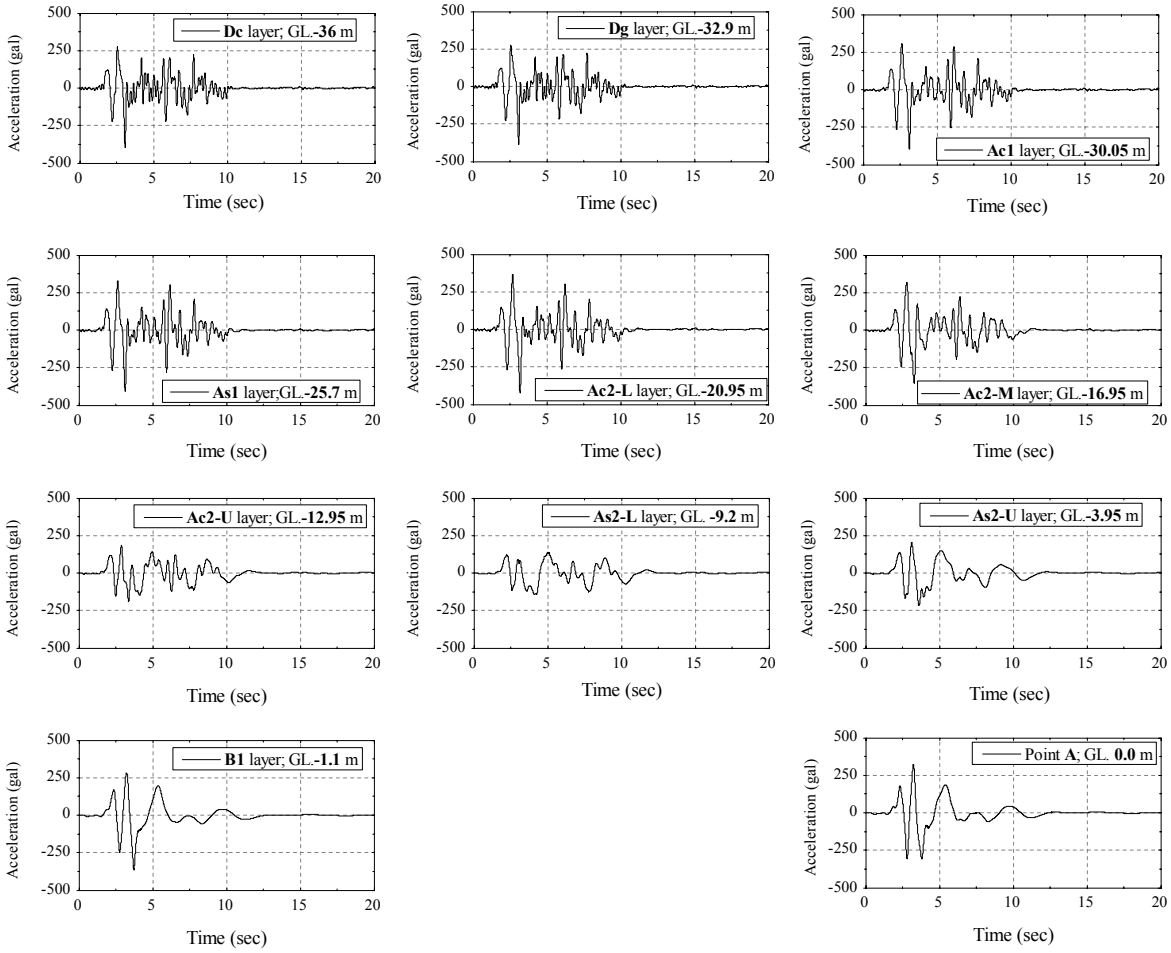


*Figure 5.28.Acceleration responses at the center of each ground layers and super levee layers for the improved ground case along Section I.*

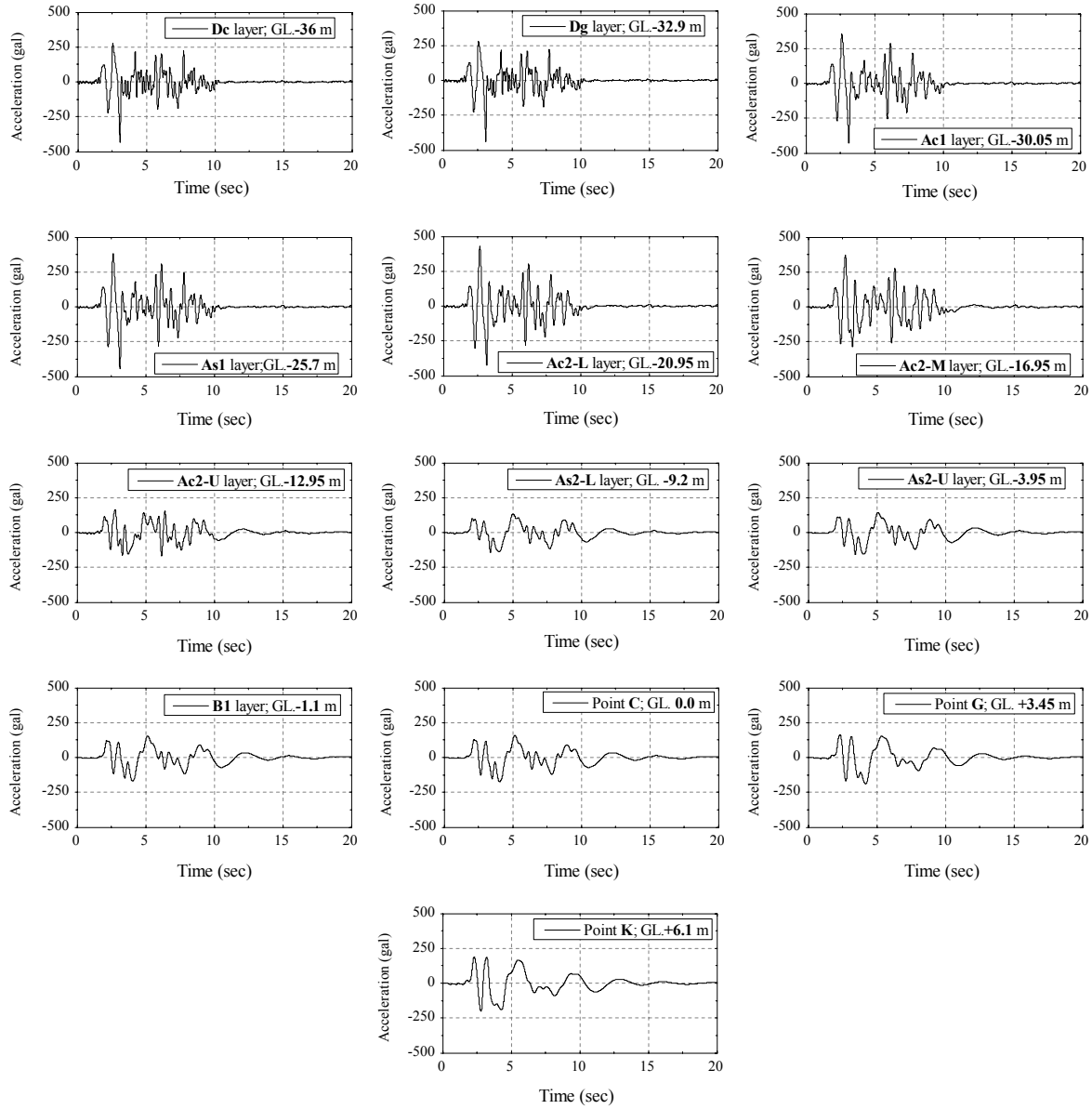


*Figure 5.29. Acceleration responses at the center of each ground layers and super levee layers for the improved ground case along Section III.*

### 5.4.4.4. Horizontal Displacements

The horizontal displacements versus time at the center of the ground layers and at some reference points in the super levee along Section IV are plotted in Figures 5.30 and 5.31 for the natural ground case and for the improved ground case, respectively. Both cases demonstrate similar feature in the fluctuation of the horizontal displacement during the major shock within 10 sec. However, the improved ground case results show smaller range of variation in comparison with the natural ground case. In the natural ground case, the liquefaction-induced lateral deformation emerges after the main

shock in the upper ground layers and in the super levee layers. The residual horizontal displacement of about 95 cm is observed at Point L atop the super levee, at the end of the analysis. This value at the center of B1 layer is about 30 cm. In the improved ground case, the liquefaction-induced lateral movement is significantly reduced, inasmuch as the residual horizontal displacement diminishes to a value about 30 cm at Point L, and to about 5 cm at the center of B1 layer.

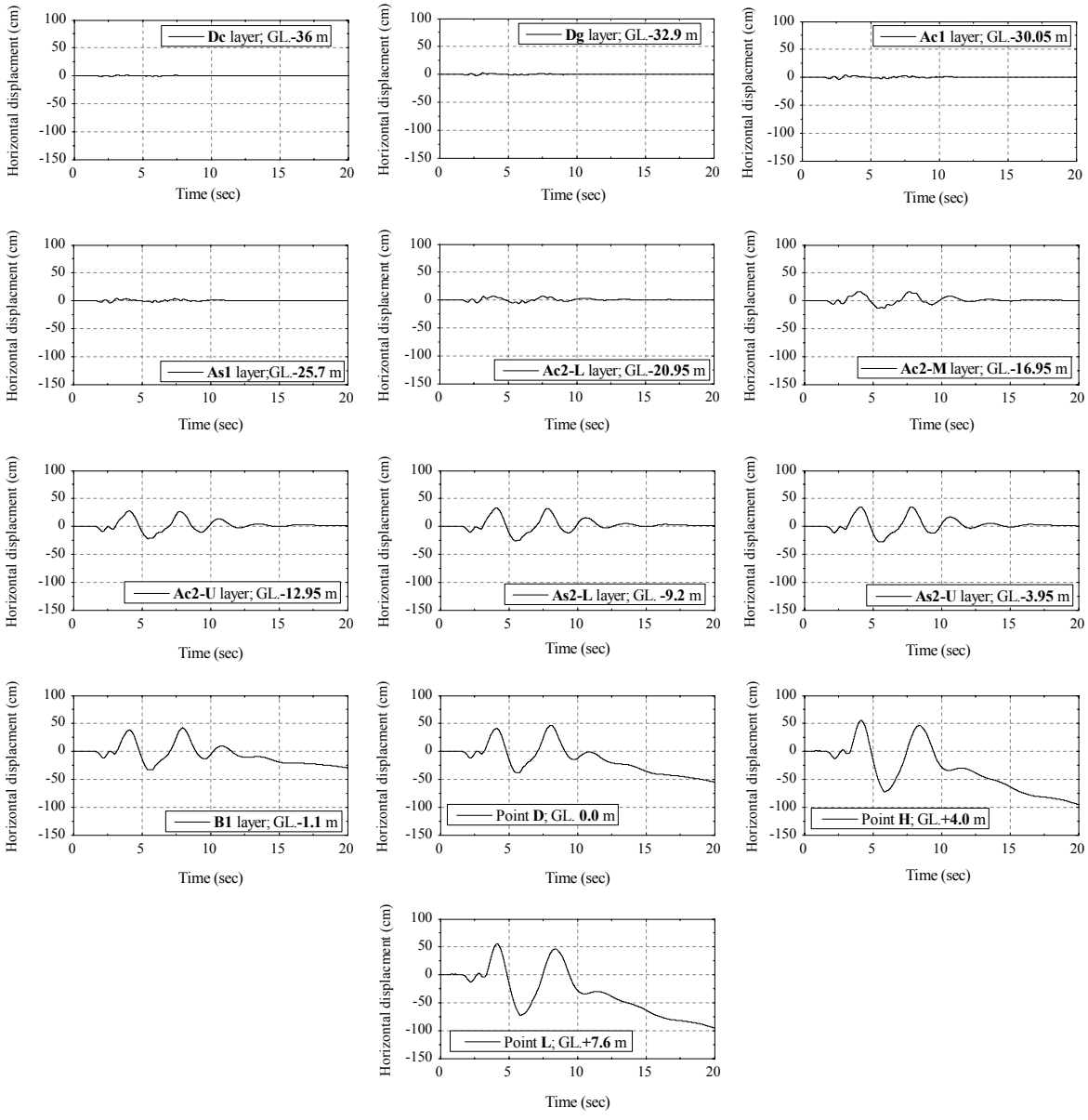


*Figure 5.30. Horizontal displacement profiles along Section IV for the natural ground case.*

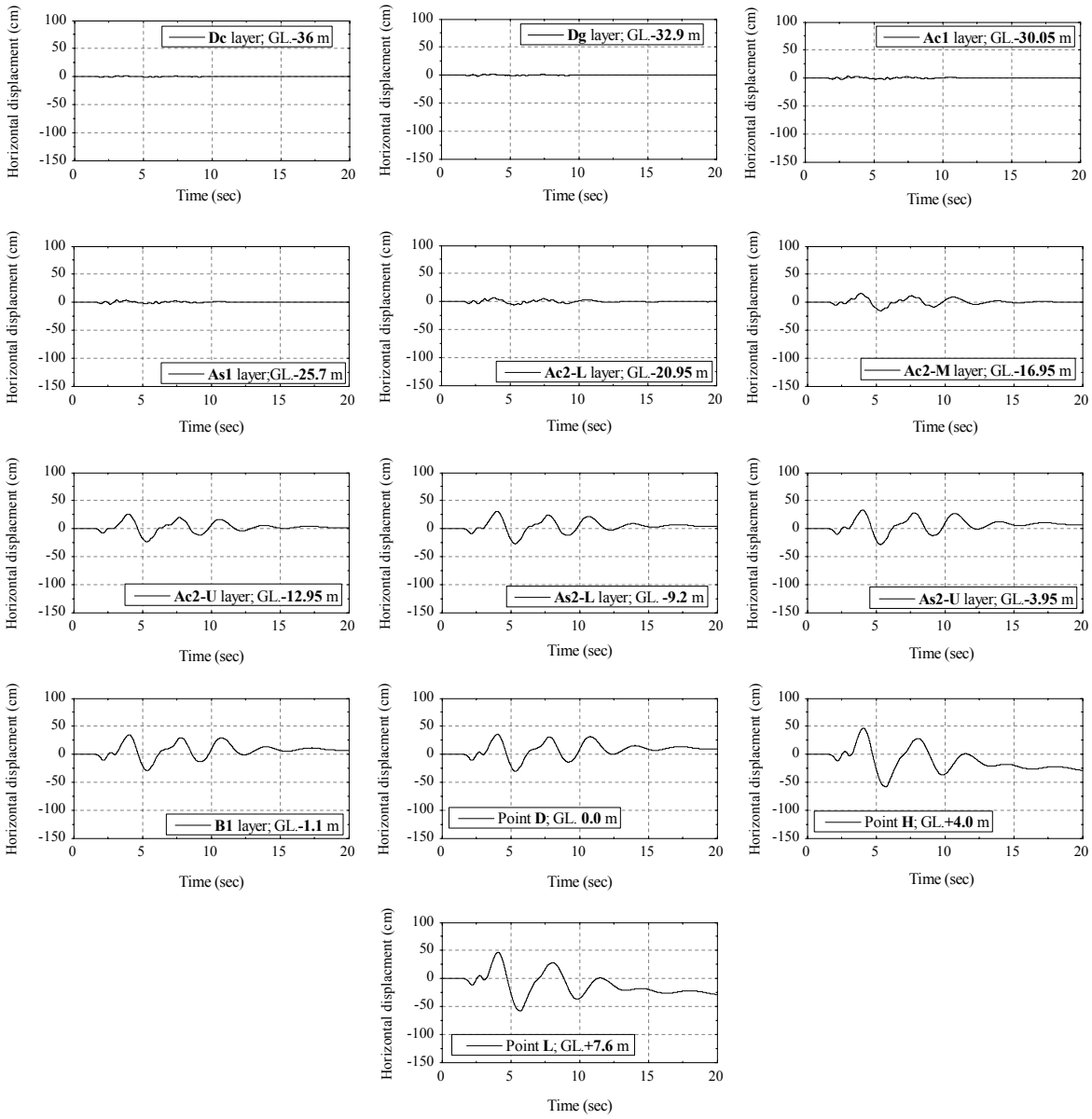


*Figure 5.31. Horizontal displacement profiles along Section IV for the improved ground case.*

### 5.4.4.5. Vertical Displacements

The time histories of vertical displacement along Section I and V are illustrated for the natural ground case in Figures 5.32 and 5.33 and for the improved ground case in Figures 5.34 and 5.35. Both cases show similar feature in the vertical displacement variation along depth. The vertical displacements at the center of the deeper layers, such as Dc, Dg, Ac1 and As1, are almost zero. In the upper layers, however, the displacement increases as the depth of the layer decreases. The large value of vertical displacement is developed in the layers near ground surface and in the super levee.

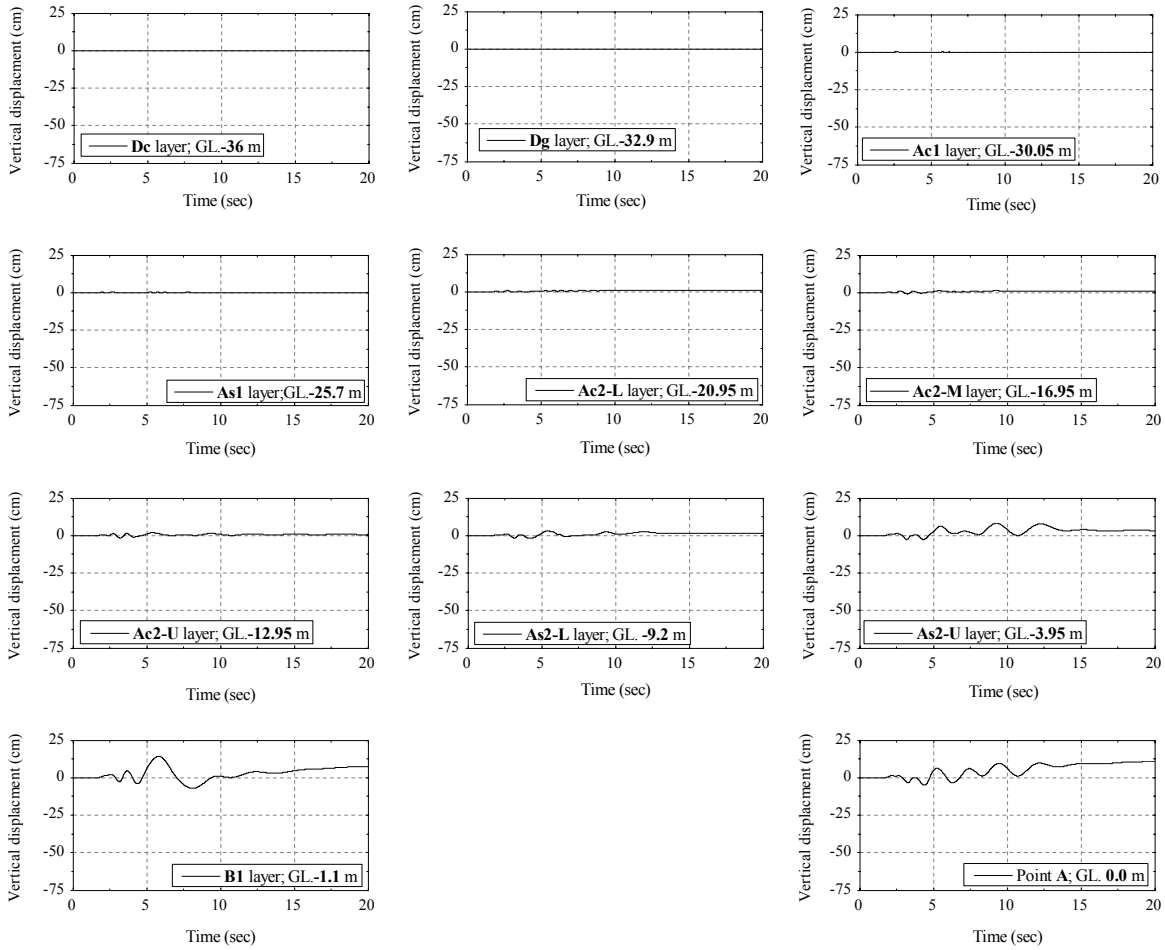


*Figure 5.32. Vertical displacement profiles along Section I for the natural ground case.*

At Section I, the vertical displacement is generally developed as upward movement in the ground layers, in which the displacement increases in the upper layers and the maximum heave is observed on ground surface at Point A with a maximum value of about 12 cm in both cases. At section V, the vertical displacement is observed mainly as the settlement in the layers. In the upper layers, the settlement increases due to the liquefaction, of which the maximum settlement is observed at Point M, atop the super levee, with a value of about 70 cm for the natural ground case. For the improved ground case, however, due to the installation of deep mixing walls in that section, the settlement substantially decreases, inasmuch as the settlement atop the main levee centerline at Point M is reduced to 40 cm, and in the other ground layers, the settlement is insignificant.

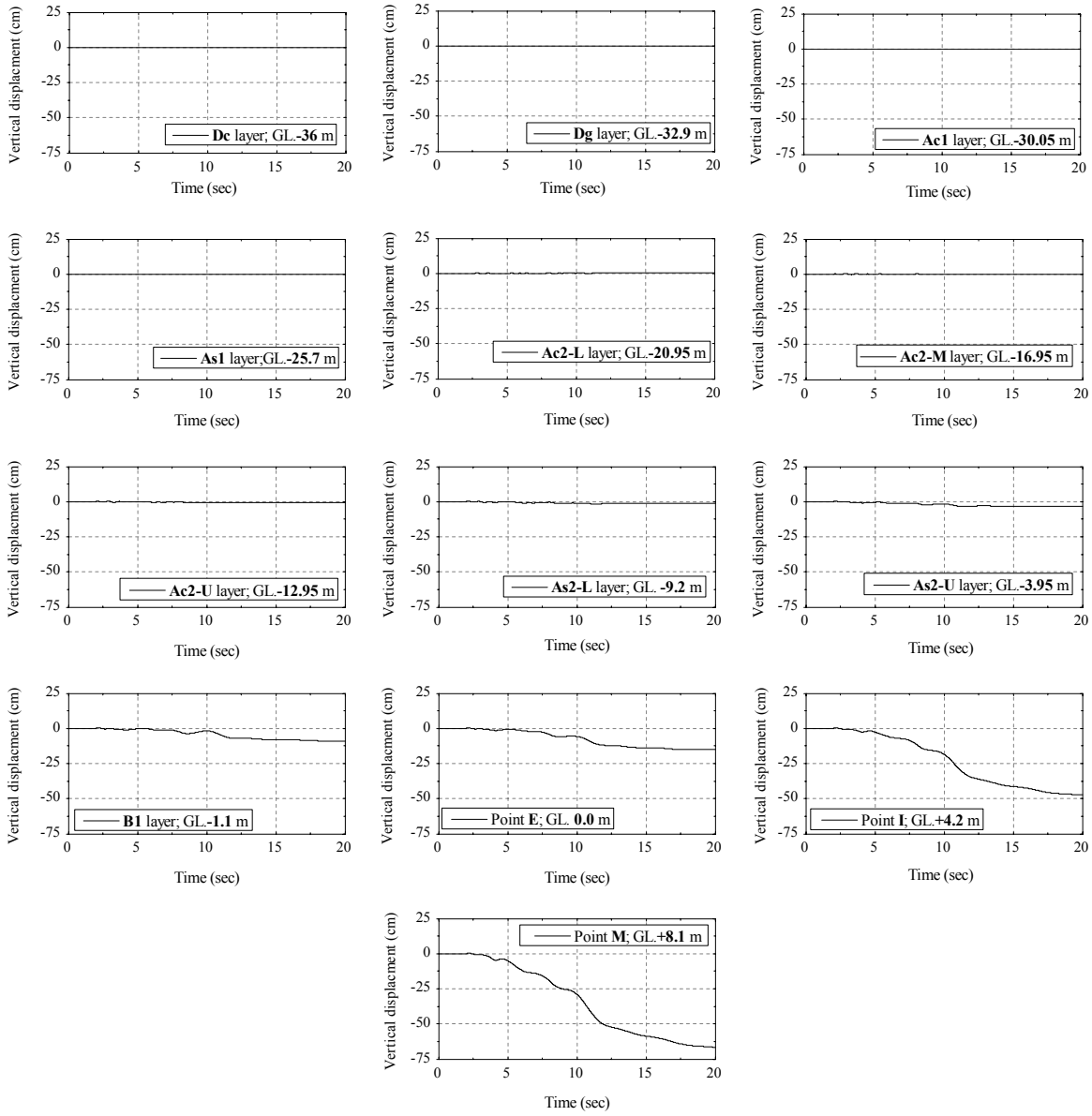


*Figure 5.33. Vertical displacement profiles along Section V for the natural ground case.*

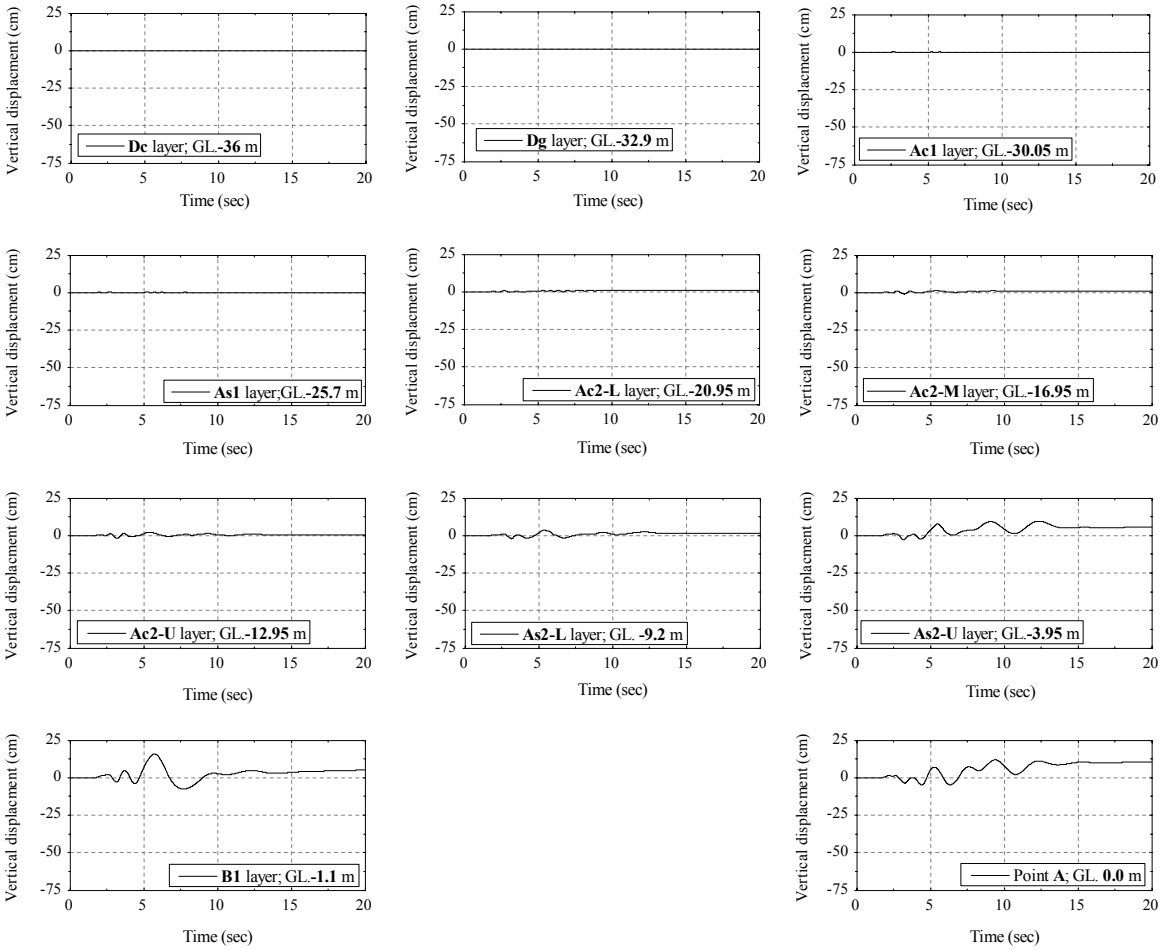


*Figure 5.34. Vertical displacement profiles along Section I for the improved ground case.*

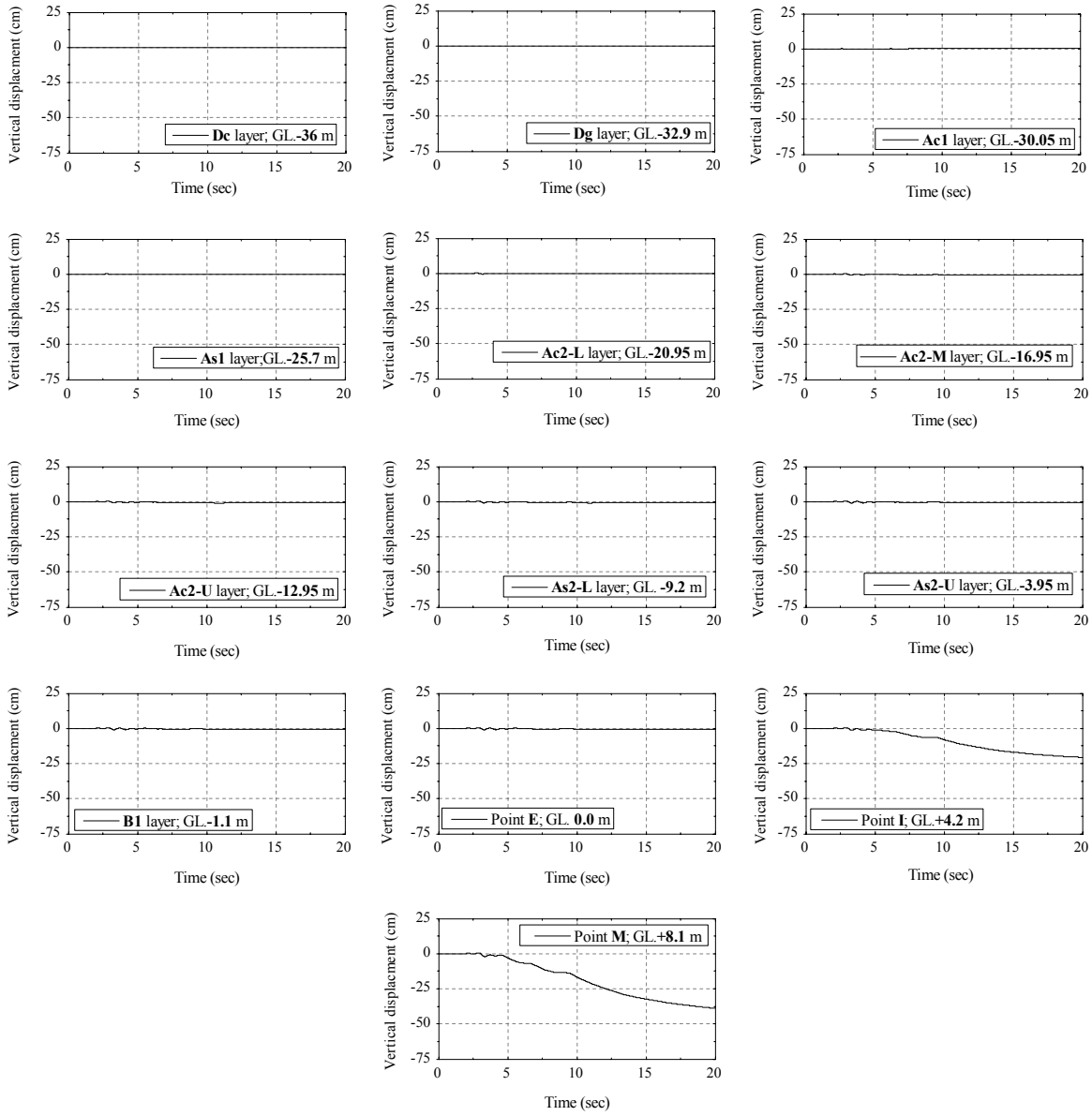


*Figure 5.35. Vertical displacement profiles along Section V for the improved ground case.*

### 5.4.4.6. Vertical Strain

The vertical strain distributions for the natural ground case and the improved ground case are presented in Figures 5.36 and 5.37 at several steps of analysis. In the natural ground case, the localization of the vertical strain is appeared as the compression with positive values around the top of the main levee and as the extension with negative values around the left- and right-side toe of the super levee. The overall feature of the vertical movements is appeared as the settlement beneath the super levee and ground heaves on the left and right side of the super levee. The values of the vertical strain in the localized areas increase by progress of the motion, and it reaches to the highest value at 20 sec. In the improved ground case, the localization of vertical strain follows the same feature as for

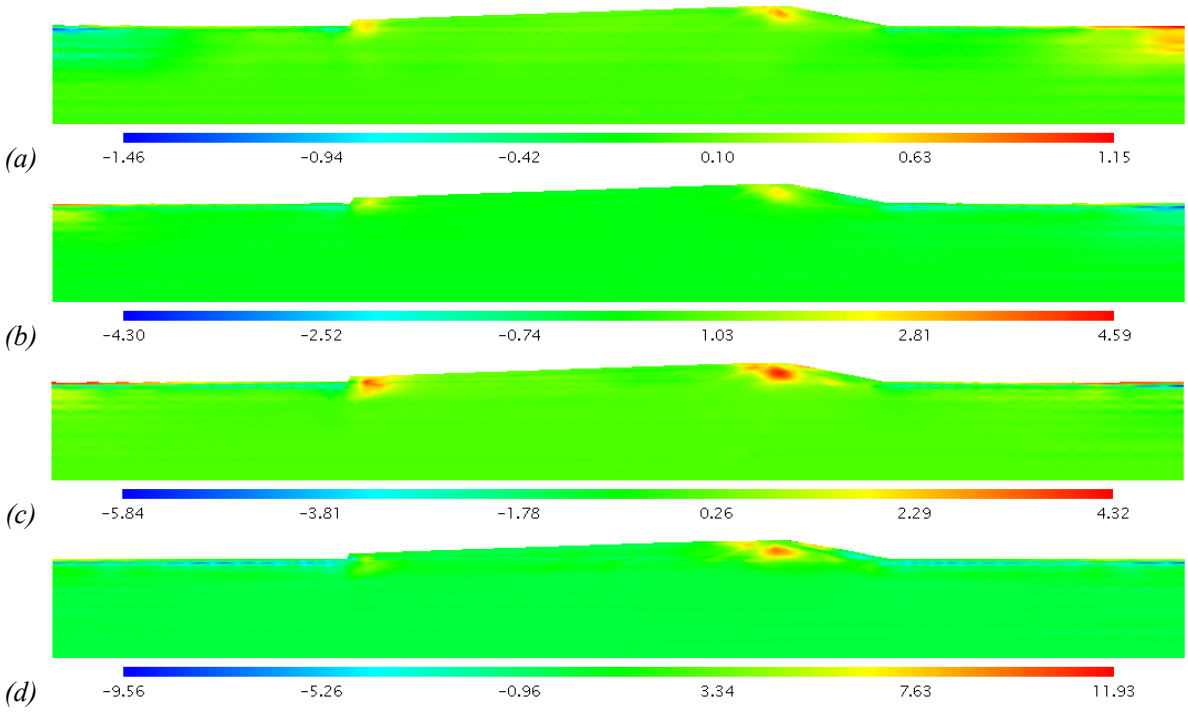


*Figure 5.36. Vertical strain distribution contours for the natural ground case at various times; (a) 5 s, (b) 7.5 s, (c) 10 s, and (d) 20 s. (legend unit: %).*

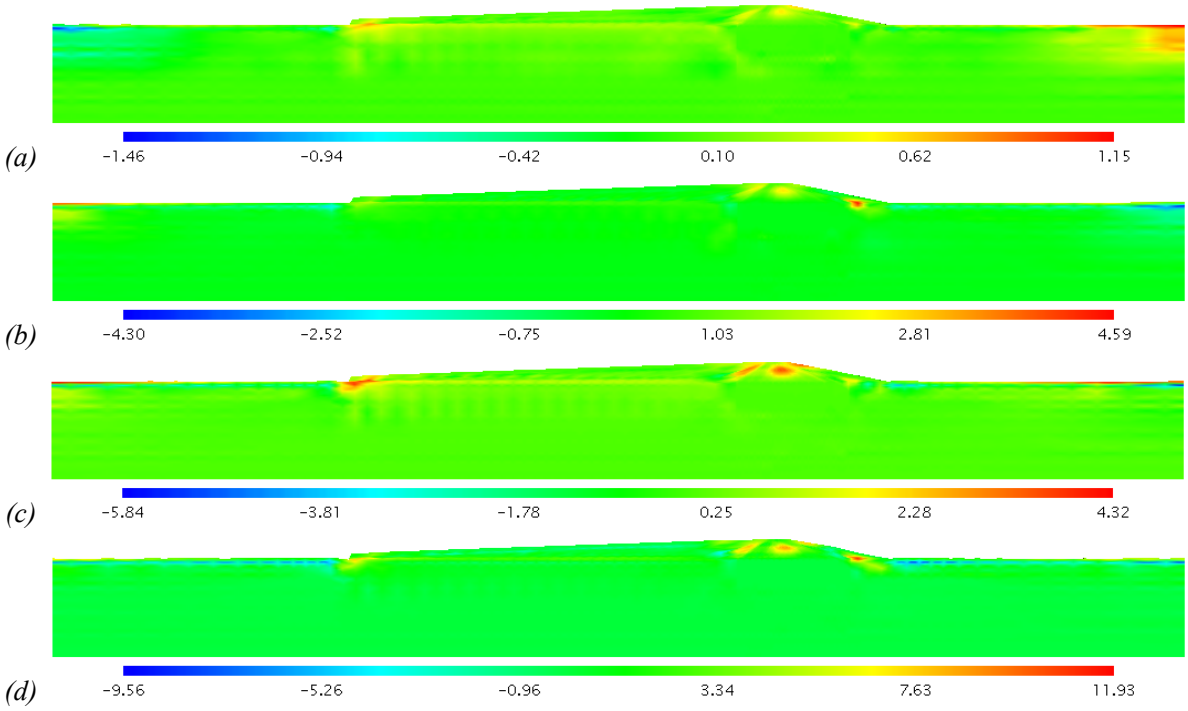


*Figure 5.37. Vertical strain distribution contours for the improved ground case at various times; (a) 5 s, (b) 7.5 s, (c) 10 s, and (d) 20 s (legend unit: %).*

the natural ground case. The vertical strain is localized in the toes of the super levee, as well as around the top of the main levee. However, the progress of the strain localization inside the super levee is smaller, since the deep mixing walls have been installed underneath the main levee.

#### 5.4.4.7. Accumulated Plastic/Viscoplastic Shear Strain

The distribution contours of the accumulated plastic/viscoplastic shear strain at several steps of analysis are shown in Figures 5.38 and 5.39 for the natural ground case and the improved ground case, respectively. In the natural ground case, the accumulated plastic/viscoplastic shear strain is localized throughout of the upper sand layers B1 and As2 and in the upper part of Ac2-U layer. In addition, the strain localization is observed in some parts of the super levee and on the ground surface beside the super levee. At the end of the analysis, at 20 sec, the high levels of localization are observed in the B1 layer beneath the super levee and on the super levee sides. In the improved ground case, the strain localization is developed in back slope part of the super levee, on the surface ground by both sides of the super levee, and notably around the right toe of the super levee over the DMM installation zone.

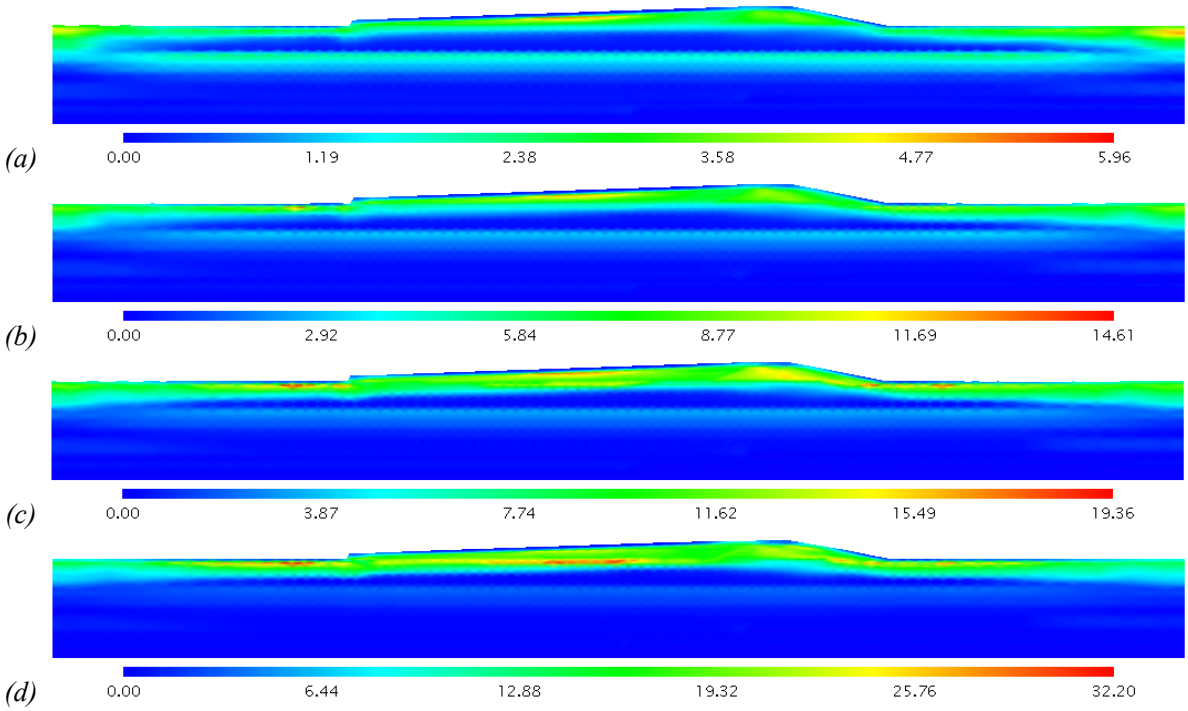


*Figure 5.38. Accumulated plastic/viscoplastic shear strain contours for the natural ground case at (a) 5 s, (b) 7.5 s, (c) 10 s, and (d) 20 s, (legend unit: %).*

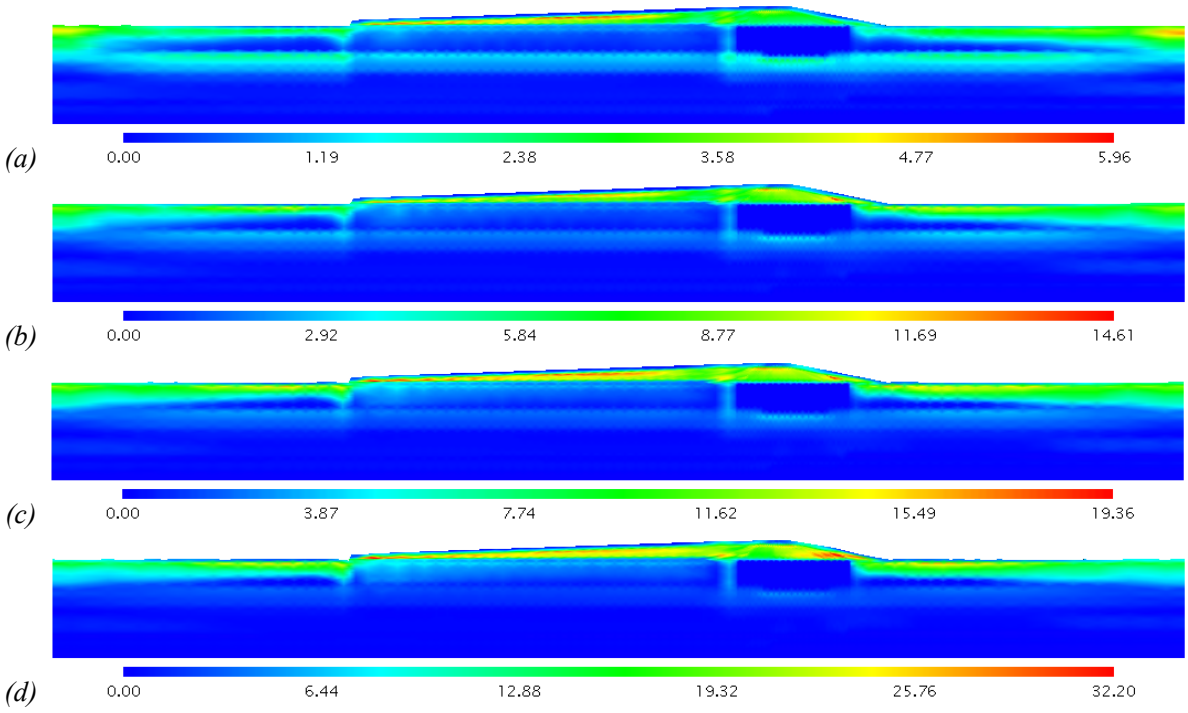


*Figure 5.39. Accumulated plastic/viscoplastic shear strain contours for the improved ground case at (a) 5 s, (b) 7.5 s, (c) 10 s, and (d) 20 s, (legend unit: %).*

## 5.5. Concluding Remarks

In order to simulate the large deformation problems under dynamic loading conditions, a FEM-based computer program was developed considering the finite deformation theory for a two-phase mixture. The cyclic elasto-viscoplastic model as described in previous chapter was adopted to represent the characteristic behavior of clay material. Furthermore, the cyclic elasto-plastic model was employed for the sandy layers to simulate properly the liquefaction phenomenon in those layers. The *u-p* formulation with the updated Lagrangian scheme was presented for the dynamic analysis. Newmark's $\beta$ method was employed for the discretization the governing equations in time. The nonlinear relation between the stress and the stretching tensor for the elasto-viscoplastic materials was then derived using the tangent stiffness method.

The dynamic strain localization, as an example of large deformation problem, was studied on clay specimen characterized by Torishima Ac2-U layer parameters. The mesh pattern of 10×20 (200 elements) was assumed as the default mesh. The shear band developing process was studied through the evaluation of the results for the axial strain, the accumulated viscoplastic shear strain, the viscoplastic volumetric strain, and the mean effective stress, in addition to the deformed mesh. Comparing the partially drained and undrained cases, the presence of drainage boundaries have not

shown significant effects, due to the rapid rate of loading and also the low permeability of the clay. Considering the mesh-size dependency, the results for different mesh configurations showed consistency in terms of the overall shape of deformation and stress-strain behavior. Furthermore, convergency in the stress-strain relations was manifested through the mesh refinement.

Finally, the dynamic analysis of the Torishima super levee was conducted through the natural ground case and the improved ground case. Fully saturated conditions were assumed for both embankment and ground layers. This assumption refers to a worst-case scenario in which earthquake occurs after the heavy rainfall. This scenario is most likely to happen in Japan due to the high risk of heavy rains and large magnitude earthquakes. After 20 sec of an earthquake with a maximum acceleration of 509 gal, the onset of the liquefaction, with the criterion of ESDR equal to 1, was observed in the upper sand layers of the ground, in the deep sand layer, and in the most parts of the super levee due to its initial saturation, for the natural ground case. Consequently, large deformations occurred in the super levee and nearby ground surface, with a maximum settlement of about 70 cm at the crest of the super levee, and with a maximum lateral movement of about 95 cm atop the back slope of super levee. However, based on the large amounts of residual excess pore pressure within the subsurface layers after 20 sec of motion, it is anticipated to develop much more deformations following the pore pressure dissipation during the subsequent consolidation.

In the improved ground case, the liquefaction beneath the super levee was substantially mitigated by installation of the SCP/SD and the deep mixing walls. Nonetheless, in the whole part of the super levee, due to its initial fully saturated conditions, and in the gap between the deep mixing part and SCP/SD installation zone, high level of ESDR was observed indicating the occurrence of liquefaction in those areas. This emphasizes the necessity of improvement in the super levee layers in addition to the ground layers. The improvement of the super levee materials can be accomplished by choosing the appropriate fill materials and proper compaction during the construction. Moreover, the complementary improvement techniques, such as drain installation or cement mixing methods, can be employed for that purpose.

# Chapter 6

# CONCLUSION AND RECOMMENDATION FOR FUTURE STUDY

## 6.1. Summary and Conclusions

In the current research, the numerical analyses of the Torishima super levee in Osaka City, Japan, were carried out in the framework of finite deformation theory, with a particular focus on the behavior of sensitive soft clay layers. The numerical analysis was divided into two main parts; i.e., the long-term consolidation analysis and the dynamic analysis. The large-scale levee has been constructed in downstream of the Yodo River, on multilayered soft soil deposits. At first, the behavior of soft clay specimens under triaxial conditions was studied through the elasto-viscoplastic modeling considering the destructuration. The effects of destructuration were investigated by comparing the predicted results with the experimental data from undrained triaxial compression tests. The effects of destructuration were then evaluated in a boundary value problem, as the consolidation analysis of an embankment construction on one-layer soft clay foundation. The construction procedure of the embankment was taken into account following the assumed loading profile. The finite element formulations based on the finite deformation theory were adopted for the numerical simulations, whereby the large deformations induced by the embankment construction on soft soil deposit can be properly taken into account. The staged construction procedure of the embankment was applied to appropriately simulate the construction sequence in which the stiffness and the consolidation of the embankment are considered in addition to the embankment loading.

Afterwards, the consolidation analysis of the Torishima super levee was conducted as the natural ground and the improved ground cases, by which the effects of the destructuration aspects and the effects of each improvement techniques were properly studied. As the second part, for the dynamic analysis, a cyclic elasto-viscoplastic model was presented and its performance was verified through the cyclic and monotonic triaxial test simulations. Based on the finite deformation theory, the finite element formulations for dynamic analysis were derived and explained in detail. A finite element based computer program was developed which incorporates the cyclic elasto-viscoplastic constitutive model for clays and the elasto-plastic constitutive model for sands. The localization analysis of the soft clay specimen was carried out under dynamic loading conditions using the developed code. Finally, the dynamic analysis of the Torishima super levee was accomplished through the natural ground case and the improved ground case. The following conclusions are drawn from the present study.

In Chapter 2, from the modeling of Osaka soft clay specimen and the comparison with experimental results, it was found that the consideration of the destructuration of sensitive soft clay, as the structural degradation and the strain-dependent shear modulus, significantly improves the predicted responses. Although consideration of the structural degradation leads to a substantial improvement, in terms of strain softening and post-peak responses, the strain-dependent shear modulus was applied to reproduce more precise behavior, particularly before the peak stress in the stress-strain relations. In the consolidation analysis of an embankment on soft clay foundation, the results clarified the effects of these considerations of which large strain and consequent deformations developed due to the structural degradation during consolidation. Moreover, the buildup of pore pressure after the completion of the construction was observed in the narrow zone close to the embankment; this is similar to the field-measured evidence reported by Mesri and Choi (1979), Leroueil et al. (1979), Mitchell (1986), etc. Considering the strain dependency of the shear modulus, however, larger strain and larger displacements developed not only during the consolidation, but also during the construction of the embankment.

In Chapter 3, as the first phase of the consolidation analyses of the super levee construction, by comparing the results of the natural (unimproved) ground cases, the same outcomes as those in Chapter 2 are obtained for the effect of the destructuration aspects. The structural degradation was found to have a significant effect on the after-construction responses of the pore water pressure and the associated strain localization. On the other hand, the strain dependency of the elastic shear modulus, as another aspect of destructuration in soft clay, was found to affect the behavior at an earlier stage of loading, which appears as relatively large deformations during the construction process, and therefore, during consolidation. As the second phase of the consolidation analyses, by comparing the results of the improved ground case with the natural ground case, the performance of

each ground improvement techniques were evaluated. The performance of sand drains, in shortening the drainage paths and accelerating the consolidation rates, was clearly observed through the settlement profiles and the excess pore water pressure contours. The effect of DM walls was observed as reducing the overall settlements beneath the main levee, and also as creating a low-permeability top layer over the clay layers which decelerate the dissipation rate beneath the main levee. It was found that even after ground improvements, large relative displacements are observed in the ground level and atop the super levee. Consequently, in order to construct a large scale river embankment for flood disaster mitigation, it is necessary to carefully estimate unequal settlement of ground.

In Chapter 4, the cyclic elasto-viscoplastic model was reformulated in terms of the inclusion of the kinematic hardening rule for volumetric strain. Through the triaxial test simulation of Nakanoshima clay by integration of the cyclic elasto-viscoplastic constitutive equations, the effect of the reformulation was found to be as more softening behavior in the stress-strain relations and consequently more deformation at the same shearing level. Furthermore, the consideration of linear evolution equation for the kinematic hardening parameter for volumetric strain has shown insignificant influence in the simulated results using the material parameter of Nakanoshima clay under undrained loading condition. However, the effects appeared to be more significant under drained loading conditions such as cyclic compression test.

In Chapter 5, the shear band developing under dynamic loading conditions was clearly observed within the strain distribution and the mean effective stress contours. Assuming partially drained conditions have notably not affected the strain localization results, since the applied loading was very fast and the adopted permeability coefficient for the clay was very low. Considering the mesh-size dependency, the results showed a higher level of strain localization within narrow width for the finer mesh size, since the shear bands span across the smaller elements. In addition, from the dynamic analyses of the super levee in the unimproved and improved ground cases, the ground improvement techniques is found to be efficient on the prevention of the liquefaction beneath the super levee. Nonetheless, the high potential of liquefaction in the super level layers and in the gap between the DM part and SCP/SD installation zone clearly indicates the inadequacy of the current ground improvement scheme.

## 6.2. Recommendations for Construction Guideline of Super Levee

A comprehensive study on the behavior of a super levee construction on soft ground was carried out in terms of the long-term consolidation analysis and the dynamic analysis. From the analysis results,

following recommendations are given for design and construction of super levees on soft deposits, which can be employed to revise the existing guideline.

1. The long-term consolidation analyses have shown a significant influence of the destructuration of sensitive soft clay layers on the long-term behavior of super levee, which appears as the strain localization and anomalous response of pore water pressure. Therefore, it is necessary to properly take into account the degradation of sensitive soft clay in the design analysis of super levees.

2. The consolidation analysis of the improved ground case has shown quite significant strain localization and ensuing surface deformations even after ground improvement. The strain localization is mainly developed in the upper part of soft clay layer Ac2, wherein the SCP/SD has been installed. Based on the super levee geometry, the highest influence of the embankment loading is applied on that region. It seems that the improvement techniques and in particular the preloading process have not been sufficient to improve the characteristic properties of the soft clay in that region. The preloading scheme show a gap between the toe of the main levee and the location of the temporary fills. Consequently, a revision on the preloading scheme is recommended for the future construction sites.

3. In the settlement profiles for the super levee construction on improved ground, relatively large displacements are observed following the unsymmetrical geometry of the super levee. The heterogeneity conditions and subsequent relative deformations become escalated due to the inequality of the ground improvement techniques in the strengthening of ground layers. Thus, it is recommended to avoid any intense changes in the ground condition induced by ground improvement. The ground improvement should be consistent with the applied loading of the embankments construction.

4. To predict the superficial cracks and settlements atop the super levee, it is recommenced to monitor the ground level settlements during the construction and a while after completing the construction. The settlements on the top of the super levee are in correspondence with the ground level profiles; hence, any large relative displacement in the ground level potentially leads to the surface deformations, which emerge as the local superficial cracks due to the weakness of embankment materials.

5. From the dynamic analysis of the super levee, it was found that the super levee layers are highly susceptible to liquefaction and the consequent large deformations. Hence, the special attentions should be paid to the selection of fill materials for the super levee layers in terms of the grain size distribution and the relative density, by which the liquefaction potential can be

mitigated. In addition, the complementary improvement techniques can be considered as another option for liquefaction mitigation.

## 6.3. Recommendations for Future Work

Besides the accomplishment of the major objectives, there are many areas of this study which have yet to be fulfilled or improved. Following recommendations are made to advance the research on this subject.

All the analyses herein were performed under fully saturated conditions assuming two-phase mixture theory, despite the partially saturated conditions in the upper parts of the super levee layers. For the dynamic and consolidation analyses, this assumption can be adequately employed since the ground layers, which play the major role on the consolidation and dynamic behavior, are located below the water table, and are fully saturated. However, for the other analyses such as rainfall infiltration and seepage, the multi-phase formulations should be employed considering the unsaturated parts of the embankment layers.

In the analysis of the improved ground case, the limited ground settlement data during the preloading process was the only available data that can be applied for the parameter calibration of the improved zone. It is desirable to provide more in situ monitoring data, by which the simulation results can be properly verified.

In the dynamic strain localization analysis of soft clay samples, it is recommended to continue the analysis evaluating the effect of other relevant aspects, such as geometry, material parameters, and loading conditions, on the shear banding phenomenon.

In the present work, the dynamic analysis of the super levee has been performed regardless the presence of the building and structures on the super levee. However, it is worthwhile to conduct the analysis including the building and structural elements such as deep piles and foundations, and to evaluate the effect of strong ground motion on the structures and on the soil-structure interactions.

In addition, in order to evaluate the vulnerability of the super levee during the worst-case scenario of earthquake, it is required to consider the effect of various input ground motions, in terms of the durations and the peak accelerations. Furthermore, it is desirable to conduct a post-liquefaction analysis to evaluate the final values of the liquefaction-induced deformations.

# References


Adachi, T., and Oka, F., 1982. Constitutive equations for normally consolidated clay based on elasto-viscoplasticity. *Soils and Foundations,* 4, 57-70.

Adachi, T., Oka, F., Hirata, T., Hashimoto, T., Nagaya, J., Mimura, M., and Pradhan, T.B.S., 1995. Stress-strain and yielding characteristics of eastern Osaka clay. *Soils and Foundations*, 35(3), 1-13.

Aifantis, E.C., 1984. On the microstructural origin of certain inelastic models, *ASME. J. Engng. Mater. Tech.* 106, 326-330.

Aifantis, E.C., Oka, F., Yashima, A., Adachi, T., 1999. Instability of gradient dependent elasto-viscoplasticity for clay. *Int. J. Numer. Anal. Meth. Geomech.* 23 (10), 973-994.

Armstrong, P.J., and Frederick, C.O., 1966. *A mathematical representation of the multiaxial Bauschinger effect*, Report RD/B/N 731.

Barends, F.B.J., 1991. Interaction between ocean waves and seabed, *Proc. Int. Conf. on geotechnical Engineering for Coastal Development, Geo-Coast'91*, Yokohama, 1091-1108.

Barron, R.A., 1948. Consolidation of fine-grained soils by drain wells. *Transactions of the ASCE*, 113, 718-742.

Burland, J.B., 1990. On the compressibility and shear strength of natural clays. *Geotechnique*, 40(3), 329-378.

Chaboche, J. L., and Rousselier G., 1983. On the plastic and viscoplastic constitutive equations; part I and Part II. *J. Pressure Vessel Technol., Trans. ASME*, 105, 153-164.

Chai, J.C., Shen, S.L., Miura, N., and Bergado, D.T., 2001. Simple method of modeling PVD-improved subsoil, *Journal of Geotechnical and Geoenvironmental Engineering*, ASCE, 127(11), 965-972.

Chen, W.F., and Mizuno, E., 1990. *Nonlinear analysis in soil mechanics, Theory and Implementation*. Book published by Elsevier, Amsterdam, 13-51.

Cheung, Y.K., Lee, P.K.K., and Xie, K.H., 1991. Some remarks on two and three dimensional consolidation analysis of sand-drained ground. *Journal of Computer and Geotechnics*, 12, 73-87.

Cormeau, I.C., 1975. Numerical stability in quasi-static elasto/viscoplasticity. *Int. J. Numer. Meth. Engng.* 9, 109-127.

Dafalias, Y., 1982. Bounding surface elastoplasticity-viscoplasticity for particulate cohesive media. *Proc. of the IUTAM Sym. on Deformation and Failure of Granular Materials*, 97-107.

de Borst, R., Sluys, L.J., 1991. Localization in a Cosserat continuum under static and dynamic loading conditions. *Comp. Meth. Appl. Mech. Engng.* 90, 805-827.

Hadamard, J.J., 1903. *Lecons sur la propagation des ondes et equations de l' hydrodynamique*. Libraire Scientifique A. Hermann, Paris.

Hansbo, S., 1981. Consolidation of fine-grained soils by prefabricated drains. *Proc. of 10$^{th}$ International Conference of Soil Mechanics and Foundation Engineering,* 3, 677-682.

Hardin, B.O., and Drnevich, V.P., 1972. Shear modulus and damping in soils: design equation and curves. *Journal of Soil Mechanics and Foundations*, ASCE, 98, SM7, 667-692.

Higo, Y., Oka, F., Kodaka, T. and Kimoto, S. (2006): Three-dimensional strain localization of water saturated clay and numerical simulation using an elasto-viscoplastic model, *Philosophical Magazine,* 86(21-22), 3205-3240.

Hird, C.C., Pyrah, I.C., and Russell, D., 1992. Finite element modeling of vertical drains beneath embankments on soft ground. *Geotechnique,* 42(3), 499-511.

Hoizumi, A., 1996. *Mechanical behavior of clay during cyclic loading and elasto-viscoplastic model.* Master Thesis, Gifu University, (in Japanese).

Hunter, G.J., 2003. *The pre- and post-failure deformation behavior of soil slopes*. Doctoral thesis, University of New South Wales, Australia.

Hutchinson, J.W., 2001. Strain gradient plasticity theory revisited. *Material Science for 21$^{st}$ Century*, Japan, May 2001, vol. 1A. The Society of Material Science, 307-315.

Indraratna, B., and Redana, I.W., 1997. Plane strain modeling of smear effects associated with vertical drains. *Journal of Geotechnical Engineering*, ASCE, 123(5), 474-478.

Ishihara, K., 1996. *Soil behavior in earthquake geotechnics.* UK: Oxford University Press, 85-152.

Kaliakin, V.N., and Dafalias Y.F., 1990. Theoretical aspects of the elasto-plastic-viscoplastic bounding surface model for cohesive soils, *Soils and Foundations*, 30(3), 11-24.

Karim, M.R., and Oka, F., 2010. An automatic time increment selection scheme for simulation of elasto-viscoplastic consolidation of clayey soils. *Geomechanics and Geoengineering: an International Journal*, (to appear).

Katona, M.G., 1984. Evaluation of viscoplastic cap model, *Journal of Geotechnical Engineering*, ASCE, 110(8),1106-1125.

KG-NET, 2007. *Ground of Kansai area especially Osaka plain to Osaka bay*, Kansai Geo-informatics Research Committee: Shin Kansai Jiban, (in Japanese).

Kimoto, S., 2002. *Constitutive models for geomaterials considering structural changes and anisotropy*. Doctoral Thesis, Kyoto University.

Kimoto, S., and Oka, F., 2005. An elasto-viscoplastic model for clay considering destructuralization and consolidation analysis of unstable behavior. *Soils and Foundations,* 45(2), 29-42.

Kimoto, S., Oka, F., and Higo, Y., 2004. Strain localization analysis of elasto-viscoplastic soil considering structural degradation. *Computer Methods in Applied Mechanics and Engineering,* 193, 2845-2866.

Kimoto, S., Oka, F., Watanabe, T., and Sawada, M., 2007. Improvement of the viscoplastic potential and static yield function for the elasto-viscoplastic constitutive model. *Proc. of 62nd Annual Meeting of JSCE,* Hiroshima, 637-638, (in Japanese).

Kinki Regional Development Bureau, 2009. *Geotechnical investigation report of Torishima super-levee project*. Osaka, Japan (in Japanese).

Kokusho, T., Yoshida, Y., and Esashi, Y., 1982. Dynamic properties of soft clays for wide strain range. *Soils and Foundations,* 22, 1-18.

Kovacs, W.D., Seed, H.B., and Chan, C.K., 1971. Dynamic modulus and damping ratio for a soft clay. *Journal of Soil Mechanics and Foundations*, ASCE, 97, SM1, 59-75.

Kundzewicz, Z.W., and Takeuchi, K., 1999. Flood protection and management: Quo vadimus, *Hydrological Sciences Journal*, 44, 417-432.

Lavallee, J.G., St-Arnaud, G., Gervais, R., and Hammamji, Y., 1992. Stability of the Olga C test embankment. *ASCE Geotechnical Special Publication No. 31, Stability and Performance of Slopes and Embankments II*, Berkeley, California, Seed and Boulanger eds. ASCE, 2, 1006-1021.

Leroueil, S., Tavenas, F., Brucy, F., La Rochelle, P., and Roy, M., 1979. Behavior of destructed natural clays. *Journal of Geotechnical Engineering*, 115(6), 759-778.

Loret, B., Prevost, J.H., 1991. Dynamic strain localization in fluid-saturated porous media. *J. Engng. Mech.*, ASCE 117 (4), 907-922.

Maleki, M., Cambou, B., 2009. A cyclic elastoplastic-viscoplastic constitutive model for soils. *Geomechanics and Geoengineering: an international journal*, 4(3), 209-220.

Matsui, T., and Abe, N., 1985. Elasto-viscoplastic constitutive equation of normally consolidated clay based on flow surface theory. *Proc. of the 5th ICONMG*, 407-413.

Matsuo, O., 1996. Damage to river dikes, *Special issue of Soils and Foundations*, 235-240.

Mesri, G., and Choi, Y.K., 1979. Excess pore water pressure during consolidation. *Proc. 6th Asian Regional Conf. on SMFE*, 1, 151-154.

Mitchell, J.K., 1986. Practical problems from surprising soil behavior. 20th Terzaghi Lecture, *Journal of Geotechnical Engineering*, ASCE, 112(3), 259-289.

Modaressi, H., and Laloui, L., 1997. A thermo-viscoplastic constitutive model for clay. *Int. J. Numer. Anal. Meth. Geomech*., 21, 313-335.

Mühlhaus, H.B., Aifantis, E.C., 1991. A variational principle for gradient plasticity. *Int. J. Solid. Struct.* 28 (7), 845-857.

Needleman, A., 1988. Material rate dependence and mesh sensitivity in localization problems. *Comput. Methods Appl. Mech. Engrg.,* 67, 69-85.

Needleman, A., 1989. Dynamic shear band development in plane strain. *J. of Applied Mechanics*, 56, 1-9.

Ogisako, E., Nishio, S., Denda, A., Oka, F., and Kimoto, S., 2007. Simulation of triaxial compression tests on soil samples obtained from seabed ground in deep sea by elasto-viscoplastic constitutive equation. *Proc. of the Seventh ISOPE Ocean Mining & Gas Hydrates Symposium*, Lisbon, Portugal, Chung and Komai eds. ISOPE, 63-68.

Oka, F., 1992. A cyclic elasto-viscoplastic constitutive model for clay based on the nonlinear kinematic hardening rule. *Proc. 4th Int. Symposium on Numerical Model in Geomechanics,* Swansea, Pande and Pietruszczak eds. Balkema, 1, 105-114.

Oka, F., 2002. *3D liquefaction analysis considering a large deformation.* Research report, Kyoto University, Japan.

Oka, F., 2009. *Study on the deformation prevention technology of the super levee,* Kinki Regional Development Bureau, MLIT, Osaka, Japan (in Japanese).

Oka, F., Tavenas, F., and Leroueil, S., 1991. An elasto-viscoplastic FEM analysis of sensitive clay foundation beneath embankment. *Proc. 7th Int. Conf. on Computer Method and Advanced in Geomechanics*. Cairns, Beer, Booker, and Carter eds. Balkema, 2, 1023-1028.

Oka, F., Adachi, T., Yashima, A., 1994. Instability of an elasto-viscoplastic constitutive model for clay and strain localization. *Mech. Matererials,* 18, 119–129.

Oka, F., Adachi, T., Yashima, A., 1995. A strain localization analysis of clay using a strain softening viscoplastic model. *Int. J. Plasticity,* 11 (5), 523-545.

Oka, F., Yashima, A., Tateishi, A., Taguchi, T., and Yamashita, S., 1999. A cyclic elasto-plastic constitutive model for sand considering a plastic-strain dependence of the shear modulus. *Geotechnique*, 49(5), 661-680.

Oka, F., Yashima, A., Sawada, K., Aifantis, E.C., 2000. Instability of gradient-dependent elasto-viscoplastic model for clay and strain localization. *Comput. Meth. Appl. Mech. Engng.* 183, 67-86.

Oka, F., Kodaka, T., Koizumi, T., and Sunami, S., 2001. An effective stress based liquefaction analysis based on finite deformation theory. *Proc. 10th IACMAG*, Tucson Arizona, Desai et al. eds., Balkema, 1113-1116.

Oka, F., Higo, Y., and Kimoto, S., 2002a. Effect of dilatancy on the strain localization of water-saturated elasto-viscoplastic soil. *International Journal of Solids and Structures*, 39, 3625-3647.

Oka, F., Kodaka, T., and Tanaka, K., 2002b. 3-D liquefaction analysis to evaluate the stability of grid-shaped stabilized ground by deep mixing method, *11th Japanese Earthquake Engineering Symposium,* 1077-1080, (in Japanese).

Oka, F., Kodaka, T., and Kim, Y.S., 2004a. A cyclic viscoelastic–viscoplastic constitutive model for clay and liquefaction analysis of multi-layered ground. *Int. J. Numer. Anal. Meth. Geomech.,* 28, 131-179.

Oka, F., Furuya, K., and Uzuoka, R., 2004b. Numerical simulation of cyclic behavior of dense sand using a cyclic elasto-plastic model. *Proc. of Int. Symp. Cyclic Behavior of Soils and Liquefaction Phenomena,* Triantafyllidis ed., Balkema, 85-90.

Oka, F., Kodaka, T., Kimoto, S., Ichinose, T., and Higo, Y., 2005. Strain localization of rectangular clay specimens under undrained triaxial compression conditions. *Proc. 16th ICSMGE*, Osaka, 2, 841-844.

Oka, F., Feng, H., Kimoto, S., Kodaka, T., and Suzuki, H., 2008. A numerical simulation of triaxial test of unsaturated soil at constant water and air content by using an elasto-viscoplastic model. *Unsaturated soils: Advances in Geo-Engineering,* Toll, Augrade, Gallipoli, and Wheeler eds. Taylor and Francis Group, 735-741.

Pierce, D., Shih, C.F., and Needleman, A., 1984. A tangent modulus method for rate dependent solids. *Computer and Structures*, 18(5), 845-887.

Perzyna, P., 1963. The constitutive equations for work-hardening and rate sensitive plastic materials. *In Proc. of Vibration Problems*, Warsaw, 3(4), 281-290.

Potts, D.M., and Zdravkovic, L., 1999. *Finite element analysis in geotechnical engineering: theory*. UK: Thomas Telford.

Prevost, J.H., Loret, B., 1990. Dynamic strain localization in elasto-(visco)-plastic solids, part 2: plane strain examples. *Comput. Methods Appl. Mech. Engrg.,*, 83, 275-294.

Rice, J.R., 1975. On the stability of dilatant hardening for saturated rock masses. *J. Geophys. Res.* 80 (11), 1531-1536.

Rice, J.R., 1976. The localization of plastic deformation. *Theoretical and Applied Mechanics*, 14th ICTAM Symposium, Koiter, ed., North-Holland, Amsterdam, 207-220.

Roscoe, K.H., Schofield, A.N., and Thurairajah, A., 1963. Yielding of clays in states wetter than critical. *Geotechnique*, 13(3), 211-240.

Sawada, M., 2008. *A cyclic elasto-viscoplastic constitutive equation and visualization of microstructures for soils,* Master Thesis, Kyoto University, (in Japanese).

Schrefler, B.A., Sanavia, L., Majorana, C.E., 1996. A multiphase medium model for localization and post localization simulation in geomaterials. *Mech. Cohes-Fict. Mater.* 1 (1), 95-114.

Seed, H.B., Wong, R.T., Idriss, I.M., and Tokimatsu, K., 1986. Moduli and damping factors for dynamics analyses of cohesionless soils. *Journal of Geotechnical Engineering*, 112(11), 1016-1032.

Takeuchi, K., 2002. Flood management in Japan: from rivers to basin. *Proc. of the International Workshop on Non-structural Measures for Water Management Problems,* Simonovic, S.P. ed., UNESCO, Paris, 37-44.

Terzaghi, K., 1944. Ends and means in soil mechanics. *Engineering Journal*, Canada, 27, 608-613.

Wang, G.X., and Kuwano, J., 1999. Modeling of strain dependency of shear modulus and damping of clayey sand. *Soil Dynamics and Earthquake Engineering*, 18, 463-471.

Watanabe, T., Oka, F., Kimoto, S., Higo, Y., and Yabuki, T., 2007. Simulation of cyclic triaxial tests of unsaturated silt by elasto-viscoplastic model. *Proc. 62th Annual Meeting of JSCE*, Hiroshima, 211-212, (in Japanese).

Zbib, H.M., and Jubran, J.S., 1992. Dynamic shear banding: a three-dimensional analysis, *Int. J. Plastic.* 8, 619-641.

Zienkiewicz, O.C., and Bettes, P., 1982. Soils and other saturated media under transient, dynamic conditions: general formulation and the validity of various simplifying assumptions. *Soil Mechanics Transient and Cyclic Loads*, John Wiley & Sons, 1-16.

Zienkiewcz, O.C., Chang, C., and Bette, P., 1980. Drained undrained consolidating dynamic behavior assumptions in soils. *Geotechnique*, 30(4), 385-395.